ADVANCED SENSING TECHNOLOGIES: FROM VANADIUM DIOXIDE MEMS RESONATORS TO POLYPROPYLENE FERROELECTRET NANOGENERATORS

By

Yunqi Cao

A DISSERTATION

Submitted to
Michigan State University
in partial fulfillment of the requirements
for the degree of

Electrical Engineering – Doctor of Philosophy

2019

ABSTRACT

ADVANCED SENSING TECHNOLOGIES: FROM VANADIUM DIOXIDE MEMS RESONATORS TO POLYPROPYLENE FERROELECTRET NANOGENERATORS

By

Yunqi Cao

This thesis presents fundamental and applied research studies designed to enable smart material-based advanced sensing technologies including the use of vanadium dioxide (VO_2) thin films in resonant frequency tuning methods, and the self-powering/energy harvesting capabilities of polypropylene ferroelectret (PPFE) polymers. The large compressive stress generated from VO_2 thin films during its insulator-to- metal transition (IMT) has been investigated in recent years for thermally actuated MEMS actuators. This same mechanism can be used to generate axial stress that produces large shifts in resonant frequencies. Nevertheless, taking full advantage of all benefits of this technique for tunable devices requires a fundamental understanding of the mechanisms involved and the influences of different parameters; such as structural aspect ratios, boundary conditions, buckling status, and actuation methods. In this work, VO_2-based MEMS bridge and cantilever resonators were developed, and their resonant frequency shifts were characterized with respect to these parameters. It is found that residual thermal stress during the fabrication process is responsible for different buckling states in bridge structures. Bi-directional tuning for a monotonic input is observed in pre-buckled structures, which is related to bending moments and actuation methods. A ferroelectret nanogenerator is also introduced in this work as a new tuning technique to provide a programming current that allows fast switching between different resonant frequency states. This demonstrates the potential use of self-powered tuning actuation of MEMS resonators. Studies of VO_2-based resonators on the power consumption and the device time constant also pave the way for integrating MEMS devices with piezoelectric energy harvesters as impact sensors.

With the goal of enabling self-powered sensing technologies, a series of studies designed to understand the parameters that determine the electromechanical coupling in ferroelectret nanogenerators are presented. The electromechanical response of the active material is analyzed based on fundamental working principles of dipole moments. A lumped model is proposed, which is developed from constitutive equations and validated with experiments. The robustness of the device is verified through a series of tests including mechanical repeatability, thermal stability, and humidity resistance. The energy conversion efficiency and maximum power transfer condition are determined under periodic mechanical input, and a complete energy harvesting system with a fully integrated power management circuit is proposed for providing DC power output to effectively charge lithium-ion batteries or power small electronics.

To those who always support, encourage, and trust me.

TABLE OF CONTENTS

LIST OF TABLES

LIST OF FIGURES

CHAPTER 1

INTRODUCTION

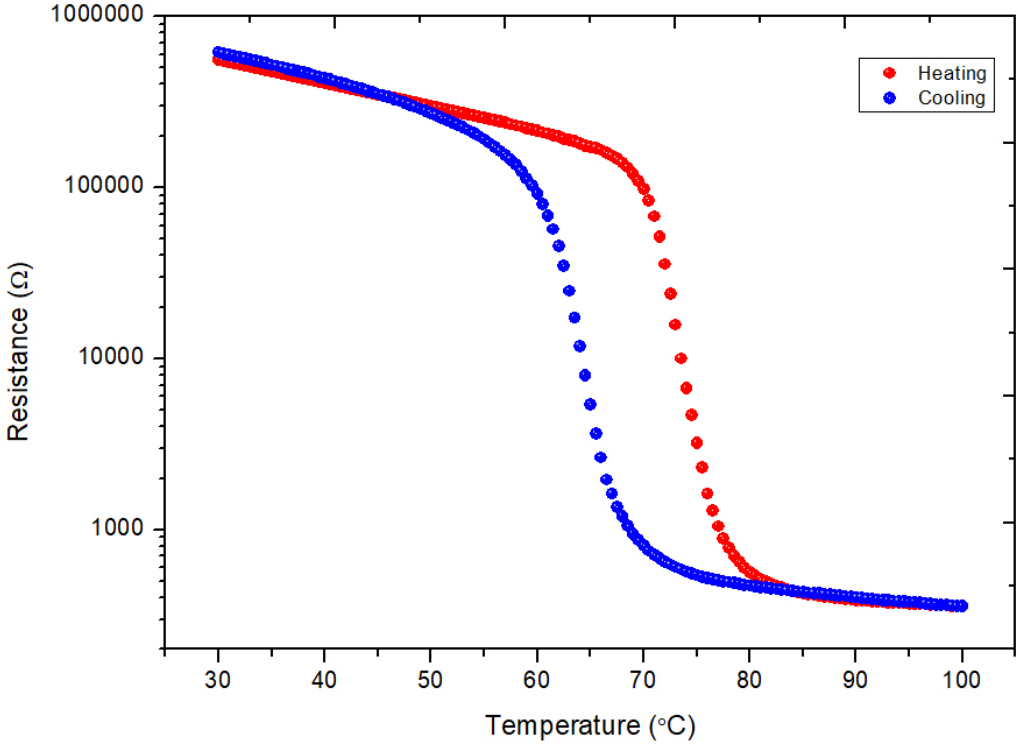

Figure 1.1 Resistance of continuous VO_2 film as a function of temperature during a full heating and cooling cycle [1].

Vanadium dioxide (VO_2) undergoes a fully reversible hysteretic first order solid-to-solid phase transition in which the crystallographic structure changes from monoclinic (M) phase to rutile (R) phase. This structural phase transition comes hand-in-hand with an electronic phase transition, in which the electrical resistance changes drastically. Thus, the phase transition is commonly referred to as a Mott-Peierls transition, where both an insulator-to-metal transition (IMT) and a structural phase transition (SPT) begin to occur almost simultaneously at a temperature of ~ 68 °C [2] upon heating, and typically spans between

5-15 °C as shown in **Figure** 1.1,

depending on the microstructural properties of the film and its composition. The phase transition has been demonstrated to be induced in multiple ways including heat conduction [4], external electric field [5], optical radiation [6], etc. More recently, VO_2-based system-on-chip micrometer-sized devices have been developed, including electrical switches [7], smart windows[8] and optical modulators [9, 10], MEMS mirrors [11, 12], and RF resonators [13, 14]. Correlated with the IMT, a structural phase transition (SPT) is also observed at the same time due to the crystal structural rearrangement. The change in average spacing of vanadium ions from M-phase to R-phase [15] induces a large strain energy density, which enables large deflection [16, 11] and fast responsivity in VO_2-based bimorph MEMS actuators.

Figure 1.2 shows the crystal structure of VO_2 in different phases. In the low-temperature monoclinic phase, the separations between two adjacent vanadium atoms along with the

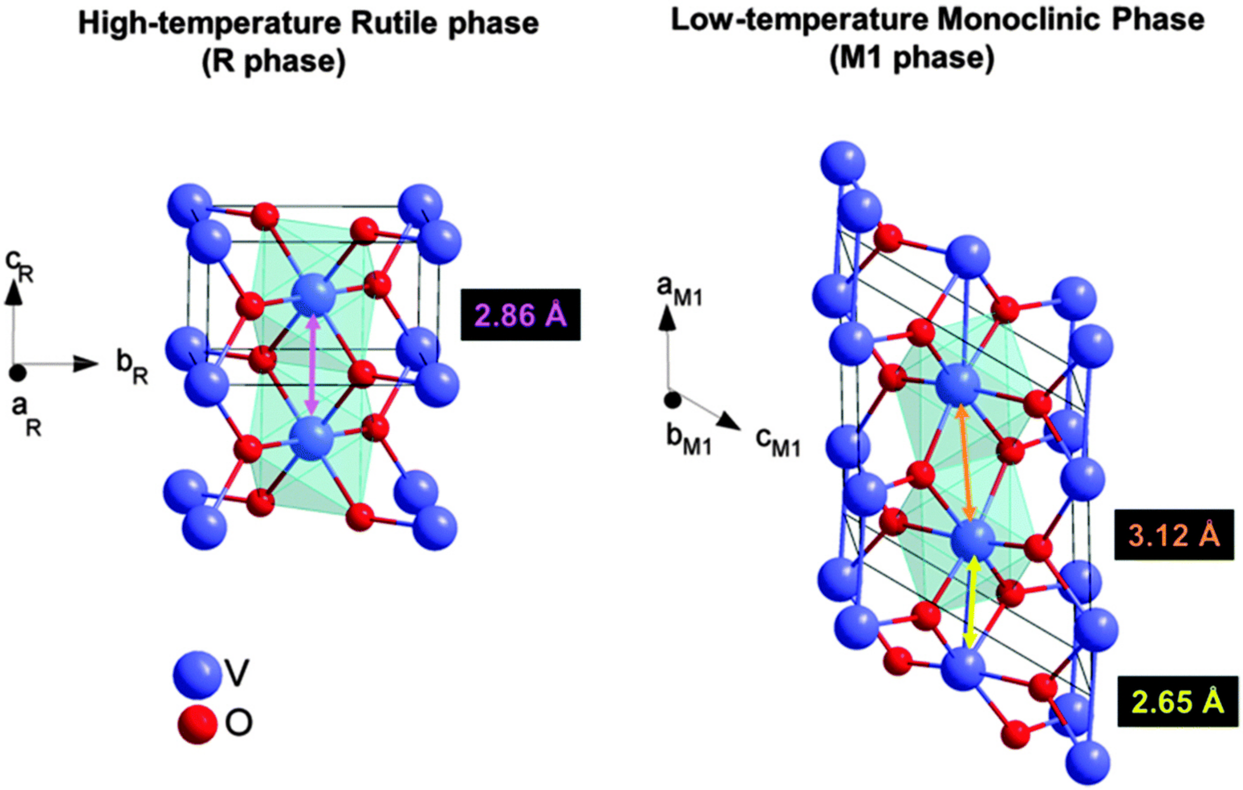

Figure 1.2 Crystal structure of VO_2 in rutile phase (left) and monoclinic phase (right). [3]

a_{M1}=2c_R axis alternate with 2.65Å and 3.12Å, thus the VO_2 is in a distorted structure with the doubling of the unit cell. On the other hand, the rutile phase, or the tetragonal phase, occupies a highly ordered body-centered cubic (BCC) structure with vanadium atoms equally spaced at a distance of 2.86Å.

Therefore, the SPT of VO_2 leads to a crystal volume contraction of about 1.7% [17] along the c_R axis. The consequently induced compressive stress can be implemented into active, fully reversible resonant frequency tuning techniques, which could be used to compensate frequency shifts due to performance degradation or random structural variations. Depending on the resonator structure, the resonant frequency shift can be induced by geometric distortion or residual axial stress [18]. The inherent hysteretic behavior also enables the programmability within multiple memory states [19, 20, 21]. **Figure** 1.3 shows the resonant frequency of a VO_2-based MEMS bridge as a function of temperature, where the separation between heating and cooling loops enables the programmability of multiple mechanical states. However, most of the efforts are focused on demonstrating larger frequency reconfigurability using simpler structures or methods, but little attention has been paid to the influence of these stress levels when added to already existing large residual stress with different distributions.

In the first part of this work, the influence of the SPT in VO_2 thin film coatings has been studied on MEMS resonators with both cantilever and bridge structures. During the phase transition, the resonant frequency shift is induced by the compressive stress generated by the thermal expansion coefficient mismatch between VO_2 and SiO_2 films. By comparing the relative resonant frequency shift of cantilevers and bridges with different aspect ratios, it has been found that a more stress sensitive structure (bridge) leads to a larger tuning range due to a high level residual axial stress, while the smaller frequency tuning range in cantilever is determined by the large geometric change. For bridge structures, small variations in the device manufacturing process produced three different buckling profiles: upward, downward and bell-shaped. The resonant frequency tuning direction is found to be heavily dependent

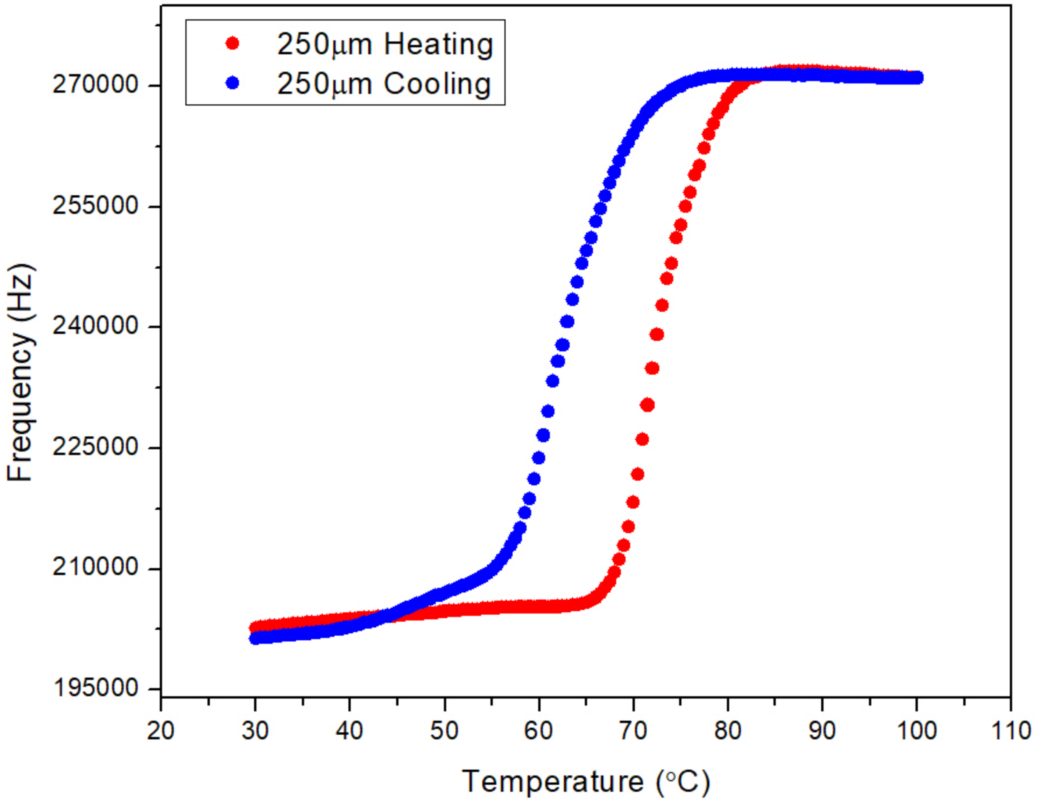

Figure 1.3 The resonant frequency of a 250 μm VO_2-based MEMS bridge as a function of temperature during a full heating and cooling cycle.

on the buckling orientations, which is associated with different stress interfaces between VO_2 and SiO_2 layers. Different actuation methods (electrical resistive heating and substrate heating) are used and the results showed very different tuning behavior. The actuation dependent frequency tunability can be attributed to the different boundary conditions, where a turning point in the frequency curve (see **Figure** 1.4) occurs when a large deflection transitions the boundary condition from "fixed-fixed" to "fixed-pinned" during the VO_2 phase change. In order to understand the energy requirements for actuation and explore the possibility of integrating MEMS resonators with piezoelectric impact sensors for the application of Head Impact Telemetry System (HITS); we introduced polypropylene ferroelectret nanogenerator

(FENG) as the transducer to convert the mechanical energy to electrical energy. A programming current pulse generated by the FENG device is sent through a monolithically integrated resistive heater, which increases the temperature of the device and induces the phase transition of the VO_2 thin film as shown in **Figure** 1.5. The pulse could come from a charged capacitor or from the FENG device directly. Next, based on the understanding of single resonator device, the potential application of VO_2-based MEMS devices as second-order bandpass filters (kHz band) with tunable band selectivity and adjustable bandwidth has also been demonstrated by using two identical on-chip microresonators excited and measured at the same time.

This work continues with the exploration of the sensing and energy harvesting capabilities of FENG. FENG is a flexible multilayer structure device with the ability of converting

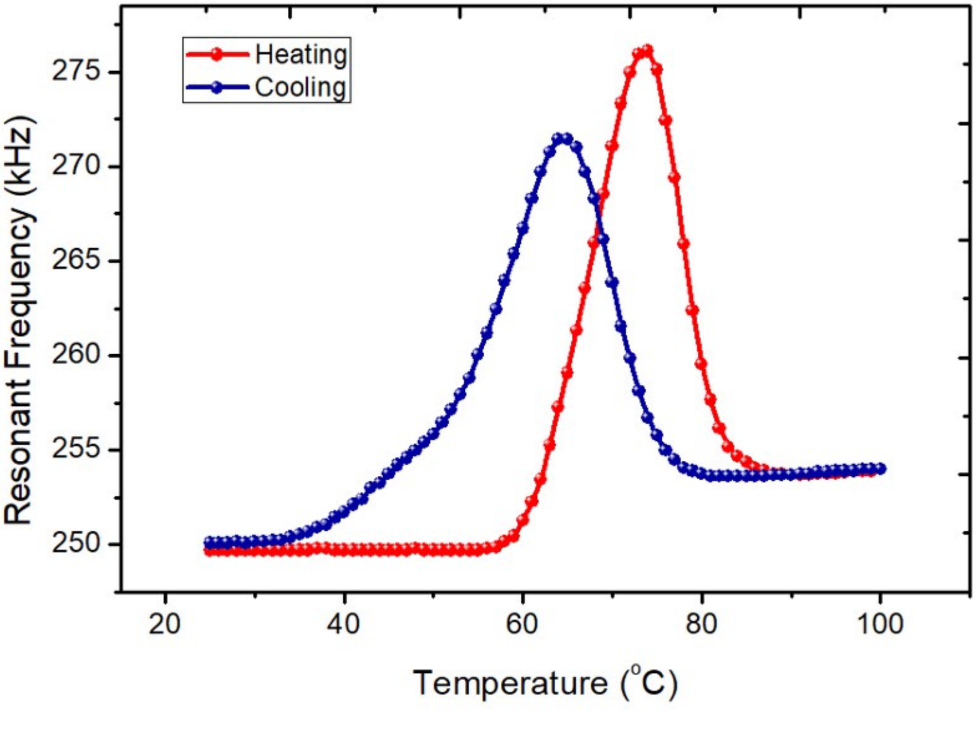

Figure 1.4 The resonant frequency of a 300 µm VO_2-based MEMS bridge as a function of temperature during a full heating and cooling cycle, where a turning point is observed at around 75 °C.

mechanical energy to or from electrical energy. The active material that exhibits the direct and inverse piezoelectric effect is a dielectric and elastic film with full-of-cell type structure. Despite that the FENG has the similar electro-mechanical response as piezoelectric nanogenerator (PENG), the fundamental working principles between these two devices are different. By applying an external mechanical force, the thickness of the porous midsection region of the polypropylene ferroelectret (PPFE) film decreases. The piezoelectricity of FENG mainly arises from the relative movement of positive charge surface to negative charge surface within each individual ellipsoid void. **Figure** 1.6 shows the working principle of FENG under an external mechanical load, the induced free charges at metal electrodes

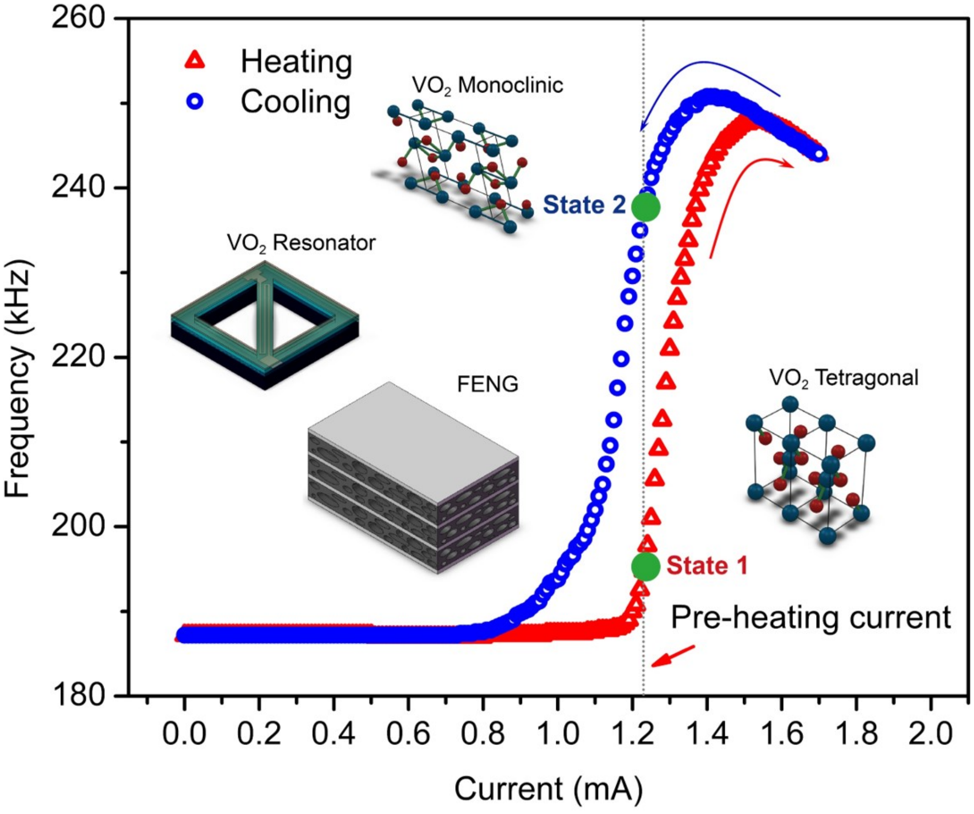

Figure 1.5 Programming resonant frequency of VO$_2$-based MEMS resonator through electric pulse generated by FENG [20].

produce an open circuit voltage across the device. This work presents a comprehensive study that uses the fundamental working principles of dipole moments in ferroelectret polymers to describe the energy conversion mechanism. The study addresses discrepancies in voltage measurement caused by instruments with different internal resistance and sampling rate. A lumped parameter model is also proposed and validated to explain the impedance mismatch at the device-machine interface. Based on the flexibility of the device, FENG-based bending sensors for human motion and structural distortion monitoring are also investigated. Theoretical analysis based on constitutive electro-mechanical equations and bi-layer bending mechanics provide a detailed understanding of the sensing mechanism and its applicability. Measured responses are evaluated in terms of instantaneous and average voltage, which reveal a more comprehensive understanding of the bending dynamics and show great agreement with theoretical predictions. The robustness of the material is also investigated in

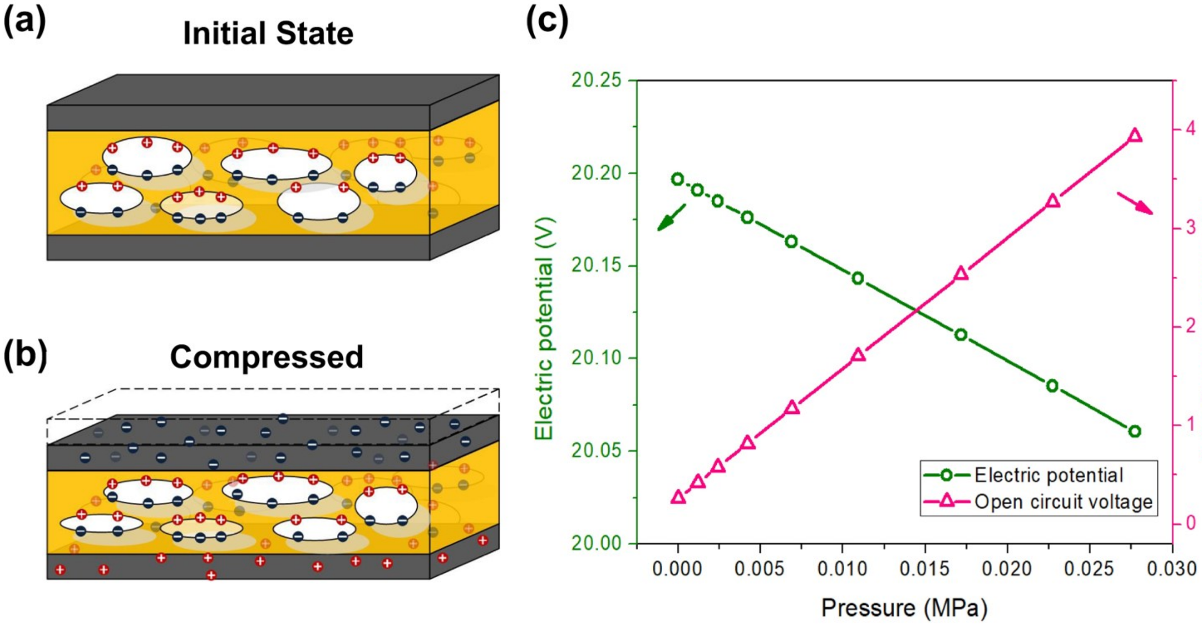

Figure 1.6 Piezoelectricity of FENG. Working principle of ferroelectric nanogenerator: (a) no external stress is applied. (b) when external boundary load is applied, the polarization field due to internal dipoles decreases and free induction charges is accumulated on metal electrodes. (c) FEM results of changes in electrode potential at the polymer-metal boundary and open circuit voltage arise from accumulated charges.

terms of mechanical repeatability, thermal stability, and humidity resistance. A new sensor configuration based on the polarity of piezoelectric materials is also proposed for detecting the structure deformation with 2D directional information.

Applying flexible materials for energy scavenging from ambient mechanical vibrations is a clean energy solution that can help alleviate electrical power demands in portable devices and wearable electronics. A fundamental study on FENG and its interface with self-powered and energy storage systems is also presented in this work. A single-layered FENG device has been used for characterizing the device's output voltage, current, transferred charge, and energy conversion efficiency. The potential capability of harvesting mechanical energy and delivering to system load is demonstrated by integrating the device into a fully integrated power management system. The theory for determining the harvested energy that is ultimately delivered to external electronic loads (or stored in a battery) is also discussed.

1.1 Problem Description and Motivation

There has been plenty of research progress in increasing resonant frequency tuning range, $f \cdot Q$ product, and decreasing power consumption in MEMS resonators. However, fundamental research on understanding stress-induced frequency shifts in bimorph MEMS resonators with different structures has not been as intensive. Due to different structural boundary conditions, the SPT of VO_2 film can induce either a large amount of residual axial stress in clamped-clamped bridges or a large deflection in clamped-free cantilevers with stress only concentrated in the vicinity of the anchor. Due to the high stress sensitivity in bridge structures, small variations in the manufacturing process –which leads to different buckling profiles and orientations– plays a major role in frequency shifts and tunability. Addressing this issue requires understanding resonant frequency shifts in a buckled structure; which is also obtained in this work. The work is extended to explore the possibility of combining VO_2 MEMS resonators with piezoelectric sensors for an integrated HITS system. The en-

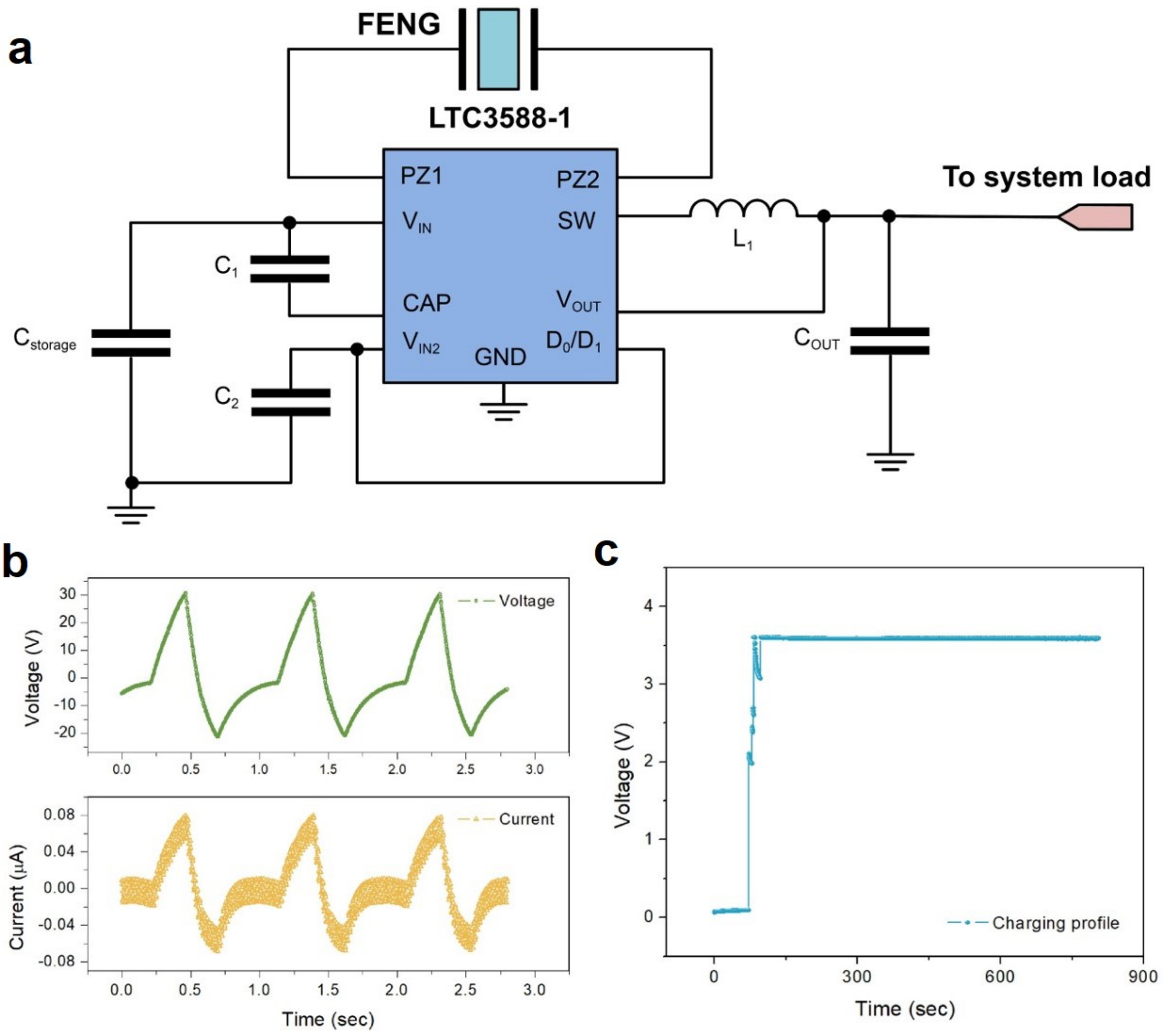

Figure 1.7 (a) A complete energy harvesting system for converting random mechanical energy to DC electric output for battery charging. (b) AC electric output generated from FENG device. (c) DC electric output delivered from the power management system to system load.

ergy consumption of VO_2-based MEMS resonators and the impedance match between FENG device and resistive load becomes essential in this application. We further exploited the self-powered sensing and the energy harvesting capabilities of FENG. Since the piezoelectricity FENG comes from engineered macro dipoles –which are different from traditional atomic level dipoles–, theoretical explanations are needed for determining the direct and transverse electromechanical response under external mechanical inputs. From the high piezoelectric coefficient of FENG, we describe the energy harvesting capability of converting ambient mechanical energy to electric energy. Practical applications require a complete power management system for delivering a DC power to rechargeable batteries or commercial electronics, which is also discussed in this work.

To summarize, the contributions of this work include:

- Determination of the dominating effect of resonant frequency tuning for VO_2-based MEMS resonators with different structures
- Evaluation of the discrepancies in the first mode resonant frequencies caused by thermal stress in VO_2-based MEMS resonators with fully integrated metal heaters
- Illustration of the influence on resonant frequency tuning in terms of different buckling orientations and profiles as well as the actuation method dependency
- Comparison of using different thermal actuation methods (conductive and resistive (i.e. Joule) heating), in resonant frequency tuning of pre-buckled bridge resonators
- Studies of the power consumption of programming resonant frequency status in VO_2-based MEMS resonators and the device thermal time constant
- Demonstration of a new frequency tuning method in VO_2-based MEMS resonators by using a piezoelectric transducer
- Demonstration of the potential application of VO_2-based bandpass filter; Proposal of a new HITS system by combining VO_2-based MEMS resonators and ferroelectret nanogenerators
- characterization of FENG in terms of short circuit current, open circuit voltage, output charge, and energy conversion efficiency

- Design of a platform for developing self-powered tactile sensors, and development of the lumped parameter model for predicting electromechanical behavior under different resistive loads
- Influence of testing instrumentation on the measurement of the electric output of FENG
- Studies on the potential use of PPFE as a bending sensor, including the comparison of different evaluation methods for a better understanding of the transverse piezoelectric effect
- Development of a complete energy harvesting system for collecting ambient random mechanical energy and charging solid-state batteries

1.2 Thesis Statement

This work presents studies on resonant frequency tuning of VO_2-based bimorph MEMS resonators with different structures; and the development of nanogenerator based tactile sensors, bending gauges, and energy harvesters. The contributions mentioned above can be circumscribed within the fields of sensing technologies based on VO_2 and FENG devices.

Thesis Statement: *Understanding the tuning and programmability of different* VO_2*-based MEMS resonator structures in terms of beam mechanics, device time constant, bandwidth tunability, power consumption, and actuation methods allows for an optimal integration with self-powering sensing technologies; thus enabling new approaches for the design of impact and tactile sensors, bending gauges, and energy harvesters.*

1.3 Overview of Research Contributions

In this thesis, the contributions listed in **Section 1.1** will be presented. As an overview of the work done, two different structures of VO_2-based MEMS resonators have been successfully designed, fabricated and tested. The bridge structure has been proven to be more stress sensitive and therefore results in a larger frequency tuning range compared to a cantilever structure. The resonant frequency tuning behavior is also found to be heavily dependent on the prebuckled state of bridge resonators. Comparison between different actuation methods are also carried out and the discrepancy of frequency tunability is found to be related to a transition of the boundary condition caused by different actuation methods. The power consumption of programming resonant frequency states of a VO_2-based resonator is analyzed by integrating with FENG as a HITS system. The potential application of implementing VO_2-based MEMS resonators into bandpass filters has been demonstrated and the theoretical maximum tuning range of bandwidth, Q-factor, and selectivity have also been carried out. The electromechanical responses of FENG under different external mechanical inputs are modeled based on the working principle of dipole moments and the constitutive equations of piezoelectric materials. FENG-based tactile sensor arrays and bending gauges are developed and modeled for impact force distribution and deflection monitoring respectively. Characterizations of FENG have been carried out in order to determine the output power and energy conversion efficiency. A FENG-based energy harvester is successfully developed with an integrated universally adapted power management system, which can be used for battery charging or powering electronics.

1.4 Dissertation Outline

The following chapters of this thesis are organized as following: **Chapter 2** presents a comprehensive background on active tuning techniques of MEMS resonators, flexible physical sensors, and energy harvesters. **Chapter 3** introduces the design, simulation, and fabrication of VO_2-based MEMS resonators with different structures as well as the manufacturing process of FENG device. In **Chapter 4**, The influence of VO_2 thin film on resonators of different structures are first presented, the influence of different buckling profiles and orientations on the resonant frequency shifts are also addressed in the following section, different actuation methods have been found to result in different tuning patterns as well. Next, the programmability of MEMS resonators through FENG and VO_2 is discussed. The studies on the device time constant, energy consumption and impact activation threshold are performed throughout the following sections. Based on a comprehensive study of single resonator devices, a prototype of VO_2-based MEMS bandpass filter is proposed in the last section. **Chapter 5** reports the comprehensive study on the working principle of FENG and explains the discrepancies in voltage measurements caused by instruments, the dynamic and static force sensing are also discussed in this chapter. **Chapter 6** presents a self-powered bending sensor using the transverse piezoelectric effect of FENG, the theoretical analysis is also carried out based on constitutive questions of piezoelectric materials. A fully integrated complete energy harvesting system is proposed in **Chapter 7**, where the FENG has been used to collect random mechanical energy and output regulated DC voltage by a power management system. Finally, **Chapter 8** summarizes the contributions of this work.

CHAPTER 2

BACKGROUND

2.1 MEMS Resonators

Performance of electronic devices is often determined by the stability and accuracy of their internal clocks and frequency reference circuits. For example, the navigation speed and precision of a global positioning system (GPS) significantly depends on its internal synchronous clock[22]. However, to implement this technology into our portable devices such as mobile phones or smartwatches, quartz crystal-based resonators are too large and energy-consuming for this application [23]. Besides clocking applications, RF communications also benefit from component miniaturization down to the micro-scale. In modern signal processing and transceiver technologies, electromechanical resonators have been widely implemented in RF circuits (e.g. oscillators, mixers, and filters) and sensing (e.g. temperature, mass, and humidity) applications [24, 25]. Their small size is a key advantage, which enables scaling for transceiver miniaturization with ultra-high $f \cdot Q$ product as shown in **Figure** 2.1. Sensitivities as high as 7×10^{-21} g and 13.89 pmK^{-1} have also been demonstrated for MEMS resonators used as mass and temperature sensors, respectively [24, 25]. In order to improve the quality and reliability of the latest developed wireless communication standards (e.g. code division multiple access (CDMA), global system for mobile communication (GSM), 3rd generation (3G), and currently using 5G [27], the performance requirements for resonators become more and more rigorous. Although quartz crystal-based resonators provide high resonant frequencies and Q-factor, the footprint and energy consumption limitations mentioned earlier still exist. Bulk acoustic wave (BAW) mode of vibration is usually preferred than a surface acoustic wave (SAW) mode, but the miniaturization technologies for incorporating a bulk quartz resonator for on-chip systems is not trivial, expensive, and still not capable

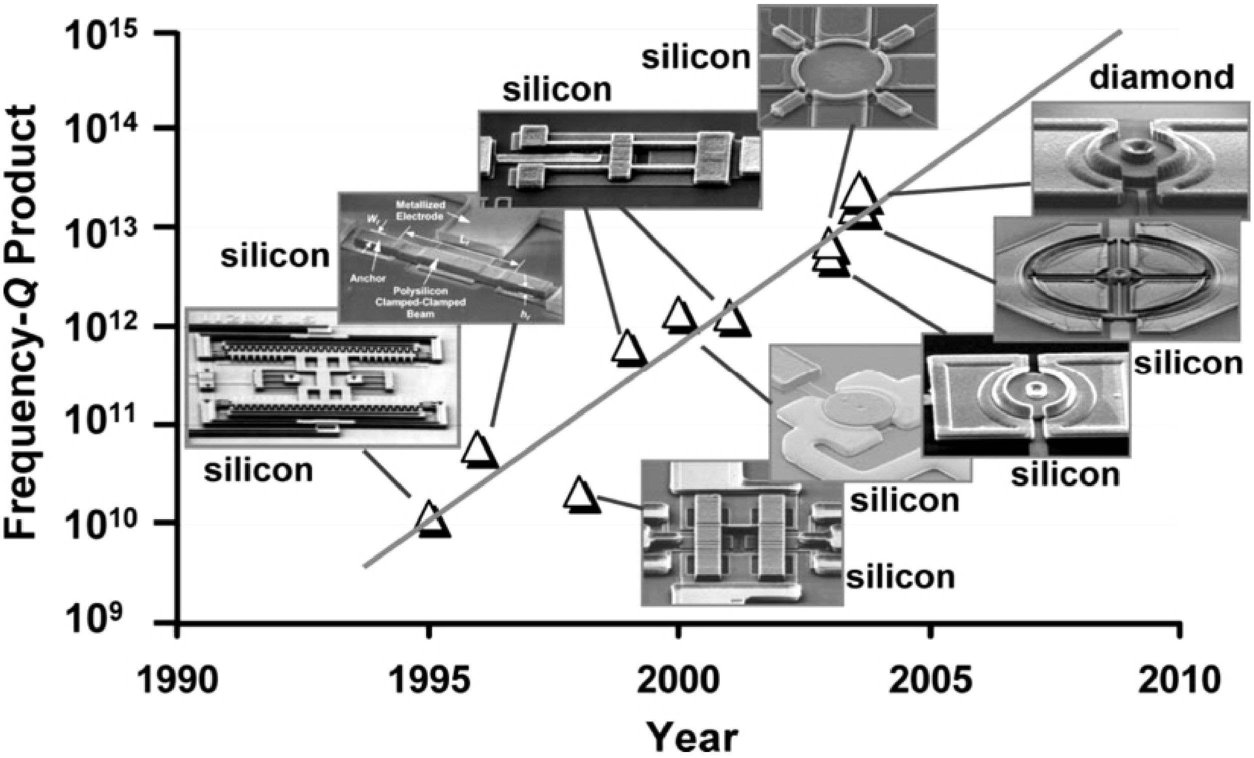

Figure 2.1 Timeline of growing $f \cdot Q$ product, a common figure of merit of resonators, from 1990 to 2010 [26].

of reducing board size implementation and power consumption to the levels that can be obtained using RF MEMS. The compatibility of quartz resonators with integrated circuit (IC) packages and the degradation in device performance (i.e. lowering Q-factor with device aging) are also major concerns. In addition, the poor shock-proof capability [28] and low energy efficiency of quartz resonators limits their applications in portable devices.

The number of applications for MEMS resonators has expanded as the technology has matured. Progress in micro-fabrication processes, design, and materials synthesis has made possible the cost-effective integration of micro-electro-mechanical resonators into electronic circuits. MEMS resonator technologies are commonly preferred over their predecessor technologies which are based on the quartz crystal-based oscillators [29]. Main advantages of MEMS include (i) small size, (ii) feasibility for on-chip integration of IC active or processing circuitry, (iii) accurate timing synchronization with external devices, and (iv) low power consumption. Table 2.1 provides a comparison between quartz crystal and SiTime's silicon-

Table 2.1 A comparison of quartz crystal and SiTime's silicon MEMS resonators[28].

Features	Quartz crystal resonator	MEMS resonator
size	2-5 mm	400µm
Frequency	1-80 MHz	1-50 MHz
Resonant Q ($\times 10^3$)	100-200	75-150
COMS integration	No	Yes
Packaging	Ceramic or metal	Plastic
Aging in first year	3-5 ppm	3 ppm
Compensated temperature stability	1-10 ppm	1-10 ppm
Shock immunity	Poor	Good
Fabrication cost	High	Low

based MEMS resonator.

2.2 Frequency Tuning Technologies

With the progress achieved in micro-fabrication technologies, MEMS resonators with complex structures and different degrees of freedom have been successfully designed and fabricated for applications with ultra-high resolutions. However, MEMS resonators still suffer from manufacturing defects and device degradation; and face particular application-specific challenges such as channel switching and frequency selection. Resonant frequencies in MEMS resonators is determined by many factors, such as geometry, material property, stress and strain, surface roughness, etc. Multiple efforts have been made to stabilize the resonant frequency throughout the lifetime of MEMS resonators in order to compensate for the frequency shift caused by fabrication flaws or aging. Hermetic packaging has helped in solving these issues but at the expense of significantly increasing the production cost of MEMS resonators [30]. Thus, frequency tunability becomes an alternative way for compensating frequency shifts in these devices, and to allow multiple channel operation for a single device [31]. The tuning technologies can be generally categorized into two types: passive tuning and active tuning. Passive tuning is usually an irreversible method since it usually relies on the use of focused ion beam (FIB) and pulsed laser deposition (PLD) techniques, which permanently

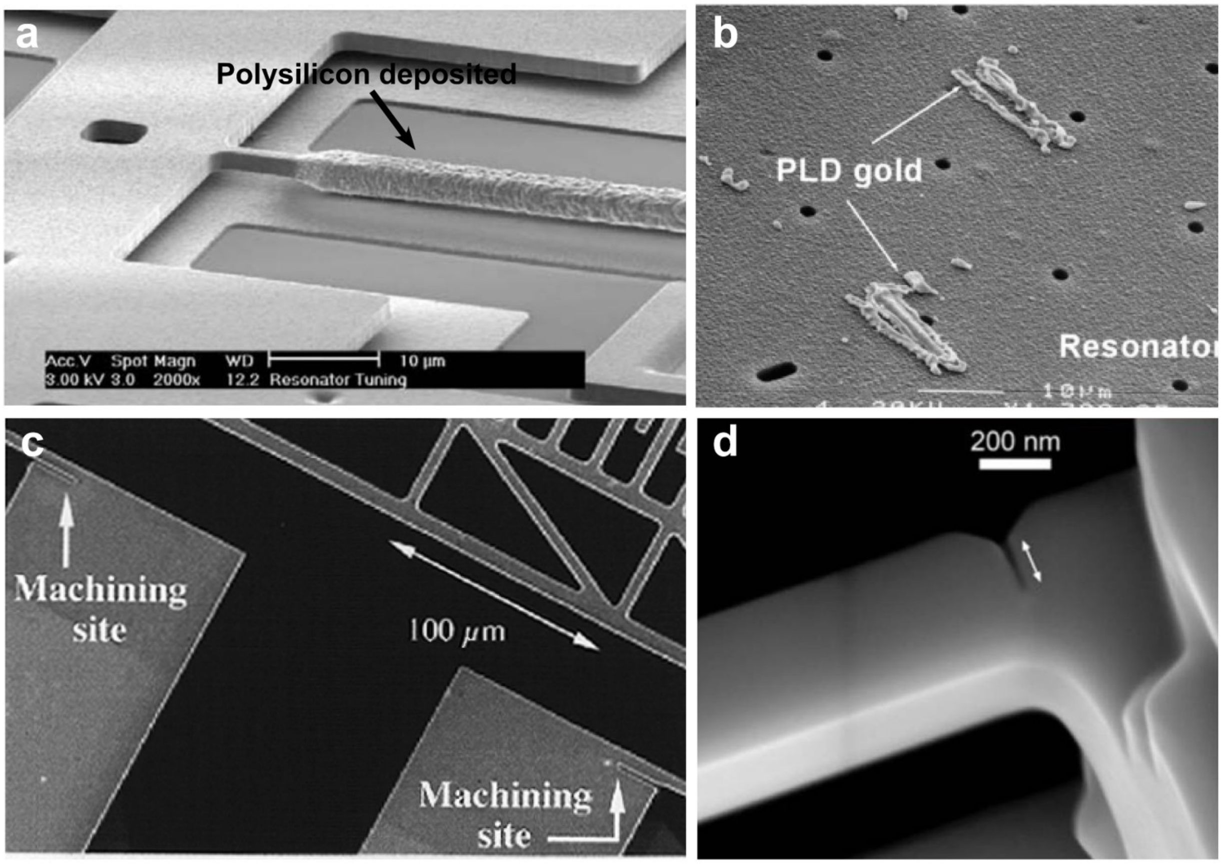

Figure 2.2 Examples of post-fabrication techniques: (a) Selective deposition of polysilicon on a comb-drive resonator[34]. (b) Two big PLD gold pieces from two-layer shots deposited on the surface of a microresonator[35]. (c) Device after FIB machining operation[36]. (d) Three-dimensional shape control of various device structures.[37]

shifts the resonant frequency towards the desired value. On the other hand, active tuning methods allow for frequency shifts in a fully controllable way. Some of these tuning methods involve the implementation of MEMS switches or varactor devices with electro-thermal [32] and electrostatic [33] tunings.

2.2.1 Post Fabrication

Post-fabrication tuning is considered to be a passive tuning method. It is often used to compensate for the resonant frequency shift caused by manufacturing defects. They permanently alter the resonant frequency and therefore no further energy is required for resonant frequency tuning during the lifetime of the device. However, they are not able to perform real-time tuning. Daphne Joachim, et al developed a set of tunable comb-drive resonators by selectively depositing polysilicon to their rotors [34]. The deposition was done through electrically heating the resonator in a silane ambient. The newly deposited material successfully increased the resonant frequency of each individual device from 0.7 to 2%. **Figure** 2.2a shows an SEM image of selective deposition of polysilicon on a comb-drive resonator. The resonant frequency shift for the sample presented is 1.96%. In addition, PLD technique is also introduced for tuning the resonant frequency by adding extra mass. **Figure** 2.2b shows two gold pieces deposited on the microresonator surface, this fine-tuning method can offer a tuning resolution of 0.5% per laser shot. R.R.A. Syms et al developed a strategy for permanently tuning the resonant frequency of a comb-drive electrostatic resonator [36]. The resonant frequency is altered by tuning the suspension stiffness and resonant mass through a focus ion beam (FIB) micromachining process (see **Figure** 2.2c). The resonant frequency tuning can also be achieved by three-dimensional shape control. D Vick et al. reported a frequency tuning method based on the FIB milling process. The ion impingement coming from multiple directions enables sculpting the shape of the device, such as notching and tapering. **Figure** 2.2d shows the three-dimensional control of device structures. The reshaping tuning technique can also be achieved by selective etching [38], local thermally-assisted chemical reaction [39], and localized annealing [40], etc. However, such tuning process has certain limitations. Firstly, passive tuning is an irreversible process and can only provide a onetime permanent tuning. Secondly, the tuning range is limited since either the reshaping process or the deposition/etching process can only provide a fine-tuning. For stress-sensitive resonators, the off-targeted resonant frequencies are often induced by the non-uniformity of the stress level during the fabrication process, in which passive tuning method may not be able to compensate that. Thirdly, the passive tuning method cannot provide real time tuning for applications such as wireless communication which requires a fast channel switching capability. Moreover, complicated post-fabrication processes inevitably increase the cost.

2.2.2 Electrical Tuning

The electrical tuning mechanism is a circuit-level active tuning method. It tunes the resonant frequency by manipulating different electrical loads. **Figure** 2.3a shows an example electrical tuning method based on MEMS technology [41]. The tuning circuit consists of three segments of conductors with different lengths. By changing the bias voltage on the MEMS switches, the effective length of the conductive segment can be switched from one length to another. For this design, three distinct resonant frequency states can be achieved. The circuit-level tuning can also be realized by creating a feedback loop, see **Figure** 2.3b. This tuning method utilizes the output current to generate a displacement or acceleration signal [42]. The generated signal is then transformed into a tuning signal which is applied to the resonator through an additional feedback signal port in order to modify the mechanical stiffness of the resonator. This tuning method provides a tuning range of 22 kHz in both positive and negative direction with a central frequency of 14.2 MHz. The active electrical tuning method is straightforward and easy to implement.

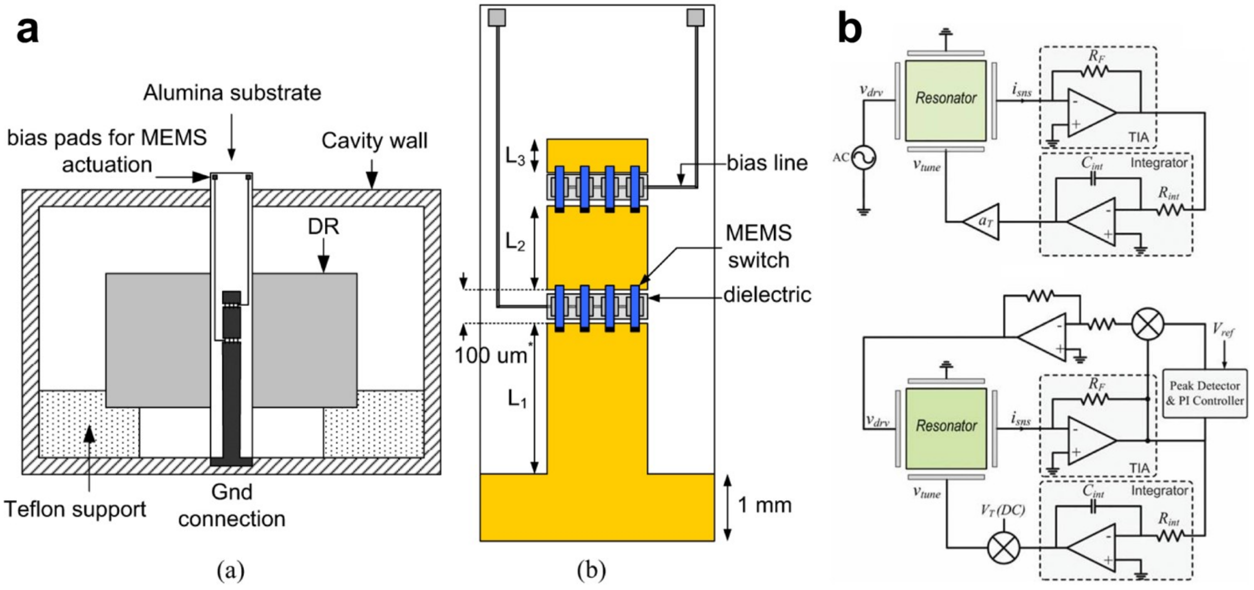

Figure 2.3 Examples of circuit-level active electrical tuning: (a) Cross-sectional view of the disk resonator with an inside tuning element and the diagram of the tuning circuit [41]. (b) Schematic diagram of a tuning feedback loop [42].

2.2.3 Electrostatic Tuning

As an active tuning mechanism, electrostatic tuning is one of the most attractive methods for resonant frequency tuning. **Figure** 2.4a shows split-ring resonator (SRR) with electrostatic tunability.

Two cantilever arrays each consisted of five beams are placed in both the inner and outer rings. The length of the cantilevers varies from 300 to 400 μm, with each beam adding about 2 pF capacitance. For each SRR, only one of the cantilevers will be actuated at the same time. The MEMS embedded SRR is able to continuously shift the higher frequency from 14.2 to 12.6 GHz by actuating the cantilever on the outer SRR [43]. In order to achieve a wider frequency tuning range with higher energy efficiency, MEMS resonators with comb structures have been extensively studied [45, 46, 47]. A variety of electrostatic tuning methods such as varactor and parallel plate have been proposed and designed. **Figure** 2.4b shows a tunable comb structure resonator with a tuning range of ∼ -3.3%, which is

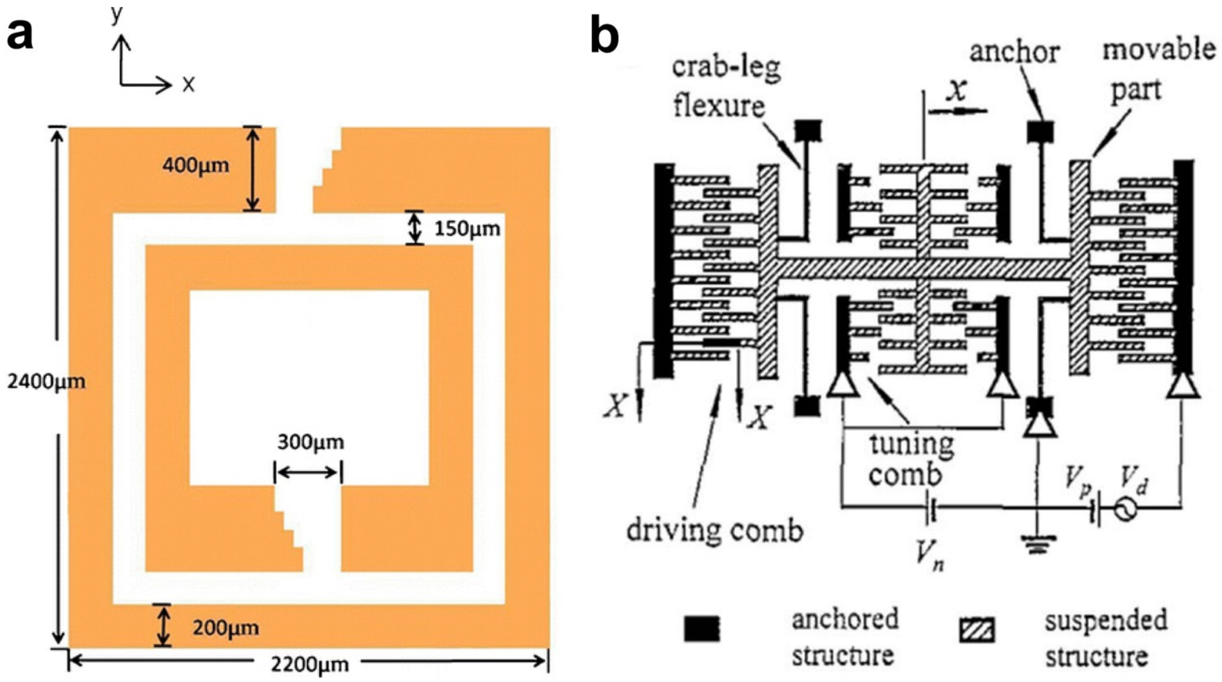

Figure 2.4 Examples of electrostatic tuning: (a) Schematic drawing of a MEMS embedded SRR unit cell, where two cantilever arrays are located in the gap regions of the inner and outer rings [43]. (b) Schematic view of a tunable comb resonator [44].

achieved by using the capacitive softening effect [44]. By applying different DC voltages across the gaps between the sensing and driving electrodes, the electrostatic force applied on the resonant mass changes with different DC voltages, leading to a shift in the stiffness of the material and the resonant frequency.

2.2.4 Electrothermal Tuning

The resonant frequency in MEMS can also be tuned by thermally inducing an expansion or contraction of the resonator structure. This technology significantly reduces the complexity of the system. Localized heating, such as Joule heating, is often used to induce thermal stress and strain. **Figure** 2.5a shows an electrothermally tuned comb resonator that consists of a straight mechanical beam which can be resistively heated to generate thermal stress. For this device, the relative resonant frequency change is around 6.5% with a central frequency at around 31 kHz. Electrothermal tuning can also be induced by external heating, which heats up both the resonator structure and the substrate. In this scenario, however, the thermal mismatch becomes less significant due to a lower thermal gradient. The resonant

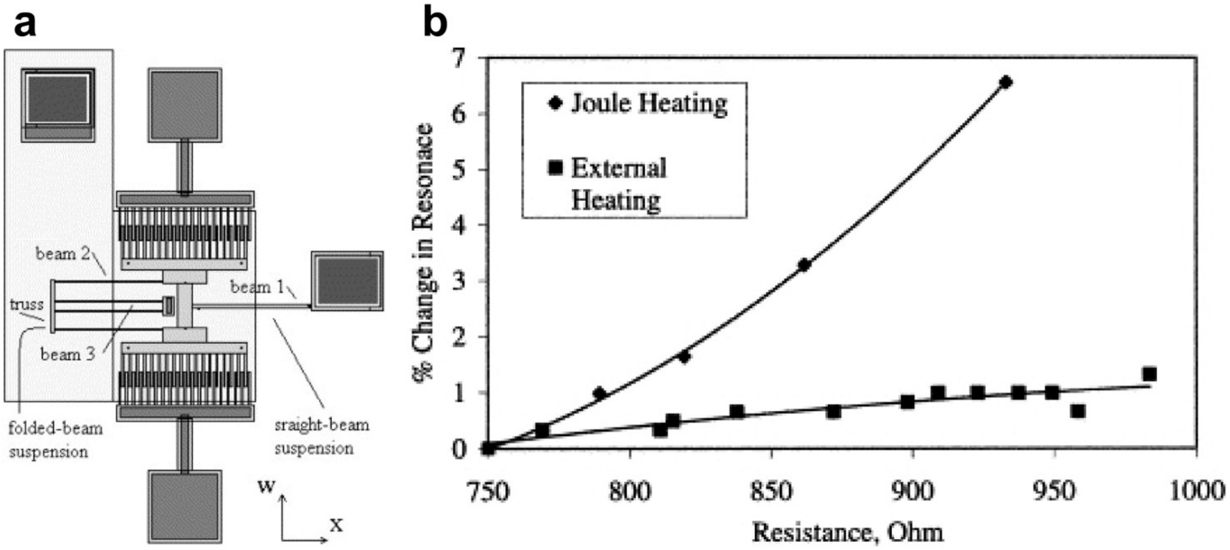

Figure 2.5 Examples of electrothermal tuning [48]: (a) Schematic diagram of a comb resonator with the straight beam for actively thermal tuning via localized heating. (b) Frequency changes by different electrothermal tuning methods.

frequency change is therefore mainly attributed to the change in Young's modulus, which generally reduces the resonant frequency shift [48]. **Figure** 2.5b shows a comparison of external heating method and Joule heating method for the same device presented in **Figure** 2.5a.

2.2.5 Photothermal Tuning

The thermal stress used to tune the resonant frequency not only can be generated electrically but also can be optically induced. Optical tuning methods introduce a remote control of the resonant frequency and provide higher resolution since localized heating can be achieved by focusing light at different places in the structure. The influence on the resonant frequency is based on the photo-thermal stress generated by the absorbed light from the laser spot

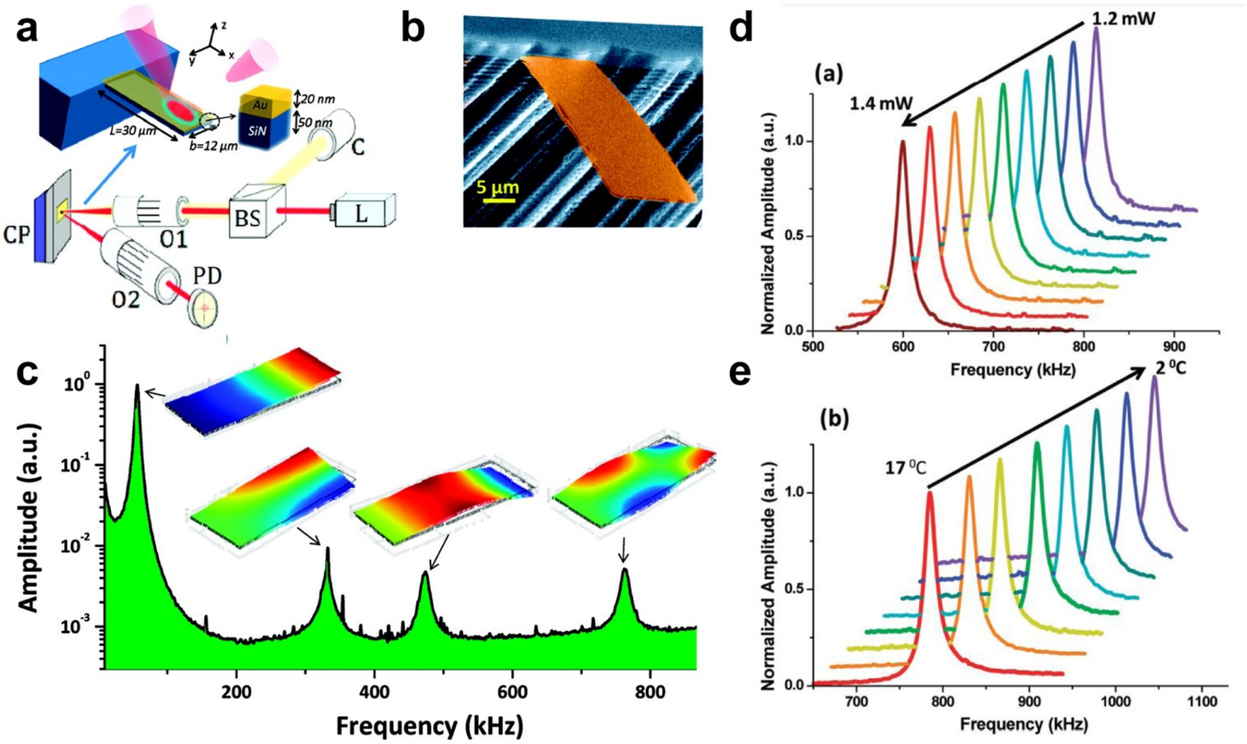

Figure 2.6 Example of photothermal tuning [49]: (a) Schematic diagram of the resonator structure and the laser deflection method used to measure the resonant frequency. (b) SEM image of the resonator. (c) The resonant frequency spectrum of the cantilever resonator with the first four modes. (d) Relative resonant frequency shift as a function of laser intensity. (e) Relative resonant frequency shift as a function of temperature.

on the structure. **Figure** 2.6 shows a resonant frequency shift induced by the laser beam heating up the cantilever. The thermally induced axial stress shifts the resonant frequencies in a nonlinear pattern.

2.2.6 Piezoelectric Tuning

Piezoelectric tuning method utilizes piezoelectricity, which directly converts an electric input to a mechanical stress/strain that shifts the device's resonant frequency. **Figure** 2.7 shows the resonant response of piezoelectric beams with different geometries and the resonant frequency shift as a function of DC voltage applied to the piezoelectric layer. The influence of surface stress on the stiffness of the resonator beam leads to a shift in the resonant frequency. Based on different beam structures with different boundary conditions and constraints, cantilevers and bridges tend to present different response in frequency shifts. The relative frequency shift for the cantilevers shows to be independent on the structure's length. On the contrary, bridges present different relative frequency shift with varying beam lengths.

2.2.7 Stress Tuning

Resonant frequency largely depends on the structure's tensile stress. Many technologies have been developed and implemented to change the structure's stress and tune the resonant frequency. The sensitivity of frequency shift per added stress is largest near the Euler buckling limit. Buckling occurs when a clamped-clamped beam has a compressive axial pre-stress level higher than the critical buckling stress limit. As the added stress becomes closer to this point, the resonant frequency shift becomes more sensitive to a change in axial, tensile, or compressive stress. D.R. Southworth et al. demonstrated a vapor sensor with high sensitivity based on a buckled silicon-polymer composite microbridge[51]. The beam is pre-stressed into a buckled configuration and the volumetric changes in the reactive polymer layer induce a large tension force in the bridge which leads to a large and fast change in the resonant frequency. The resonant frequency shift as a function of stress in the operation region is presented in **Figure** 2.8a. Stress frequency tuning can also be realized in a more straightforward way. Scott S. Verbridge et al. employed a direct chip-bending method to

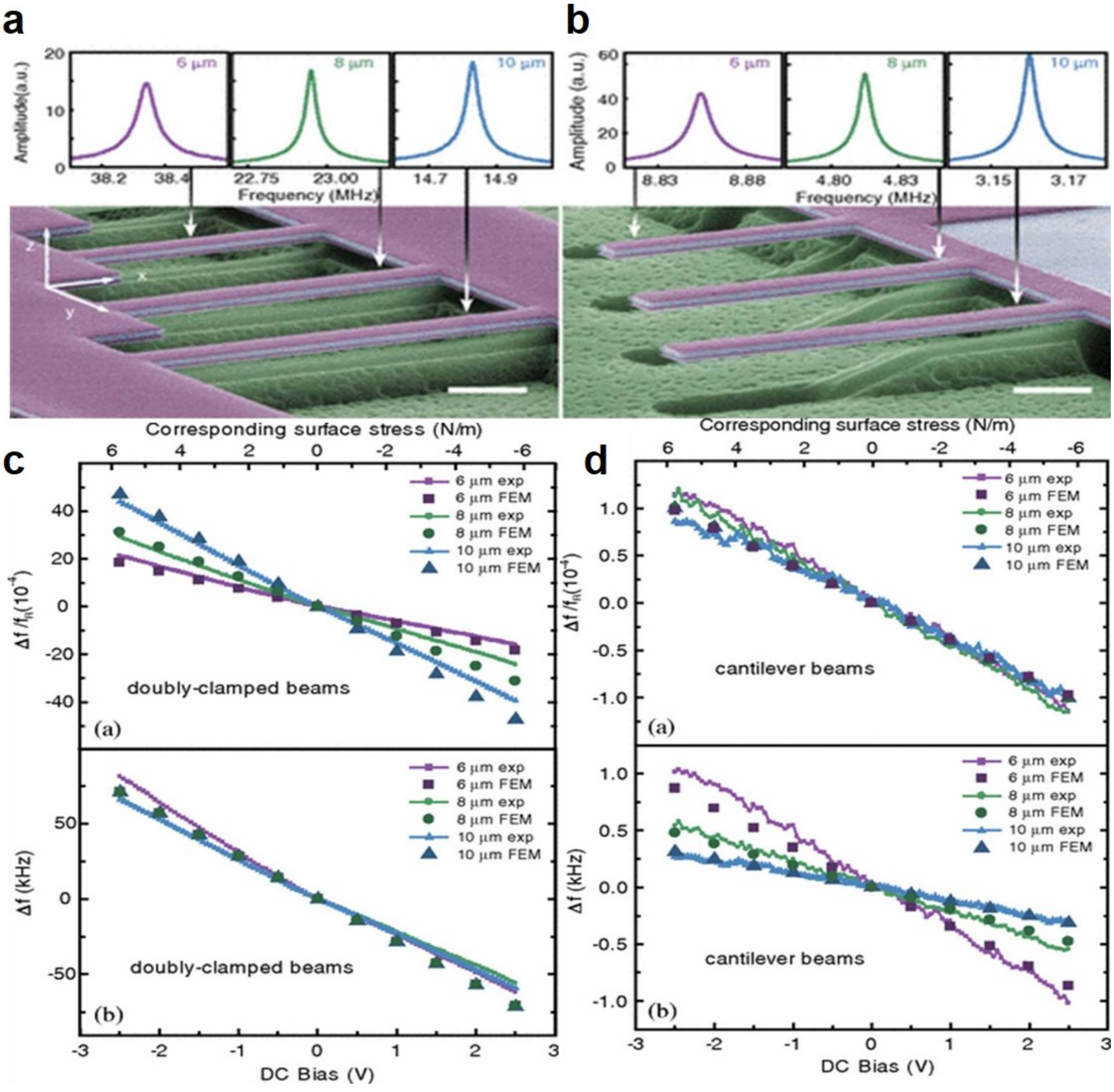

Figure 2.7 Example of piezoelectric tuning [50]: (a) Resonant response of piezoelectric beams with clamped-clamped structure. (b) Resonant response of piezoelectric beams with clamped-free structure. (c) Frequency shift results for doubly clamped beams. (d) Frequency shift results for cantilever beams.

realize a fully reversible stress control over a clamped-clamped NEMS resonator. **Figure** 2.8b shows the schematic diagram of the bending apparatus and the measurement setup. The external tension force is shown to have the ability to efficiently increase the resonant frequency and Q-factor of both silicon nitride and single-crystal silicon resonators.

2.3 Vanadium Dioxide

Most of the advances in MEMS have been made along the lines of using silicon and other common CMOS standard compatible materials. This trend for technological improvement has been exploited through the use of strategic and complicated geometries, which provides excellent performance for well-defined applications. However, the improvement achieved by using complex structures is ultimately limited by the underlying physical capabilities of the materials used. To improve the tunability and to reduce the complexity of the system, smart materials have been widely investigated and exploited in MEMS resonators techniques. As a smart material with high strain energy density and near room temperature phase transition,

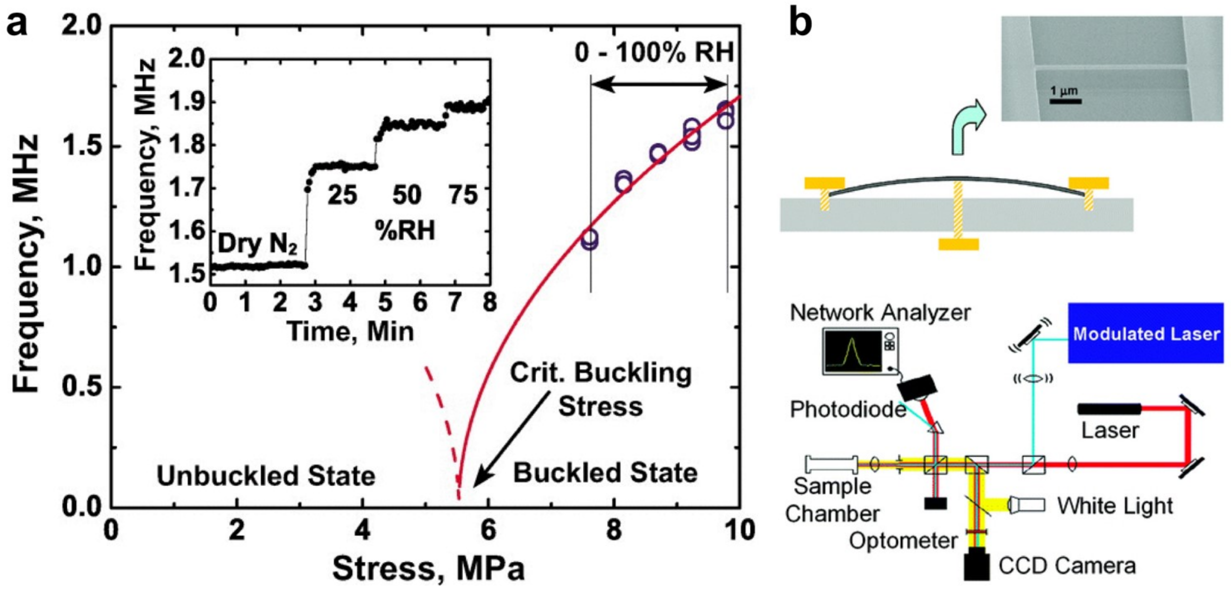

Figure 2.8 Examples of stress tuning: (a) Changes in the resonant frequency of a buckled beam, the hygrometric polymer coating expands in proportion to relative humidity [51]. (b) Schematic diagram of the bending apparatus and the measurement setup [52].

VO_2-based MEMS resonators provide a wide tuning range.

2.3.1 Insulator-to-Metal Transition

The underlying physics in the phase change region of VO_2 has drawn the attention of both the physics and the materials science community for more than five decades. The extreme sensitivity and the characteristic hysteresis are resulted from VO_2 being a strongly correlated electron system with narrow *d*-electron bands. Within the phase transition region, complex interactions occur between the dynamics of spin, orbital and lattice degrees of freedom, resulting in the association of the change in band diagram with the rearrangement of the atoms [53]. **Figure** 2.9 shows the schematic electronic band diagram of VO_2 in both the monoclinic phase and rutile phase. Each vanadium cation in VO_2 accommodates one electron in its 3*d* orbital and is surrounded by the oxygen anions located at the vertices of an octahedron. The degenerate five 3*d* orbitals are split into a double degenerate e_g state with higher energy and lower energy t_{2g} state with degeneracy in three degrees under the crystal

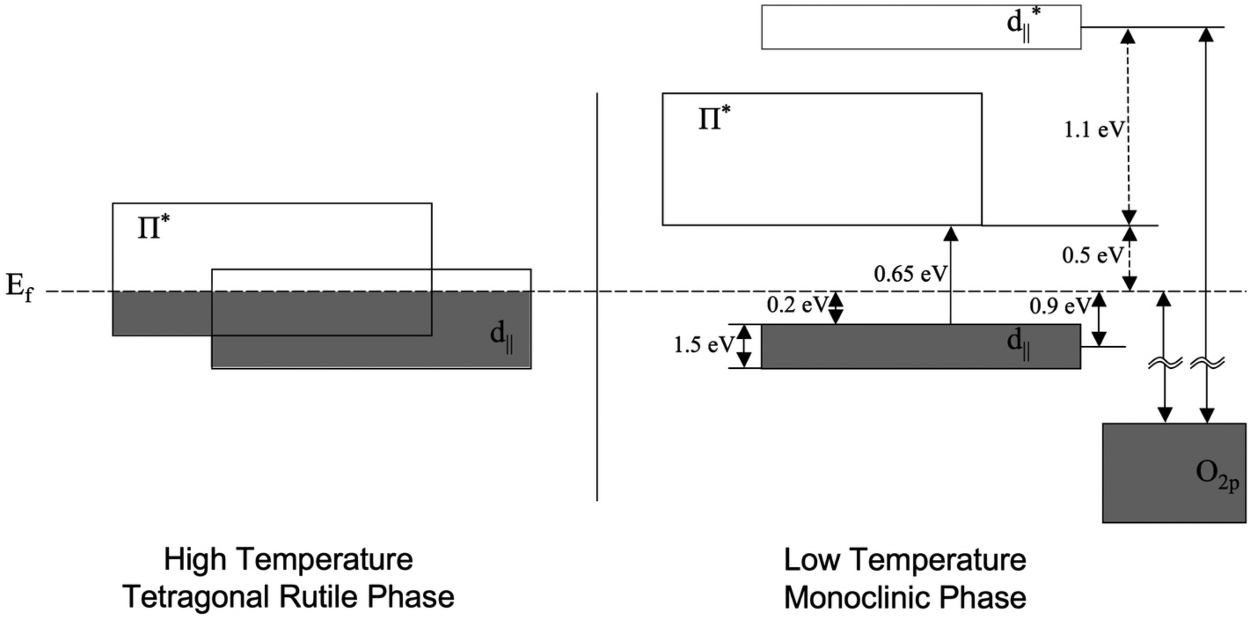

Figure 2.9 Schematic electronic band diagram of VO_2 in both rutile phase (left) and monoclinic phase (right) [53].

field of a regular octahedron. Under the crystal field of the tetragonal structure, the t_{2g} orbital is further split into an a_{1g} state with two degrees of degeneracy and a lower energy e_g state which interacts with the $2p$ orbital of the oxygen anion to form the molecular orbital. In the monoclinic phase, the dimerization of the vanadium cation pairs splits the a_{1g} state into a higher energy antibonding state and a lower energy bonding state, leaving a bandgap of around 0.7 eV between the valance band and the conduction band.

2.3.2 Structural Phase Transition

VO_2 undergoes a first-order solid-to-solid phase transition around the temperature of 68°C where its hysteretic behavior spans about 15°C. During the SPT, the crystal structure changes from its low-temperature monoclinic phase to its high-temperature rutile phase, leading to volume shrink along the c_R axis about 0.6%. The material's electrical, optical, and mechanical properties change drastically during the IMT and show hysteretic behavior. When VO_2 is used as a thin film coating over a micro-mechanical structure, the changes in the mechanical properties generate large stress that has been exploited to demonstrate high-performance MEMS actuators with programmable capability. These large stress levels could also be used to shift the resonant frequency of a micro-mechanical structure. The tuning mechanism for VO_2-based MEMS resonator belongs to electrothermal tuning technology, the mismatch in thermal stress between VO_2 layer and substrate such as amorphous VO_2 or single crystal silicon (SCS) is induced during the SPT to shift the resonant frequency. Thus, the deposition of VO_2 tends to align its (011) plane in the monoclinic phase and (110) plane in the rutile phase parallel to the substrate [**?**].

2.3.3 Vanadium Dioxide Synthesis

The synthesis of VO_2 thin film can be achieved in multiple ways, such as chemical vapor deposition (CVD)[55], sol-gel technique[56], and physical vapor deposition (PVD)[57], etc.

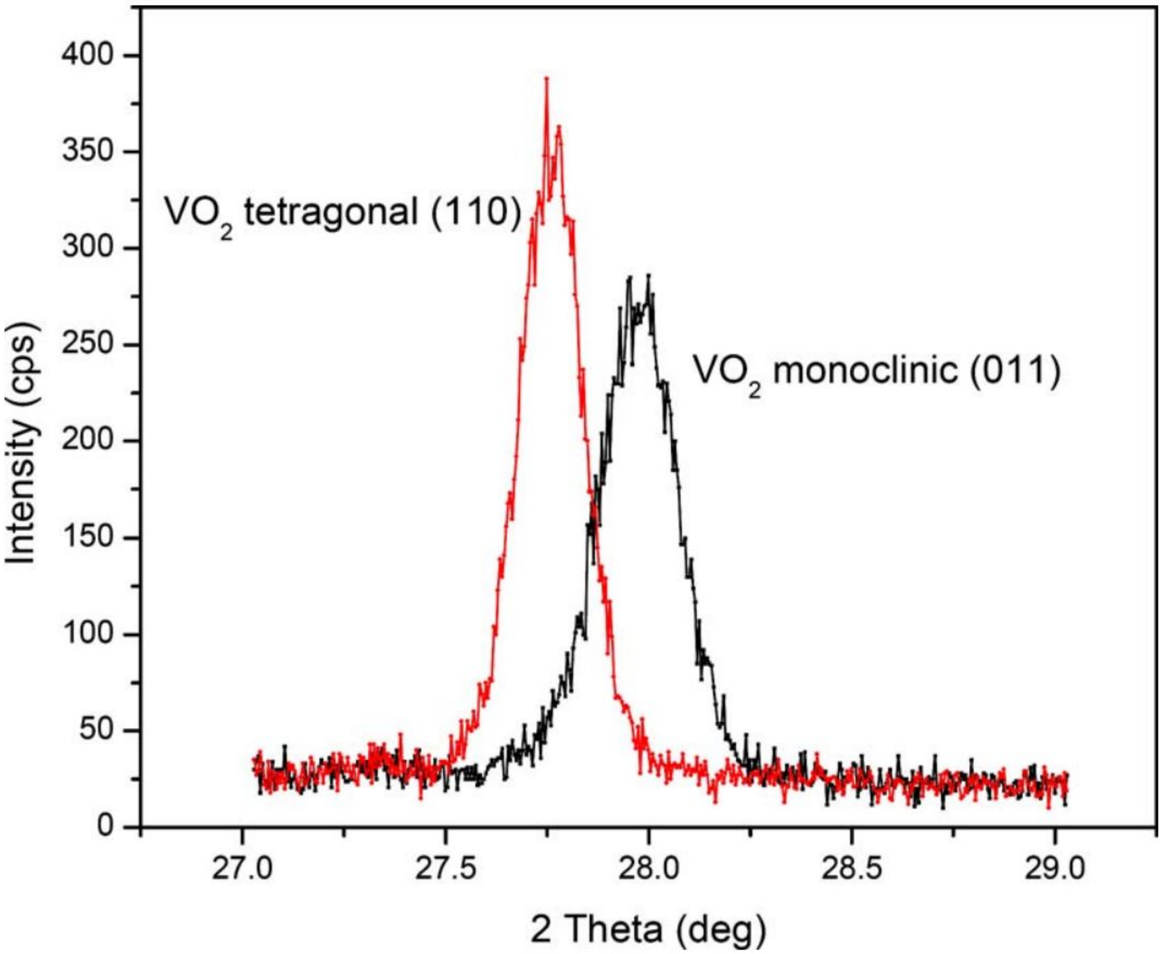

Figure 2.10 XRD scans of VO_2 thin film deposited on Si substrate with temperatures below and above transition temperature [54].

CVD is the first deposition technology used for VO_2 synthesis and has been extensively used for about half a century. In 1966, Koide and Takei successfully synthesized bulk single crystal VO_2 by introducing vanadium oxychloride ($VOCl_3$) carried by nitrogen gas into the chamber[58]. VO_2 thin film was also synthesized by the same group in the following year. Other precursors such as vanadium acetylacetonate ($(C_5H_7O_2)_4V$), vanadyl tri-isopropoxide ($VO(OC_3H_7)_3$) and vanadium chloride (VCl_4) have also been widely implemented to deposit VO_2 thin film coatings.

Sol-gel technique is also one of the most commonly used deposition methods for VO_2 thin film synthesis. It has many advantages such as low cost, ease of doping, and better uniformity. The sol-gel process starts with the conversion of monomers into a chemical solution (sol) which acts as precursors. Then the sol gradually forms an integrated network (gel) of discrete particles and polymer networks, the gel contains both a liquid phase and solid phase. The formation of metal oxides involves connecting the metal centers with oxo (M-O-M) or hydroxo (M-OH-M) bridges and hence generating metal-oxo or metal-hydroxo polymers in solution. The chemical solution used for VO_2 synthesis includes vanadium isopropoxide ($C_{15}H_{40}O_5V$), diluted $VO(OC_3H_7)_3$ in ethanol, hydrolysis of vanadium oxo-alkoxides ($VO(OR_3)$), and sodium metavanadate ($NaVO_3$), etc.

Sputtering is one of the most common PVD processes for depositing high-quality thin films. VO_2 thin films can be grown by reactive ion beam sputtering of a vanadium target in an argon-oxygen atmosphere. The bombardment of argon (Ar) ions transfers kinetic energy to the target material, resulting in vanadium ions ejected from the surface of the target. DC and RF power supplies are often used to enhance the bombardment, DC sputtering is often favored when a high deposition rate is required. However, for depositing insulating oxides, DC sputtering causes an accumulation of charges on the surface of the sample, leading to a lower deposition rate and a poor film quality. Thus, RF sputtering is more preferred in VO_2 deposition. PLD, as another PVD technique, possess a similar function as RF sputtering. Instead of using ion bombardment to knock out target ions, PLD uses high energy pulsed laser to enable the kinetic energy transfer process. PLD provides an accurate control of the newly deposited film and is able to perform deposition on a variety of substrates, including silicon, quartz, sapphire, etc. In this work, all the samples are fabricated by the PLD technique.

2.4 Flexible Physical Sensors

Flexible physical sensors have demonstrated to have promising applications in sensing networks where the complex environmental stimulus is considered. Bio-compatible soft elec-

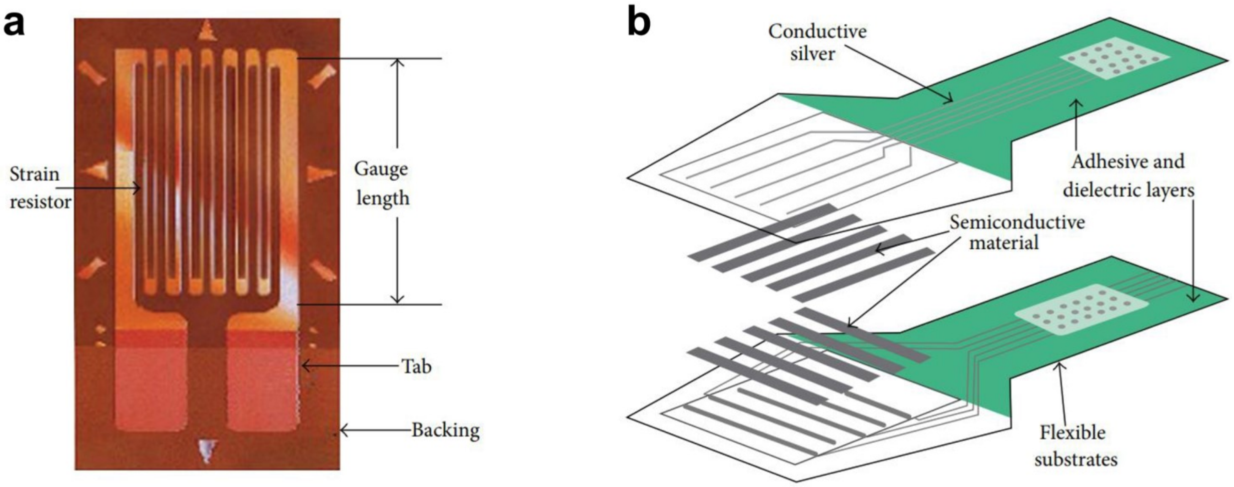

Figure 2.11 Example of resistive bending sensor and pressure sensor: (a) Structure of a strain gauge [59]. (b) Structure of a tactile pressure sensor [60].

tronic skins that are capable of force distribution visualization have been exploited extensively in the field of soft robotics [61] and human motion monitoring [62, 63]. Despite the different approaches in integrating each individual sensing element, the functionality of each sensing unit can be classified into several groups according to its working principles. Generally, resistive, capacitive and piezoelectric mechanisms are often considered for various applications [64]. For example, bending strain gauges can play a major role in motion monitoring wearable gadgets, which can be used for detecting large deflections. Progresses in flexible electronics of making deformable, stretchable and biocompatible bending sensors also extends their integration in IoT systems.

2.4.1 Resistive Physical Sensors

Resistive pressure sensors are most widely used in real applications due to their simple device structure, high signal-to-noise (S/N) ratio, and easy readout features [66]. Conventional resistive sensors are usually based on metal foils and semiconductor coatings which utilize the resistance change due to geometrical effect. Limited by the low mechanical compliance, metal foil sensors only provide a detection range of 2% $\sim$ 5%. Higher sensitivity can be achieved by utilizing microstructural disconnection mechanism in metallic nanomaterials, such as nanoparticle (AgNP) [67], gold nanofilm [65], and gold nanowire (AuNW) [68], coated on polymer substrates. **Figure** 2.12 shows an example of Au nanoparticle film-based flexible bending sensor. Recent progresses have also demonstrated fully elastomer-based resistive strain sensors based on carbon nanotube (CNT) [69, 70], graphene [71], and laser scribing technique [72], etc. However, those passive sensors still require external power supported sensing elements which are problematic during their integration in IoT systems with sustainability requirements.

2.4.2 Capacitive Physical Sensors

Capacitive pressure sensors measure different forces by monitoring the capacitance variations, caused by the change in separation between parallel plates[73, 74]. By optimizing micro-

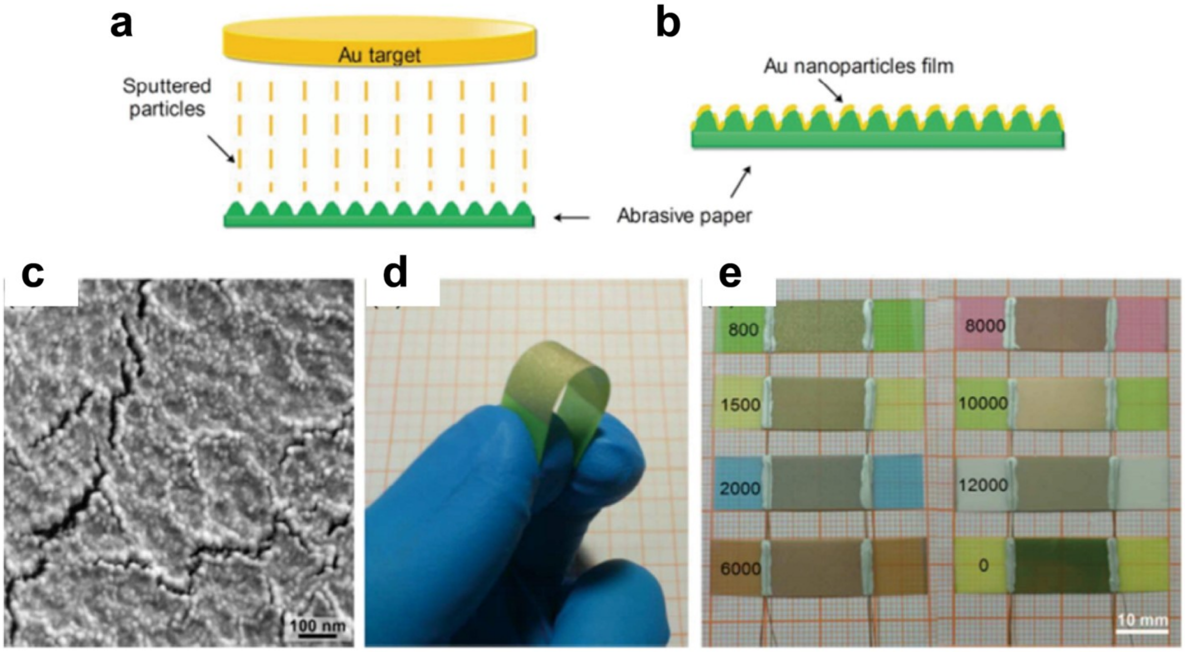

Figure 2.12 Example of gold nanofilm-based resistive bending gauge [65]: (a) Fabrication of Au nanofilm bending sensor on paper substrate. (b) Model of the sensor. (c) SEM image of Au nanoparticles film. (d) Photograph of the flexible bending sensor. (e) Top view of bending sensors on different substrates.

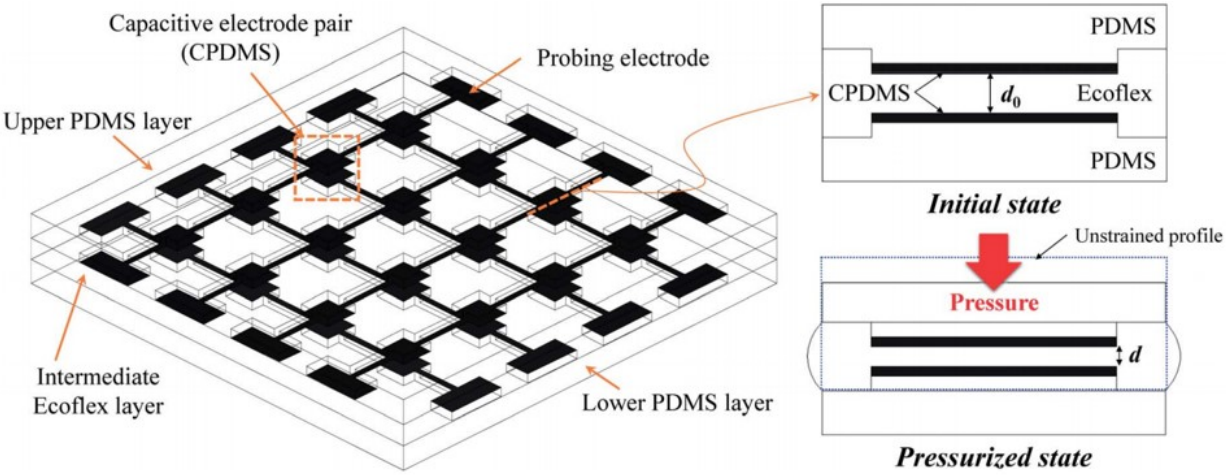

Figure 2.13 Example of capacitive-based physical sensors for bending and pressure monitoring [76].

structures within each sensing element and the material's dielectric constant [75], capacitive sensors with high spatial resolution and large dynamic range have been developed [76, 77]. However, the rather complicated evaluation system and the inherent hysteresis error still remain a problem. **Figure** 2.13 shows a capacitive type of flexible sensor for pressure sensing and bending radius monitoring. The sensor has an address line configuration, where each sensing element consists of a sandwiched structure as shown in **Figure** 2.13(right).

2.4.3 Self-Powered Physical Sensors

Although the choice of physical sensing technology is determined by specific applications, battery-based resistive and capacitive pressure sensors are not considered to be optimal approaches for the Internet of Things (IoT) devices, which impose sensor network with lightweight, miniature size, and energy sustainability requirements. Therefore, a direct energy conversion between mechanical input and electrical sensing output becomes imperative. Nanogenerator-based self-powered pressure sensors using piezoelectric or triboelectric effect have been demonstrated as emerging technologies in flexible electronics [80, 81]. Inorganic piezoelectric nanostructures are introduced by micro-fabrication techniques to improve the detecting sensitivity and sensing resolution. Nanowires (NWs) such as ZnO [78], CdS [79], and $NaNbO_3$ [82] with high electric output are often used as piezoelectric sensors. Mechanical energy from the bending motion of nanowires is converted to an electric output. Composite nanoparticles (NPs), e.g. $BaTiO_3$ [83, 84], are also often used to improve the piezoelectric effect by increasing the total dipole moment. To overcome the low flexibility of inorganic piezoelectric nanogenerators (PENGs) sensors, foldable and stretchable substrates such as polydimethylsiloxane (PDMS), polyethylene terephthalate (PET), or polyethylene (PEN) can be used [85]. **Figure** 2.14 shows a summary of the triboelectric series wearable electronics for different applications. Triboelectric sensors convert the mechanical energy by utilizing the internal friction of the material, the selection of the active materials are therefore broadened from NWs/NPs to polymers [86] and soft fabrics [87], which significantly improve flexibility. Their high performance has also been demonstrated by optimization of the microstructure such as surface etching [88], topology casting [89], injection molding, etc. The compatibility with micro-fabrication techniques also makes it more adaptable to the

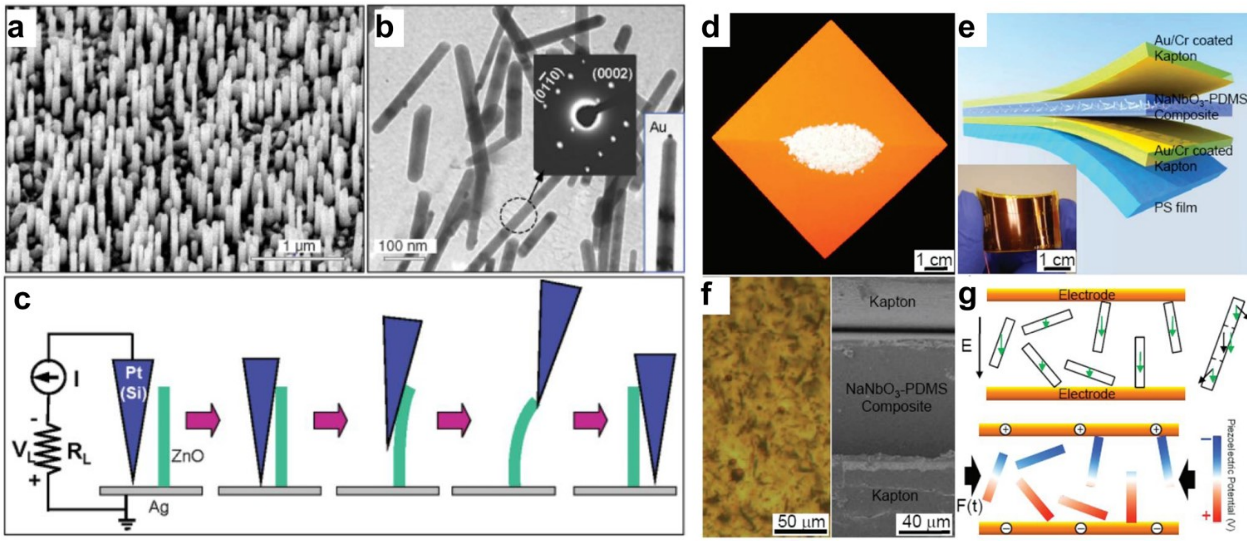

Figure 2.14 Examples of piezoelectric-based physical sensors [78, 79]: (a) SEM image of aligned ZnO NWs grown on Al_2O_3 substrate. (b) The TEM image of ZnO NWs. (c) Working principle of ZnO NW-based nanogenerator, the electric output is generated by NWs sliding against each other. (d) Photograph of $NaNbO_3$ nanowires. (e) Schematic image of m, $NaNbO_3$ - PDMS composite-based nanogenerator. (f) OM and SEM view of the device shown in (e). (g) Energy generation mechanism of $NaNbO_3$ NWs-based nanogenerator.

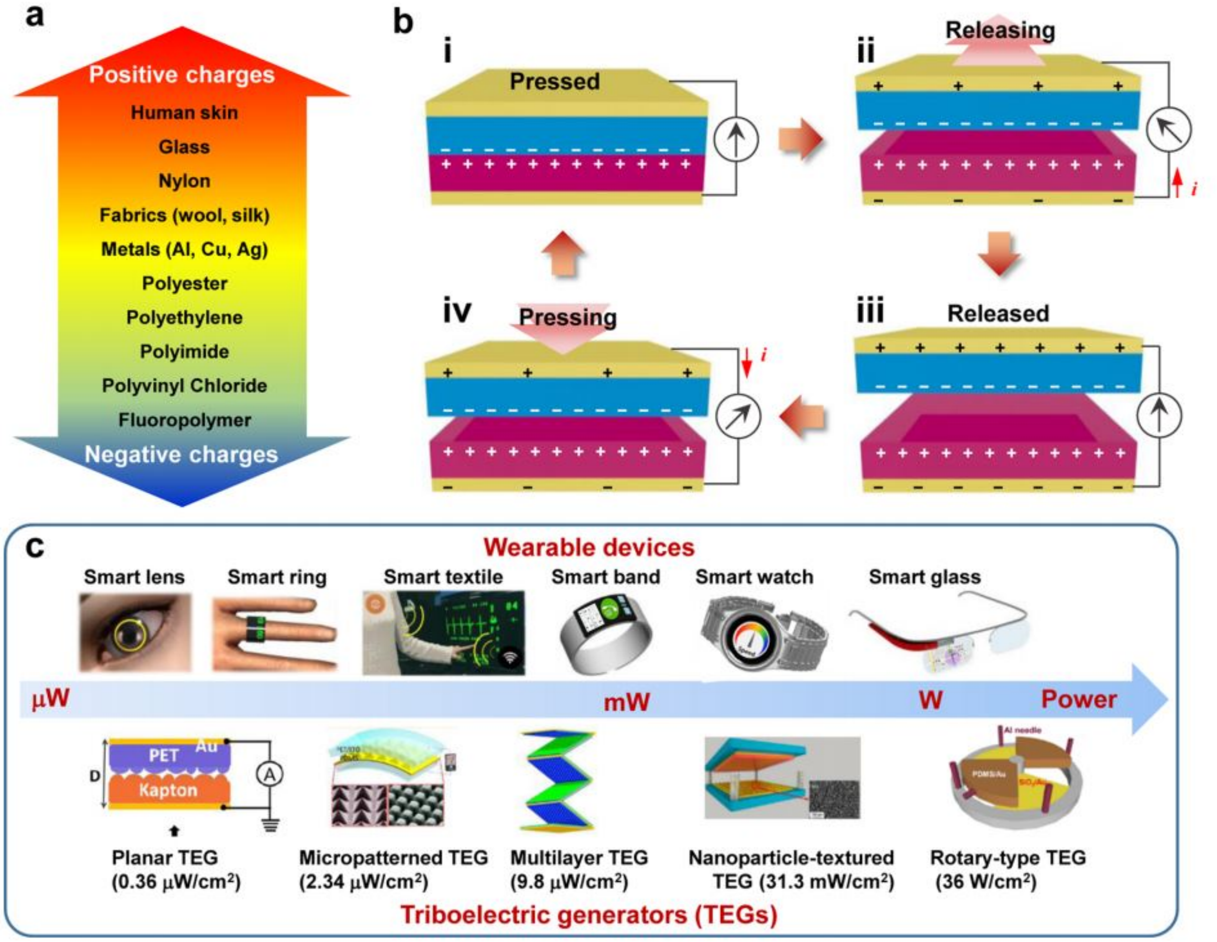

Figure 2.15 Illustrations of triboelectric self-powered physical sensors [81]: (a) Series of materials in TENG family. (b) Working principle of TENG device. (c) Comparisons between power consumption in commercial electronics and power output in TENG devices.

high spatial resolution requirements [90, 91].

2.5 Nanogenerator-based Energy Harvesters

With the incredible growth of the internet over the past few decades, the world's economic structure has been rapidly shifted to rely heavily on information technology. Not long ago, it was enough for a mobile phone to be able to make calls and send texts. Nowadays, mobile phones are essentially terminals of all kinds of information and utilities. Internet of Things (IoT) and big data enable data exchange among health monitor apps, wireless sensor sys-

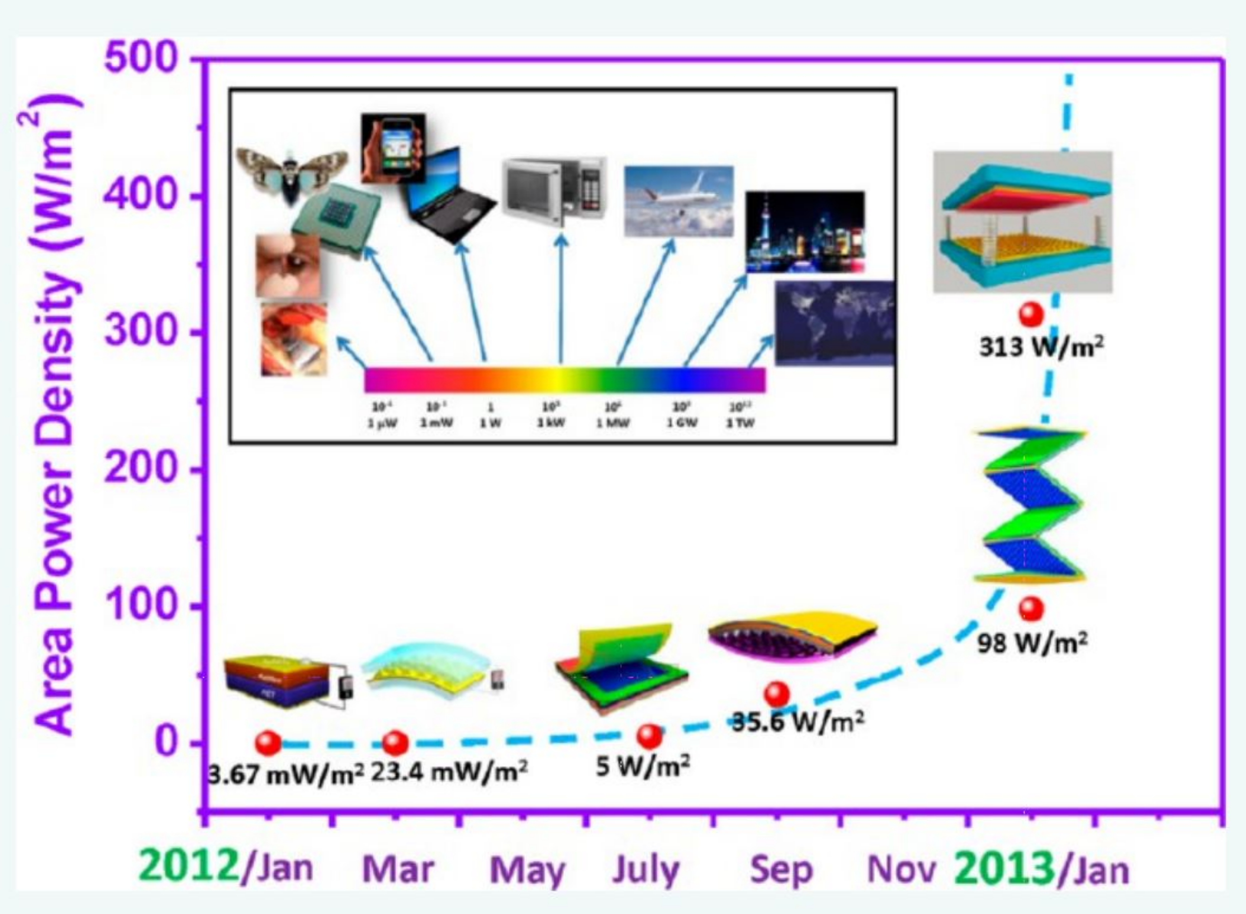

Figure 2.16 Road-map of improvements on the power output of nanogenerators [103].

tem, and smart automation in order to create a more robust and direct way to integrate real-world decision-making processes into artificial intelligence (AI) networks. Hence, multifunctionalities have been imposed on personal electronic devices such as smartphones and even bracelets. However, the future progress of all these technological advances is tied to the energy budget that comes with all these tools. Self-powering technologies [92, 93, 94, 95] that converts ambient energy sources from multiple forms (e.g. solar [96, 97], thermal [98, 99] and mechanical [100, 101, 102]) to electricity have become potential energy solutions for the smart, multifunctional phones and wearable electronics.

However, the path for a solution to the increasing energy demands needs to be comprehensive and inclusive. Approaches should consider scavenging, storing, and using as many different forms and magnitudes of energy. Unlike solar energy, the energy produced by random mechanical vibrations can be obtained nearly at any time from multiple sources. Energy harvesting devices such as piezoelectric (PENG) [104, 105], triboelectric (TENG) [106, 107, 108, 109] and ferroelectric (FENG) [110, 111] nanogenerators that are capable of converting kinetic energy to electrical energy are considered to be the most promising devices for integrated self-powered systems [112]. Even though those nanogenerators exhibit the piezoelectric effect, the origins of the piezoelectricity are quite different. PENG usually uses inorganic nano piezoelectric materials such as ZnO nanoparticles and nanowires; and their flexibility can be achieved by their integration with soft substrates such as polyimide (PI), polyurethane acrylate (PUA), etc. TENG makes use of the triboelectric effect, and are often considered at the device level for high-efficiency energy harvesting. Their power densities can be as high as 313 W/m^2 [103].

2.6 Summary

In this chapter, a comprehensive review of the background of MEMS resonator, tuning technology, vanadium dioxide, flexible physical sensors, and energy harvester is presented. First of all, the motivation for replacing quartz resonators with MEMS resonators is illustrated in this section. Then, the tuning technologies of both passive tuning mechanism and active tuning mechanism are discussed in the following section. Passive tuning methods, such as post-fabrication tuning and post-packaging tuning, are one-time permanent tuning methods which have less tuning flexibility. Active tuning, on the other hand, provides a real time tuning configuration, the tuning is fully reversible and covers a wide tuning range. The active tuning methods discussed in this section include: electrostatic tuning, electrothermal tuning, photothermal tuning, piezoelectric tuning, and tensile or compressive tuning. Next, the properties of VO_2 thin film are introduced including the insulator-to-metal transition, spatial phase transition, and synthesis methods of the material. In the second half of this chapter, flexible physical sensors are introduced. Based on different operating mechanisms, such devices can be categorized into three groups: resistive, capacitive, and piezoelectric. Advantages and disadvantages of each type of sensor are discussed and compared. To meet the sustainability requirement imposed by IoT devices, piezoelectric sensors are often preferred due to their lightweight, high flexibility, and self-powering capability. The high d_{33} value also enables potential applications in energy harvesting systems.

CHAPTER 3

DESIGN, FABRICATION OF VANADIUM DIOXIDE MEMS RESONATORS AND FERROELECTRET NANOGENERATORS

3.1 Fabrication of VO_2 based MEMS Resonators

3.1.1 Fabrication Flow

The VO_2-based resonators (cantilevers and bridges) reported in this paper are all within the same chip. The fabrication processes of VO_2-based cantilevers are schematically described in **Figure** 3.1. Uncoated MEMS resonators (before VO_2 deposition) used in this paper are 2 µm thick, with a 200 nm layer of titanium/platinum (50 nm Ti / 150 nm Pt) heater electrode placed in between two 1 µm SiO_2 layers. This symmetric stack of layers is designed

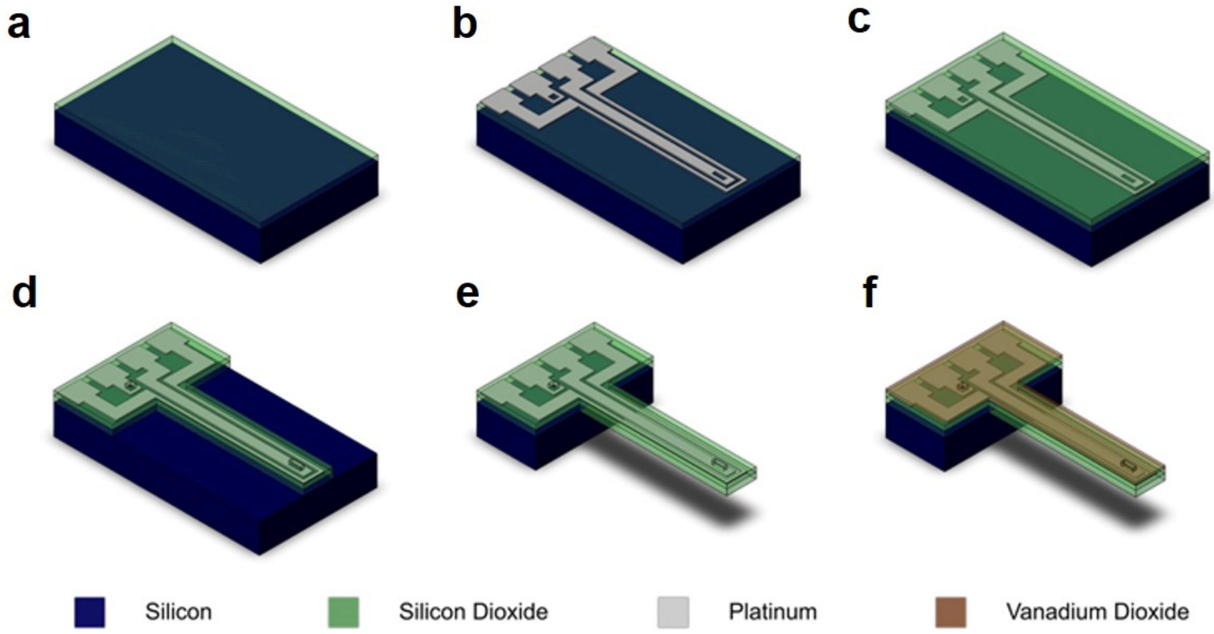

Figure 3.1 Fabrication flow of VO_2-based cantilever. (a) PECVD deposition of SiO_2 layer on Si substrate. (b) Thermal evaporation of Ti/Pt heater trace, patterned by lift-off. (c) PECVD of second layer SiO_2. (d) The structure defined by dry etching. (e) MEMS structure released by XeF_2. (f) PLD deposition of VO_2 coating.

to reduce the extrinsic thermal stress during the deposition of the VO_2 thin film, which can produce bending of the structure in the process and an uneven VO_2 thin film deposition. In summary, a SiO_2 layer is deposited on a Si wafer using Plasma Enhanced Chemical Vapor Deposition (PECVD) method, followed by deposition and patterning of Ti/Pt (Ti only used for adhesion purposes), deposition of a second 1 µm layer of SiO_2 (again, using PECVD), and patterning of the resonator structures through both SiO_2 layers. The wafers are then diced, and released, which is done by isotropic etching of the silicon substrate using xenon difluoride (XeF_2) gas. VO_2 thin film is deposited using PLD (see **Figure** 3.2). During the deposition process, the chamber is first pumped down to a vacuum level below 10^{-6} Torr by using a turbomolecular pump connected with a mechanical scroll pump. Then the oxygen is

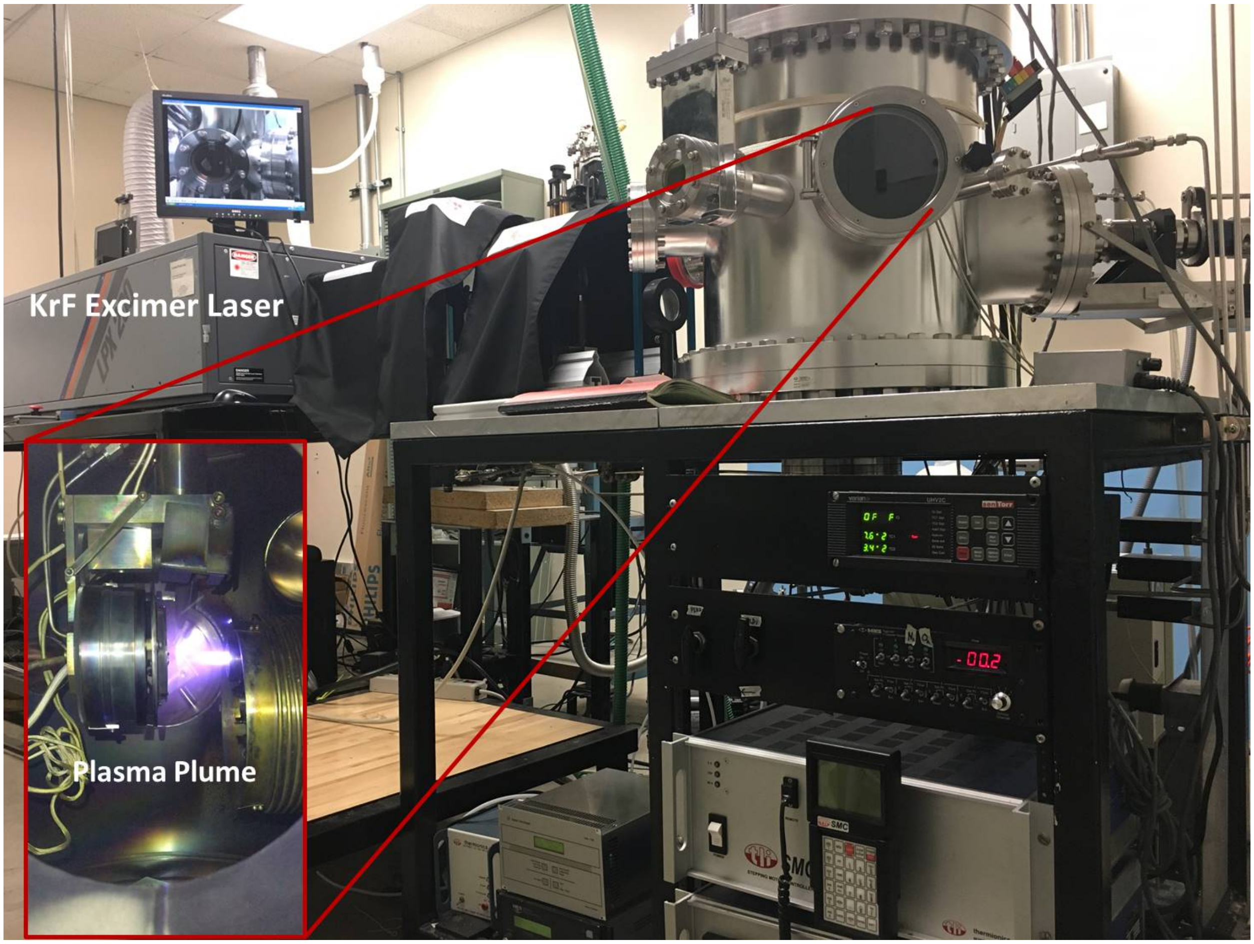

Figure 3.2 The PLD equipment for VO_2 deposition, the inset shows the plasma plume coming off of the vanadium target.

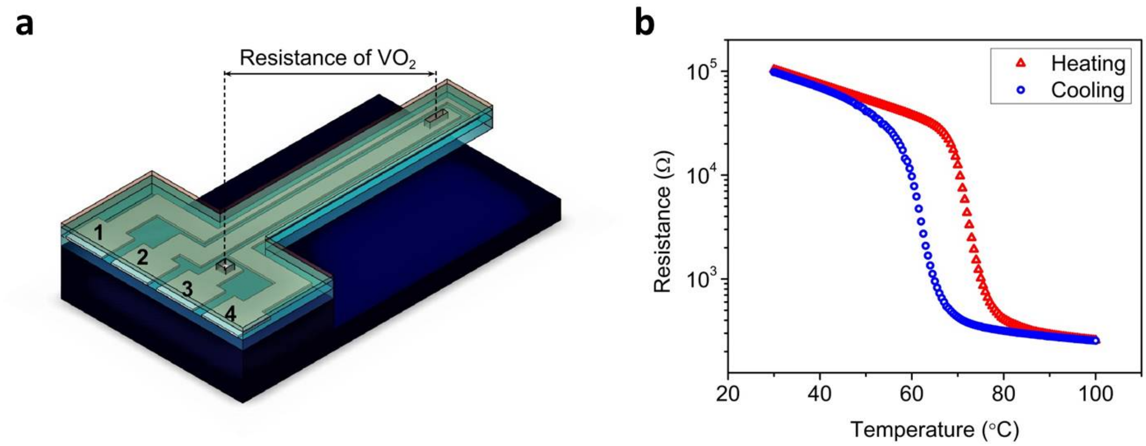

Figure 3.3 (a) Schematic diagram of the released cantilever structure. Contacts ”1” and ”4” complete the heater loop around the cantilever structure, contacts ”2” and ”3” are used to measure the resistance of theVO$_2$ film. (b) Measured resistance of the patterned VO$_2$ film as the temperature is increased and decreased by Peltier heating.

introduced into the chamber at a flow rate of 20 sccm and a butterfly valve is controlled to keep the chamber oxygen atmosphere pressure at 15 mTorr. A heater located approximately 2 inches behind the sample is preheated to 595 °C. After reaching this temperature, a metallic vanadium target is ablated by a Krypton Fluoride (KrF) excimer laser with 560 mJ in energy and 10 Hz in frequency for 10 min. After VO$_2$ deposition, a 30 min annealing step is performed under the same deposition conditions.

After the deposition is completed, a resistance measurement is performed as the temperature is varied across the phase transition of VO$_2$. The measured drop in resistance of approximately 3 orders and the hysteretic behavior observed verified the quality of the VO$_2$ thin film. The measurement is performed on the VO$_2$ thin film coated on a 550 µm long cantilever, which is shown in **Figure** 3.3. At this point, the devices are ready to be mounted on an IC package, wire-bonded and tested. The fabricated and tested resonators, shown in **Figure** 3.4, include microcantilevers and micro bridges with different lengths.

For the VO$_2$ coated micro-bridges, the initial first mode resonant frequency can be esti-

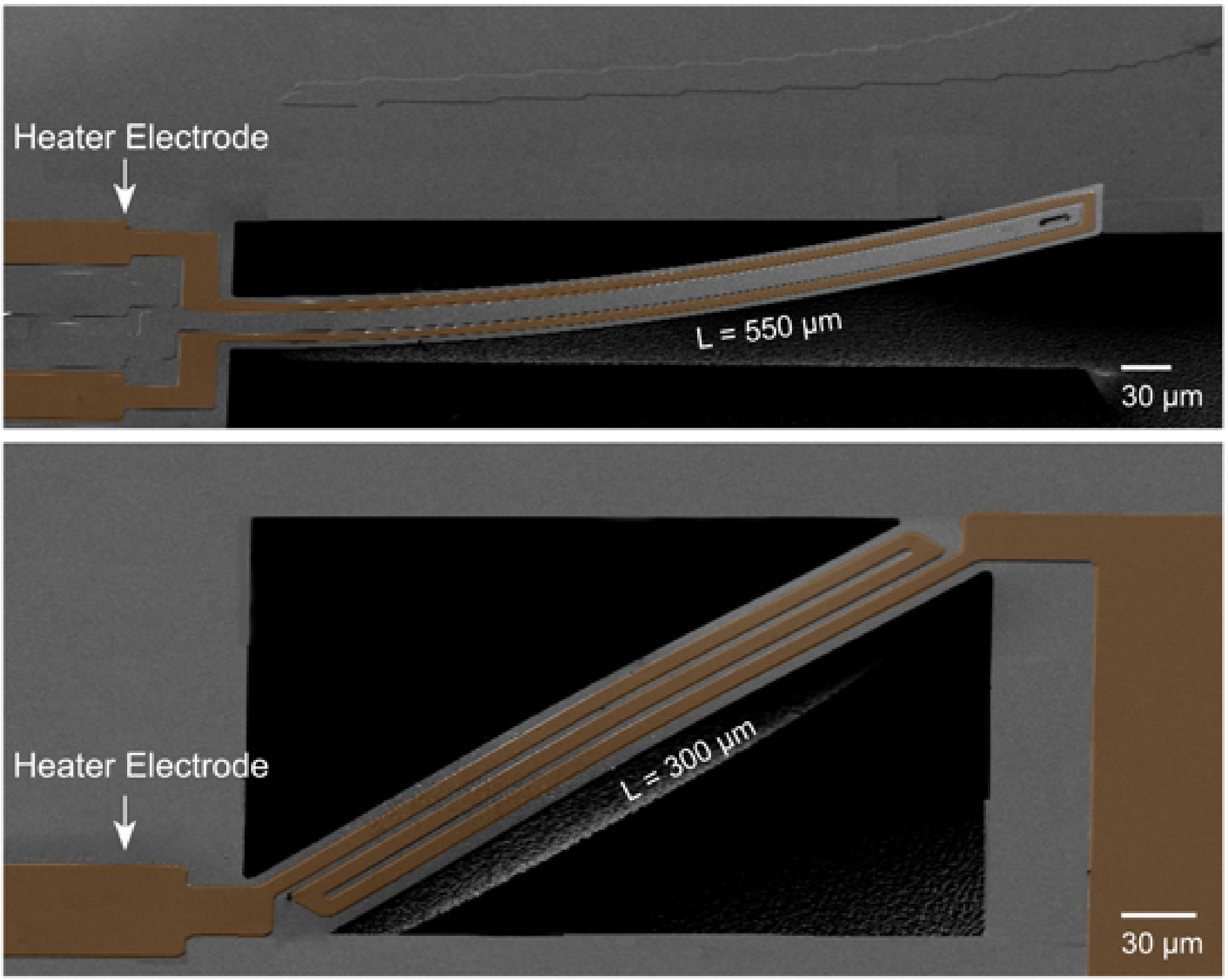

Figure 3.4 SEM images for the test structures. Top: cantilever of 550 μm long. Bottom: bridge of 300 μm. The electrodes for resistive heating actuation are artificially colored for clarity.

mated by the following equation [21]:

$$f_b^2 = 1.06\frac{[E_1^2 h_1^4 + E_2^2 h_2^4 + E_1 E_2 h_1 h_2 (4h_1^2 + 4h_2^2 + 6h_1 h_2)]}{(\rho_1 h_1 + \rho_2 h_2)(E_1 h_1 + E_2 h_2) l^4} \tag{3.1}$$

where E_1, h_1, ρ_1 and E_2, h_2, ρ_2 are the Young's modulus, thickness and density of the SiO_2 and the VO_2 layer, respectively, and l is the length of the bridge. On the other hand, the initial first mode resonant frequency of the VO_2 coated cantilever can be given by [113]:

$$f_c^2 = \frac{0.26h_1^2}{\pi^2 l^4} \times \frac{E_1 w h_1 + 12E_2 h_2[(w + 2h_2)(\frac{1}{2} + \frac{h_2}{h_1} + \frac{h_2^2}{2h_1^2}) + \frac{h_1}{6}]}{\rho_1 h_1 w + 2\rho_2 h_2 (w + h_1 + 2h_2)} \tag{3.2}$$

With the same variables used for equation (3.1) and w is the width of the cantilever. The equations above determine the initial resonant frequencies of the two resonator structures used in this work in the static state (i.e. un-actuated at room temperature). It should be noted that the equations do not take into account the thin metal layer used for Joule heating and tuning, but they do provide a good approximation that can be used for initial device design. The calculated resonant frequencies for a 300 µm bridge and a 550 µm cantilever are shown in **Figure ??** along with the experimental value. Here, a 9% under-etching effect is assessed for the bridges and 4.5% for the cantilevers. Thus, the effective length of the bridges and cantilevers are estimated to be 328 µm and 576 µm respectively. The resonant frequency of the bridges determined by equation (3.1) is about 102.3 kHz, which is far from the measured frequency. This is due to the strong influence of stress in the resonant frequency of a bridge structure. To match the experimental curve, the initial residual stress in the bridge was estimated to be 38.9 MPa— which is within the value found for similar structures. Thus, considering the stress effect, the resonant frequency for the bridge is found to be 237.6 kHz. It should be noted that this thermal residual stress does not play such a strong influence on the resonant frequency of cantilever structures, since the stress is partially released, producing an initial bending. Thus, the estimated resonant frequency of the cantilevers determined by equation (3.2) is 5.49 kHz, which is not that far from the measured resonant frequency (5.09 kHz).

3.1.2 Buckling States in VO_2 MEMS Resonators with Bridge Structures

The residual axial stress that causes the large discrepancy in resonant frequency for bridge structures comes from the residual thermal stress among different materials in the microbeam. After the SiO_2 deposition at 300 °C, there is residual thermal stress induces compressive axial stress (σ_l) on the beam, which is larger than the critical Euler buckling load σ_c[114]:

$$\sigma_c = -\frac{\pi^2 E_{eff} h^2}{3L^2}, \tag{3.3}$$

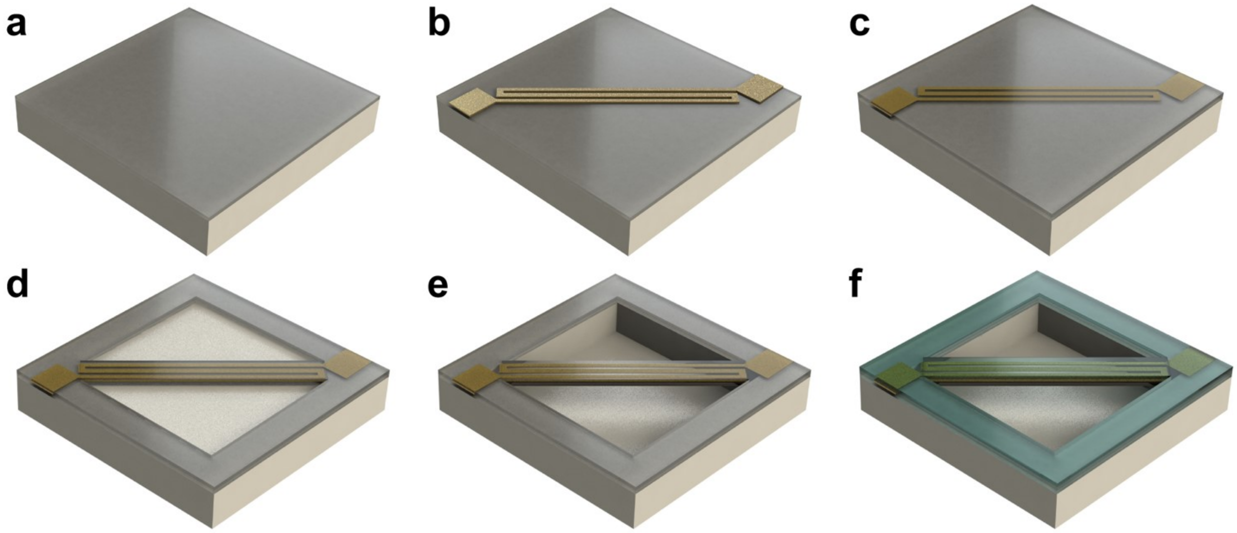

Figure 3.5 Fabrication processes of VO_2-based bridge resonators. (a) Deposition of 1 µm SiO_2 layer on Si substrate by PECVD. (b) Metalization of 200 nm Pt/Ti thin film by sputtering coating and the heater traces are patterned by the lift-off method. (c) PECVD Deposition of the second SiO_2 layer of 1 µm. (d) Resonator beam structure defined by plasma dry etching of SiO_2. (e) MEMS structure released by isotropic etching with XeF_2. (f) Deposition of 100 nm VO_2 thin film by PLD deposition.

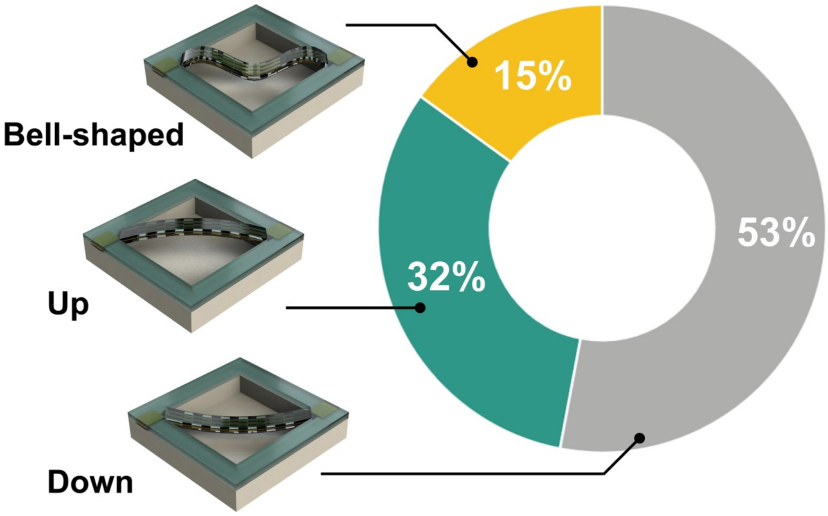

Figure 3.6 Statistic of buckling preference after the MEMS structure release.

where E_{eff} is the effective Young's modulus of the beam material, h is the thickness, L is the beam length and the negative sign represents the compressive load. In this case, the microbridge will deform into a buckled state with a sinusoidal shape by minimization of the total energy[115]. For an ideal bridge, the beam has no preference in the buckling orientations which leads to an equal probability of buckling down or up. However, structural imperfections cause concave anchor boundary conditions due to diagonal beam configuration and gradient in film stress; which makes the buckling orientation highly related to L and h[116]. In this work, the buckling orientation preference of the devices used is statistically demonstrated by reviewing 400 microbridges in the same fabrication condition before VO_2 deposition (i.e. until **Figure** 3.5e). **Figure** 3.6 shows the buckling distribution for these devices: 32% of the devices have an up buckling state while 53% are buckled down. The remaining structures (15%) show a downward bell-shaped buckling state.

After the VO_2 deposition, the device is cooled down from 595 °C to 85 °C while an axial tensile stress induced by the contraction of the VO_2 film[21]. This tensile stress would alleviate the buckling state by decreasing the buckling amplitude but is not large enough to overcome the Euler buckling limit and flatten the beam structure. As the device is further cooled down from 85 °C to room temperature, the VO_2 thin film goes through its phase transition from R-phase to M-phase, and the crystal planes parallel to the surface increase their areas, which leads to additional stress that consolidates the buckled state. Thus, the VO_2 deposition condition does not change the initial buckling orientation for the bridge structure. **Figure** 3.7a-c show SEM images of three VO_2-based microbridges with different buckling profiles from a 75° side view. The SEM images for three different types of microbridges without VO_2 coating are shown in **Figure** 3.8. Magnified views of the beam center and anchor are presented in **Figure** 3.7d and **Figure** 3.7e, respectively, where the metal resistor lines can be seen clearly. **Figure** 3.7f shows the cross-sectional view of the film layout and **Figure** 3.7g shows a closer look at the VO_2 thin film coating.

3.1.3 Effect of Residual Axial Stress

Three VO_2-based microbridges with same dimensions but different buckling profiles are tested and analyzed. Because of the diagonal arrangement of the beam, the under-etching effect results in a concave boundary condition which causes a minimum elongation of the effective beam length of $L_{eff} = L + \frac{1}{2}W$, where W is the beam width[116]. From the SEM images, the L, W and h are measured to be 316 µm, 42 µm and 2.27 µm, respectively (see **Figure** 3.9), thus the minimum value of L_{eff} is estimated to be 337 µm. However, the actual effective length could be much longer than this value depending on the isotropic

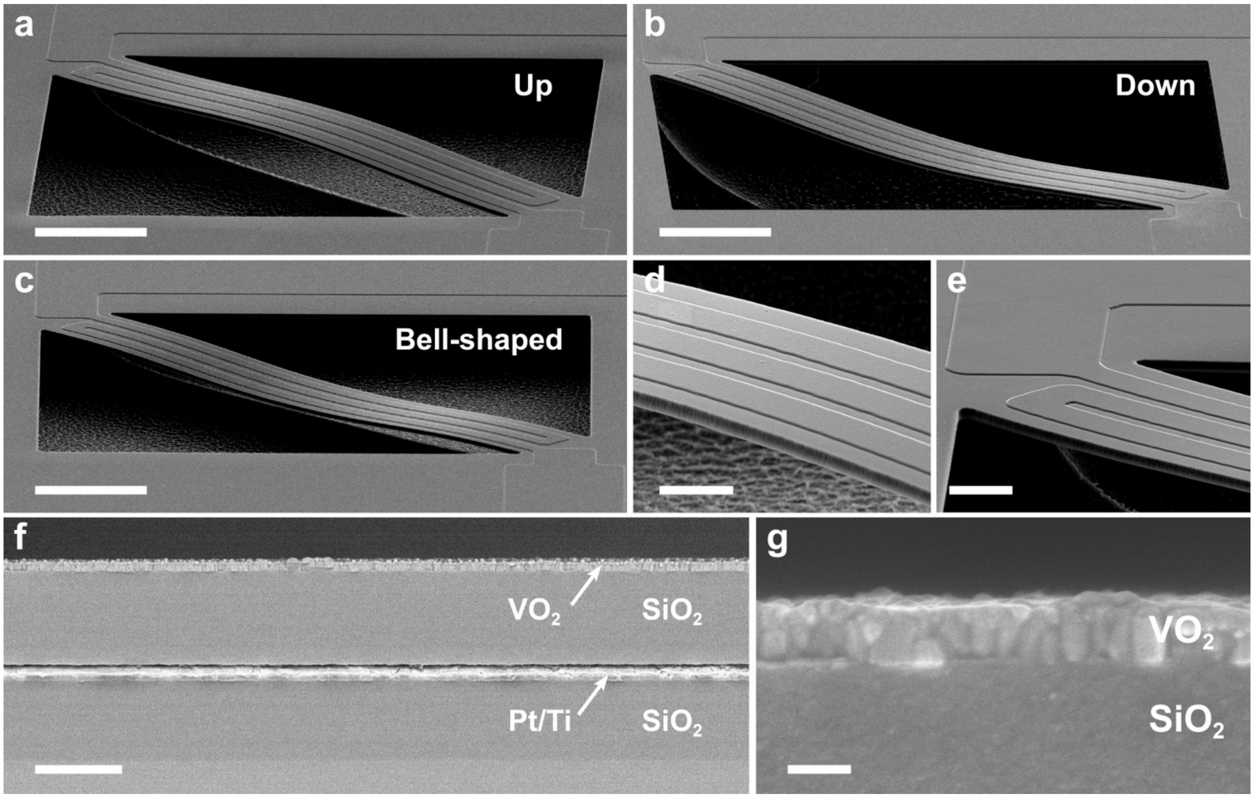

Figure 3.7 SEM images of VO_2-based bridge resonators used in this work. (a) A 300 µm VO_2-based bridge resonator with up-buckled profile, scale bar: 50 µm. (b) A 300 µm VO_2-based bridge resonator with down-buckled profile, scale bar: 50 µm. (c) A 300 µm VO_2-based bridge resonator with bell-shape buckling profile, scale bar: 50 µm. (d) Beam center, scale bar: 10 µm. (e) Beam anchor, scale bar: 10 µm. (f) A cross section view of the stacked layers, scale bar: 1 µm. (g) A cross section view of the VO_2 thin film coating, scale bar: 100 nm.

etching time. After scratching out the suspended structure, the actual L_{eff} is revealed to be 377 µm as shown in **Figure** 3.8. Given that the beam body is made of 91.9% SiO_2, 3.3% Pt, and 5% VO_2, E_{eff} is approximated as 76.6 GPa, where the Young's modulus of each individual material can be found in Table 3.1. Thus, the σ_c is estimated from equation (3.3) to be - 9.14 MPa for the coated device and - 7.84 MPa for the uncoated beam. For an uncoated beam, the residual axial stress (σ_l) can be calculated by considering the difference

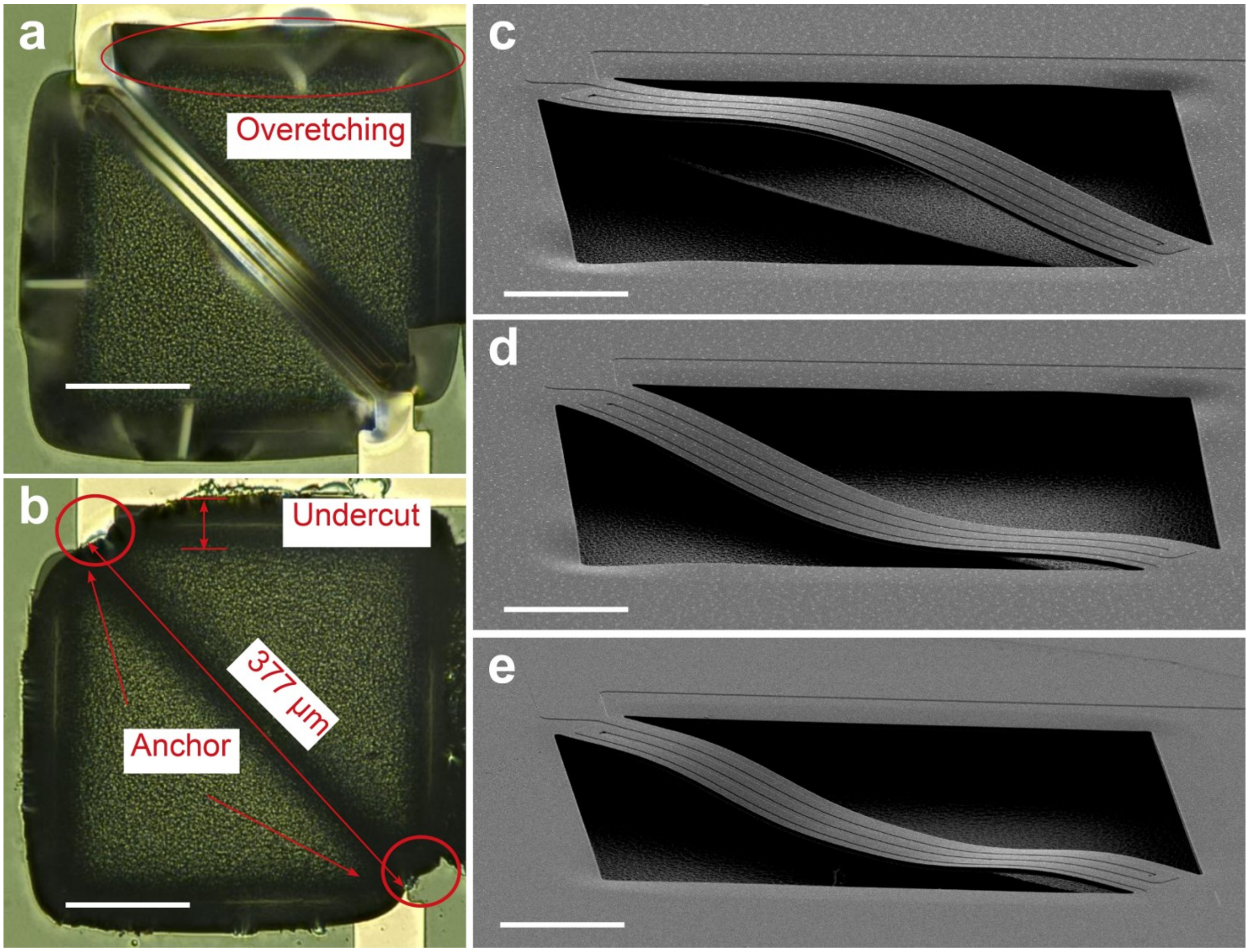

Figure 3.8 Images of the uncoated bridges. (a) Top view optical microscope image of uncoated microbridge, the over-etching edge is highlighted in the red circle, where the Si substrate underneath the transparent SiO_2 layer is etched away, scale bar: 100 µm. (b) Top view optical microscope image of uncoated microbridge with top SiO_2 layer scratched off, the side undercut and anchor are highlighted, the effective length is measured to be 377 µm, scale bar: 100 µm. (c) SEM side view of upward sinusoidal uncoated microbridge, scale bar: 50 µm. (d) SEM side view of downward sinusoidal uncoated microbridge, scale bar: 50 µm. (e) SEM side view of downward wavy uncoated microbridge, scale bar: 50 µm.

in thermal expansion coefficients in SiO_2 layer and Si substrate as[117]:

$$\sigma_l = \frac{E_{SiO_2}}{1-\nu_{SiO_2}}(\alpha_{SiO_2} - \alpha_{Si})\Delta T \tag{3.4}$$

where $E_{SiO_2} = 70\ GPa$ and $\nu_{SiO_2} = 0.17$ are the Young's modulus and Poisson's ratio of SiO_2, $\alpha_{SiO_2} = 0.7 \times 10^{-6}\ K^{-1}$ and $\alpha_{Si} = 2.8 \times 10^{-6}\ K^{-1}$ are the thermal expansion coefficients of SiO_2 and Si, respectively, and ΔT represents the temperature difference between room temperature and SiO_2 deposition temperature. It should be noted that here the influence of Pt is not considered since it is deposited while the sample remains at room temperature. The estimated residual axial stress for the uncoated beam is estimated (from equation (3.4)) to be - 49.6 MPa at room temperature. This value indicates compressive stress much larger than σ_c and therefore the devices exhibit buckled state as shown in **Figure** 3.8.

For a VO_2 coated microbridge, the Finite Element Method (FEM) (see **Figure** 3.10)

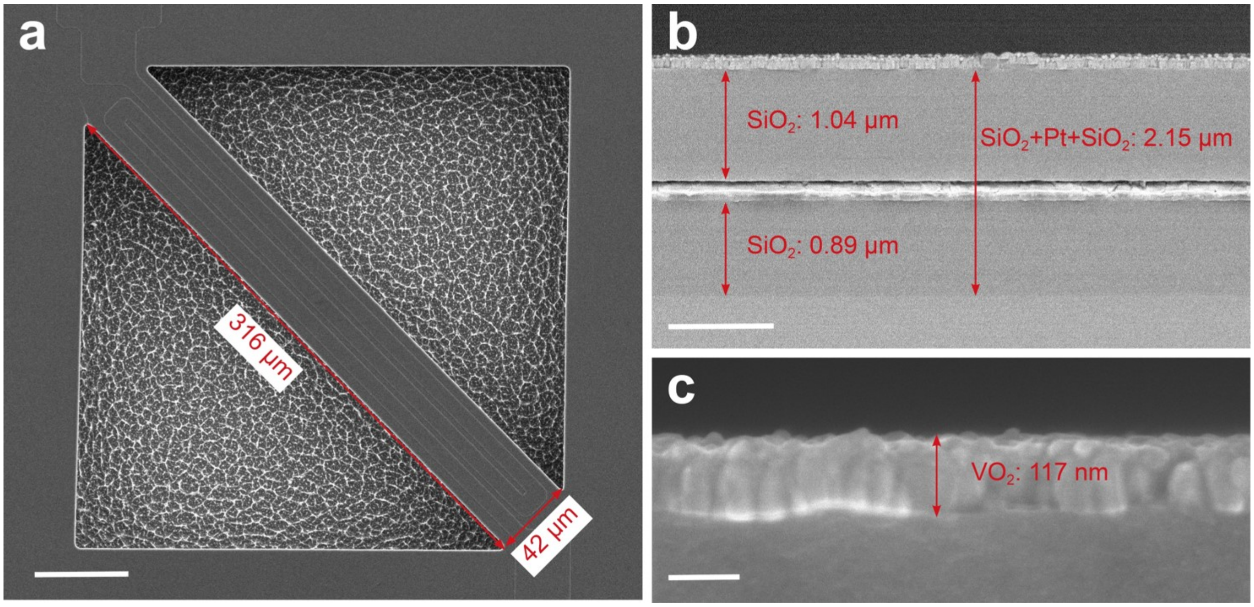

Figure 3.9 Dimensions of VO_2 coated bridge. (a) SEM top view of VO_2-based microbridge, the width is 43 μm and the length is 319 μm, scale bar: 50 μm. (b) SEM cross section view of stacked film layout, the thickness of the beam body is 2.15 μm, the first SiO_2 layer is 0.89 μm, the second SiO_2 layer is 1.04 μm and the Pt heater is 0.22 the second SiO_2 layer is 1.04 μm, scale bar: 1 μm. (c) SEM cross section view of VO_2 thin film coating, the thickness is 117 nm, scale bar: 100 nm.

shows a first mode resonant frequency of 70.2 kHz, and the parameters used for the simulation are summarized in Table 3.1. However, the resonant frequencies of the three devices are

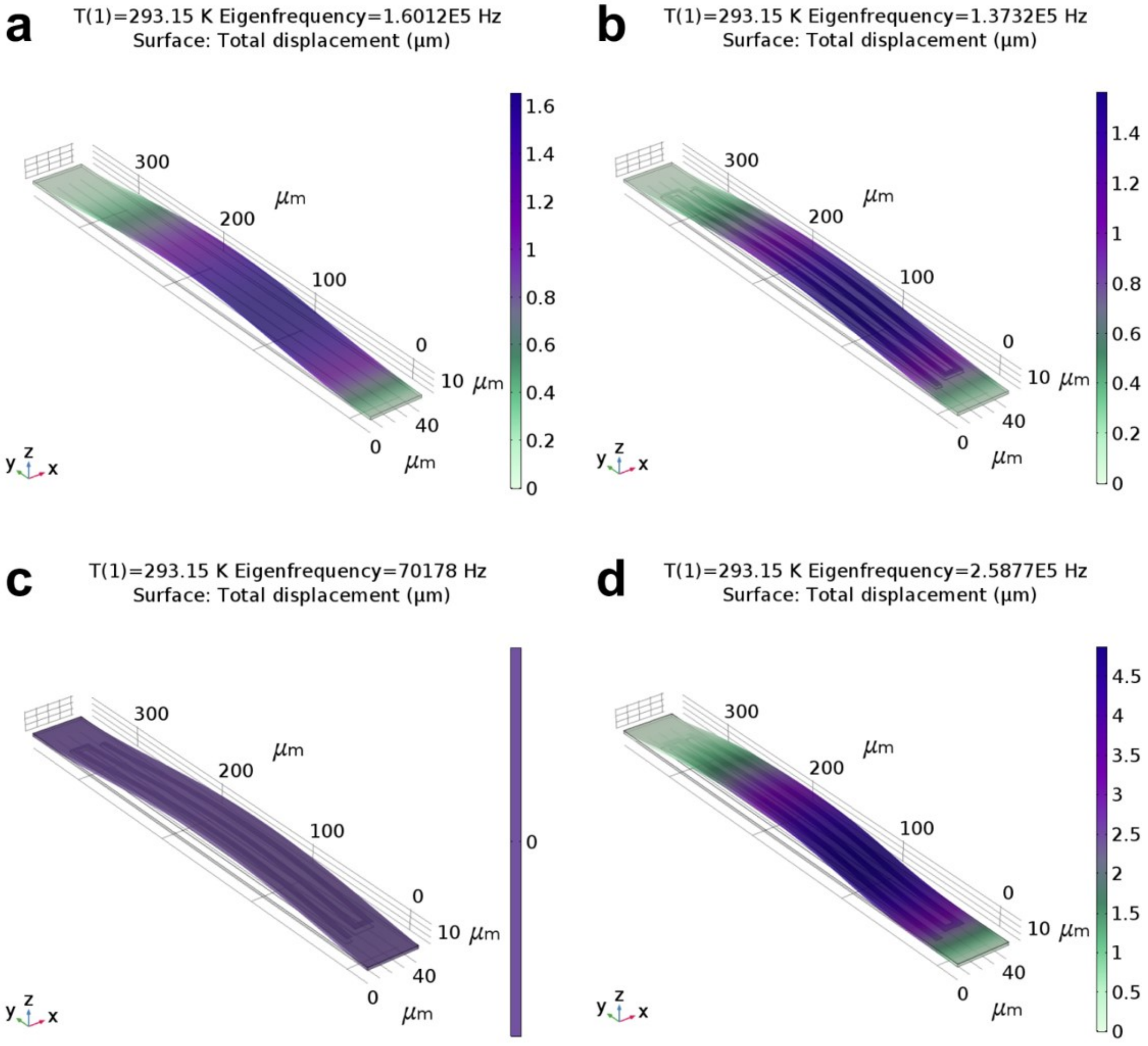

a T(1)=293.15 K Eigenfrequency=1.6012E5 Hz
Surface: Total displacement (µm)

b T(1)=293.15 K Eigenfrequency=1.3732E5 Hz
Surface: Total displacement (µm)

c T(1)=293.15 K Eigenfrequency=70178 Hz
Surface: Total displacement (µm)

d T(1)=293.15 K Eigenfrequency=2.5877E5 Hz
Surface: Total displacement (µm)

Figure 3.10 FEM simulation of first mode resonant frequency (f_1) at room temperature from COMSOL, the scale bars show the lateral deflection at room temperature. (a) First mode resonant frequency of a pure SiO_2 microbridge, $f_1 = 160.1kHz$. (b) First mode resonant frequency of a SiO_2 microbridge with embedded Pt metal heater, $f_1 = 137.3kHz$. (c) First mode resonant frequency of a VO_2 coated microbridge without considering the thermal mismatch between VO_2 and SiO_2 layer, $f_1 = 70.2kHz$. (d) First mode resonant frequency of a VO_2 coated microbridge considering the thermal mismatch between VO_2 and SiO_2 layer, $f_1 = 258.8kHz$.

measured to be 236.5 kHz, 247.6 kHz, and 266.7 kHz for down-buckled beam, up-buckled beam, and "bell-shape"-buckled beam, respectively. The large discrepancy between the simulation and experimental results is attributed to the mismatch of the thermal expansion coefficient between the VO_2 and SiO_2 layers. Given that all materials are deposited at different temperatures, the mismatch in the thermal coefficients leads to a large residual film stress at room temperature. With this taken into account, the FEM simulation gives an estimation of the first mode resonant frequency to be 258.8 kHz, which is close to the experimental measurements. According to Euler-Bernoulli beam theory, the first mode resonant frequency of a buckled microbridge increases when the beam body undergoes compressive axial stress and decreases when the axial load is tensile. The relation between resonant frequency and residual axial stress can be expressed as:

$$f = \sqrt{\frac{2}{\rho_{eff} {L_{eff}}^2}(|\sigma_l| - |\sigma_c|)} \tag{3.5}$$

where $\rho_{eff} = 2920\ kg/m^3$ is the effective density of the beam. Equation (3.5) indicates that when σ_l equals to σ_c, the resonant frequency is not measurable, which is the Euler buckling limit condition. Any deviation of the σ_l from σ_c, by either adding compressive or tensile stress, would lead to a rapid increase in the resonant frequency. The σ_l is estimated to be -20.7 MPa for the up-buckled beam, -21.9 MPa for the down-buckled beam, and -23.9 MPa for the bell-shaped beam. It can be seen that the compressive residual stress in the beam after VO_2 deposition becomes smaller, (compared to the estimated value of - 49.6 MPa before deposition), but it is still larger than σ_c of the coated beam. This is also consistent with the observations by comparing **Figure** 3.7 and **Figure** 3.8 that the buckling amplitudes are reduced after VO_2 deposition.

When VO_2 is thermally actuated, the material undergoes an SPT from M-phase to R-phase. In the low-temperature region before the phase transition, the vanadium atoms are alternatively spaced at distances of 2.65 Å and 3.12 Å. During the phase transition, the crystalline structure is rearranged into a more organized phase with vanadium atoms equally spaced at 2.87 Å [120]. This distortion in the structure leads to a 0.7% contraction of the film along the c-axis direction[121]. Thus, high strain energy is induced into the beam body with a significant amount of stress and strain[15]. The added compressive stress in the VO_2 thin film will induce tensile stress in the SiO_2 beam body –note that no external force is added to the beam during the SPT. Thus, a bending moment is generated to distort the beam structure into a curved shape with the film of a larger thermal expansion coefficient on the convex side. For a C-C bridge structure, the two fixed anchors restrict the large lateral deflection and lead to a high residual stress level along the beam longitudinal direction. This residual tensile stress in the SiO_2 beam body causes a resonant frequency increase in an unbuckled microbridge[21] and a resonant frequency decrease in a buckled microbridge[122].

3.2 Fabrication of Ferroelectrect Nanogenerators

3.2.1 Fabrication of Polypropylene Ferroelectrect Films

PPFE exhibits a strong piezoelectric effect where its ”piezoelectricity” originates from the distortion of the µm-sized charged air ellipsoids inside the PPFE. Those engineered macro-scaled dipoles change dipole moments upon compression and releasing operation. In this section, the fabrication process is briefly described and schematically shown in **Figure** 3.11. First, the fabrication process starts with the polypropylene (PP) film filled with inorganic silicate particles as stress concentrator [123, 124]. When the material undergoes a bi-directional

Table 3.1 Properties of the materials used in FEM simulation, properties of SiO_2 and Pt are taken from COMSOL, and the property of VO_2 is taken from the literature[118, 119].

Materials	SiO_2	Pt	VO_2
Thermal expansion coefficient (1/K)	0.7×10^{-6}	8.8×10^{-6}	5.7×10^{-6}
Density (kg/m^{-3})	2200	21450	4670
Young's modulus (GPa)	70	169	140
Poisson's ratio	0.17	0.38	0.33
Strain reference temperature (K)	573.15	293.15	743.15

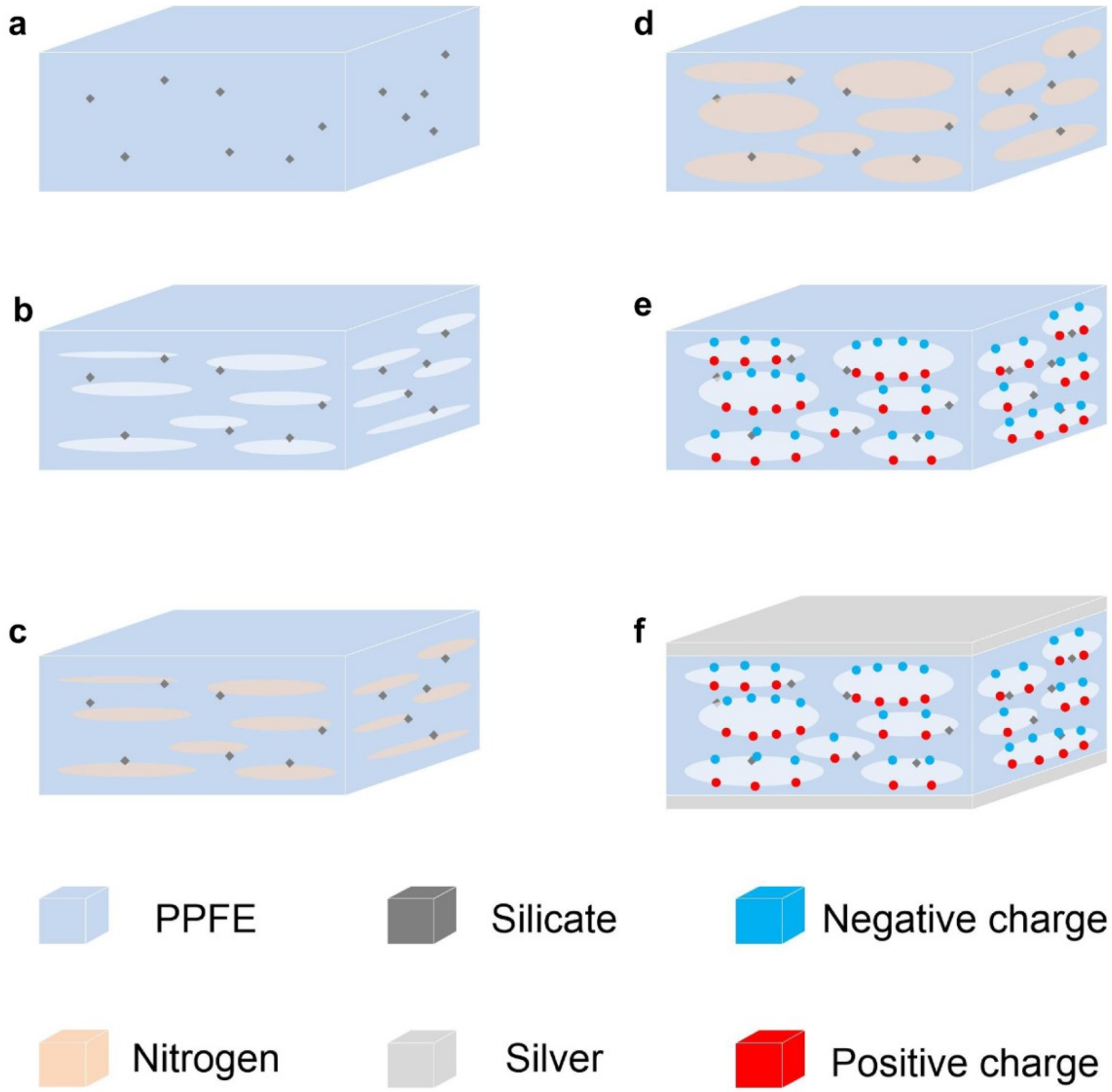

Figure 3.11 Fabrication process. (a) Polypropylene (PP) film filled with inorganic silicate particles. (b) Biaxial in-plane stretching of the PP film to create the air ellipsoids. (c) Diffusion of N_2 gas. (d) Ellipsoids expansion by a sudden decrease in pressure. (e) Plasma discharging. (f) Electrodes metalization.

stretching process, the stress starts to accumulate at the silicate location. When the material's cohesive strength is reached, the PP film fails and micro-cracks propagate along the stretching axis with the help of stress concentrator [125]. Next, the PP film is introduced in a high-pressure nitrogen (N_2) environment of above 5 MPa where the N_2 gas is able to diffuse into the micro cracks through the PP film. Then, the high-pressure ambient is suddenly removed and the air ellipsoids are expanded rapidly creating ellipsoid structure [126]. A heat treatment at ~ 100 °C follows in order to increase the strength of the void structure [127, 128]. After that, the high electric field is applied to the PP film and plasma discharging occurs in the air ellipsoid resulting in two opposite surfaces of the voids are charged with different polarities. Finally, silver thin films are sputtered on both sides of the PPFE film as metal electrodes by using sputtering coater (Hummer X, Anatech Inc.) as shown in **Figure** 3.12. The PPFE film is placed in a vacuum chamber beneath the silver target at the distance of 30 mm. During the deposition, the base vacuum level of 20 mTorr is reached and N_2 gas is introduced to the chamber until the pressure is stabilized at 65 mTorr. A high voltage of 1.5 kV is then applied to generate a large electric field inside the chamber to create N_2 plasma bombardment on the silver target, leading to a thin film of silver deposited on PPFE surface. The above setting would give an approximately 500 nm thick silver thin film for a 30 min deposition.

3.2.2 Piezoelectric Effect and Multilayer Devices

This section discusses the linear coupling between the electrical and mechanical domain of the PPFE and justifies the piezoelectric effect for the electromechanical response. Although the fundamental working principle of PPFE differs from the piezoelectric material, the electromechanical response shares very similar behavior. For piezoelectric material, the fundamental equations establish a linear coupling between electric polarization field and mechanical force by:

$$P = d_{33}\frac{F}{A}, \tag{3.6}$$

where P is the polarization field, d_{33} is the piezoelectric coefficient, F is the mechanical input force and A is the contact area. Charges accumulated at the boundaries due to this induced P and surface charge density σ can be determined as $\sigma = P$. By using a capacitive

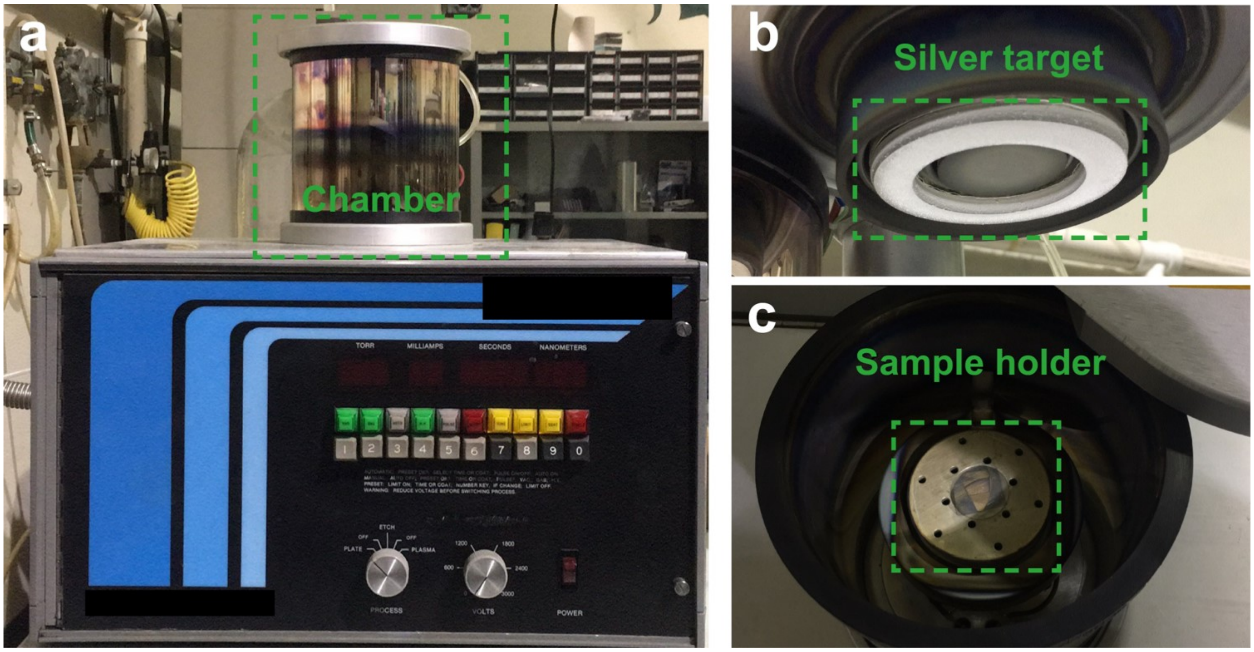

[redacted]
[redacted]

Figure 3.12 Sputtering coater used for depositing silver electrodes on PPFE film. (a) Overview of the sputtering coater (Hummer X, Anatech Inc.). (b) The silver target mounted on top of the vacuum chamber. (c) The sample holder at the bottom of the chamber where PPFE is placed for metalization.

model, the accumulated charges Q_{sc} and open circuit voltage V_{oc} can be expressed as:

$$Q_{sc} = \sigma A = d_{33} \cdot F, \tag{3.7}$$

and

$$V_{oc} = \frac{Q_{sc}}{C} = \frac{d_{33} g}{\epsilon A} \cdot F, \tag{3.8}$$

where C is the equivalent capacitance of the device. Equations (3.7) and (3.8) show that both Q_{sc} and V_{oc} have linear relation with F. When output terminals of the device are short connected, Q_{sc} is released as short-circuit current (I_{sc}) and can be described as:

$$I_{sc} = \frac{dQ_{sc}}{dt} = \frac{d_{33} g}{\epsilon A} \cdot \frac{dF}{dt}, \tag{3.9}$$

which takes the derivative form of F (and also V_{oc}) as shown in **Figure** 3.13. **Figure** 3.13a shows the V_{oc} output in a compression and releasing cycle, the triangular waveform follows the same profile as the mechanical input F_1. The I_{sc} which takes the derivative form of V_{oc}

exhibits a square waveform as shown in **Figure** 3.13b. The measured signal waveform is in accordance with equation (3.8) and equation (3.9) and verifies the piezoelectric effect.

Changing polarity test is also carried out to justify that the output signal comes from the device. **Figure** 3.14a and **Figure** 3.14c show the V_{oc} and I_{sc} output in a forward connection - i.e. connecting the device and testing instrument through terminals with the same polarity. Switching the connecting terminals produces the results shown in **Figure** 3.14b and **Figure** 3.14d.

Since the device can be modeled as a capacitive model. Therefore, the output should follow the corresponding behavior. For a single layer device with a fixed thickness under a given mechanical force, the output in terms of voltage and current can be magnified by increasing the contact area. Thus, by connecting N pieces of single-layer devices in parallel, both V_{oc} and I_{sc} can be increased by N times. This can be easily done by stacking N layers as shown in **Figure** 3.15, where all the positive and negative electrodes are respectively connected with each other. In this configuration, V_{oc} and I_{sc} can be expressed as:

$$V_{oc} = N \cdot \frac{d_{33}g}{\epsilon A} \cdot F \tag{3.10}$$

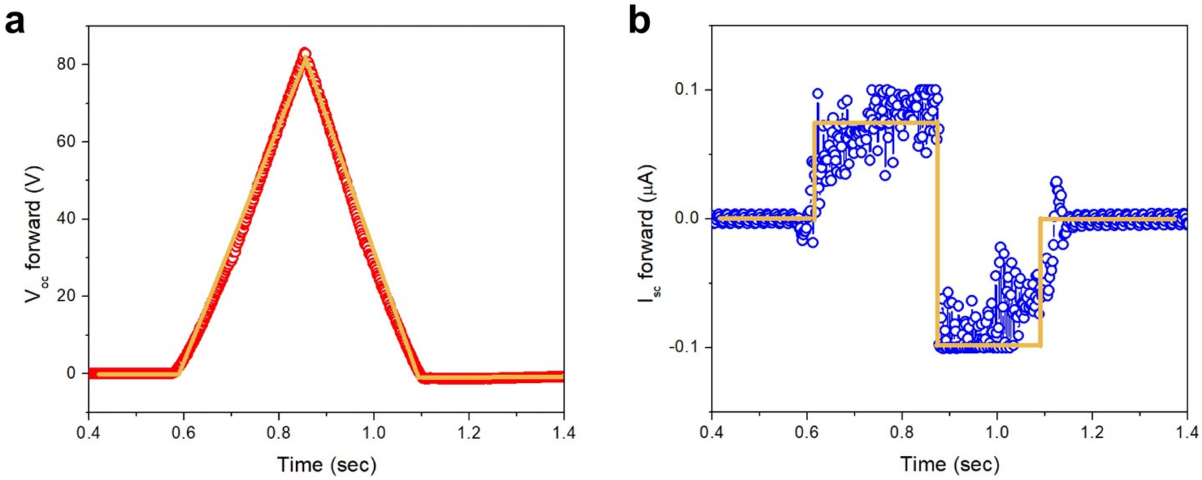

Figure 3.13 Signal profile compare of V_{oc} and I_{sc}. (a) Triangular waveform V_{oc} output in compression and releasing cycle. (b) Square waveform I_{sc} output in compression and releasing cycle.

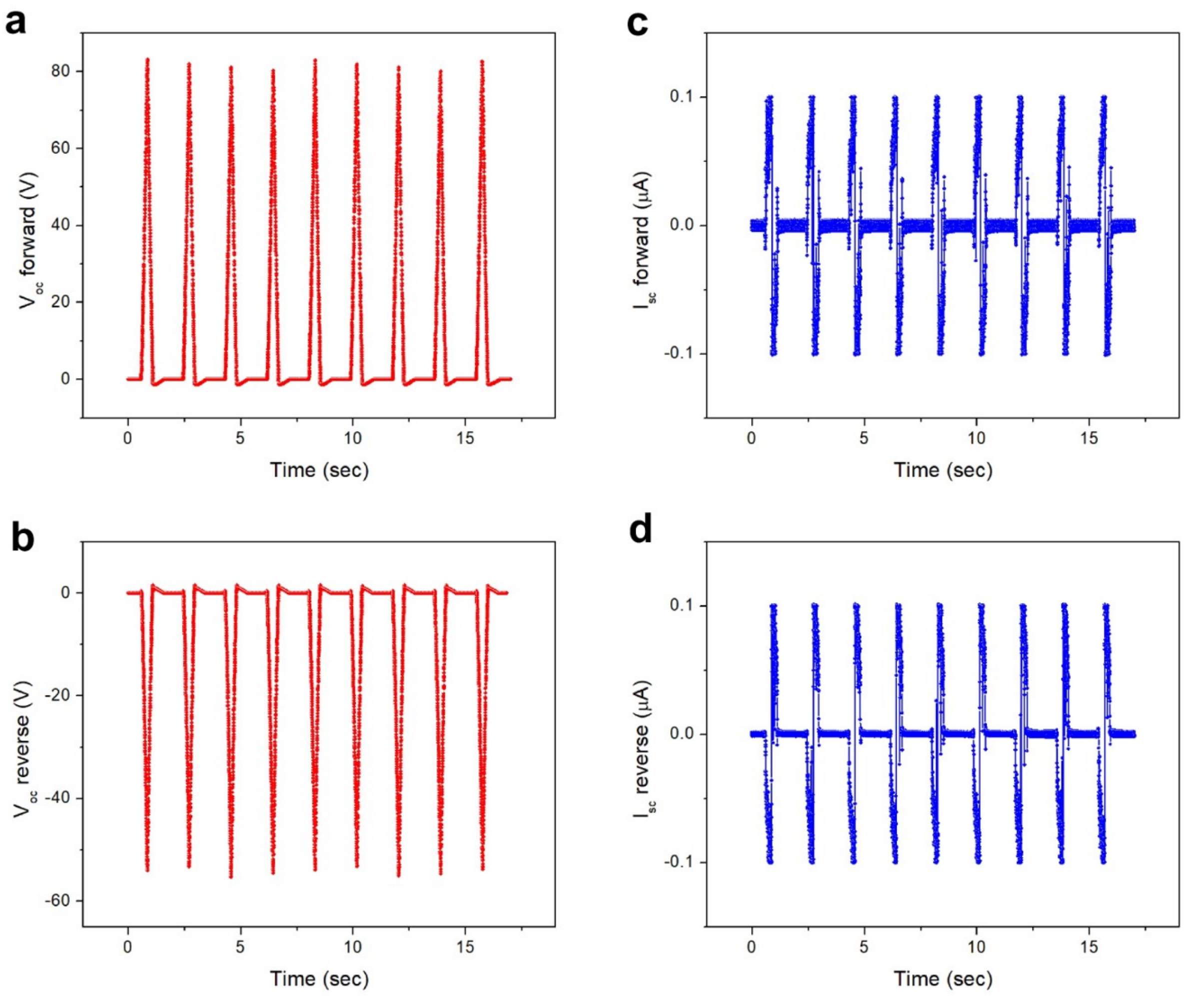

Figure 3.14 Changing polarity test of electric output. (a) Open circuit voltage (V_{oc}) measurement in the forward bias connection. (b) Open circuit voltage (V_{oc}) measurement in the reverse bias connection. (c) Short circuit current (I_{sc}) measurement in the forward bias connection. (d) Short circuit current (I_{sc}) measurement in the reverse bias connection.

and

$$I_{sc} = N \cdot \frac{d_{33}g}{\epsilon A} \cdot \frac{dF}{dt} \tag{3.11}$$

3.3 Summary

This chapter presents the design and fabrication of VO_2-based MEMS resonators and the development of ferroelectret nanogenerators. The resonators used throughout this work are

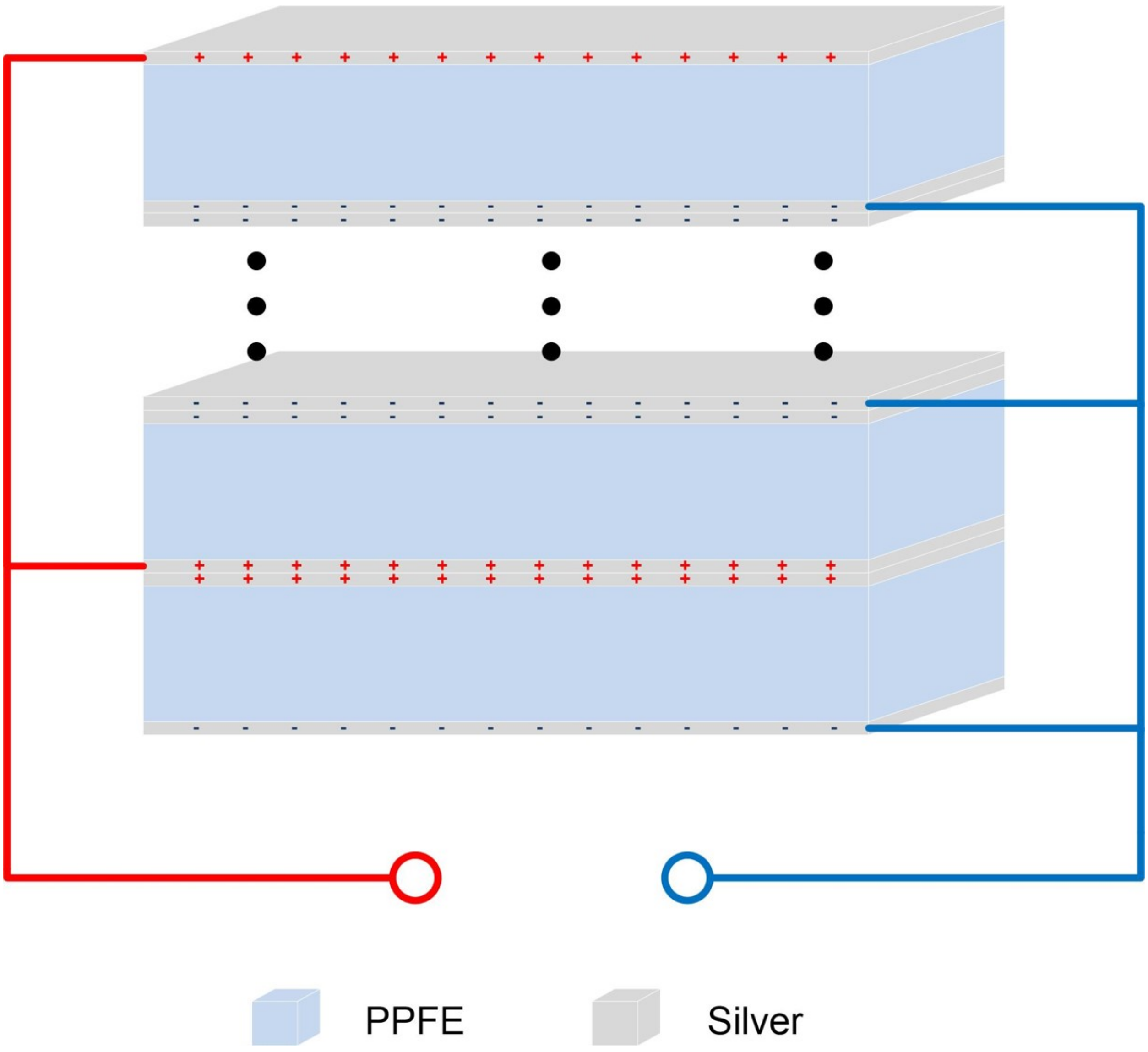

Figure 3.15 Schematic demonstration of stacking multilayer structure.

three bridges with the lengths of 200, 250 and 300 µm as well as three cantilevers of 350, 450 and 550 µm. The resistance measurement is performed after the VO_2 deposition to confirm the film quality. First mode resonant frequencies of both structures are measured and compared to simulated values. The discrepancy in the experimental and simulated data can be attributed to the residual thermal stress and the under etching effect. Moreover, microbridges with different buckling profiles are observed even when the same fabrication conditions are used. The buckling amplitude and orientation preference are found to be related to boundary conditions, geometric dimensions, and residual thermal stress. FEM simulation, as well as analytical methods, are used to estimate the residual thermal stress.

The fabrication process of ferroelectret nanogenerator (FENG) is also introduced in this chapter. The strong piezoelectric effect of the material comes from the engineered macro dipoles upon external mechanical load occurs. The working principle of the device is explained in the point of view of changing dipole moment and a capacitive model. Changing polarity test is also carried out to confirm the success of the device fabrication.

CHAPTER 4

INFLUENCE OF VO_2 THIN FILM COATINGS ON THE PERFORMANCE OF MEMS RESONATORS

This chapter discusses the performance of VO_2 based MEMS resonators with both cantilever and bridge structures. The study first focuses on the resonant frequency tuning behavior at the two ends of the phase transition region where VO_2 is either in its monoclinic or rutile phase. Opposite trends have been found before and after the phase transition region. By comparing the relative resonant frequency shifts in both structures, it has been found that the bridge structure is more stress-sensitive while the cantilever structure is dominated by the geometric effect. The large residual thermal stress in bridge structures would also lead to different types of buckling profiles and amplitudes. Thermal actuation is achieved by applying an electrical current to integrated heaters, or by uniform substrate heating. Bidirectional tunability is found when substrate heating is used, while Joule heating shows a monotonic change in frequency. This phenomenon can be attributed to the transition in boundary conditions, where the turning points are indicated by the prominent changes in buckling amplitude. The devices' power consumption, response time constant are also discussed in this chapter. A pulse width modulation (PWM) method is used to find out the underlying mechanisms for programming the resonant frequency states within the phase transition region. By combining VO_2-based MEMS resonators with ferroelectret nanogenerators, a new type of head injury telemetry system is developed for compact sports injury evaluation. Finally, a prototype of second-order MEMS bandpass filter is inspired by the tunability and the programmability of the VO_2-based resonators. In a specific measuring configuration analog to laser interferometer, the bandwidth tunability and Q-factor enhancement have been demonstrated.

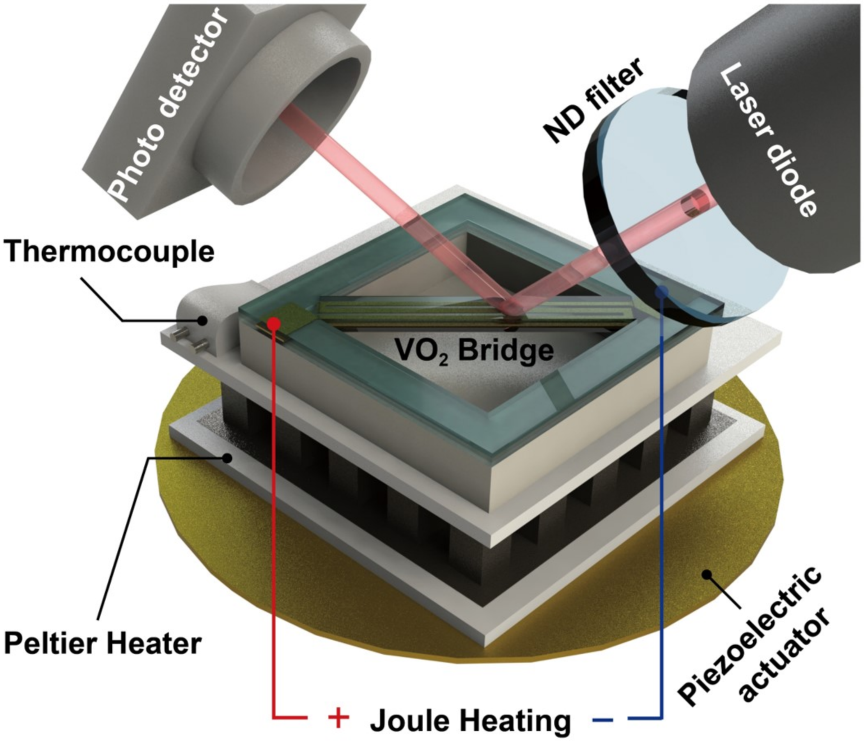

Figure 4.1 Schematic diagram of the laser deflection method used to measure the resonant frequency of a 300 µm VO_2-based bridge resonator, the VO_2 phase transition can be induced either by electro-thermal (i.e. resistive, or Joule) heating or substrate heating. Mechanical vibration input is provided by the piezoelectric disk.

4.1 Experimental Setups

The first mode resonant frequency of the VO_2-based MEMS resonator is measured by the laser deflection method which is briefly described as a schematic diagram shown in **Figure 4.1**. The device is first attached on the thermal conductive IC package, which is also fixed onto a Peltier heater, by thermally conductive silver paste. A thermocouple is then placed onto the IC package close to the device in order to monitor the temperature. A piezoelectric actuation disk is also placed beneath the Peltier heater which provides the AC sweeping mechanical force in order to determine the resonant frequency. Then the whole package is placed into a vacuum chamber and pumped down to below 10 mTorr. An AC electrical sweeping signal is provided by a network analyzer (HP-3589A) and drives the piezoelectric

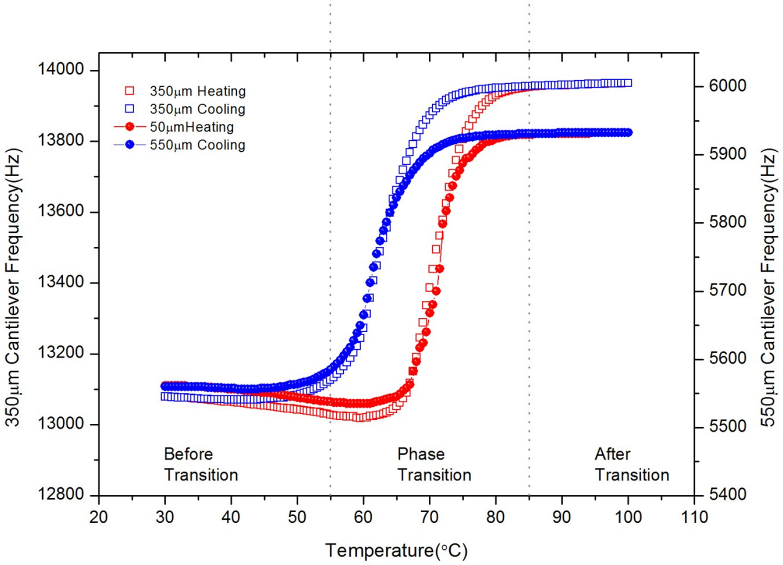

Figure 4.2 Resonant frequency change for VO_2 coated cantilever beams of different lengths through full heating and cooling loop.

actuator into vibration. The VO_2 resonator exhibits strong vibration at its natural resonant frequency and deflects away the laser beam focused onto the beam center. This difference in the light intensity is captured by a photodiode detector, which is also connected with the network analyzer. To avoid any undesirable heating effect caused by the laser beam, especially in the phase transition window of VO_2, a neutral density filter (ND = 1) is used to reduce the laser power shine on the device while still providing a detectable optical signal.

4.2 Comparison of Different Structures

Measurement of the first mode resonant frequency has been performed for VO_2 coated cantilevers and bridges through the full heating and cooling curves. Different lengths of each type of beams were used to analyze the structure dependence of the resonant frequency shift. The geometries used for the three cantilevers are 2 µm thickness and 50 µm width for all and 350/450/550 µm length for each, while the geometries used for the other three bridges are 2 µm thickness and 40 µm width and 200/250/300 µm length for each. The thickness of the VO_2 coating is approximately 0.2 µm for all the beams.

4.2.1 Observations of Different Frequency Shifts

The resonant frequencies increase rapidly during the IMT phase transition region for both the C-C (unbuckled) structures and the C-F structures. This behavior is due to a large amount of stress generated by the VO_2 thin film. However, in order to completely understand the behavior of VO_2-based MEMS resonators, the slopes at the two ends of the frequency-temperature curves should also be given attention. By comparing the frequency curves between the cantilevers (**Figure** 4.2) and the bridges (**Figure** 4.3) both with the VO_2 coatings, we found that the frequencies of the cantilevers always decrease before the phase transition and become almost flat after the transition has been completed. However, the trend for bridges is different. The resonant frequency will increase in the low-temperature region and then decrease after the phase transition. If we further compare coated and uncoated beams (In **Figure** 4.2, 4.3, 4.4, and 4.5, only the 350 and 550 µm cantilevers and

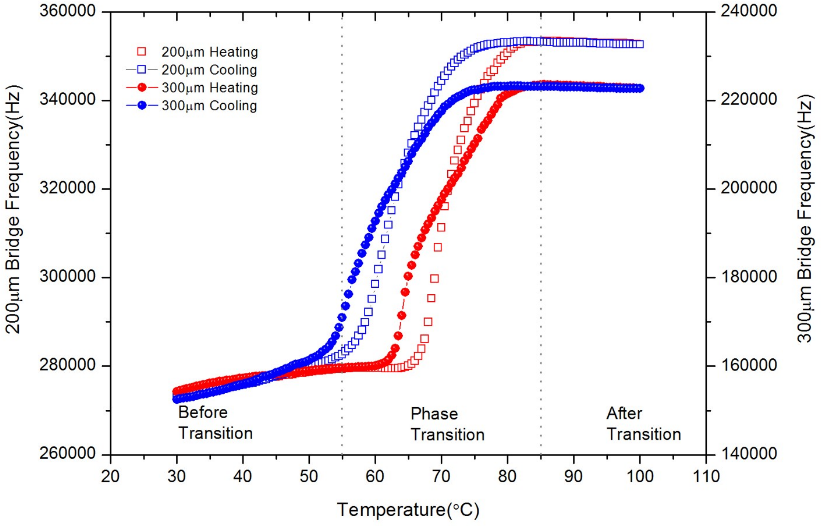

Figure 4.3 Resonant frequency change for VO_2 coated bridge beams of different lengths through full heating and cooling loop.

200 and 300 µm bridges have been plotted but the data is also listed in Table 4.1 and Table 4.2), we find that at the higher temperature region, they share the same trend (not the slope). Thus, the discrepancy in frequency shift pattern between the coated and uncoated beams with the same structure can be explained by the difference in stress levels.

Table 4.1 Relative frequency change for coated and uncoated cantilever beams with different lengths. The phase transition region is from 65°C to 85°C.

Cantilever length (µm)	Before transition	Phase transition	After transition	SiO_2
350	-0.39%	6.91%	0.08%	0.53%
450	-0.40%	7.26%	0.09%	0.57%
550	-0.43%	6.94%	0.04%	0.53%

Table 4.2 Relative frequency change for coated and uncoated bridge beams with different lengths. The Phase transition region is from 62°C to 85°C for the 300 µm and 65°C to 85°C for the others.

Bridge length (µm)	Before transition	Phase transition	After transition	SiO_2
200	2.21%	25.20%	-0.18%	-0.24%
250	1.21%	30.46%	-0.30%	-0.48%
300	3.47%	37.19%	-0.38%	-0.51%

4.2.2 Stress Effect

For a certain beam structure, the factors in determining the frequency shift involve Young's modulus and stress. However, Young's modulus of the SiO_2 increases very slowly as a function of temperature at a rate of 178 ppm/°C[129], which cannot be the main factor in determining the frequency change in **Figure** 4.4 and **Figure** 4.5. So Young's modulus can be taken as a constant value and thus the frequency change can be taken as stress-induced. For instance, the uncoated bridge will undergo compressive stress as the temperature increases due to the constraint of the thermal expansion. This induced negative stress will lead to a decrease in the resonant frequency[130]. On the other hand, for the VO_2 coated beams, the

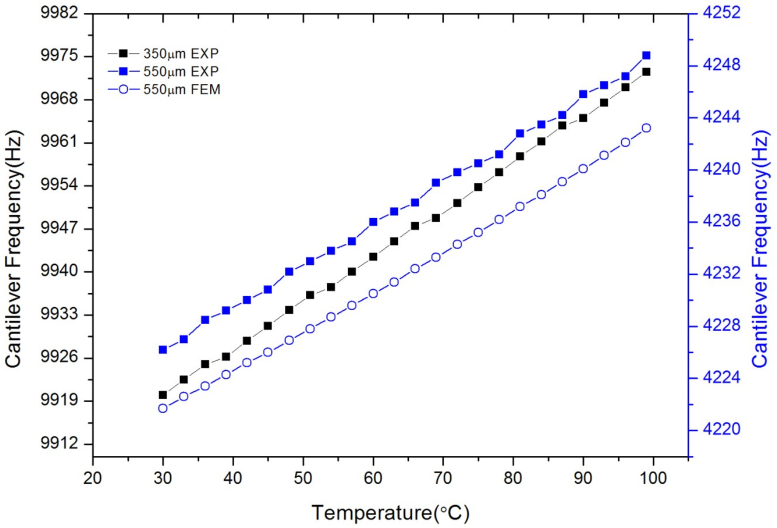

Figure 4.4 Resonant frequency change for uncoated cantilever beams of different lengths as a function of temperature.

large difference in the thermal expansion coefficient between VO_2[21] and SiO_2 will apply a tensile force to the bridge which will increase the frequency. It is also important to note that before the phase transition, where VO_2 is in its monoclinic phase, the thermal coefficient is larger than that of in the rutile phase (The thermal expansion coefficient of VO_2 in the monoclinic phase is about $5.7 \times 10^{-6}\ \ K^{-1}$[21, 118]).

So, before the phase transition, the surface stress generated by the VO_2 film and applied to the SiO_2 beam dominates in determining the frequency shift pattern. As for the rutile phase, the thermal coefficient of VO_2 is smaller so that the surface stress generated by VO_2 can no longer suppress the thermal stress and thus the frequency shift follows the same trend of the uncoated beams. One thing that needs to be clarified here is that unlike the bridges, applying surface stress to a cantilever will induce axial stress in the opposite direction within the beam[131, 132, 133]. Based on this, we can predict that the relative frequency change of the VO_2 coated cantilevers will be independent of the beam length because the increase of the resonant frequency for a cantilever under a compressive surface stress indicates that the geometric effect dominates in the frequency shift[130], and this is

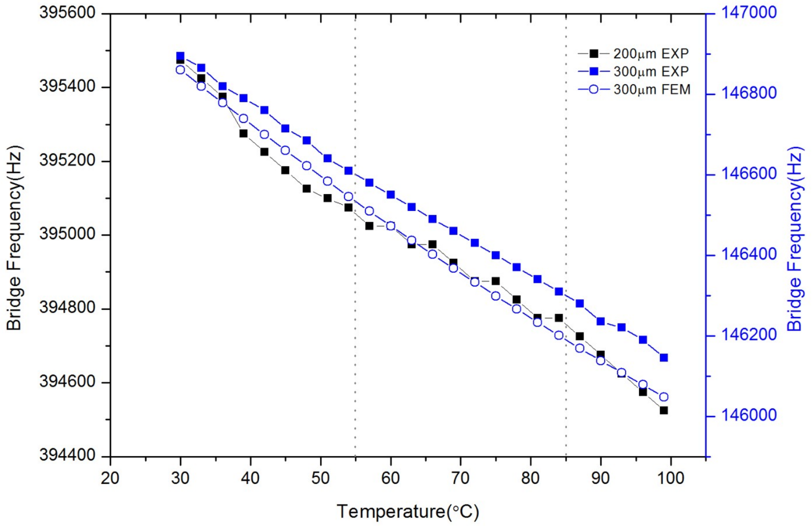

Figure 4.5 Resonant frequency change for uncoated bridge beams of different lengths as a function of temperature.

also confirmed by the data listed in Table 4.1. Although the external stress dominates at the lower temperature while the thermal stress dominates at the higher temperature, the increase of the frequency for the cantilevers at higher temperature is very small but the frequency drop for the bridges within the same temperature region is lager and comparable to that of the uncoated beams. The reason is that the resonant frequency is much more sensitive to the stress for a C-C structure than a C-F structure according to the prediction of Euler-Bernoulli beam theory[131, 132, 133].

4.2.3 FEM Simulation of Two Ends

A finite element method (FEM) simulation has been done on the 550 µm cantilever and the 300 µm bridge to analyze the thermal expansion effect on the frequency shift. The simulation is simplified by applying mixing rule to the density and Young's modulus since the beams we used contains a small portion of Pt. Initial stress and strain, as well as the under etching effect, should also be taken into consideration for the simulation to meet the measurement.

The simulation for the bridge is not as straightforward and requires a deeper understanding of the system. For the bridge, we cannot apply a fixed constraint at the two ends in the longitudinal direction because in this case, the generated thermal force is calculated by applying the thermal strain generated under the free thermal expansion condition. Any object that undergoes thermal expansion will induce the thermal stress below that value. However, the exact stress magnitude cannot be calculated[134]. The fundamental principle here is to reduce the physical constraints in the simulation. This can be done by simply applying a fixed constraint at one end of the silicon substrate and a roller constraint at the other.

4.3 Stress Interfaces in Bridge Structure

It is well known that the resonant frequency of an unbuckled microbridge structure increases with increasing axial tensile stress, while the opposite is true for a buckled microbridge. However, microbridge resonator structures usually deviate from ideal C-C structures in terms of the flexibility of the anchor, which changes the fixed-fixed boundary condition into a pinned-pinned or fixed-pinned condition. This section addresses the influence of different buckling profiles and amplitudes in bridge structures on the performance of resonant frequency tuning[135]. The microbridges that used for this study have the same dimensions with different buckling states, the fabrication process is introduced in detail in chapter 2.

4.3.1 Bending moment in the up-buckled beam

For an up-buckled microbridge with profile as shown in **Figure** 4.6, the VO_2 thin film deposited on the SiO_2 surface is under tension at room temperature[136]. When the VO_2 is thermally actuated, compressive surface stress is induced to the convex side of the beam surface due to the SPT. This leads to a decrease in the surface tensile stress and consequently, a positive bending moment is generated on the pinned axis A and A' (see **Figure** 4.7). On the other hand, the upper edges B and B$'$ of the beam (see **Figure** 4.7) tend to move toward the beam center. When Joule heating is used for the electrothermal actuation method, the heat is mainly concentrated along the suspended beam (not the substrate). Unlike the uniform heating that occurs during conduction heating, a large thermal gradient is expected between the suspended beam and its anchor; which results in ”cold anchors” that remain in fixed-fixed condition. In this case, the lateral deflection and the relative movement of edges B and B$'$ are significantly lower, and axial tensile stress is induced at the beam boundaries AB and A$'$B$'$. As the temperature increases and the SPT proceeds, this residual axial tensile stress accumulates and results in a monotonically decrease in the resonant frequency as shown in **Figure** 4.6a (as expected for a buckled C-C beam).

The resonant frequency tunability is also found to be correlated with the actuation method. As shown in **Figure** 4.6b, when the substrate heating is used to induce the VO_2 SPT, the resonant frequency shift behaves in a very different way compared to the Joule heating method shown in **Figure** 4.6a. During the heating loop, the resonant frequency decreases at the onset of the SPT, similarly to the case for Joule heating. When the temperature reaches about 76°C, the resonant frequency approaches its minimum value ($\sim$ 235 kHz) and then start to increase as the heating loop continues. It should be noted that this turning point, which leads to a bidirectional tunability, happens in the middle of the SPT –from the cooling curve, this value of temperature remains within the hysteresis region. Thus, the microbridge is still subjected to a positive bending moment. **Figure** 4.6c shows the 3D reconstruction image of this up-buckled bridge with its height distribution information, taken by using the bottom of the etched cavity as the reference plane. The normalized buckling amplitude with respect to the fixed top surface is plotted along the beam longitudinal direction and shown as a function of substrate heating temperature in **Figure** 4.6d. It can be seen that the buckling amplitude decreases by $\sim$ 5% between 70 to 90°C, and the first noticeable change occurs between 70 and 80°C, which includes the turning point shown in **Figure** 4.6b. Thus, for substrate heating, the lateral deflection is no longer restricted by the

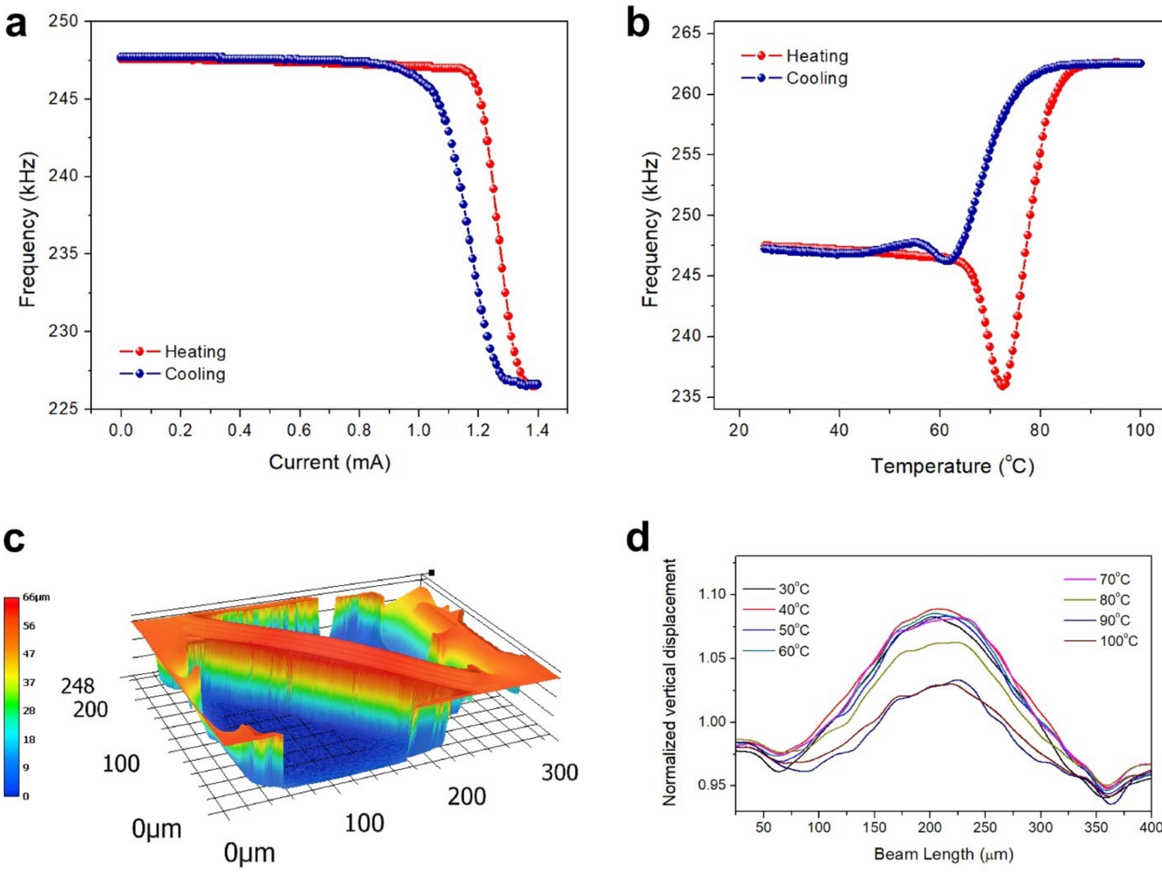

Figure 4.6 The resonant frequency shift of a 300 µm VO_2-based microbridge in the up-buckled state. (a) Resonant frequency shift through a complete heating and cooling cycle by using integrated resistive heaters. (b) Resonant frequency shift through a complete heating and cooling cycle using substrate conduction heating. (c) 3D reconstruction of the device showing the buckling amplitude in $+z$ direction. (d) Normalized buckling amplitude change as a function of substrate heating along the beam axial length.

fixed-fixed boundary condition that exists when using Joule heating. The relative movement of edges B and B$'$, therefore, induces compressive axial stress and results in an increase in the resonant frequency. This transition from a fixed-fixed boundary condition to a fixed-pinned boundary condition can be attributed to different thermal distribution profiles upon the actuation methods used. Unlike the Joule heating method, the substrate heating provides a more uniform thermal distribution, with a much lower temperature gradient between the suspended beam and the two anchors.

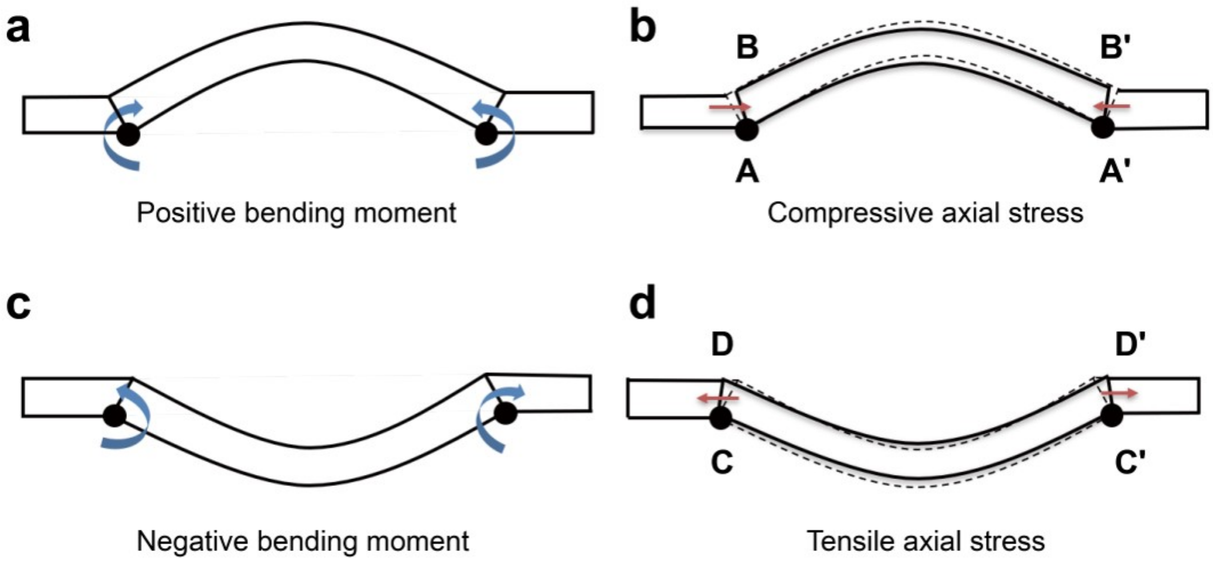

Figure 4.7 Schematic illustration of geometric distortion and axial stress upon different bending moments. (a) The initial state of an upward buckled microbridge with a sinusoidal profile under a positive bending moment. (b) The lateral deflection in the structure reduces the buckling amplitude, the rotational force on the pinned boundaries leads to a relative movement of edges B and B′ towards each other. Compressive axial stress is therefore induced, which causes an increase in resonant frequency after the turning point shown in **Figure** 4.6b. (c) The initial state of a downward buckled microbridge with a sinusoidal profile under a negative bending moment. (d) The lateral deflection in the structure reduces the buckling amplitude, the rotational force on the pinned boundaries leads to a relative movement of edges D and D′ against each other. Tensile axial stress is therefore induced, which causes a decrease in resonant frequency after the turning point shown in **Figure** 4.8b.

4.3.2 Bending moment in the down-buckled and bell-shaped beam

When considering a down-buckled beam, the VO_2 thin film is coated on the concave side of the beam. During the SPT, compressive stress is added to this side of the beam body, which causes a negative bending moment exerted on the bridge. The boundary interfaces D and D′ tend to move against each other. **Figure** 4.8a shows the resonant frequency measurement as a function of Joule heating for a full heating and cooling cycle. The fixed-fixed boundary condition, in this case, results in compressive axial stress, which increases the resonant frequency in the heating loop. Similar to what happened in the up-bucked beam, at the onset of critical lateral deflection (between 70 and 80 °C –see **Figure** 4.8d), the fixed-fixed boundary condition transitions into a fixed-pinned condition where the rotational force on

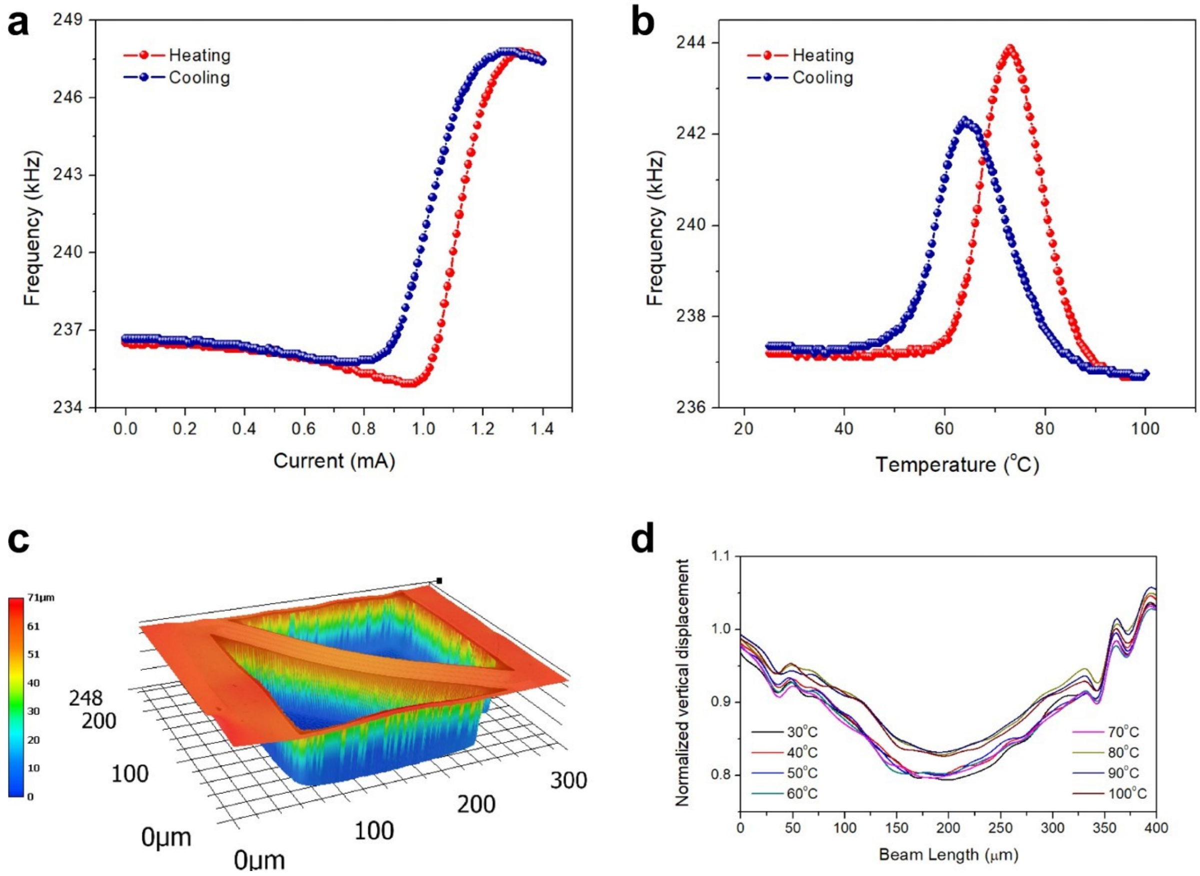

Figure 4.8 The resonant frequency shift of a 300 µm VO_2-based microbridge in the down-buckled state. (a) Resonant frequency shift through a complete heating and cooling cycle by Joule heating. (b) Resonant frequency shift through a complete heating and cooling cycle by substrate heating. (c) 3D reconstruction of the device showing the buckling amplitude in $-z$ direction. (d) Normalized buckling amplitude change as a function of substrate heating along the beam axial length.

the anchor pushes the edges D and D′ (in **Figure** 4.7d) against each other, leading to a tensile stress along the beam axis. As shown in **Figure** 4.8b, the sign of the change in frequency with temperature turns at a similar temperature ($\sim$ 76 °C) to that observed for up-state buckled bridges (**Figure** 4.6b). It should be noted that the change in frequency for these cases have opposite signs (i.e. up-state buckled beam turns from increasing to decreasing frequency; while the opposite is true for the down-state buckled beams). The change in buckling amplitude along the beam length is shown in **Figure** 4.8d. This bidirectional resonant frequency tunability observed for VO_2 buckled bridges under substrate heating also explains the unclear phenomena observed in a previous work, where a bump is observed in the frequency-temperature curve[122].

As indicated in **Figure** 3.6, down-buckled microbridges with the downward bell-shaped profile are also observed. The buckling amplitude for these devices is plotted in **Figure** 4.9d along the beam length with respect to different substrate heating temperatures. It can be seen that the buckling plots for this type of bridges are in a bell-shaped profile, which is different from the sinusoidal profiles observed for up- and down-state buckled bridges. In the bell-shaped buckled bridges, the resonant frequency tunability exhibits more complicated patterns as demonstrated in **Figure** 4.9a-b. However, both actuation methods (i.e. Joule heating and substrate heating), show similar resonant frequency shift patterns across the SPT region, since the general trend of the geometric distortion in this type of beam is also reducing the buckling amplitude upon a negative bending moment.

4.4 Power Consumption of Programming Resonant Frequency

Programming resonant frequency states in a mechanical structure allow for the operation of a single device in multiple frequency channels. This not only broadens the spectrum of applications for the device, but also reduces interference, noise, and enables anti-jamming in communication systems. In this section, the study on the power consumption of programming resonant frequencies in VO_2 MEMS resonators is presented by means of pulse width modulation (PWM) methods. It is found that the tuning of the frequency states is determined by the supplied energy, and the programming is more efficient for larger, shorter pulses –even if the duration of the pulse is shorter than the system's thermal time constant. We explore two different mechanical structures, bridge, and cantilever. A wider tuning range is found for the bridge structure (22%), which is due to the larger frequency sensitivity with stress for this configuration. The tuning/programming action uses harvested mechanical energy, which could come from the user. The potential use of the developed system as an

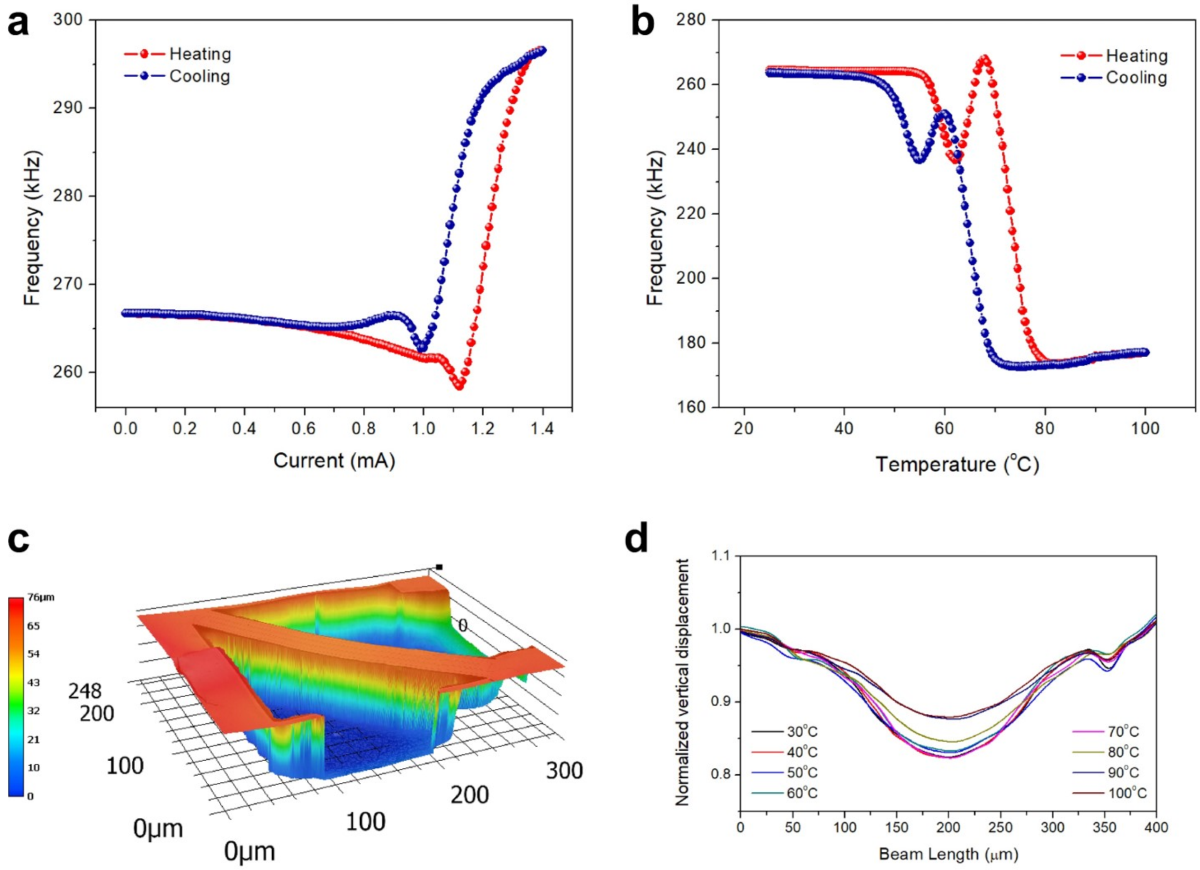

Figure 4.9 The resonant frequency shift of a 300 μm VO_2-based microbridge with bell-shape buckle state. (a) Resonant frequency shift through a complete heating and cooling cycle by Joule heating. (b) Resonant frequency shift through a complete heating and cooling cycle by substrate heating. (c) 3D reconstruction of the device showing the buckling amplitude in $-z$ direction. (d) Normalized buckling amplitude change as a function of substrate heating along the beam axial length.

accelerometer or impact sensor for monitoring brain injuries in contact-sports is discussed.

4.4.1 Determining Device Time Constant

The testing configuration consisted of connecting the device's metal heater to a DC current source which provided a pre-heating current to the VO_2-based resonator (see **Figure** 4.10a). The pre-heating level was selected at the point where the resonant frequencies between the heating and cooling major hysteretic curves have the largest difference. A capacitor was then charged by the FENG device through a rectifier. A single-pole-single-throw switch was used

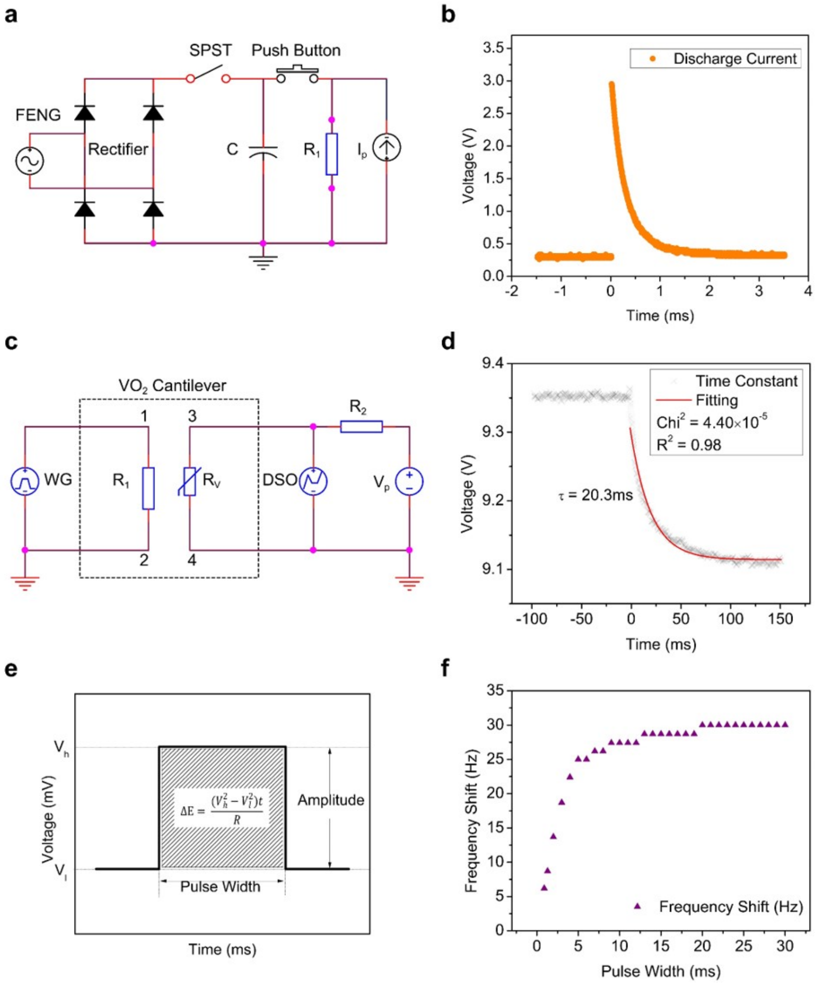

Figure 4.10 (a) Circuit of resonant frequency programmability by combing VO_2-based resonator and FENG device. C is the capacitor of 1μF, R_1 is the resistance of the heater (252 and 228 Ω for the cantilever and bridge, respectively), I_p is the pre-heating current (1 and 1.22 mA for the cantilever and bridge structures, respectively). (b) Voltage profile of the discharge current across the heater. (c) The circuit used for measuring the time constant. A wave-function generator (WG) is connected to the heater R_1. The VO_2 film (R_V)is connected to a resistor (R_2), a pre-heating voltage source (V_p), and an oscilloscope (DSO). (d) Thermal time constant of the VO_2-based cantilever. (e) Schematic of the rectangular pulse supplied by the WG for time-constant and energy calculation experiments. (f) Frequency shift as the function of the pulse width.

to avoid capacitor leakage after charging. Once the capacitor was charged, the discharge current pulse was added to the pre-heating current. The temperature increase due to the current pulse was large enough to heat the structure across the phase transition. When the pulse ended, the temperature of the sample returned to the pre-heating value, but this time following the cooling curve of the hysteresis curve. Thus, the resonant frequency before and after the pulse corresponding to the values in the heating and cooling curves, respectively.

In order to find the conditions of the tuning current pulse for increasing the sample's temperature across the phase transition, it is necessary to know the system's response time. The dynamics of the system is governed by two main processes (thermal and mechanical), and each one has a corresponding time constant. The thermal process is the mechanism by which the current pulse increases the temperature of the sample, while the mechanical process is the mechanism by which the system responds to the phase change of the VO_2 film. The relation between the thermal time constant and the mechanical time constant can be described as follows:

$$\tau^{'} = \tau_T + \tau_M, \tag{4.1}$$

where τ_M is the mechanical time constant, τ_T is the thermal time constant and $\tau^{'}$, is the response time of the device to the new thermal equilibrium. The thermal time constant is mainly determined by how fast the external heat can be distributed in the device[137, 138]. The thermal process is the slowest of the two [139] and thus, it will determine the time response of the entire system.

Since the changes in the structural and electrical properties of VO_2 across the phase transition have similar time constants [140, 141, 142, 143], the thermal time constant of the system can be obtained by simply applying a current pulse and monitoring the change in resistance of the VO_2 film. The measurement setup is shown schematically in **Figure** 4.10c. In this experiment, the thermal time constant was defined as the time required for the device to respond when the current was increased from the preheated level of 1 mA to 1.7 mA. The measured thermal time constant of this 450 µm long VO_2-based cantilever was 20.3 ms, (see **Figure** 4.10d). To validate the measured time constant for the electro-mechanical system, rectangular pulses of the same amplitude but varying width were applied, while the resonant frequency shift was measured. As the pulse width was increased, the frequency shift also increased until the frequency shift reached a maximum value. Thus, the minimum width of

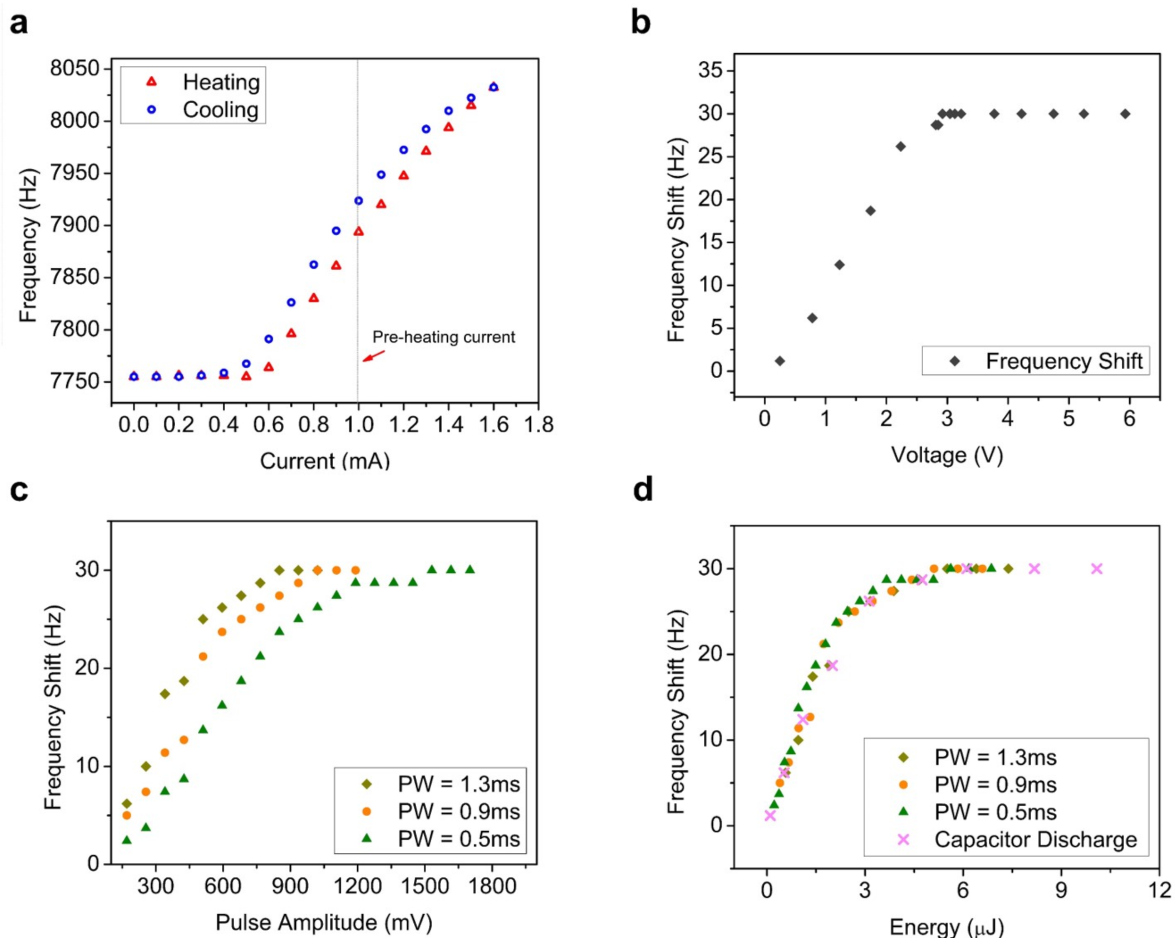

Figure 4.11 Tuning and programming frequency states in cantilever structures. (a) Hysteretic major resonant frequency loops for cantilever structure as a function of the current. (b) Frequency shift as a function of the voltage in the capacitor before the discharge pulse. (c) Frequency shift as a function of pulse amplitude for three different pulse widths (PW). (d) Frequency shift as a function of energy delivered by the pulse.

the pulse that was able to obtain the maximum frequency shift should be approximately the value of the time constant. The frequency shift as a function of the pulse width is plotted in **Figure** 4.10f. The thermal time constant in this case was estimated to be 21 ms, which is very close to the value determined in **Figure** 4.10d.

4.4.2 Frequency Programmability In Cantilevers

The resonant frequency of the cantilever as a function of the current is plotted in **Figure** 4.11a. The programmability of the resonant frequency was achieved by first apply a DC current to a pre-heated level where the heating curve and the cooling curve have the maximum separation[144, 145, 146]. A transient current pulse was then induced in order to complete the phase transition in the VO_2 film and switch the resonant frequency from the heating curve to the cooling curve. Even though the single layer FENG device is able to generate large open circuit voltage, the short circuit current is still on the scale of μA. Thus, directly connecting a single layer FENG device to the resonator does not produce enough temperature increase to cross the phase transition completely. Therefore, the single-layer FENG device was stacked to 7 layers, which amplified the output to 7 times larger than the single-layer device. Second, a capacitor was previously charged by the FENG device through a rectifier to a level high enough to go through the phase transition completely. Then, the stored energy was released in the form of discharge current for tuning action by using a push-button switch. The current pulse used for the tuning can be determined by the following equation:

$$I = \frac{V_0}{R} e^{-\frac{t}{RC}} + I_p, \tag{4.2}$$

where V_0 is the voltage charged to the capacitor, R is the resistance of the heater in the cantilever, C is the capacitance of the capacitor and I_p is the pre-heating current. In this experiment, the pre-heated current level was chosen to be 1 mA where the resonant frequency separation between the heating curve and the cooling curve is 30 Hz. The capacitor was previously charged to different voltage levels, and then the discharge current was induced for the tuning. This results in pulses of different amplitude, but the same duration, since the time constant remained unchanged. As shown in **Figure** 4.11b, the resonant frequency shift increases with the voltage stored in the capacitor. This suggests that the tuning/programming of the resonant frequency in the devices is determined by the supplied energy. The maximum frequency shift was obtained when the capacitor was charged to 2.9 V.

As discussed earlier, the thermal time constant of the cantilever is approximately 20.3 ms. This means that in order to get the maximum frequency shift, the applied current pulse should be at least 20 ms. However, the discharge current pulse used for the tuning in this experiment has the decay time constant of around 0.27 ms and the transient current only lasts about 1.3 ms. Although the pulse width (PW) was much shorter than the time constant of the device, the transient current still provided enough energy for the resonant frequency to completely across the phase transition region. This finding is crucial for the use of a single strike on a FENG device for programming action. The energy released from the capacitor to the heater can be determined by:

$$\Delta E = \frac{1}{2}C({V_0}^2 - {V_1}^2), \tag{4.3}$$

where V_1 is the voltage of the capacitor after discharging. To confirm that the tuning mechanism is determined by the supplied energy –independently on how fast was the energy delivered– the following experiment was performed. Instead of applying the RC discharge current, three rectangular pulses of different widths were applied from a waveform generator. The frequency shift as a function of the pulse amplitude was measured (see **Figure** 4.11c). The maximum frequency shift was achieved by the different rectangular pulses respectively at different amplitudes. The energy delivered by the rectangular pulses can be calculated by using the parameters shown in **Figure** 4.10e:

$$\Delta E = \frac{({V_h}^2 - {V_l}^2)t}{R}, \tag{4.4}$$

where R is the resistance of the heater, V_h is the high voltage, V_l is the low voltage, and t is the width of the pulse. **Figure** 4.11d shows the resonant frequency shift as a function of the energy delivered by three different pulses, and by the discharge current from the capacitor. All four curves show very similar behavior. This confirms that the tuning mechanism is dominated by the supplied energy. The energy required for tuning this 450 µm VO_2-based cantilever is about 5.1 μJ. Moreover, if the cantilever was applied a rectangular pulse of V_h=578 mV and V_l=280 mV (considering the TCR of the heater is around 33.5 Ω/mA^2), the duration of the pulse should be at least 20 ms. In this case, the energy consumed by the cantilever is about 18.2 μJ. This larger energy consumption is probably due to the larger heat dissipation during a longer tuning process. Thus, it is more energy-efficient to apply a shorter pulse with higher amplitude.

4.4.3 Frequency Programmability in Bridges

The resonant frequency programmability was also demonstrated for a 300 µm long VO_2--based micro-electro-mechanical bridge structure. The resonant frequency as a function of current was plotted in **Figure** 4.12a. The current step here was chosen to be 0.01 mA since the bridge structure is more sensitive to the stress, which also translates into a much larger tuning frequency than the cantilever structure (32% for the bridge, and 4% for the cantilever). For the bridge structure, the pre-heating current was 1.22 mA. The resonant frequency tuning based on the RC discharge current is illustrated in **Figure** 4.12b. The frequency shift increases with the voltage in the capacitor, and saturates at around 1.6 V. The maximum resonant frequency shift was measured to be around 42 kHz, which is consistent with the value estimated from **Figure** 4.12a. This indicates that a voltage of 1.6 V in the capacitor provided enough energy to completely cross the phase transition region (for a pre-heating current of 1.22 mA). The thermal time constant was also measured for the bridge using the same method used for the cantilever. The value was determined to be around 9 ms, which is much shorter than the cantilever. This is due to two reasons: (i) the bridge has one more anchor than the cantilever, which represents a more uniform temperature distribution and one more heat sink that helps dissipate temperature; and (ii) the bridge is shorter than the cantilever, which means the bridge has less thermal mass and therefore the response time is shorter.

The energy was also found to be the tuning parameter for the bridge structures. **Figure** 4.12c-d show the frequency shift as a function of rectangular pulse amplitude and energy, respectively. The same pattern shown in **Figure** 4.11c-d was observed, and the minimum energy required for inducing a frequency shift of around 30 Hz was 5.11 μJ. In **Figure** 4.12d, there is a small discrepancy between the discharge current and the rectangular pulse. This

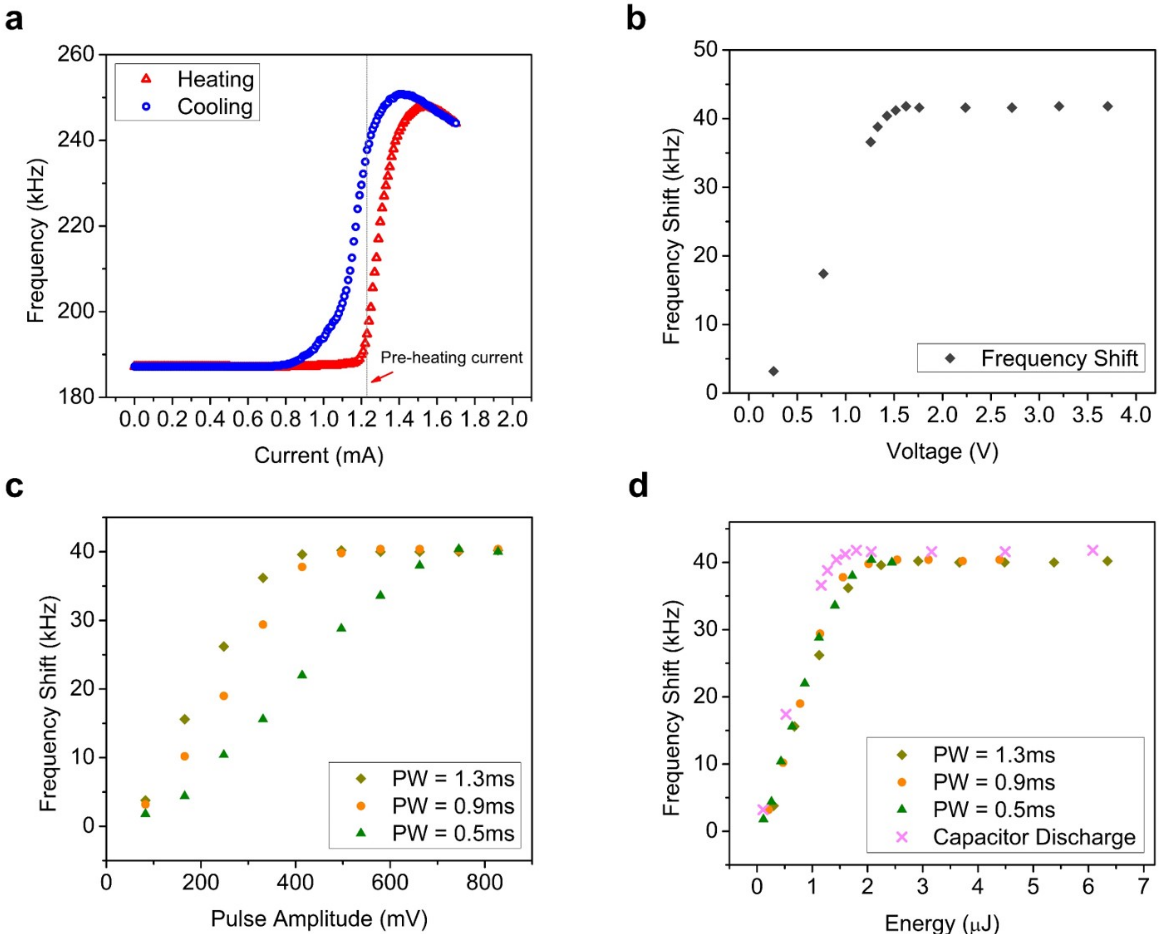

Figure 4.12 (a) Hysteretic major resonant frequency loops for bridge structure as a function of the current. (b) Frequency shift as a function of the voltage in the capacitor before discharge. (c) Frequency shift as a function of pulse amplitude for three different pulse widths (PW). (d) Frequency shift as a function of energy delivered by the pulse.

can be attributed to the high sensitivity to stress. The rectangular pulses were provided by the waveform generator as a voltage signal. The energy consumption for programming (i.e. dynamic power consumption) required by the bridge was estimated to be 2.07 μJ.

4.4.4 Monitoring Brain Injury in Contact Sports

As discussed above, the tuning/programming of multiple frequency states can be achieved by very short pulses, as long as the delivered energy is enough. Thus, practical applications could include impact sensors, such as those needed for monitoring injuries in high-contact

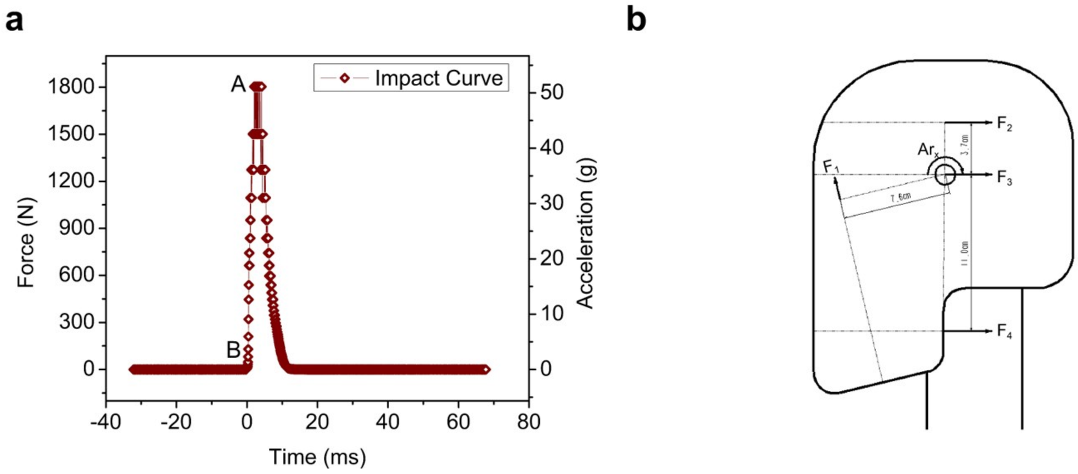

Figure 4.13 (a) Representative impact profile, jerk = $(F_A\text{-}F_B)/(\mathrm{m}\Delta_{A-B})$, where F_A and F_B are the force at point A and B respectively, m is the mass of the head and Δ_{A-B} is the time from point A and B. The acceleration is calculated by using an average human head mass of 3.6 kg. (b) The force exerted on the head, F_1, F_2, F_3, and F_4 represent the peak force of around 1800 N applied at different locations, Ar_x is the rotational axis of the head, the size of the head is selected to be the value at 50th percentile of male adults.

sports, where a single, quick (but intense) impact generates enough energy to program a different frequency state. The flexibility of the FENG device and the size of the resonator structure enables the required flexibility for the integration of this system in wearables or even textiles. This subsection includes the discussion of an application note for monitoring head injuries and shows how a single impact can transition the VO_2-based resonator completely, and program a frequency state about 40 kHz different than the pre-heated state.

To evaluate the severity of the impact, several criteria are used in the biomechanics. For example, the threshold for concussion under the acceleration is estimated to be 70-75 g[147, 148] (where g is the gravitational acceleration. An angular acceleration of 7900 radian/s^2 applied to the head will cause an 80% probability of Mild Traumatic Brain Injury (MTBI)[149]. A Head Injury Criteria (HIC) of more than 1000 relates to an 18% risk of severe head injury, a 55% risk of serious injury and a 90% risk of moderate head injury[150]. However, different evaluation methods (e.g. MTBI and HIC) use different criteria. The acceleration threshold for the concussion and MTBI focuses on the peak force and how fast is the force applied. On the other hand, the HIC value emphasizes on the impulse of the impact, which includes the real time force and the duration of the impact, the value can be determined by the following expression[151, 152]:

$$HIC = \{[\frac{1}{t_2 - t_1} \int_{t_1}^{t_2} a(t)dt]^{2.5}(t_2 - t1)\}_{max} \tag{4.5}$$

where t_1 and t_2 are the initial and final times of the impact interval which gives the maximum HIC value, $a(t)$ is the acceleration measured in the number of gravitational acceleration (i.e. the number of gs). However, the HIC value may not reflect the real significance of the impact. A quick inspection tells us that, for a profile like this, Equation (4.5) can give low HIC values for short duration pulses, even if the force amplitude is relatively large. For example, an impact with a long duration and a small force magnitude can lead to a large HIC value while a large force magnitude with short duration would give low HIC values. Thus, the criteria here is selected to be the acceleration threshold for causing a concussion or an MTBI. The impact used to induce the maximum frequency shift from the pre-heating level of 1.22 mA for the bridge described in the previous subsection is shown in **Figure** 4.13a. In this experiment, the FENG was directly connected to the VO_2 resonator without charging a capacitor and the output of the FENG from a single impact from a human punch was used to induce the frequency shift. The real-time force is plotted as a function of time. The peak force was measured to be around 1800 N and the acceleration was determined based on the average head mass of about 3.6 kg[153]. The maximum acceleration is therefore calculated to be 51 gs. The severity of applying this force to the head of a human being will depend on the location of the point-of-contact. The severity of the head injury in terms of the rotational acceleration is summarized in Table 4.3. Even though the calculation does not include the

Table 4.3 Evaluation of the impact

Location	F_1	F_2	F_3	F_4
Force (N)	1800	1800	1800	1800
Jerk (m/s^3)	13883	13883	13883	13883
Linear Acceleration (gs)	51	51	51	51
Rotational Acceleration ($radian/s^2$)	5067	2467	NA	7333

resistance of the neck and may enlarge the real rotational acceleration, the combination of the VO_2 and the FENG still provides the potential of sensing the threshold acceleration which causes the brain injury.

4.5 Enabling Tunable Micromechanical Bandpass Filters

In this section, we demonstrate the potential use of VO_2-based MEMS devices as second-order kilohertz (kHz) bandpass filters with tunable band selectivity and adjustable bandwidth. Two identical on-chip microresonators are actuated using mechanical excitation and measured using optical detection. One of the resonators is not actuated while the other is tuned by applying electric currents across an integrated resistive heater, which induces the phase transition of the VO_2, and consequently a large stress to the mechanical structure. The responses of both MEMS resonators are combined, resulting in a resonant peak of tunable bandwidth controlled by the input current. The bandwidth can be extended to 2.62 times by using two bridges or 2.39 times by implementing one pair of cantilevers. The results for both devices are discussed.

4.5.1 Experimental Setup

The experimental setup for measuring resonant frequencies of both resonators is shown in **Figure** 4.14. After the first mirror and beam splitter, the beam was split and focused on both samples using two long working distance objectives (10X Mitutoyo MY10X-803 Objective lens). Each sample represented a chip that contained resonator structures that were fabricated simultaneously. A piezoelectric transducer was attached to the back of each sample, and both transducers were driven into mechanical vibration by the output signal of a network analyzer (HP3589A). The laser was focused on identical resonator structures, and the reflected beam was directed to a photodetector through another beam splitter. The output of the photodetector was connected to the input of the network analyzer. In this configuration, the network analyzer would display the voltage output of the photodetector as a function of frequency. The network analyzer drove the piezoelectric transducers at different frequencies, inducing the resonator's largest vibration amplitude at a frequency close to their natural frequency. Vibrations from the resonator structure produced oscillations in the reflected laser beam (of magnitude proportional to the vibration amplitudes), which were converted to a voltage by the photodetector and sent back to the network analyzer. It should be noticed that in this measurement setup, the input/output characteristics of the system does not require coupling of electrical and mechanical signals. The input signal applied to the filter system was a time-dependent electrical signal, but the actuation signal was the mechanical vibration provided by the piezoelectric transducer. The tuning signal is the current applied to the heater of the active element, which is an electrical signal, but the output is a mechanical vibration detected optically. This method is an adaptation of laser deflection and interferometer techniques commonly used to characterize MEMS –in fact, it also allows for the testing of a single resonator structure by simply blocking the optical path to one of the structures.

In the reported experiments, the temperature for one of the samples (active sample) was increased by applying a current to the integrated resistive heater (i.e. by Joule heating); while the other sample (static sample) remained at room temperature. The current supplied to the active sample was computer-controlled and provided through wire bonding connections to pads at the border of the chip. Both samples were mounted on two individual three-axis moving stages to facilitate alignment of the laser beam on the resonator structure.

4.5.2 Bandwidth Tunability for Bridges

Two different structures of microbeam resonators (cantilevers and bridges) were tested in this experiment and the bandwidth tunability of each structure was demonstrated and compared. The maximum bandwidth amplification, Q-factor, and bandwidth tuning window will be discussed in the following sections. The bandwidth was calculated using the 3dB of the

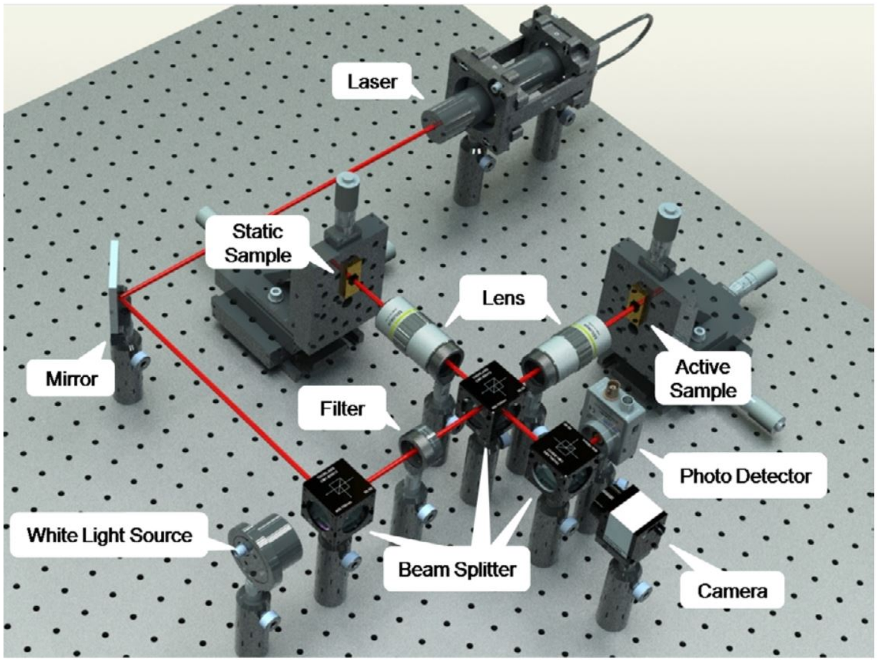

Figure 4.14 Experimental setup. The active sample is the resonator (cantilever or bridge) actuated by Joule heating, while the static sample is the resonator (cantilever or bridge) that is not actuated. Two identical piezo-disks were placed underneath the static sample and the active sample respectively and they are sharing one driving AC source signal provided by the network analyzer. The output of the photodetector is connected to the input of the network analyzer. The laser beams passing through the beam splitters are not contributing to the measurement and therefore are not shown for clarity.

resonant peak method using the following equation:

$$BW = f_2 - f_1, \tag{4.6}$$

where BW stands for the bandwidth. f_1 and f_2 are the two frequencies on each side of the resonant frequency (f_r) where the amplitude of the signal is $1/\sqrt{2}$ of its maximum value. The Q-factor (Q) is then calculated based on the bandwidth value using the equation as below[154]:

$$Q = f_r/BW. \tag{4.7}$$

First, two identical bridges were used to create the bandpass filter. The active bridge was activated by Joule heating, and the resonant frequency was measured through the whole heating and cooling cycle (**Figure** 4.15-left) by blocking the laser beam coming from the

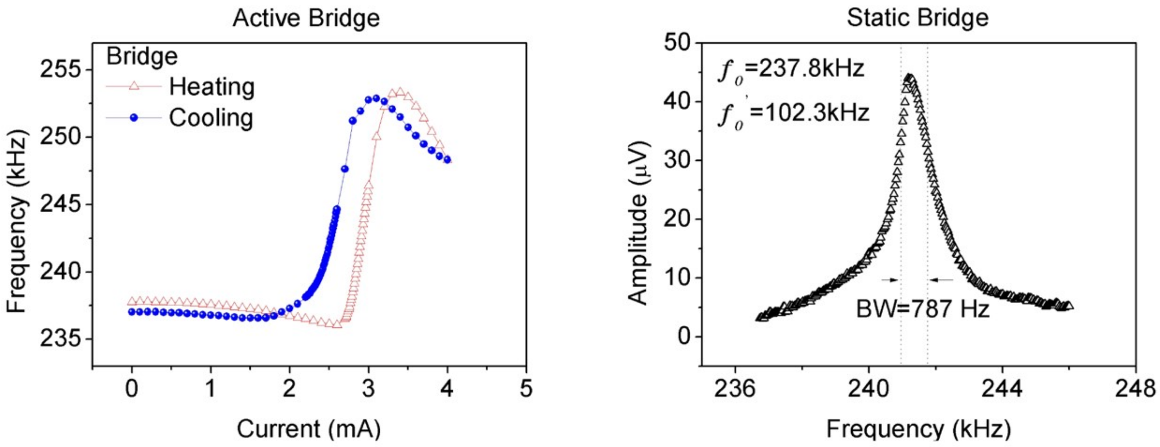

Figure 4.15 *Left:* Resonant frequency versus actuation current through a full heating and cooling cycle for the active bridge. *Right:* Resonant frequency signal for the static bridge at room temperature. The measured (f_0) and calculated ($f_0^{'}$) resonant frequencies are shown. The value for $f_0^{'}$ was obtained from Equation (3.1), and it does not take residual thermal stress into account.

static sample. The frequency shift comes as the result of a large amount of stress generated by the VO_2 thin film coating during its phase transition region. When the laser beam coming from the static sample was unblocked, we were able to get two resonant signals, one from the static bridge and the other from the active bridge. These optical signals were routed to the photodetector, and its output to the network analyzer, which showed the resonant peaks for both devices. The top-left plot in **Figure** 4.16 (Stage "*a*") shows the output of the spectrum analyzer for both bridges at room temperature i.e. while the active bridge was not actuated ($I_{act} = 0$ mA). The current step is 0.01 mA within the bandwidth tuning window and 0.1 mA for the outside region. It should be noted that, although both bridges are geometrically identical, their resonant frequencies at room temperature are not the same. This could be due to any slight difference between the fabrication processes of both devices; we believe that the most likely cause was a difference in "effective length" for the two structures, which could have occurred during isotropic release step.

When a current was applied to the active bridge (I_{act}), its resonant frequency would shift to a certain value according to the hysteresis curve shown in **Figure** 4.15. **Figure**

4.16 shows a sequence of over-imposed resonant frequency peaks for the static and active bridges for different I_{act} values. The sequence starts at room temperature (Stage "*a*"), goes through a heating cycle (increasing I_{act}), until the transition of VO_2 is completed (Stage e in **Figure** 4.16). At this point, the cooling cycle begins (reducing I_{act}), until we reach room temperature again (Stage "*j*" in **Figure** 4.16). Starting at room temperature, the combination of both resonant peaks resembles the behavior of a band-pass filter; and its width is tuned by current steps of increasing magnitude that induce the phase transition of VO_2. As the actuation current increases from room temperature, the active peak moves towards the static peak, reducing the filter's bandwidth. When $I_{act} = 2.89$ mA (b Stage), the active and static peaks show very similar resonant frequencies, and both responses are merged into one signal peak. As I_{act} is further increased, the resonant frequency of the active bridge keeps increasing, and the active peak continues starts moving to the right of the static peak. At $I_{act} = 2.92$ mA (Stage "*d*"), the resonant frequency of the active bridge begins to separate, and by $I_{act} = 3.00$ mA, the two f_r curves clearly become two separate peaks. The largest measured bandwidth during the heating cycle was around 1.85 kHz (at $I_{act} = 2.92$ mA). The cooling cycle (Stage "*f*" through "*j*") was performed to demonstrate the reversibility of the system. As the actuation current decreases, the active peak moves towards the static peak and the peaks begin to merge at $I_{act} \sim 2.57$ mA. The maximum bandwidth of the cooling cycle is around 2.06 kHz (at $I_{act} = 2.57$ mA), which is 2.62 times larger than a single device. As the current further decreases, the difference in the resonant frequencies become smaller. At $I_{act} = 2.52$ mA (Stage "*i*") the two peaks become one, and the system goes back to its initial condition when I_{act} is turned off. The stages included in **Figure** 4.16 are displayed for similar frequency measurements between the heating and cooling cycle i.e. the two plots in a single row show similar output. However, the I_{act} values are different between these similar stages. This is due to the hysteresis of VO_2 which does not show a linear correspondence between the two cycles (see **Figure** 4.15).

It can be noticed that at the stages where the signal snaps into two individual peaks

Table 4.4 Bandwidth tunability for bridges

	Static bridge				
Bandwidth (Hz)	787				
Q-factor	306				
	Active heating				
Stage	a	b	c	d	e
Bandwidth (Hz)	Snap	732	1391	1849	Snap
Q-factor	NA	330	174	131	NA
I_{act} (mA)	0.00	2.89	2.91	2.92	3.00
	Active cooling				
Stage	f	g	h	i	j
Bandwidth (Hz)	Snap	2062	1607	666	Snap
Q-factor	NA	117	151	362	NA
I_{act} (mA)	2.70	2.57	2.55	2.52	0.00

(Stages “*a*”,“*e*”,“*f*”,“*j*”), the signal level for each individual peak is of equal amplitude to the signal of a single bridge (**Figure** 4.15-right). However, for the stages which have extended bandwidth (Stages “*b*”,“*c*”,“*d*”,“*g*”,“*h*”,“*i*”), the signal level is higher than the one generated by the single bridge resonator. This is due to the additive effect of the two individual signals generated by the static resonator and the active resonator, which occurs only during stages with band-pass filter behavior. Also, at Stages “*b*” and “*i*”, the bandwidths are smaller and therefore, a higher Q-factor is achieved (see Table 4.4).

The resonant peak of the single static bridge used in this system has a bandwidth of 787 Hz (see **Figure** 4.15). Thus, a tunable bandwidth amplification up to 2.62 was achieved by using one pair of identical bridges. It should be noted that, in this particular case, the shift in f_r for the active bridge ”crossed” the f_r of the static bridge. Therefore, the tunable bandwidth could include a different range of frequencies by increasing or reducing the separation between the two peaks at room temperature. It is important to clarify that the applied current I_{act} is the tuning parameter but not the input to the system that generates oscillation. During the entire heating-cooling cycle, the input is the frequency of the AC signal applied to the piezo-disks (supplied by the network analyzer). The measured output is the combined resonant peaks. The data for actuation current, bandwidth and Q-factor

Table 4.5 Bandwidth tunability for cantilevers

	Static cantilever				
Bandwidth (Hz)	135				
Q-factor	38				
	Active heating				
Stage	A	B	C	D	E
Bandwidth (Hz)	155	212	279	332	Snap
Q-factor	33	24	18	16	NA
I_{act} (mA)	3.0	3.4	4.2	5.4	6.2
	Active cooling				
Stage	F	G	H	I	J
Bandwidth (Hz)	Snap	331	284	228	174
Q-factor	NA	16	18	22	29
I_{act} (mA)	6.0	5.2	4.0	3.2	2.8

are summarized in Table 4.4.

4.5.3 Bandwidth Tunability for Cantilevers

The VO_2-based bandpass filter could also be achieved by using a pair of identical cantilever structures. The measurement method and the tuning method are the same as those used for bridges. The bandwidth tunability is shown in **Figure** 4.17 and all the related data is summarized in Table 4.5. The resonant frequency of the active peak follows the hysteresis curve shown in **Figure** 4.18-left. The resonant frequency signal for the single static cantilever was measured (**Figure** 4.18-right) and the bandwidth was calculated to be 135 Hz. The starting stage here is chosen to be the one with an I_{act} = 3.0 mA rather than 0 mA. The reason is that the initial bending of this active cantilever cannot produce a signal comparable to that of the static cantilever. Nevertheless, this difference does not affect significantly the results obtained and drawn conclusions, since the difference between the resonant frequency at I_{act} = 0.0 mA and at 3.0 mA was found to be only 12 Hz. The maximum bandwidth for this system is reached at I_{act} = 5.4 mA and at I_{act} = 5.2 mA for the heating and cooling cycles, respectively. The maximum bandwidth obtained by this system is about 322 Hz, which is 2.39 times the bandwidth of a single cantilever.

4.5.4 Bandwidth Tunability Comparison

The room temperature measurement in **Figure** 4.17 (Stage "*a*") shows that the f_r for both cantilevers (active and static) are much closer than the f_r for both bridges at room temperature. When both devices were measured independently, the difference in f_r between the active and static devices was found to be about 8% and 1% for the bridges and cantilevers, respectively. This supports the claim that different effective lengths due to irregular under-etching during isotropic release play a major role in the different f_r for the two bridges at room temperature. A bridge structure has two anchors, and therefore, a difference in the effective length due to under-etching difference will have a stronger influence in a bridge structure than in a cantilever structure. Due to the much smaller difference in the f_r for the cantilevers, the measurement at room temperature for both cantilevers (active and static) is simply a slightly broader peak than the single cantilever, shown in **Figure** 4.18. Unlike the case for the bridges, as the tuning actuation begins for the active cantilever (by increasing I_{act}), the bandwidth begins to increase monotonically during the heating cycle. There is no "crossing" between resonant peaks for the cantilevers. This monotonic bandwidth tuning behavior for the cantilever also holds during the cooling cycle. Another striking difference between both results is the required "tuning energy". Starting at the onset of the phase transition, crossing the entire phase-change to generate maximum deflection in cantilevers requires $I_{act} \sim 3.5$ mA (**Figure** 4.18-left), while the bridges require less than 0.75 mA (**Figure** 4.15-left).

The actuation current required to reach the maximum bandwidth for the cantilevers and the bridges (from stage "A" to stage "D" for the cantilevers and from stage "b" to stage "d" for the bridges) is 2.4 and 0.03 mA, respectively. Considering the resistance of the heater traces of the cantilevers and bridges (285 and 245 Ω, respectively), the power consumption for maximum bandwidth tuning is calculated to be 5.75 mW for the cantilever, and 0.04 mW for the bridge structures.

The main reason for this larger energy requirement for the cantilever relates to two main differences between the device structures: (i) thermal mass, and (ii) heat distribution. Notice that the bridge structures are almost half as long as the cantilever structures. A larger length translates to a larger thermal mass, which means that a larger amount of energy will be required to increase temperature. Thus, it is more energy demanding to induce the phase transition of VO_2 in the cantilever structure than in the bridge structure. Also, note that the heater design for the bridge covers a larger surface of the bridge structure, which allows for a more uniform. Finally, there is a significant difference between the change in frequency for the active device per unit current (i.e., sensitivity); and the total tuning range between bridges and cantilevers. The explanation for the different sensitivities and tuning ranges share the thermal mass issue described above – larger energy is required in a cantilever structure to induce the same temperature increase, but this mechanism does not play a major role. The dominant mechanism (for both larger sensitivity and tuning range) relates to the stronger dependence of resonant frequency with stress for the bridge structure. In fact, this higher sensitivity of the resonant frequency of a bridge structure to stress is the reason why the pairs of equivalent stages in the heating and cooling cycle look more similar for the cantilevers than for the bridges. The tuning experiments for the cantilevers involved current steps of 0.1 mA, while the bridges required steps 10 times smaller.

The relation between the resonant frequency and the stress for both structures is now qualitatively discussed. During the VO_2 IMT phase transition region, the VO_2 crystal structure changes from its low-temperature monoclinic phase to its high-temperature rutile phase with a contraction in the c-axis. Essentially, the area of the crystal planes parallel to the surface of the substrate is reduced during the phase transition (heating cycle). This generates compressive stress at the surface of the beam material, which in turn will induce elastic deformation and changes in the geometry of the beam. The deformation will then change the dimensions and the density of the beam, which will further shift the resonant frequency of either the bridge or the cantilever. Thus, the influence of the stress on the resonant frequency is not only due to the induced stress (stress effect) but also caused by geometric variations (geometric effect). However, different beam structures have different responses to the same type of axial stress. For the case of a cantilever (clamped-free structure), the deformation along the longitudinal direction is not constrained and the axial stress is released. This results in a zero net axial stress along the longitudinal direction and a net in-plane stress in the clamped end. For the cantilevers used in this paper, where the width is about 30 times larger than the thickness, the resonant frequency shift is then dominated by the geometric effect and can be described by the following expression[155]:

$$\Delta f/f_r = \{(1+2\nu)/(1-\nu)\}\,\sigma \tag{4.8}$$

where Δf stands for the relative resonant frequency change, ν is the Poisson's ratio, and σ is the applied surface stress. The bridges, on the other hand, have more net axial stress than the cantilevers due to their clamped-clamped structure. The resonant frequency shift is mainly dominated by the stress effect and can be estimated by the following expression[155]:

$$\Delta f/f_r = 0.1475(L/h)^2\sigma \tag{4.9}$$

where L and h are the length and thickness of the bridge. Given that the Poisson's of SiO_2 (which makes up for about 90% of the resonator's structure) is 0.2; and the $(L/h)^2$ for the bridges and cantilevers is in the order of 10^4, the frequency shift per stress unit is much larger for the bridges. Furthermore, unlike in the case of a cantilever, the added stress during the phase transition in a clamped-clamped structure is not "released" in the form of structural bending – unless it reaches the Euler stress limit, which was not the case for the present structures. The resonant frequencies shift for the cantilevers and bridges reported in this work when transitioned across the entire phase transition were about 3.1% and 7.3%, respectively.

4.6 Summary

In this chapter, the first mode resonant frequency has been measured for the cantilevers and bridges both with and without VO_2 to analyze the influence of VO_2 thin film coating on VO_2-based MEMS resonators. For the structures we used in this experiment, the geometric effect dominates in the frequency change for the cantilevers and the stress effect dominates for the bridge frequency behavior.

The influence of VO_2 thin film on pre-buckled bridge resonators is also studied in this work. Due to the mismatch in the thermal expansion coefficients between layers, the microbridges exhibit buckling status with various buckling profiles which can be classified into three groups: up, down, and bell-shape. The resonant frequency is measured throughout the full heating and cooling cycles. The tunability shows a strong dependency on the actuation methods and the buckling profile of the bridge. This phenomenon is attributed to a transition in the boundary condition from a fixed-fixed constraint to a fixed-pinned constraint. Resistive (or Joule) heating shows a monotonic change in frequency, whereas the substrate heating exhibits a bi-directional change in frequency. When a lateral deflection happens in the beam structure, the magnitude of the present axial stress is released, and the resonant frequency starts to shift in the opposite direction. A significant difference in the frequency tunability is also observed for those microbridges with different buckling profiles. By depositing the VO_2 thin film on either the concave or convex side of the beam (corresponding to up- and down-buckled bridges, respectively), different bending moments are induced and exerted on the microbridges. This results in opposite trends in the frequency tunability across the SPT.

The programmability of frequency states in electro-mechanical resonators was demonstrated by combing VO_2-based resonators with a stacked FENG device. The tuning action was achieved by first applying a DC current to a pre-heated level where the frequency separation between the heating curve and the cooling curve is the maximum. Then, a short energy pulse was applied to program a different resonant frequency state in the structure. It was found that shorter pulses with larger amplitudes are more energy-efficient than longer pulses of smaller amplitudes. The pulse could also come from a capacitor charged by multiple small impacts - as long as the supplied energy is above the minimum threshold for actuation. This threshold will depend mainly on the type of structure and pre-heating level. The maximum tuning range for the cantilever was around 30 Hz (0.38%) while it was about 40 kHz (22%) for the bridge since the resonant frequency of the bridge is more stress sensitive.

Finally, a prototype of VO_2-based tunable MEMS bandpass filter is presented. The resonant frequency curves of two MEMS structures were measured simultaneously. One of the devices was actuated by current pulses sent through an integrated resistive heater, while the other structure was not actuated. Each current pulse increased the temperature of the mechanical structure, inducing the phase transition of the VO_2 film in the actuated sample. The generated stress during the phase-change of VO_2 induces resonant frequency shifts. Two different resonator structures, cantilevers and bridges, were used to demonstrate fully reversible bandwidth tunability action. The bandwidth was increased 2.39 and 2.62 times the value of a single resonator for the cantilever and bridge system, respectively. The required power for inducing full tuning action in both systems is much larger for the cantilever system (approximately 5.75 mW) than for the bridge system (approximately 0.04 mW). This is due to the much larger sensitivity of the bridge structures to added stress.

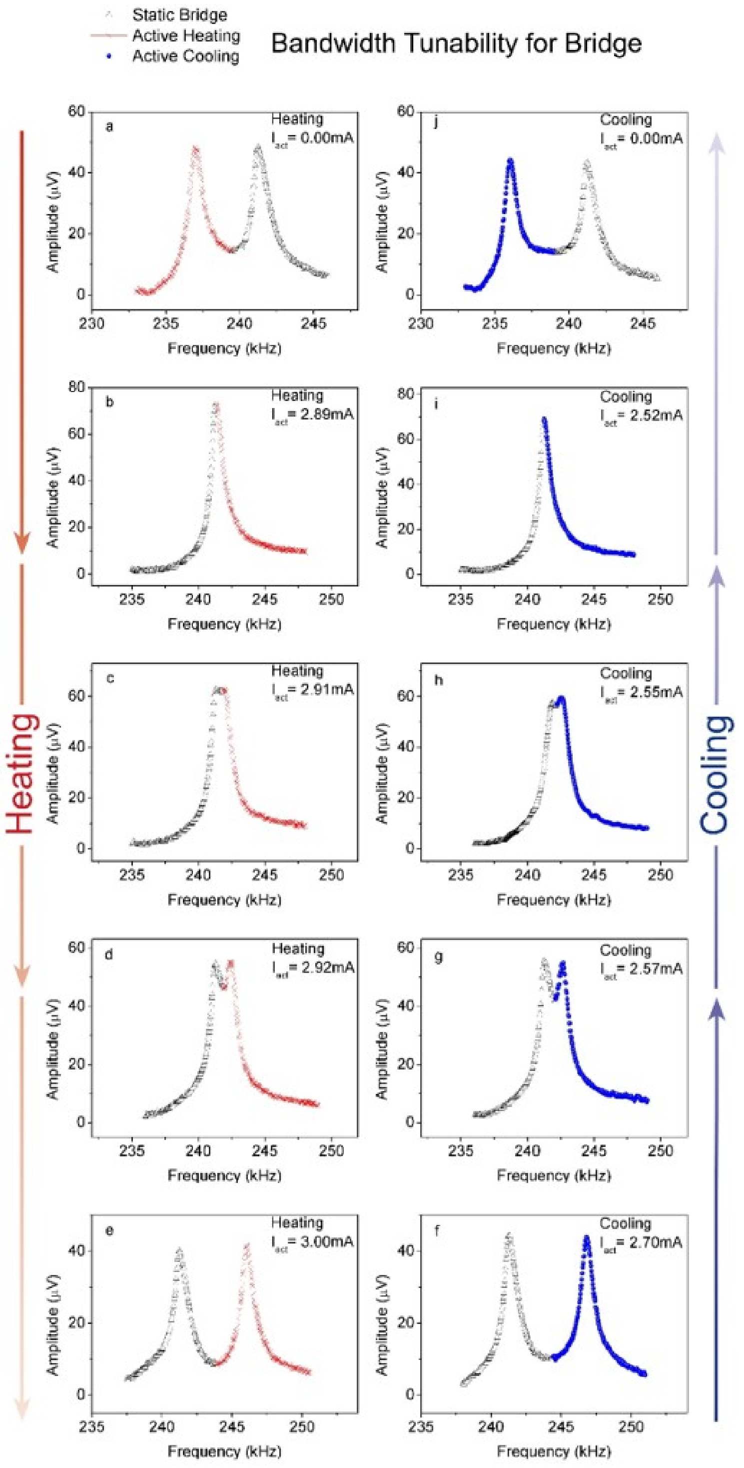

Figure 4.16 The sequence of different stages for the VO_2-based tunable band-pass filter using bridge resonators during a heating/cooling cycle. Plots show selected stages with pairs of similar output for each cycle. The resonant peaks for the static and active bridges are represented by the black and red/blue curves, respectively. I_{act} is the actuation current applied to the active bridge.

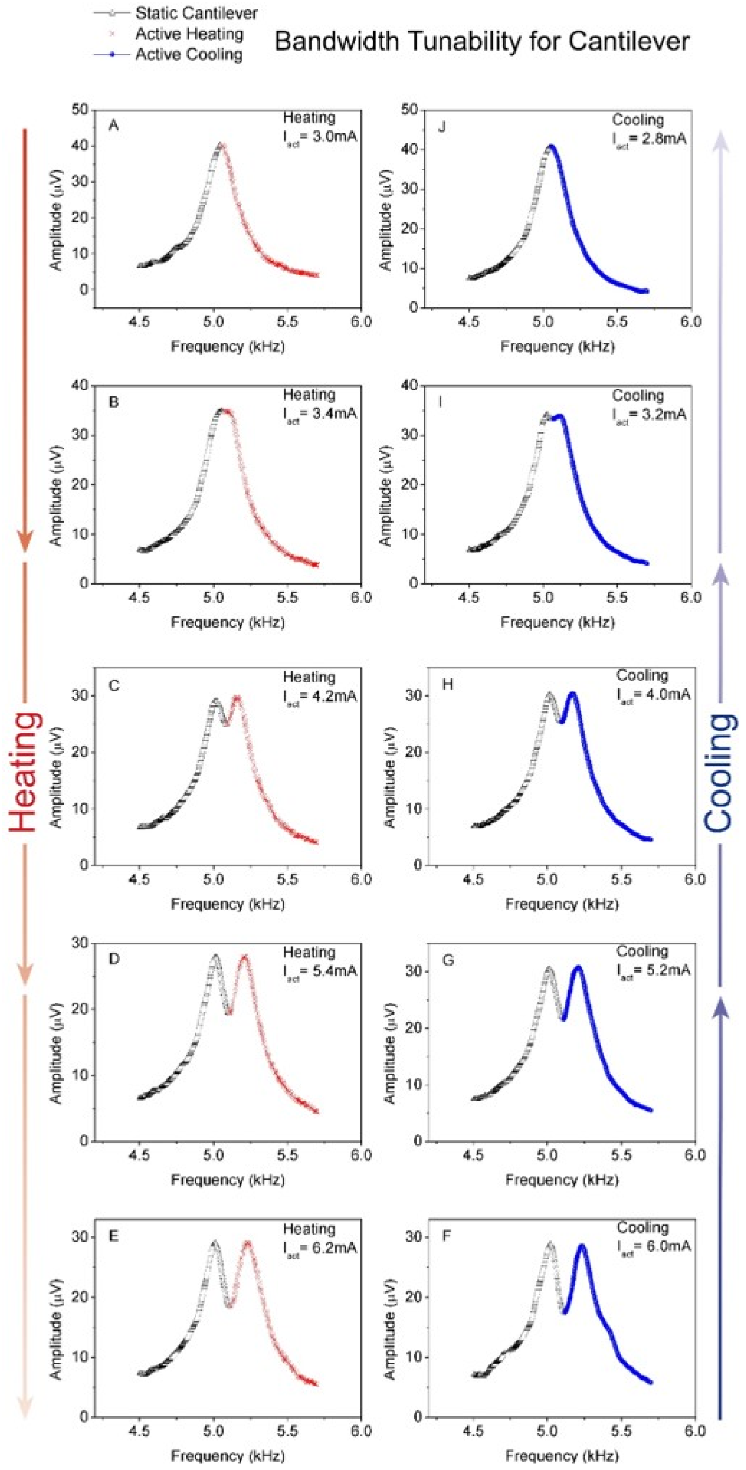

Figure 4.17 The sequence of different stages for the VO_2-based tunable band-pass filter using cantilever resonators during a heating/cooling cycle. Plots show selected stages with pairs of similar output for each cycle. The resonant peaks for the static and active bridges are represented by the black and red/blue curves, respectively. I_{act} is the actuation current applied to the active bridge.

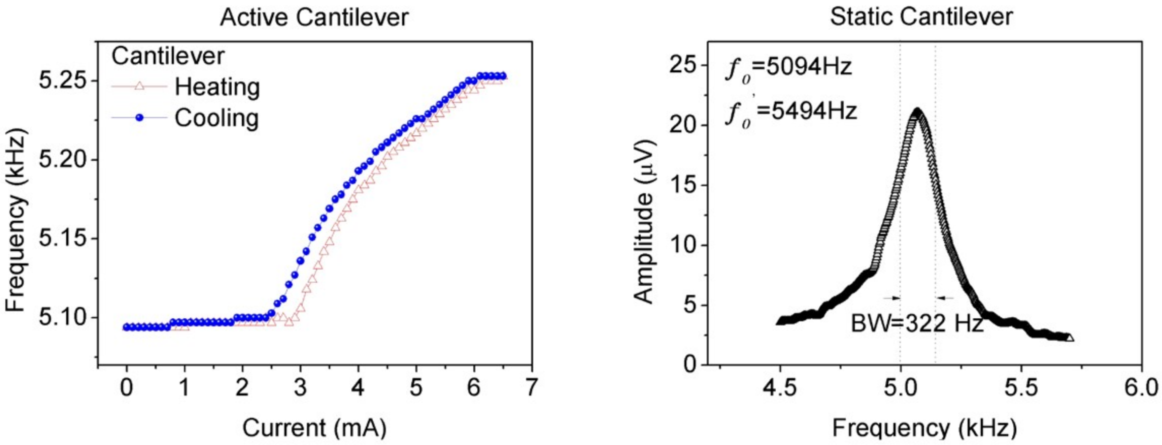

Figure 4.18 *Left:* Resonant frequency versus actuation current through a full heating and cooling cycle for the active cantilever. *Right:* Resonant frequency signal for the static bridge at room temperature. The measured (f_0) and calculated ($f_0^{'}$) resonant frequencies are shown. The value for $f_0^{'}$ was obtained from Equation (3.2), and it does not take residual thermal stress into account.

CHAPTER 5

UNDERSTANDING DYNAMIC RESPONSES IN FERROELECTRET NANOGENERATORS

Self-powered pressure sensors are critical devices in IoT sensing networks. Continuous efforts have been made in the community to improve the device performances by optimizing the materials selection and structural configurations. Therefore, a design platform for understanding the device-machine interface is imperative. This chapter presents a comprehensive study that uses the fundamental working principles of dipole moments in ferroelectret polymers to describe the energy conversion mechanism. The study addresses discrepancies in voltage measurements caused by instruments with different internal resistances and sampling rates. A lumped parameter model is also proposed and validated to explain the impedance mismatch at the device-machine interface. Applications including control of MEMS microactuator through static response and dynamic pressure sensor array for impact distribution sensing have also been demonstrated.

5.1 Electromechanical Response of Ferroelectret Nanogenerator

This section addresses the development of the electromechanical behavior of the ferroelectret polymer in terms of open circuit voltage (V_{oc}) and short circuit current (I_{sc}). The derivation starts with the fundamental physics in the point of view of dipole moments and is supported by FEM simulation. The electric output is characterized by different resistive loads with various mechanical inputs. The influences of instruments' internal resistance and sampling rate on the measurements of electric output are also demonstrated in section.

5.1.1 Derivation of Electric Output

FENG is a flexible multilayer structure device with the ability of converting mechanical energy to or from electrical energy. The active material that exhibits the direct and inverse piezoelectric effect is a dielectric and elastic film with full-of-cell type structure. Despite that the FENG has a similar electrical-mechanical response as piezoelectric nanogenerator, the fundamental working principles are different. By applying external mechanical pressure (F/A), the thickness of the porous midsection region of the polypropylene ferroelectret (PPFE) film decreases. The piezoelectricity of FENG mainly arises from the relative movement of positive charge surface to negative charge surface within each individual ellipsoid void. Each ellipsoid has a permanent dipole moment p_i which can be expressed as $p_i = q_i l_i$, where q_i is the trapped charges and l_i is the initial separation. For a FENG device of volume V and consisting of N ellipsoids, the initial permanent polarization field is therefore determined to be $P_0 = \Sigma_{i=1}^{N} p_i/V$. When external mechanical load is applied, the structure distortion causes a change in the void separation from l_i to l_i' and the polarization field needs to be modified as $P' = \Sigma_{i=1}^{N} p_i'/V = \Sigma_{i=1}^{N} q_i l_i'/V$. Thus, the change in polarization field induces free charges on metal electrodes and can be expressed as: $Q = \Sigma_{i=1}^{N} q_i(l_i - l_i')/h$, where h is the thickness of the FENG. This expression for Q can be further rewritten as $Q = (F/EV)\Sigma_{i=1}^{N} p_i$, where F, E, and A are the applied force, Young's modulus of PPFE, and area, respectively. Since the FENG device shares a capacitive model[112, 156], V_{oc} under F can be described as:

$$V_{oc} = \frac{hP_0}{\epsilon EA}F, \tag{5.1}$$

where ϵ is the relative dielectric constant of PPFE. It can be seen from Equation (5.1) that there is a linear coupling between V_{oc} and P (or F). As shown in **Figure** 5.1a-b, the decrease in distance between the charged surfaces, from l_i to l_i', produces a relative movement of charges with different types. This change in dipole moments generates a displacement current and is accounted for the I_{sc} output under a short circuit condition, which can be

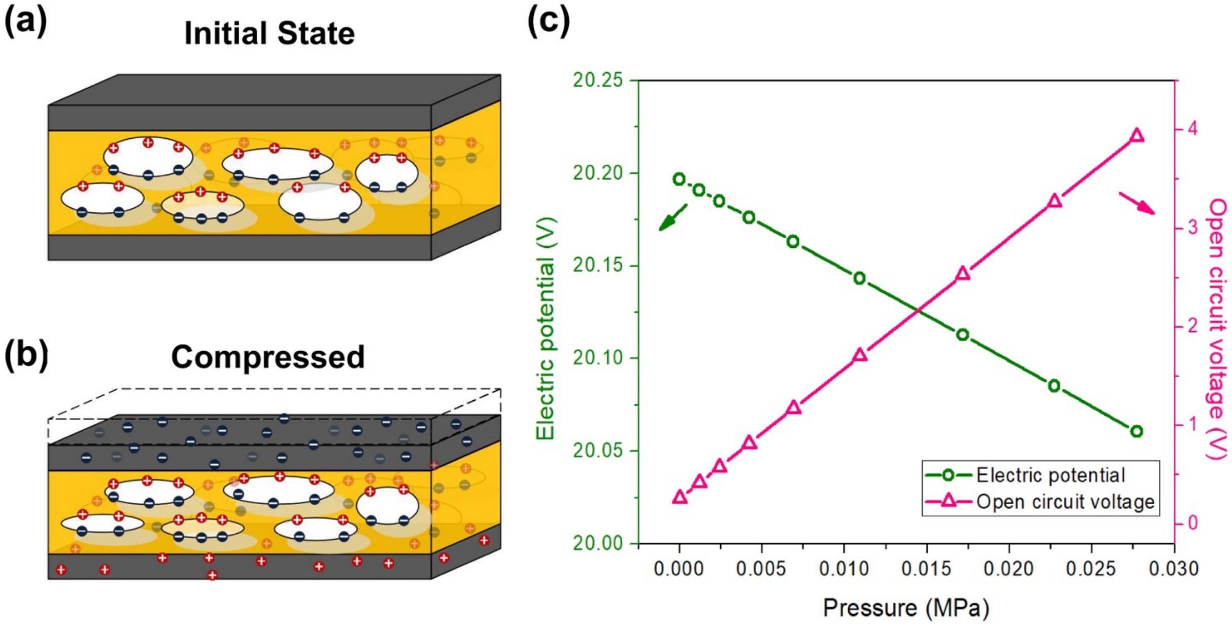

Figure 5.1 Working principle of ferroelectric nanogenerator: (a) No external stress is applied. (b) When external boundary load is applied, the polarization field due to internal dipoles decreases and free induction charges are accumulated on metal electrodes. (c) FEM results of changes in electrode potential at the polymer-metal boundary and open circuit voltage arise from accumulated charges.

expressed as:

$$I_{sc} = \frac{P_0}{E} \cdot \frac{\partial F}{\partial t}. \tag{5.2}$$

The derived expressions for V_{oc} and I_{sc} of a FENG (Equations (5.1) and (5.2)) indicate that the open circuit voltage and short circuit current produced by FENG increase with compression load and rate of change in dipole moments, respectively. From this derivation, it follows that the electric output is frequency-dependent; but only in the I_{sc} term –not V_{oc}. This is explained and demonstrated experimentally in the next section. Some of the previously reported observations on frequency-dependent V_{oc} could be due to the use of low-input impedance instruments. **Figure** 5.1c shows the electromechanical behavior of the PPFE film based on a 250 µm × 90 µm 2-D finite element method (FEM) model. At the initial state, the permanent polarization field induced boundary charges lead to an electric potential at the polymer-metal interface. When the compression load occurs, the polarization field is reduced due to the decrease in dipole moments. This results in a lower electric potential and therefore free charges accumulate on metal electrodes. Because the device shares a capacitive electrical model, the accumulated charges give rise to an open circuit voltage, which is dependent on the mechanical input.

5.1.2 Characterization of Electric Output under Sinusoidal Pressure Input

The experimental demonstration of the parameters that determine the V_{oc} and I_{sc} of a FENG follows. The electric outputs of a FENG in terms of: *(i)* V_{oc}, *(ii)* I_{sc}, and *(iii)* voltage with resistive load (V_{load}) are measured during repetitive external mechanical inputs, which consist of both: pressing and releasing stages in each pulse. Since the open circuit voltage and short circuit current outputs will be different from those with a load, the input impedance of the equipment used to measure these two parameters (V_{oc} and I_{sc}) has an influence on the measurements. When measuring I_{sc}, an ammeter usually directly converts the input current to a reading through a galvanometer. Therefore the measurement is less dependent on the instrument's internal circuit and should be an accurate reading of the current when a short circuit is connected to the FENG. However, a voltmeter consists of a galvanometer with a large internal resistor connected in series. The obtained voltage reading is the input current flowing through the galvanometer times the internal resistance. Therefore using voltmeters with different internal resistances will result in different measurements. Specifically, using a voltmeter with lower internal resistance will show V_{oc} with two peaks during a single mechanical pulse input (one peak with positive magnitude in the pressing stage and one peak with negative magnitude in the releasing stage). According to Equation (5.1), these two peaks of opposite signs do not correctly represent the physics of the process, since the releasing step also represents a pressure of positive magnitude - which should produce a positive V_{oc} output. In other words, the instant of peak pressure (i.e. the instant where pressing stops and releasing begins) should also represent a peak in the V_{oc} output (not $V_{oc} = 0V$). Considering the high impedance of the PPFE film in the low-frequency range, a

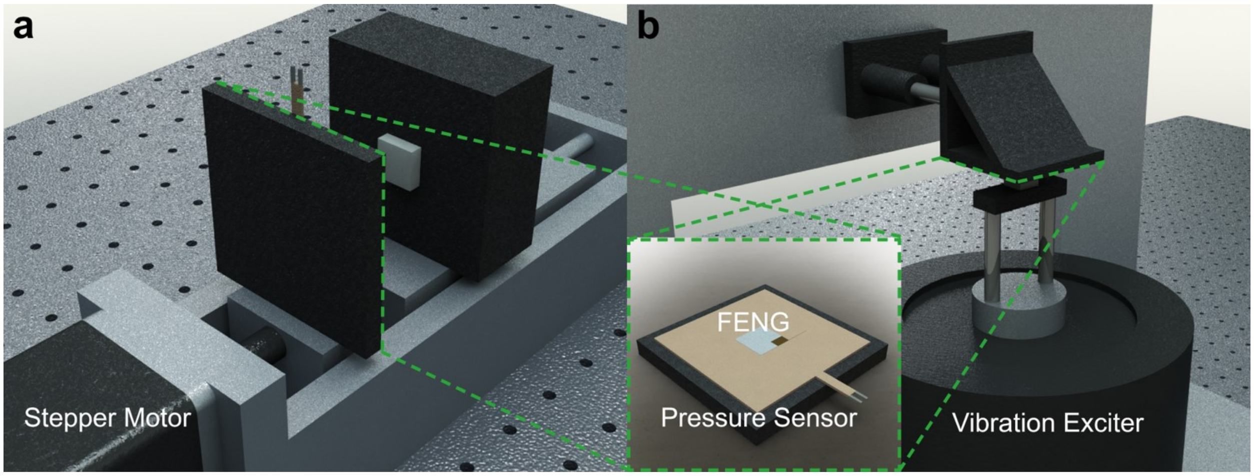

Figure 5.2 Schematic experimental setup. (a) Linear pressure input generated from a stepper motor. (b) Sinusoidal pressure input provided by the vibration exciter and the stacking layout of FENG and pressure sensor is shown in the inset.

testing instrument with much higher internal impedance is required for getting an accurate V_{oc} measurement. In this experiment, V_{oc} is measured by Keithley 2450 Source Measure Unit. The internal impedance of the voltmeter is in the trillion Ohm (TΩ) range which provides more accurate results.

The electric outputs under periodic nonlinear pressure inputs generated by a vibration exciter (**Figure** 5.2) are shown in **Figure** 5.3. The changing polarity test is also carried out to confirm that the electric signal comes from the FENG. As shown in **Figure** 5.3a and **Figure** 5.3b, the electromechanical response of FENG exhibits similar behavior as the piezoelectric effect. The V_{oc} follows the change of the external mechanical input while the I_{sc} is proportional to the derivative of the input according to Equations (5.1) and (5.2). An oscillation of exponentially decaying amplitude is observed at the rising edge of the signal (See **Figure** 5.3b, **Figure** 5.3c). And the nearly infinite peak at the rising edge is related to the derivative of the sinusoidal pressure input at $P = 0\ N$. The observed oscillation can be related to the mechanical properties of the PPFE film and the electrical impedance match which reveals the electromechanical model of FENG. Also, it can be seen from **Figure** 5.3c that folding a 30 mm × 15 mm patch of FENG along a symmetry axis into a smaller patch

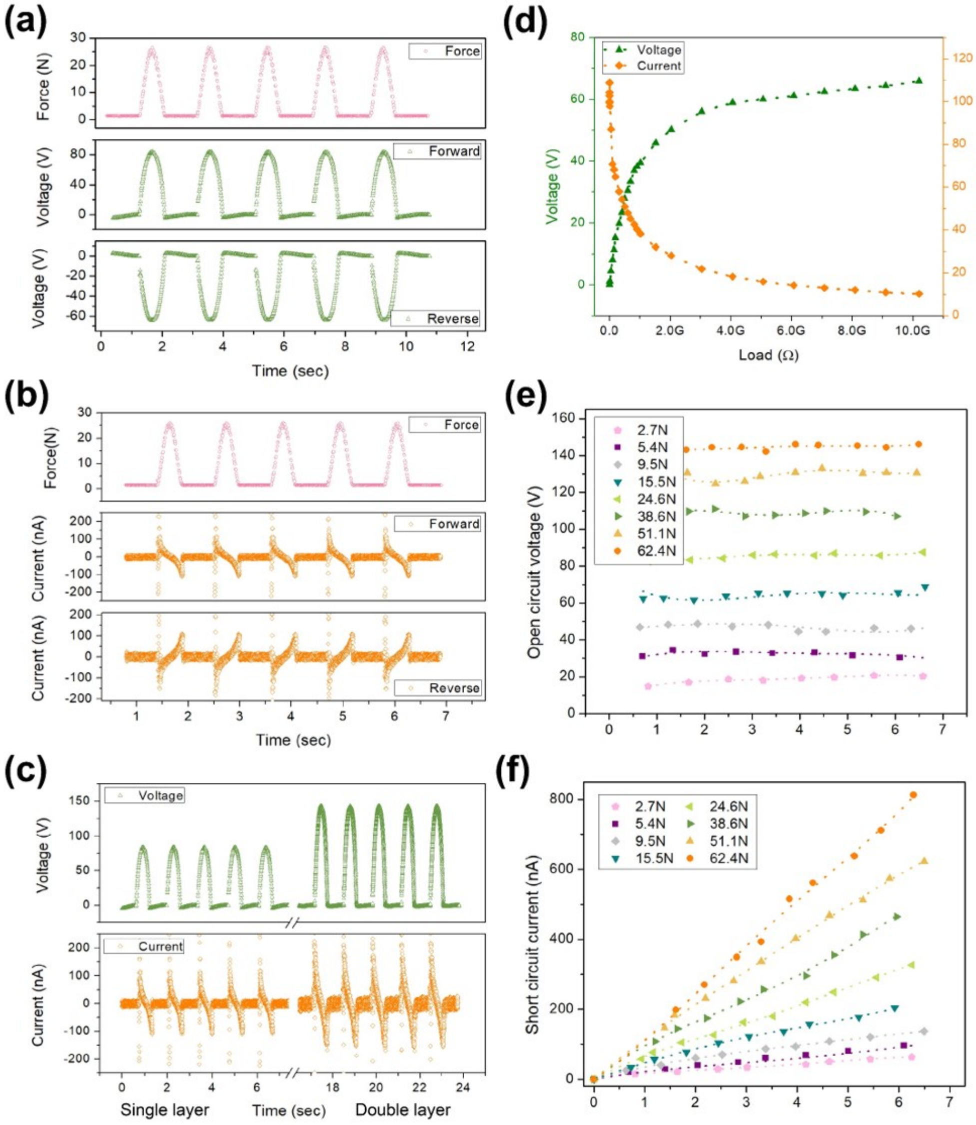

Figure 5.3 Electromechanical characterization of FENG under sinusoidal pressure input. (a) Forward and reverse V_{oc} of FENG under sinusoidal pressure input. (b) Forward and reverse I_{sc} of FENG under sinusoidal pressure input. (c) Amplification of V_{oc} and I_{sc} of FENG by a symmetric folding process under sinusoidal pressure input. (d) Electric output, voltage, and current, under sinusoidal pressure input with increasing resistive load. (e) V_{oc} of FENG under sinusoidal pressure input with variable pressure amplitudes and frequencies. (f) I_{sc} of FENG under sinusoidal pressure input with various pressure amplitudes and frequencies.

of 15 mm × 15 mm can double both the V_{oc} and I_{sc} for a given mechanical input.

The electric outputs under different resistive loads are also investigated and results are shown in **Figure** 5.3d. A mechanical input with a pressure amplitude of 110 kPa and frequency of 1.7 Hz shows a voltage output that increases with resistive load, approaching V_{oc}. **Figure** 5.3e and 5.3f show V_{oc} and I_{sc} as a function of pressure amplitude and frequency. V_{oc} increases with pressure amplitude but remains constant for different frequencies from a given pressure amplitude as indicated by Equation (5.1). I_{sc}, on the other hand, increases with the changing rate of the mechanical input, which is related to pressure amplitude and frequency, as shown in **Figure** 5.3f. These experimental results are consistent with the theoretical and conceptual rationale explained above.

5.1.3 Characterization of Electric Output under Linear Pressure Input

The electric output under a periodic linear pressure input is shown in **Figure** 5.4. The changing polarity test is also carried out to confirm that the electric signal comes from the FENG. As we can see in **Figure** 5.4a and **Figure** 5.4b, the electromechanical response of FENG exhibits similar behavior as the piezoelectric effect. The V_{oc} follows the change of the external mechanical input while the I_{sc} is proportional to the derivative of the input. A similar linear pressure input of the same amplitude but the higher frequency is also used to study the electromechanical response of FENG with different frequencies (See **Figure** 5.4d, e, and f). The V_{oc} shown in **Figure** 5.4d shows the same peak value as in **Figure** 5.4a due to the same amplitude of the pressure input. **Figure** 5.4b and **Figure** 5.4e show how the magnitude of I_{sc} increases with frequency. Since the stepper motor applies a continuous linear input by accumulating the mechanical step inputs through the control of the duty cycle of the electric driving signal, the linear electromechanical behavior is, in fact, a static state response. Strong oscillations can be observed at the rising edge of the signal even when a linear mechanical input posses a lower acceleration than the sinusoidal input. The observed oscillation can be related to the mechanical properties of the PPFE film and the electrical impedance match which reveals the electromechanical model of FENG.

By comparing **Figure** 5.4a with **Figure** 5.3a, although the pressure inputs have the same amplitude and frequency, different V_{oc} outputs are measured due to different pressure

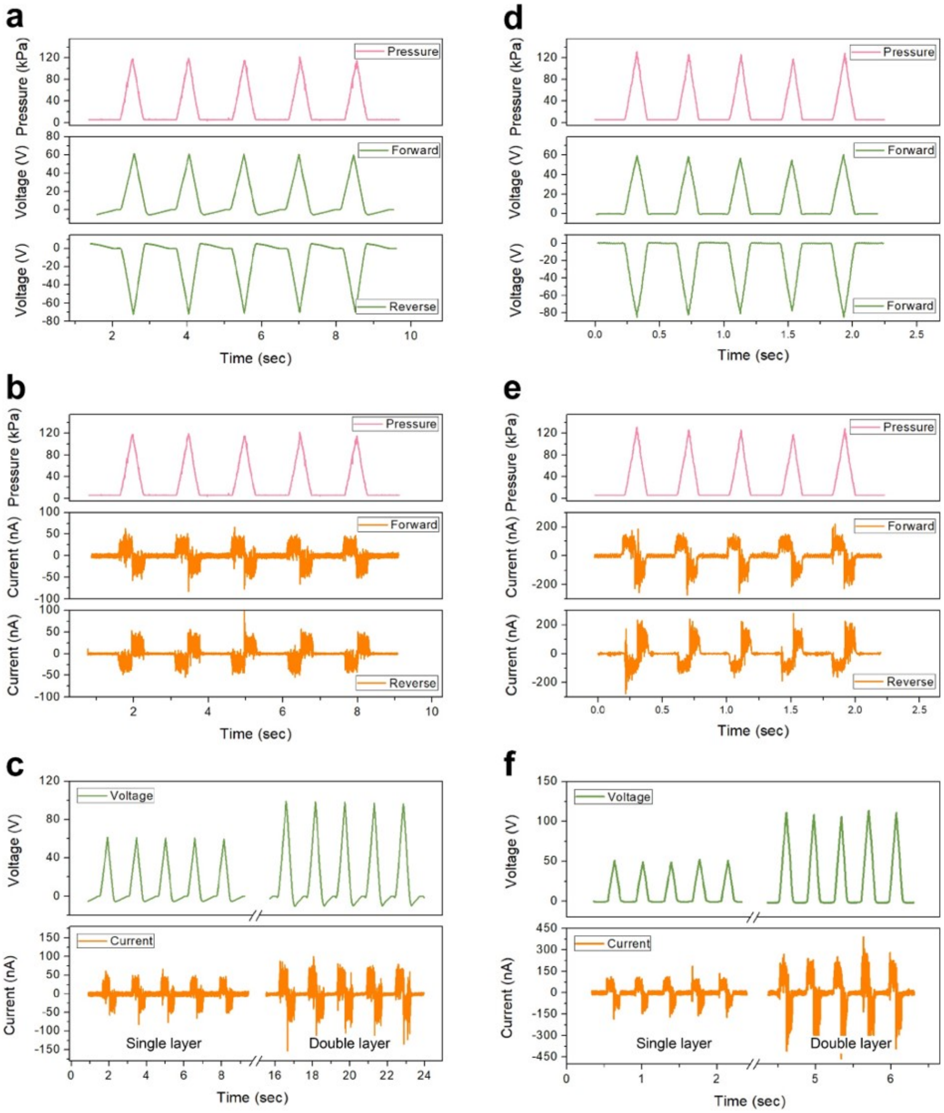

Figure 5.4 Electromechanical characterization of FENG under linear pressure input. (a) Forward and reverse V_{oc} of FENG under low-frequency linear pressure. (b) Forward and reverse I_{sc} of FENG under low-frequency linear pressure. (c) Amplification of V_{oc} and I_{sc} of FENG by a symmetric folding process under low-frequency linear pressure. (d) Forward and reverse V_{oc} of FENG under high-frequency linear pressure. (e) Forward and reverse I_{sc} of FENG under high-frequency linear pressure. (f) Amplification of V_{oc} and I_{sc} of FENG by a symmetric folding process under high-frequency linear pressure.

input profiles (linear and sinusoidal). The different I_{sc} amplitudes shown in **Figure** 5.4b and **Figure** 5.3b under the same pressure input further validate this result. The oscillation is also observed at the rising edge of the signal (See **Figure** 5.3b and **Figure** 5.3c). And the nearly infinite oscillation peak at the very beginning of the rising edge is related to the derivative of the sinusoidal pressure at $P = 0\ N$ point (higher acceleration than the linear pressure).

5.1.4 Lumped Parameter Model for Electric Responses

Many lumped parameter models have been developed for different types of piezoelectric film materials in different operating frequency regions. In the low-frequency region, a simple RC model can be effectively used for modeling the electrical behavior[157]. For piezoelectric polymer, the internal resistance is nearly infinite, thus the electrical model is purely capacitive. Multiple electromechanical lumped models for piezoelectrics have been proposed, which consider the underlying physics and specific applications [158, 159, 160]. However, a lumped model for describing the electromechanical response of nanogenerators is still needed to analyze the electric output under different impact pressure profiles and resistive loads. The overshoot presented in the I_{sc} at the rising edge of the pressure input shown in **Figure** 5.4b suggests a second-order system model. When external mechanical stress is applied, a change in dipole moments of the mid-section layer is induced in terms of the charge separation. This produces a displacement current that is proportional to the changing rate of the dipole moment. Hence, a second-order system is used to describe the electrical domain. The electromechanical lumped parameter model and its equivalent electrical circuit are shown in **Figure** 5.5a and **Figure** 5.5b respectively. The variable φ represents the transduction from the mechanical domain to the electrical domain.

The derived lumped model can be used to compare the outputs due to sinusoidal inputs used in **Figure** 5.5a. **Figure** 5.5c shows the pressure due to a sinusoidal input. **Figure** 5.5d shows the I_{sc} under this sinusoidal pressure input. The transduction to the electrical domain involves differentiating the mechanical input with respect to time. When the load (R_2) equals zero (i.e. short circuit condition), the system presents an underdamped response with the strongest oscillation as shown in **Figure** 5.5d. Based on the derived model, it is possible to predict the electric output under different resistive loads. When the resistance

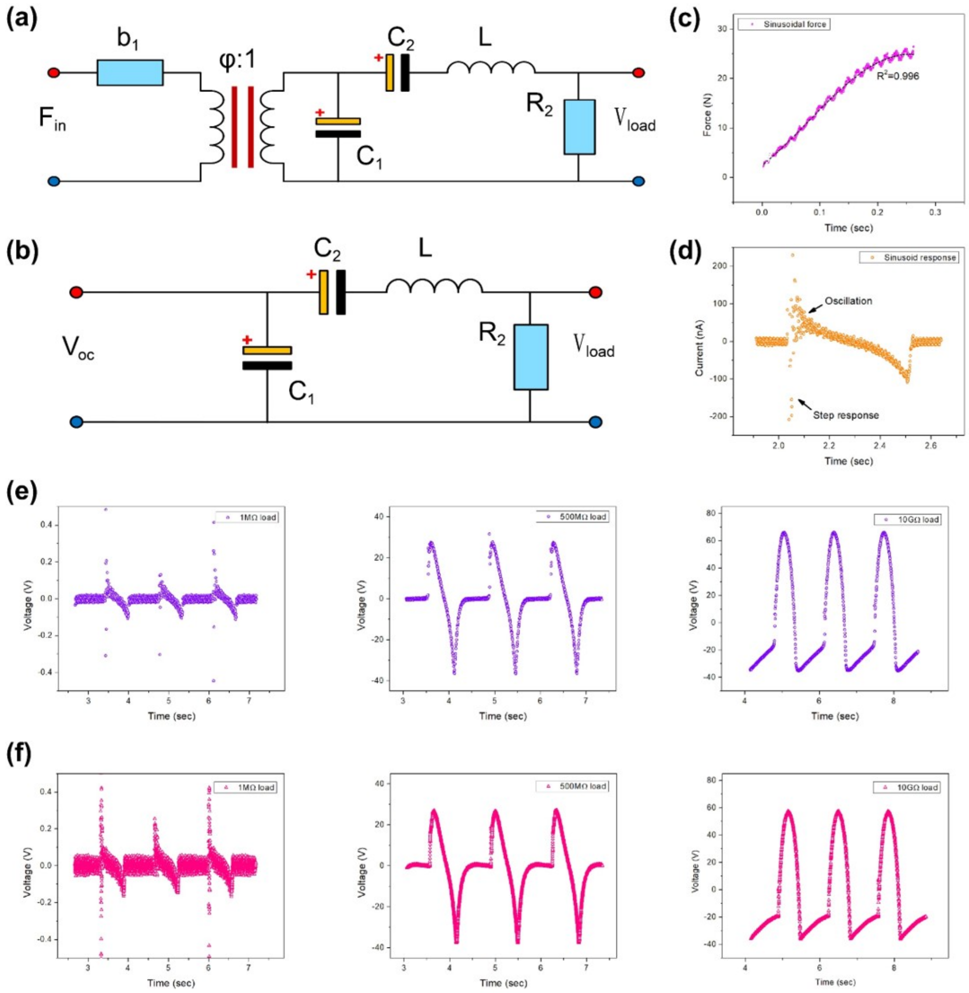

Figure 5.5 Illustration of the lumped model. (a) Lumped electromechanical model of FENG. (b) Equivalent electrical circuit model of FENG. (c) Impact profile of a sinusoidal pressure input. (d) I_{sc} under a sinusoidal pressure input. (e) Experimental electromechanical response with different load resistances. (f) Simulated electromechanical response with different load resistances.

of the load increases, the system evolves from an underdamped system to an overdamped system. The oscillation will decrease with increasing load resistance and the output voltage (V_{load}) changes its profile from an I_{sc}-like signal to a V_{oc}-like signal. **Figure** 5.5e shows the measured electromechanical response under different resistive loads. The large transient oscillation only occurs with low resistive loads. It should also be noted how the measured output voltage profile keeps approaching the open circuit voltage and input pressure profiles shown in **Figure** 5.3a. This means that the profile (and value) of the measured open circuit voltage will be highly dependent on the internal resistance of the instrument used. **Figure** 5.5f shows the simulated response based on the model shown in **Figure** 5.5b, where the parameter C_1 is 32 pF (which is the capacitance of the PPFE film), C_2 and L are chosen to be 0.15 nF and 2000 H in order to fit the experimental data. The system exhibits an underdamped response for low resistive loads and an overdamped response for higher resistance loads.

5.1.5 Instruments with Different Internal Resistances and Sampling Rates

This subsection studies the influence of testing instruments with different input resistances on the open circuit voltage (V_{oc}) of FENG. As discussed in previous subsections, the experimentally measured V_{oc} heavily depends on the internal resistance of the voltmeter. Hence, four instruments with different internal resistive impedances are used to measure the V_{oc} and the results are compared. **Figure** 5.6 shows the measured data of testing instruments: Keithley 2450, Keithley 2182, Tektronix TDS2004C and National Instruments 9201. The internal impedances for those testing instruments are measured to be 0.41 TΩ, 10 MΩ, 1 MΩ, and 1 MΩ respectively. All the measurements are made under the same pressure input of 110 N and 1.7 Hz. As can be seen in **Figure** 5.6a, the Keithley 2450 (which has the highest internal resistance and sampling rate) shows results that follow the pressure profile. This is expected since the instant of peak pressure (i.e. the instant where pressing stops and releasing begins) should also represent a peak in the V_{oc} output. **Figure** 5.6b shows the results for Keithley 2182, which offers intermediate internal resistance but very low sampling rate. Therefore the V_{oc} plots behave like the short current (I_{sc}) pattern with much lower amplitude than the V_{oc} measured with the Keithley 2450. **Figure** 5.6e and **Figure** 5.6f show the data obtained from Tektronix TDS2004C and National Instruments 9201. These two instruments have the lowest internal resistance of around 1 MΩ but high sampling rate. The readings for both instruments have the same amplitude for V_{oc} with some ripple observed due to the under-damped response in the low load condition. As discussed, the FENG

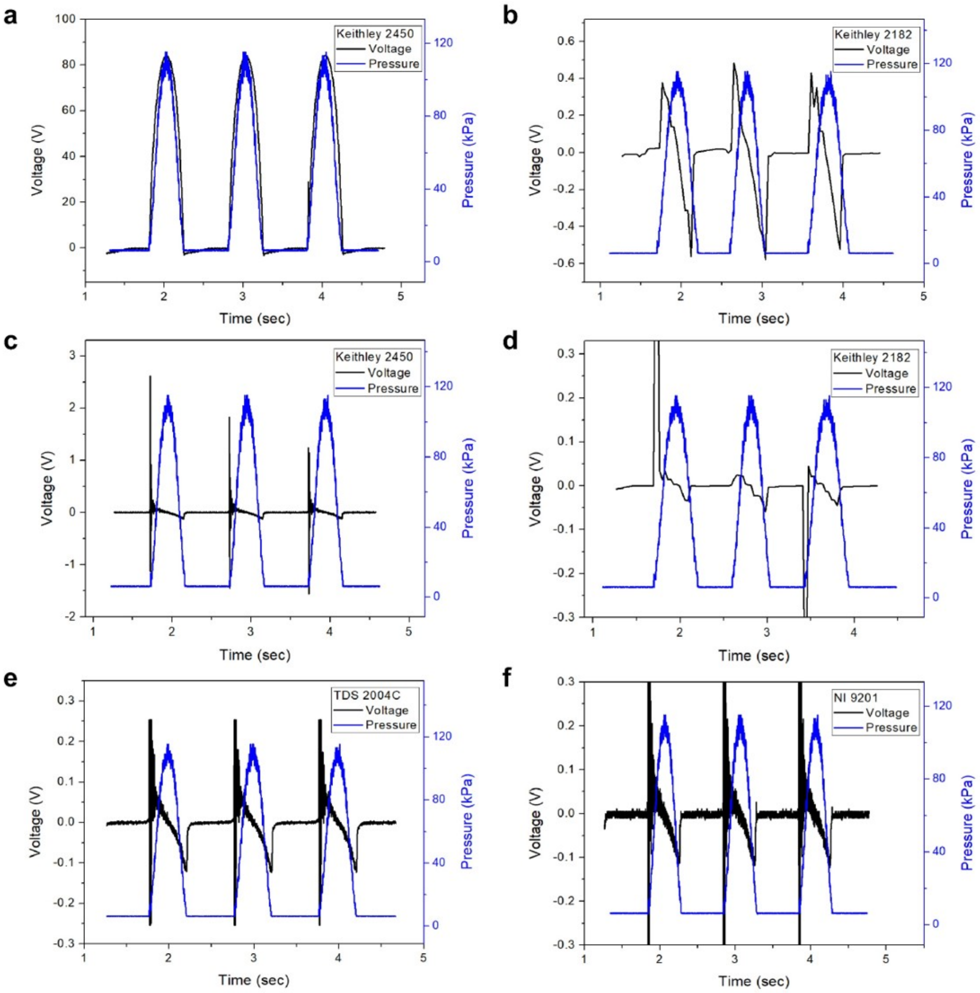

Figure 5.6 FENG voltage output measurement with different instruments: (a) Keithley 2450 and V_{oc}. (b) Keithley 2182 and V_{oc}. (c) Measured voltage output when using a Keithley 2450 and a 1 MΩ load resistor. (d) Measured voltage output when using a Keithley 2182 and a 1 MΩ load resistor. (e) Tektronix TDS2004C and measured V_{oc}. (f) National Instruments 9201 and measured V_{oc}.

can be modeled as a second-order system, therefore the electromechanical response can be determined by the damping ratio ξ from the following expression:

$$\xi = \frac{\alpha}{\omega_0}, \tag{5.3}$$

where α is the attenuation factor and ω_0 is nature resonant frequency. Those factors can be determined by the lumped parameters as:

$$\alpha = \frac{R}{2L} \tag{5.4}$$

and

$$\omega_0 = \frac{1}{\sqrt{LC}}, \tag{5.5}$$

where R and L are the lumped resistance and inductance, while C is the effective capacitance of C_1 and C_2 in **Figure** 5.5. When a small resistive load, e.g. $R = 1\ M\Omega$, the damping ratio ξ is calculated to be 0.057, which indicates an underdamped response for the system and therefore a strong oscillation is observed. As the resistive load increases to beyond 17.4 MΩ, the system presents an overdamped response where the decay of the transient current does not exhibit an oscillation behavior.

In order to further validate the influence of internal resistance on the measurement outcome, the voltage output of FENG under 1MΩ load is measured with Keithley 2450 and Keithley 2182. **Figure** 5.6c and **Figure** 5.6d shows the results. Since the 1 MΩ load is much smaller than the internal resistance of both instruments (Keithley 2450 and Keithley 2182), most of the generated current will flow through the load resistor (and not into the instrument), thus providing an accurate reading of the voltage drop at the load. By comparing the voltage measurements in **Figure** 5.6e and **Figure** 5.6f with those in **Figure** 5.6c and **Figure** 5.6d, we can see that the V_{oc} measured by an instrument with 1 MΩ internal resistance matches the voltage under a 1 MΩ load. Moreover, because the Keithley 2182 has a very low sampling rate, some of the ripple oscillations are not captured in the measurement, and the nature of the second-order response of FENG may also be neglected. This demonstrates that the internal resistance of the voltmeter can have a significant influence on the V_{oc} measurement of the FENG as well as other nanogenerators with high impedance.

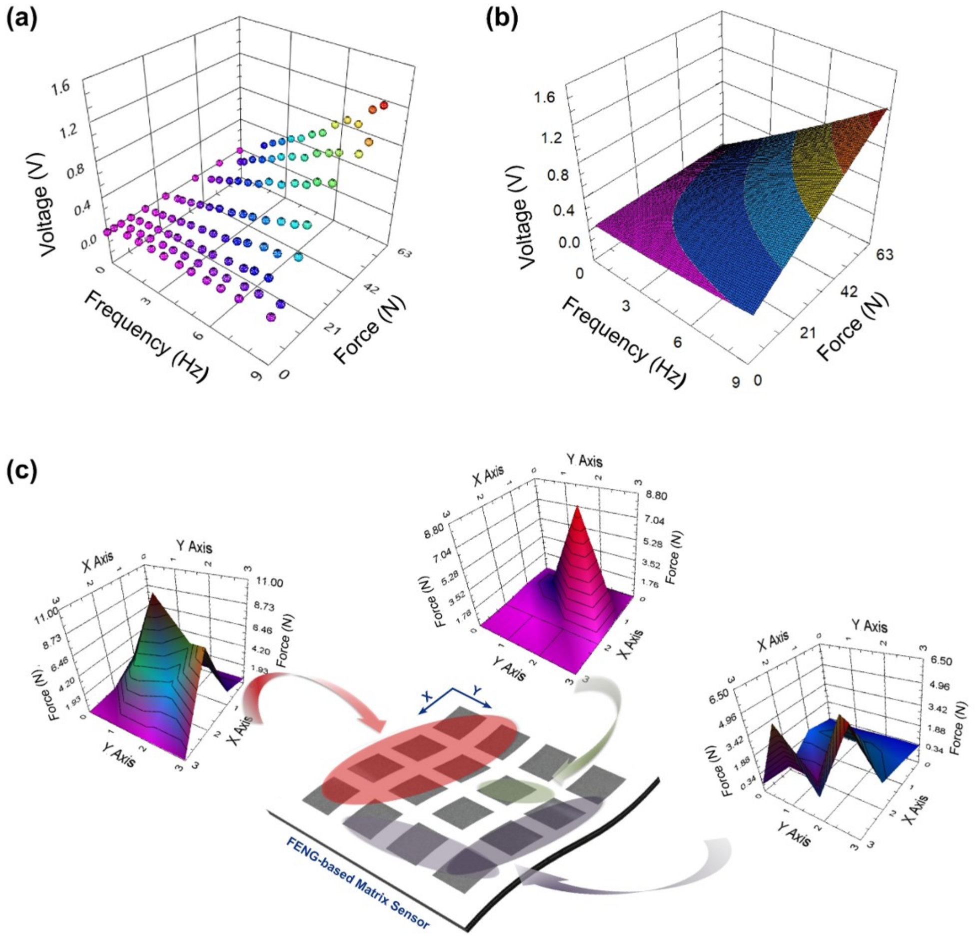

Figure 5.7 FENG-based matrix pressure sensor. (a)The voltage output of a 15 mm × 15 mm single layer FENG as a function of input pressure amplitudes and frequencies. (b) 3D surface fitting of the single-pixel electromechanical response, $R^2 = 0.93$. (c) 16-pixel FENG-based matrix sensor and 3D contour maps of the pressure distribution over the sensor upon an impact from the user.

5.1.6 FENG-based Tactile Sensor

As discussed above, the V_{oc} is proportional to the input mechanical pressure amplitude and is independent of its rate of change with time. However, most of the commercial voltmeters have internal resistances in the range of 1 $\sim$ 10 MΩ. When using such low-impedance instruments to measure V_{oc}, the measurement is misleading, since it is actually the voltage drop across a resistive load V_{load}, which can be approximated by I_{sc} times the internal resistance R_{in} of the voltmeter. Thus, V_{load} changes with both: pressure amplitude and its

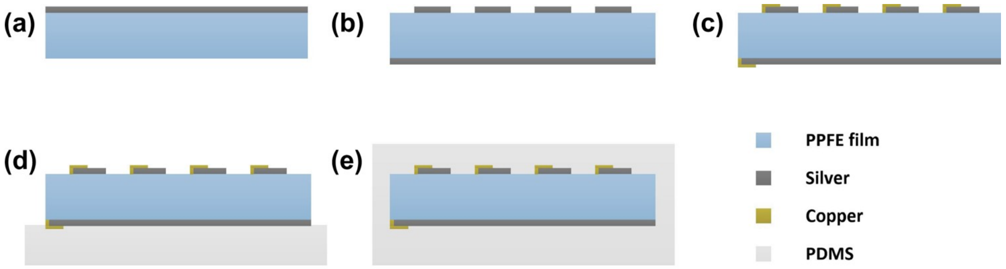

Figure 5.8 The fabrication process of a single layer FENG-based matrix sensor with 16 individual positive electrodes and 1 common negative electrode. (a) Deposition of the common negative silver electrode on PPFE film. (b) Deposition of 16 positive silver electrodes. (c) Wire connection by conductive copper tape. (d) Spin coating of PDMS substrate and partially cured. (e) Spin coating of another PDMS layer to encapsulate the device and the two layers are completely cured.

rate of change with time. Because the FENG is able to output voltage signal which depends on the input pressure profile, no external power supply is required for device operation as a pressure sensor (i.e. FENG can be implemented as a self-powered flexible dynamic pressure sensor). In this work, the electromechanical response is characterized for a 15 mm × 15 mm single layer FENG device and the V_{load} is measured by using a voltmeter with 1 MΩ resistive internal resistance (NI9201, National Instruments). Given that the sinusoidal pressure input can be expressed by $P = P_{max} sin(2\pi ft)$, where P_{max} is the peak pressure amplitude, f is the frequency; V_{load} can be expressed as:

$$V_{load} = \alpha P_{max} f cos(2\pi ft) \tag{5.6}$$

where $\alpha = 2\pi A P_0 R_{in}/E$. The maximum value V_{peak} is therefore found to be at $V_{peak} = V_{load}(t = 0)$ and is linearly related to $P_{max} f$. **Figure** 5.7a and **Figure** 5.7b show the 3D surface plot of the V_{peak} as a function of the input pressure amplitude and frequency. By fitting the data into a polynomial function, the relation between V_{peak}, P_{max}, and f can be given by: $V_{peak} = 3.1 \times 10^{-7} P^{1.1} f^{0.85}$, which is expected from Equation (5.6).

A single FENG-based pressure sensor can be easily integrated into an N × N array of pressure sensor by a specific arrangement of the positive electrodes. **Figure** 5.7c shows an array of 16 individual FENG devices, each with an area of 15 mm × 15 mm. All the elements

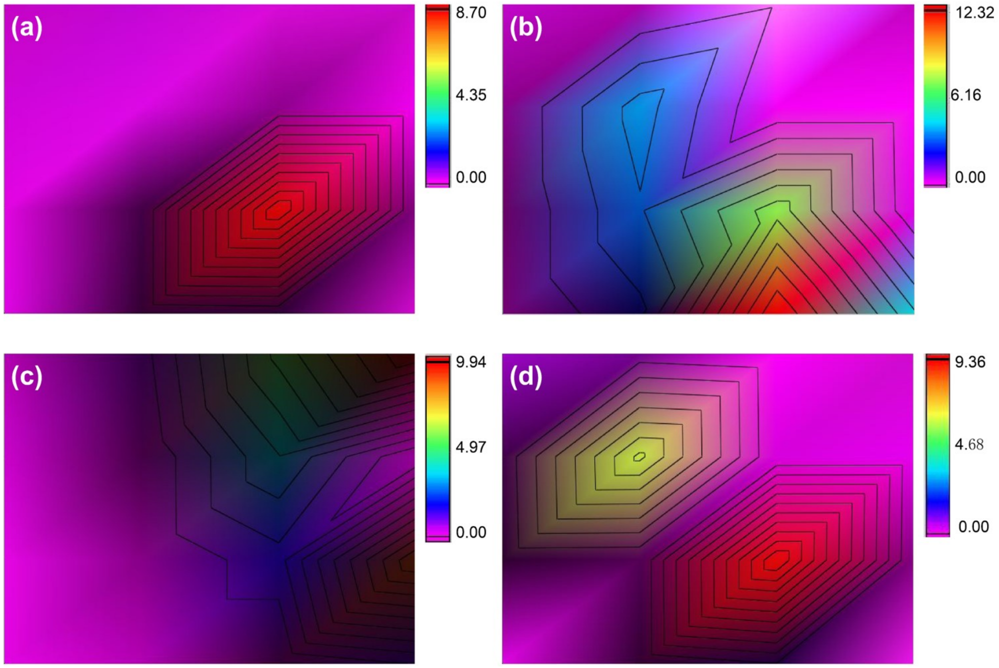

Figure 5.9 Contour map of the pressure distribution over the sensor with different impacts applied to different locations.

in the array are equally spaced in both the X and Y directions. A common negative electrode is patterned on the backside of the PPFE film. To protect the silver electrodes from wearing during repeated use and humidity, the device is encapsulated into a polydimethylsiloxane (PDMS) protective layer (See detailed fabrication process in **Figure** 5.8). Since the positive electrodes are electrically insulated from each other, each electrode can be taken as an independent pixel pressure sensor. Hence, this 4 × 4 matrix pressure sensor with a resolution of 16 pixels can be implemented to map the distribution of an impact. **Figure** 5.7c shows the 3D contour map of the pressure distribution upon an external impact from the user's hand press. The different magnitudes of pressures are labeled and presented in different colors (see **Figure** 5.9 for 2D contour map of pressure distributions). The pressure distribution under different impacts is also presented.

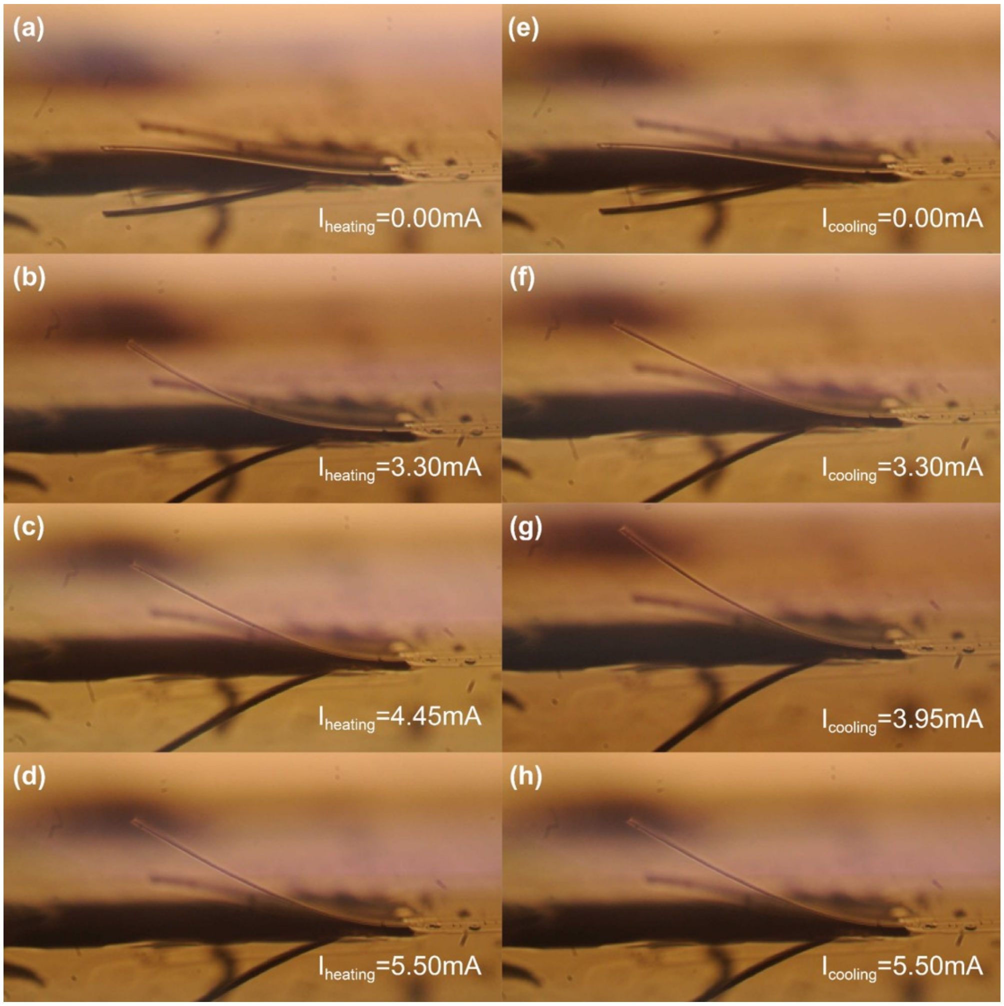

Figure 5.10 Deflection of VO_2-based actuator at different actuation currents. (a) Deflection of VO_2-based actuator at room temperature in the heating cycle. (b) Deflection of VO_2-based actuator at 3.30 mA in the heating cycle. (c) The maximum deflection of VO_2-based actuator at 4.45 mA in the heating cycle. (d) Deflection of VO_2-based actuator at 5.50 mA in the heating cycle. (e) Deflection of VO_2-based actuator at room temperature in the cooling cycle. (f) Deflection of VO_2-based actuator at 3.30 mA in the cooling cycle. (g) The maximum deflection of VO_2-based actuator at 3.95 mA in the cooling cycle. (h) Deflection of VO_2-based actuator at 5.50 mA in the cooling cycle.

5.1.7 FENG-based Micro Robot Arm Controller

Due to FENG's large internal impedance, almost any commonly used voltmeters could cause a discharge of the self-charged electrical energy in the device and results in transient signal output. Thus, the application is limited to dynamic pressure monitoring. When static response needs to be addressed, an electronic switch can be induced where the FENG can

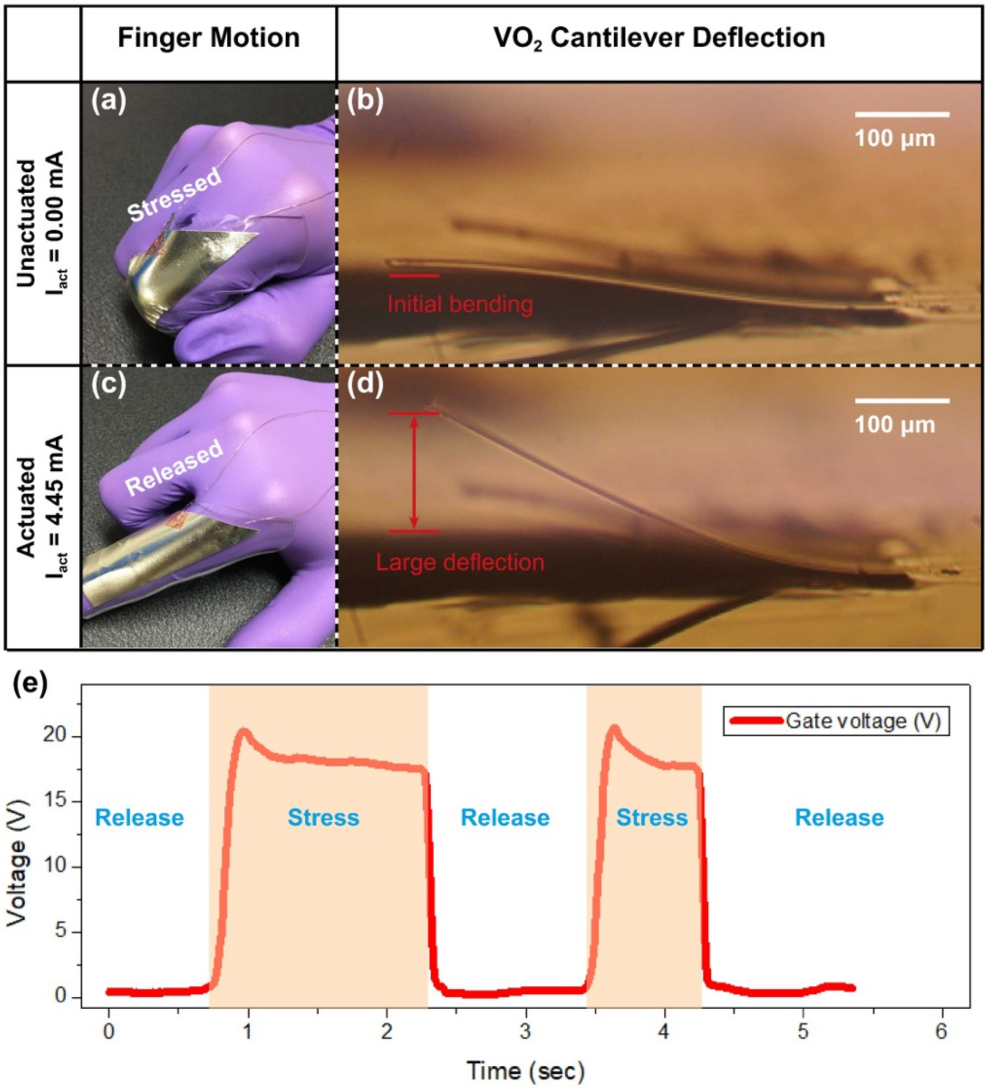

Figure 5.11 FENG-based micro robotic arm controller. (a) Stress applied to the FENG device. (b) VO_2-based MEMS actuator without applying actuation current. (c) Stress released from the FENG device. (d) VO_2-based MEMS actuator with a maximum deflection at actuation current of 4.45 mA. (e) The gate voltage of the p-channel MOSFET controlled by the output of FENG, the voltage change tracks the motion of the finger.

be used to control the gate voltage. Here we demonstrate this application by using a micro-robotic arm controlled through the movement of the human body (e.g. movement of a finger) by combining the FENG and a VO_2-based bimorph microelectromechanical systems (MEMS) actuator. The VO_2-based actuator can be thermally actuated by utilizing the large difference in the thermal expansion coefficient of the VO_2 coating and SiO_2 substrate in the bimorph beam structure. Therefore the beam structure bends up towards the out of plane direction (see **Figure** 5.10). In this work, the VO_2-based MEMS actuator has dimensions of 550 µm in length, 50 µm in width and 2.3 µm in thickness. The actuation is induced by applying a current to the resistive metal heater which is embedded into the beam material. To enable the control of the deflection of the VO_2 actuator, a single layer FENG device of 15 mm × 35 mm is fabricated and encapsulated into a PDMS ring structure and then put onto the user's finger. As shown in **Figure** 5.11, the FENG senses the stress coming from the flexing of the finger, and the voltage output is used to control the actuation current through the gate terminal of a p-channel metal-oxide-semiconductor field-effect transistor (MOSFET), which in turn controls the current through the VO_2-based MEMS actuator.

5.2 Summary

In this chapter, a polypropylene ferroelectret polymer thin film with the large piezoelectric effect is presented. The discussion is mainly focused on the design platform for implementing the PPFE film as a flexible pressure sensor. Both static and dynamic pressure responses are studied when different device-machine interfaces are considered. The characterizations in terms of V_{oc} and I_{sc} are performed on a 15 mm × 15 mm single layer FENG thin patch under different mechanical impacts provided by a vibration exciter. The results show that the energy conversion process from mechanical to electrical domain could be significantly affected by the internal impedance of instruments. Measurement results can also be affected by the instrument sampling rate since the transient oscillation signal occurs at the starting edge within a short time window. A lumped parameter model is also proposed to explain the load-dependent voltage measurement variations and the results are validated by the experiment. Applications in terms of the pixelated sensor array and the human-robotic control interface are also demonstrated at the end. This paper provides useful information on the design of sensor/machine interface, especially when polymer-based sensor with high internal impedance is used, and in troubleshooting the variations caused by instruments.

CHAPTER 6

FERROELECTRET NANOGENERATOR BASED SELF-POWERED BENDING SENSOR

The significant growth of wearable electronics is in constant search for optimizing systems with high flexibility and self-powering capacity. In this chapter, we utilize flexible polypropylene ferroelectret (PPFE) thin film polymer with the large transverse piezoelectric coefficient for bending curvature self-powered sensing. The electric energy comes from the geometry distortion of the built-in macro dipoles with initial surface charge distributions. Theoretical analysis based on constitutive electromechanical equations and bi-layer bending mechanics provide a detailed understanding of the sensing mechanism and its applicability. Different evaluation methods are used to have a more comprehensive understanding of the electromechanical responses under different bending conditions. It has been found that the velocity and magnitude of the mechanical input influence the average voltage output, while instantaneous voltage is not dependent on the latter. The robustness of the material is also investigated, where the device shows no performance degradation by immersion into the water up to 12 hours and under 10k bending cycles. Thermal stability tests reveal degradation starting at $\sim 75°\mathrm{C}$ and an immediate failure of the device at $\sim 150°\mathrm{C}$. Finally, an application is demonstrated by showing the potential use of the characterized system as a self-powered sensor for athletic assessment[161].

6.1 Analysis of Piezoelectricity Under Bending Test

In this section, we present the theoretical analysis of the piezoelectricity of ferroelectret polypropylene (PP) polymer under a bending condition. This piezoelectric effect is originated from the transverse piezoelectric coefficient which leads to a decrease in the dipole separation distance under an axial compression. The analysis starts with the fundamental constitutive equations for piezoelectric materials, which addresses the linear coupling between electrical and mechanical domain. Expressions for electrical outputs (current and voltage) are deducted as a function of mechanical input.

6.1.1 Current Output Under Bending Test

The constitutive equations of a typical piezoelectric material among stress σ_{ij}, strain ϵ_{ij}, electric field E_i and displacement field D_i can be described as below:

$$\begin{bmatrix}\sigma_{11}\\ \sigma_{22}\\ \sigma_{33}\\ \sigma_{23}\\ \sigma_{32}\\ \sigma_{12}\end{bmatrix} = \begin{bmatrix} c_{11} & c_{12} & c_{13} & 0 & 0 & 0\\ c_{12} & c_{11} & c_{13} & 0 & 0 & 0\\ c_{13} & c_{13} & c_{33} & 0 & 0 & 0\\ 0 & 0 & 0 & c_{44} & 0 & 0\\ 0 & 0 & 0 & 0 & c_{44} & 0\\ 0 & 0 & 0 & 0 & 0 & (c_{11}-c_{12})/2 \end{bmatrix} \begin{bmatrix}\epsilon_{11}\\ \epsilon_{22}\\ \epsilon_{33}\\ 2\epsilon_{23}\\ 2\epsilon_{31}\\ 2\epsilon_{12}\end{bmatrix} - \begin{bmatrix} 0 & 0 & d_{31}\\ 0 & 0 & d_{31}\\ 0 & 0 & d_{33}\\ 0 & d_{15} & 0\\ d_{15} & 0 & 0\\ 0 & 0 & 0 \end{bmatrix} \begin{bmatrix}E_1\\ E_2\\ E_3\end{bmatrix}, \tag{6.1}$$

and

$$\begin{bmatrix}D_1\\ D_2\\ D_3\end{bmatrix} = \begin{bmatrix} 0 & 0 & 0 & 0 & d_{15} & 0\\ 0 & 0 & 0 & d_{15} & 0 & 0\\ d_{31} & d_{31} & d_{33} & 0 & 0 & 0 \end{bmatrix} \begin{bmatrix}\epsilon_{11}\\ \epsilon_{22}\\ \epsilon_{33}\\ 2\epsilon_{23}\\ 2\epsilon_{31}\\ 2\epsilon_{12}\end{bmatrix} + \begin{bmatrix} k_{11} & 0 & 0\\ 0 & k_{22} & 0\\ 0 & 0 & k_{33} \end{bmatrix} \begin{bmatrix}E_1\\ E_2\\ E_3\end{bmatrix}, \tag{6.2}$$

where c_{ij} is the elastic constant, d_{ij} is the piezoelectric constant, and k_{ij} is the dielectric constant. Given $\sigma_{22} = 0$ under a perfect bending condition and $\epsilon_{22} = 0$ due to the symmetric structure, the relation between E_i and ϵ_{ij} can be revealed as:

$$0 = c_{12}\epsilon_{11} + c_{13}\epsilon_{33} - d_{31}E_3. \tag{6.3}$$

Equation (6.2) also gives the relation between D_i and ϵ_{ij}, which results in the transverse piezoelectric effect:

$$D_3 = d_{31}\epsilon_{11} + d_{33}\epsilon_{33} + k_{33}E_3. \tag{6.4}$$

Combining Equation (6.3) and Equation (6.4) yields:

$$\overline{k}E_3 = \overline{d}\epsilon_{11} + D_3, \tag{6.5}$$

where $\overline{k} = k_{33} + d_{33}d_{31}/c_{13}$ and $\overline{d} = d_{33}c_{12}/c_{13} - d_{31}$ and the longitudinal strain ϵ_{11} can be given by[162]:

$$\epsilon_{11} = -w''(x)(h_{PPFE} + h_{PI})/2, \tag{6.6}$$

where $w''(x)$ is the second derivative of buckling amplitude $w(x) = A[1 + cos(2\pi x/L_0)]/2$ and $A = (2/\pi)\sqrt{L_0\Delta L}$ is the maximum buckling amplitude solved by minimization of the total energy[115]. Therefore, ϵ_{11} can be described as:

$$\epsilon_{11} = \frac{2\pi(h_{PPFE} + h_{PI})\sqrt{\Delta L}}{L_0\sqrt{\Delta L}} cos(\frac{2\pi x}{L_0}). \tag{6.7}$$

Considering the PPFE sample is located at the middle of the PI substrate, ϵ_{11} can be approximated by taking the maximum value[163]:

$$\epsilon_{11} \approx \frac{2\pi(h_{PPFE} + h_{PI})\sqrt{\Delta L}}{L_0\sqrt{L_0}}. \tag{6.8}$$

Given that $V_{oc} = E_3 h_{PPFE}$ and $D_3 = 0$ for open circuit voltage V_{oc} measurement, Equation (6.5) yields:

$$V_{oc} = \frac{\overline{d}h_{PPFE}}{\overline{k}}\epsilon_{11} = \frac{2\pi(h_{PPFE} + h_{PI})\overline{d}h_{PPFE}}{\overline{k}L_0\sqrt{L_0}}\sqrt{\Delta L}. \tag{6.9}$$

Equation (6.9) indicates that V_{oc} is proportional to ϵ_{11} and $\sqrt{\Delta L}$.

When measuring the short circuit current, the device is connected to an ammeter and no voltage drop is expected across the instrument. Solving Equation (6.5) for D_3 results in:

$$D_3 = -\overline{d}\epsilon_{11} = -\frac{2\pi\overline{d}(h_{PPFE} + h_{PI})\sqrt{\Delta L}}{L_0\sqrt{L_0}}. \tag{6.10}$$

Therefore, the short circuit current can be determined by $I_{sc} = -S_{PPFE}(\partial D_3/\partial t)$, which can be further expressed as:

$$I_{sc} = \frac{\pi \bar{d} S_{PPFE}(h_{PPFE} + h_{PI})}{L_0\sqrt{L_0}\sqrt{\Delta L}} \frac{d\Delta L}{dt}. \tag{6.11}$$

For the linear axial compression displacement used in this work, ΔL can be expressed as:

$$\Delta L = \begin{cases} vt & \text{if } t < T/2 \\ v(T-t) & \text{if } T/2 < t < T, \end{cases} \tag{6.12}$$

where v is the constant axial compression velocity and T is the time period of a full compressing and releasing cycle. Thus, Equation (6.11) can be rewritten as:

$$I_{sc} = \begin{cases} \frac{\pi \bar{d} S_{PPFE}(h_{PPFE}+h_{PI})\sqrt{v}}{L_0\sqrt{L_0}} t^{-\frac{1}{2}} & \text{if } t < T/2 \\ -\frac{\pi \bar{d} S_{PPFE}(h_{PPFE}+h_{PI})\sqrt{v}}{L_0\sqrt{L_0}} (T-t)^{-\frac{1}{2}} & \text{if } T/2 < t < T. \end{cases} \tag{6.13}$$

It can be seen from Equation (6.13) that the maximum short circuit current I_{sc-max} can be found at $t = 0$ and $t = T$ which leads to an infinite value. However, in real materials, this value is limited to a finite value by the different loss mechanisms within the process, which are partly determined by the material's properties. Nevertheless, it can be deduced from Equation (6.12) and Equation (6.13) that I_{sc-max} is independent of the maximum compression displacement $\Delta L_{max} = vT$. The dependency can be found when the average short circuit current I_{sc-ave} is considered for a given compression stage. Given that I_{sc-ave} can be expressed as:

$$I_{sc-ave} = \frac{\int_0^{\frac{T}{2}} I_{sc} dt}{T/2}. \tag{6.14}$$

The expression of I_{sc-ave} can be found by combining Equation (6.13) and Equation (6.14):

$$I_{sc-ave} = \frac{2\sqrt{2}\pi \bar{d} S_{PPFE}(h_{PPFE} + h_{PI})v}{L_0\sqrt{L_0 \Delta L_{max}}}. \tag{6.15}$$

6.1.2 Voltage Output Under Bending Test

Measuring voltage output V, or open circuit voltage V_{oc} using a voltmeter with small internal resistance is considered. **Figure** 6.1a and b show the schematic configurations for measuring V_{oc} and V, respectively. When measuring V, the voltage reading is given by Ohm's law as $V = I'R$, where R is the internal resistance of the instrument and I', which is the current flowing through R, is also affected by R. In this case, the expression for D_3 shown in Equation (6.5) can be combined with $E_3 h_{PPFE} = V$ to result in:

$$D_3{}' = \frac{\bar{k}}{h_{PPFE}} V - \bar{d}\epsilon_{11}. \tag{6.16}$$

Thus, the current passing through the instrument internal resistance is given by $I' = -S_{PPFE}(\partial D_3{}'/\partial t)$ and the measured voltage V can be determined by solving the following differential equation:

$$\begin{aligned} V &= -\frac{S_{PPFE}\bar{k}R}{h_{PPFE}}\frac{dV}{dt} + S_{PPFE}\bar{d}R\frac{d\epsilon_{11}}{dt} \\ &= -\frac{S_{PPFE}\bar{k}R}{h_{PPFE}}\frac{dV}{dt} + \frac{\pi\bar{d}R\ S_{PPFE}(h_{PPFE} + h_{PI})\sqrt{v}}{L_0\sqrt{L_0 t}}. \end{aligned} \tag{6.17}$$

The maximum instantaneous voltage (V_{max}) can be found at $dV/dt = 0$ and expressed as:

$$V_{max} = \frac{\pi\bar{d}R\ S_{PPFE}(h_{PPFE} + h_{PI})\sqrt{v}}{L_0\sqrt{L_0 t}}. \tag{6.18}$$

When small internal resistance of voltmeter is selected, $R \ll R_{PPFE}$, where R_{PPFE} is the internal resistance of PPFE film, I' can be approximated as $I' \approx I_{sc}$ and Equation (6.17) can be simplified as $V \approx I_{sc}R$. Therefore the voltage measured by a voltmeter with small internal resistance shows similar dynamic behavior as expected from I_{sc}.

6.2 Characterization of Piezoelectricity Under Bending Test

In this section, we focus on the distortion of the macro dipoles and the consequent electric output under a bending operation caused by an axial displacement. As shown in **Figure**

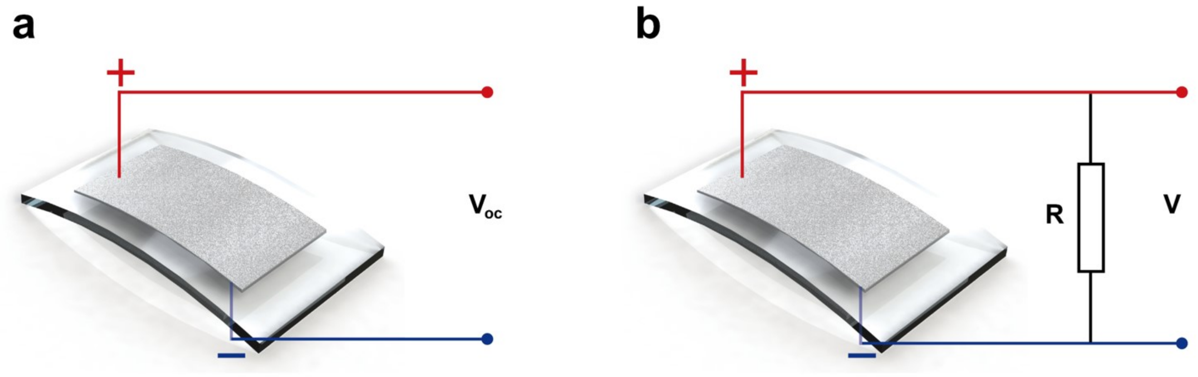

Figure 6.1 Comparison of voltage measurements V_{oc} and V by different instruments. (a) V_{oc} measurement by high impedance voltmeter (Keithley 2450). (b)V measurement by low impedance voltmeter (Keithley 2182), where $R = 10\ M\Omega$ is the instrument's internal resistance.

6.2a, the PPFE film is attached to a flexible PI substrate. In this configuration, the electromechanical response can be described by characterizing the output voltage/current to the generated deflection due to an axial load that results in a buckled bridge shape shown in **Figure** 6.2b. The experiment is assisted by using a computer-controlled stepper motor as the linear actuator to provide the horizontal compressive axial stress that causes axial displacement ΔL and vertical displacement w. In order to compare different electromechanical responses under different bending conditions, ΔL and the compression velocity v were programmed by pulse width modulation (PWM) of DC voltages applied to the motor.

6.2.1 Open Circuit Voltage and Short Circuit Current Under Bending Test

Assuming the initial length of the PI substrate is L_0, the flexible sample buckles into a sinusoidal shape with w described as a function of horizontal axial parameter x as: $w(x) = A[1 + cos(2\pi x/L_0)]/2$, where the origin of x is at the center and A is the maximum buckling amplitude given by $A = (2/\pi)\sqrt{L_0 \Delta L}$[115]. The in-plane x-axial strain (ϵ_{11}) within the PPFE can be estimated by using the curvature of the buckled shape as: $\epsilon_{11} = -w''(x)(h_{PPFE} + h_{PI})/2$, where $w''(x)$ is the bending curvature, h_{PPFE} is the thick-

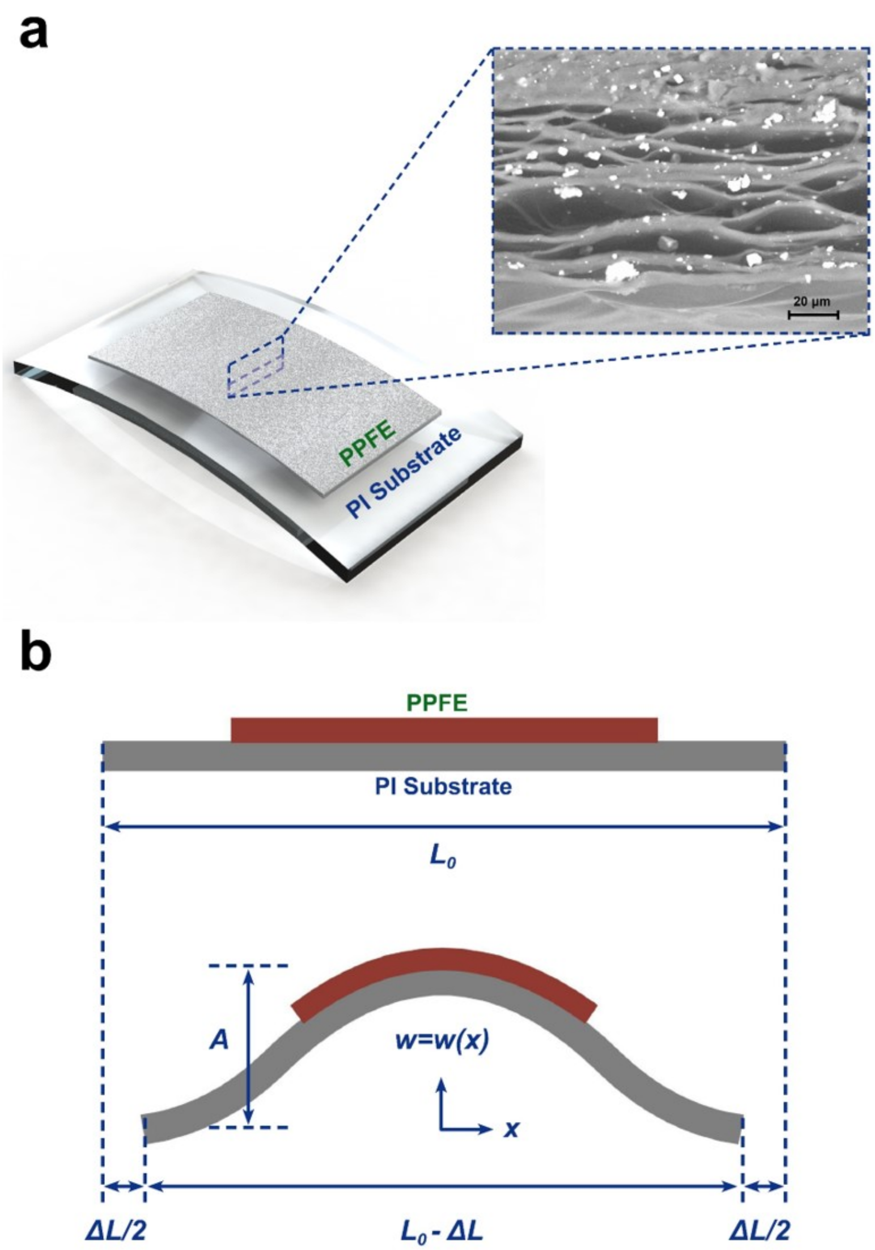

Figure 6.2 Bending configuration of PPFE thin film mounted on the flexible PI substrate. (a) 3D schematic drawing of silver coated PPFE film mounted on a PI substrate, inset shows the SEM image of the cross-sectional view of PPFE film. (b) 2D Schematic diagram of a sinusoidal shape buckling profile under a horizontal axial compression displacement.

ness of PPFE film and h_{PI} is the thickness of the PI substrate. Given that the PPFE film is located at the center of the PI substrate where maximum longitudinal strain occurs, ϵ_{11}

can be approximated as:

$$\epsilon_{11} = \frac{2\pi(h_{PPFE} + h_{PI})\sqrt{\Delta L}}{L_0\sqrt{L_0}}, \tag{6.19}$$

from which we can use the fundamental equations that relate strain to the electric field in piezoelectric materials to obtain:

$$V_{oc} = \frac{2\pi(h_{PPFE} + h_{PI})\overline{d}h_{PPFE}}{\overline{k}L_0\sqrt{L_0}}\sqrt{\Delta L}, \tag{6.20}$$

where $\overline{d} = d_{33}c_{12}/c_{13} - d_{31}$ and $\overline{k} = k_{33} + d_{33}d_{31}/c_{13}$, d_{33}, c_{12}, c_{13}, d_{31} and k_{33} come from piezoelectric matrix and stress/strain transformation matrix. Thus, V_{oc} is proportional to the strain in PPFE film which is exactly the linear coupling relation between mechanical and electrical properties in piezoelectric materials.

However, V_{oc} measurements are often taken by connecting a voltmeter across the open circuit terminals at the output of the device[164]. Therefore, the profile of the measured V_{oc} will be dependent on the instrument's internal resistance; and its proximity to a real open-circuit scenario will increase with this internal resistance value. In this work, a Keithley 2450 is used to measure V_{oc}, which has an internal resistance $\geq$ 10 GΩ. **Figure** 6.3 shows the relation between ΔL, ϵ_{11}, and V_{oc}. The bidirectional linear axial displacement provided by stepper motor as shown in **Figure** 6.3a gives a normalized strain profile determined by Equation (6.19) as shown in **Figure** 6.3b. The measured V_{oc} also shows a similar profile as ϵ_{11} which is also indicated by Equation (6.20). **Figure** 6.3d shows the measured peak value of V_{oc} (scattered points) as a function of different maximum axial displacement ΔL_{max}, and the theoretical curve for these V_{oc} maximum points, taken from evaluating Equation (6.20) at ΔL=ΔL_{max}.

For short circuit current measurements, the device is connected to an ammeter, where the voltage drop across is minimal. This results in a simple linear relation between displacement field D_3 and ϵ_{11}. Given that $I_{sc} = -S_{PPFE}(\partial D_3/\partial t)$, (where I_{sc} is the short circuit current and S_{PPFE} is the area of PPFE film), I_{sc} can be further expressed as:

$$I_{sc} = \frac{\pi\overline{d}S_{PPFE}(h_{PPFE} + h_{PI})}{L_0\sqrt{L_0}\sqrt{\Delta L}}\frac{d\Delta L}{dt}. \tag{6.21}$$

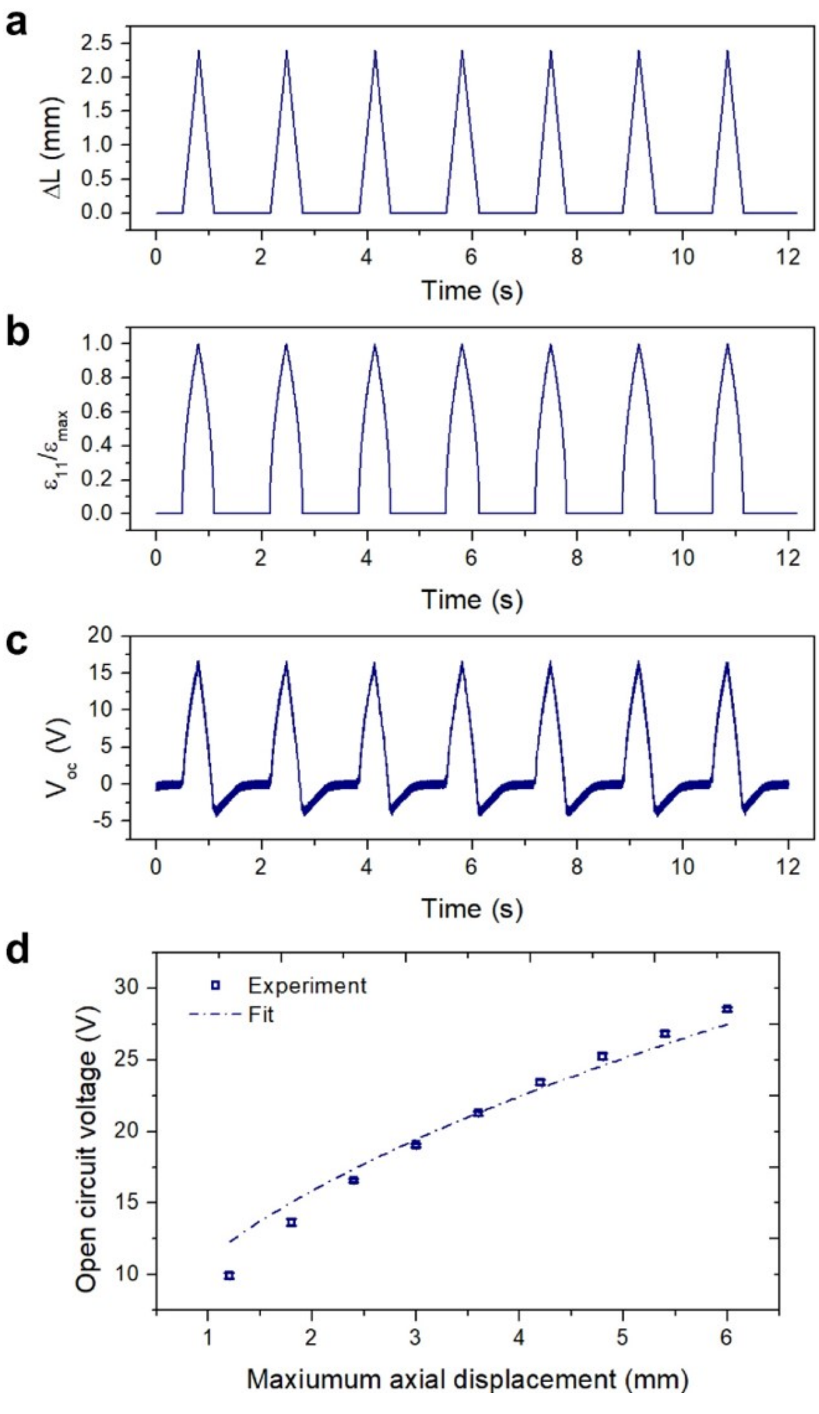

Figure 6.3 Measured electrical response due to axial displacement ΔL and film strain ϵ_{11}. (a) Profile of linear axial compression displacement ΔL as a function of time. (b) Theoretical normalized film strain ϵ_{11} from Eq.(1) as a function of time. (c) Measured V_{oc} as a function of time. (d) Peak V_{oc} value as a function of ΔL_{max} for a given compression velocity of 14 mm/s.

Equation (6.21) shows that I_{sc} is proportional to the changing rate of compressive load ($\frac{d\Delta L}{dt}$), and its magnitude increases with PPFE film area; which can be achieved by stacking multiple layers or connecting them in parallel. For linear axial compression, the compression velocity v (input parameter), is given by:

$$\Delta L = \begin{cases} vt & \text{if } t < T/2 \\ v(T-t) & \text{if } T/2 < t < T, \end{cases} \tag{6.22}$$

where T is the time period for a complete compressing and releasing cycle. Thus, $I_{sc}(t)$ can be determined as:

$$I_{sc}(t) = \frac{\pi \bar{d} S_{PPFE}(h_{PPFE} + h_{PI})\sqrt{v}}{L_0\sqrt{L_0}} t^{-\frac{1}{2}}, \tag{6.23}$$

for the compression stage and its negative value can be used for the releasing stage. Equation (6.23) indicates that the short circuit current increases with increasing v, which is also shown in **Figure** 6.4a-c. The PPFE acts as a current transducer, which translates energy from mechanical to the electrical domain. Therefore, the internal resistance R of the voltage measuring instrument must be taken into consideration. To distinguish the voltage measured by a voltmeter with low input impedance from the V_{oc} measured by an instrument with high input impedance, the symbol V is used for the clarity. In this case, the current flowing through the device-instrument circuit loop is also affected by R through the induction of an electric field. Thus, the measured voltage V can be determined by solving the differential equation. When the internal resistance of the voltmeter is much lower than the impedance of PPFE, V can be approximated to:

$$V \approx I_{sc}R, \tag{6.24}$$

where $R = 10\ M\Omega$ for the voltmeter Keithley 2182A used in this work. Therefore, voltage measurements (**Figure** 6.4d-f) have the same curve profile as I_{sc} (**Figure** 6.4a-c).

The characterization is performed for a PPFE film mounted on a PI substrate under axial stress that generates buckling (and bending), while the current and voltage are measured

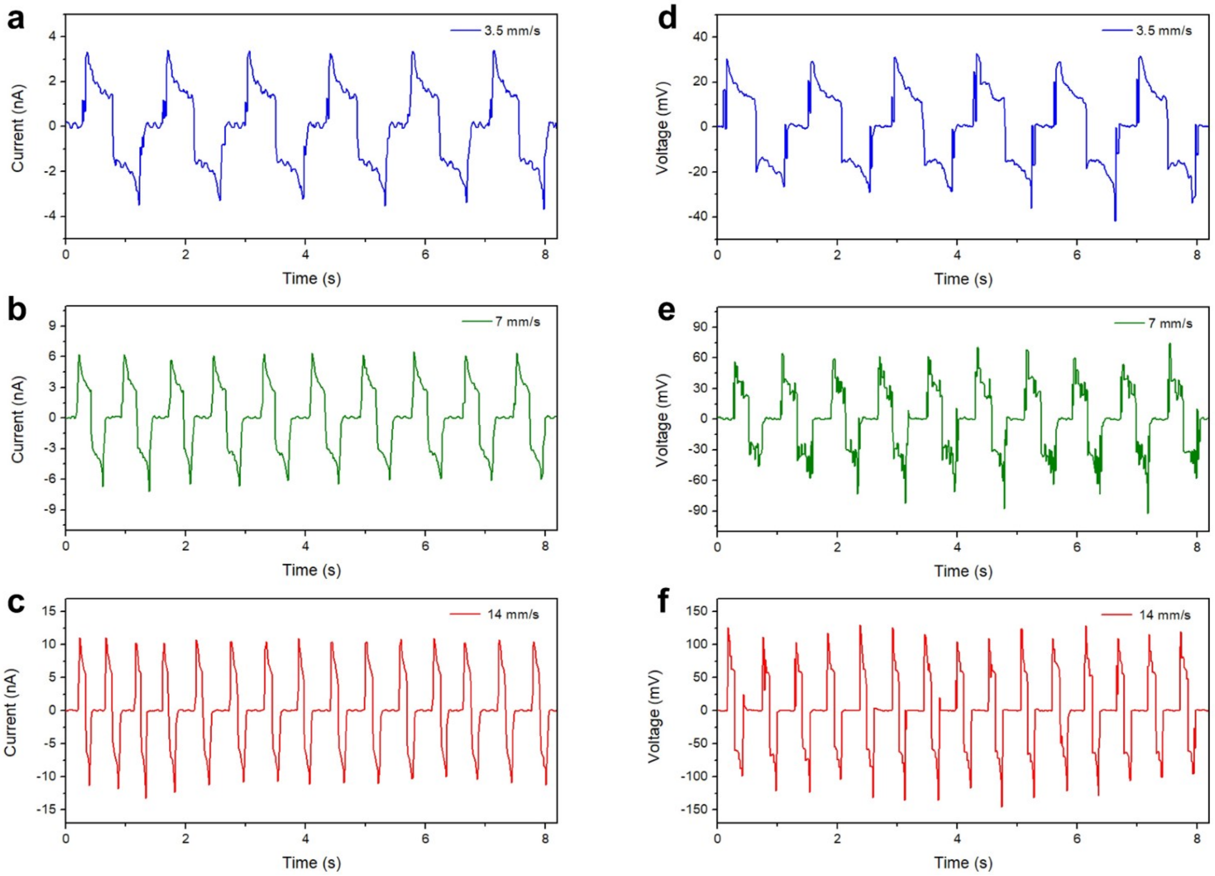

Figure 6.4 Characterization of electrical output under bending test. (a,b,c) Short circuit current I_{sc} under the same $\Delta L_{max} = 3\ mm$ and different v. From top to bottom: 3.5 mm/s, 7mm/s, and 14 mm/s. (d,e,f) Voltage measurement under the same $\Delta L_{max} = 3\ mm$ and different v, from top to bottom: 3.5 mm/s, 7 mm/s, and 14 mm/s.

across the device. The axial compressive displacement is provided by a stepper motor with bi-dimensional displacement. The PPFE used for the bending test is 15 mm wide, 50 mm long, and 80 µm thick. Two 500 nm silver thin films are sputtered on both sides of the PPFE as electrodes. The device is mounted on a 25 mm × 60 mm PI substrate with a thickness of 0.8 mm. The ΔL_{max} and v are programmed and controlled through the FPGA interface. **Figure** 6.4a-c show the measured I_{sc} under different compression velocities with the same maximum compression displacement of 3 mm, which is converted to curvature of 46.8 m^{-1}. As predicted by Equation (6.23), the current output increases with increasing compression velocity. **Figure** 6.4d-f show the measured output voltage V under the same conditions used for measuring I_{sc}. The voltage output follows a similar relation with compression velocity to the one observed in I_{sc} measurements; which agrees with the described theory.

6.2.2 Different Evaluation Methods Under Bending Test

Characterizing self-powered sensors is often done in terms of peak short circuit current (I_{sc-max}) and measured peak voltage (V_{max}) values [162]. However, since I_{sc} is proportional to $t^{-\frac{1}{2}}$, the I_{sc-max} and V_{max} are found at $t = 0$ for any applied axial stress. This means that the largest generated electrical output occurs at the moment an axial displacement begins to occur; and therefore, I_{sc-max} and V_{max} should be independent of the maximum range of axial displacement, ΔL_{max}. This usually goes unnoticed, because for a commonly used bending condition, the ΔL_{max} is always coupled with a faster compression velocity v; e.g. when ΔL_{max} is increased, the compression time period $T/2$ is kept the same, leading to a higher v.

The relation between the maximum instantaneous current and voltage output is further characterized by using different compression velocities and axial displacements (or curvatures). **Figure** 6.5a shows the I_{sc-max} under different axial displacement velocities ranging from 3.5 mm/s to 14 mm/s with different maximum axial displacements from 1.2 mm to 6 mm, which converts to a bending curvature range of 29.6 m^{-1} to 66.2 m^{-1}. No obvious changes in I_{sc} and V_{oc} are observed for different ΔL_{max} under the same compression velocity, indicating that the compression velocity is the dominant factor in determining the peak electrical outputs under the bending operation. An estimation of the peak value can be made from Equation (6.21) by giving a certain small (nonzero) time –usually determined by the instrument's sampling rate– and assuming the traveled distances in this time are comparable for different velocities. Then, the I_{sc-max} can be approximated to be linearly proportional to v, which is also indicated in **Figure** 6.5a.

As indicated by Equation (6.23) and **Figure** 6.5, the I_{sc-max} and V_{max} values are found at the beginning of each compression and releasing cycle, then decaying as a function of $t^{-\frac{1}{2}}$.

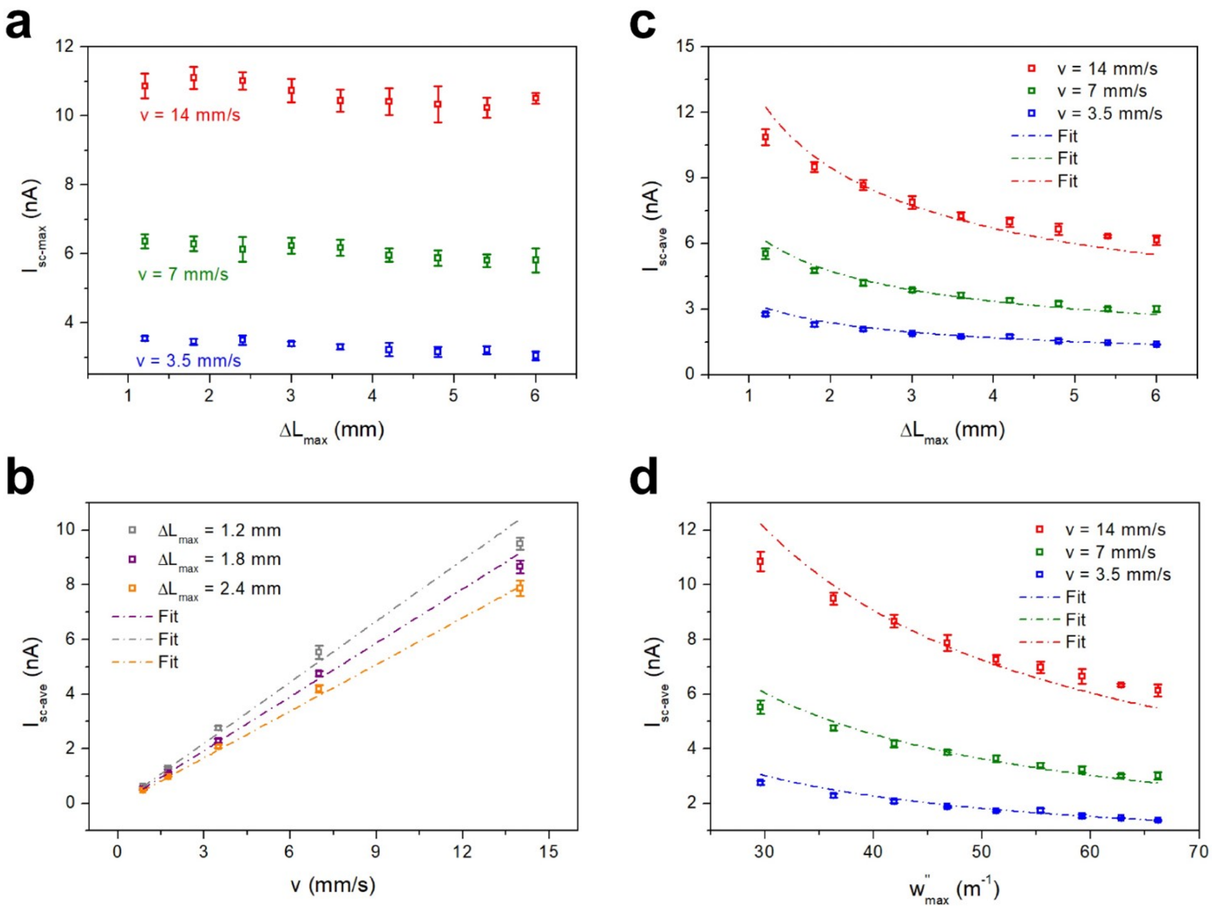

Figure 6.5 Characterization of I_{sc-max} and I_{sc-ave} under bending test. (a) I_{sc-max} as a function of ΔL_{max} under different v. (b) I_{sc-ave} as a function of v under different ΔL_{max}. (c) I_{sc-ave} as a function of ΔL_{max} under different v. (d) I_{sc-ave} as a function of w'' under different v. The fit curves are obtained from Eq.(7) by using proportional constants that best fit the measured data.

For a compression stage, the average current output, I_{sc-ave}, can be calculated by averaging I_{sc} over the compression time period $T/2$, leading to:

$$\begin{aligned} I_{sc-ave} &= \frac{\int_0^{\frac{T}{2}} I_{sc} dt}{T/2} \\ &= \frac{2\sqrt{2}\pi\bar{d}S_{PPFE}(h_{PPFE}+h_{PI})v}{L_0\sqrt{L_0\Delta L_{max}}}. \end{aligned} \tag{6.25}$$

Equation (6.25) gives the relation among I_{sc-ave}, v, and ΔL_{max}. **Figure** 6.5b shows that I_{sc-ave} is linearly proportional to v for each given ΔL_{max}, which is in agreement with the theory. **Figure** 6.5c shows measurements of I_{sc-ave} as a function of ΔL_{max} for different

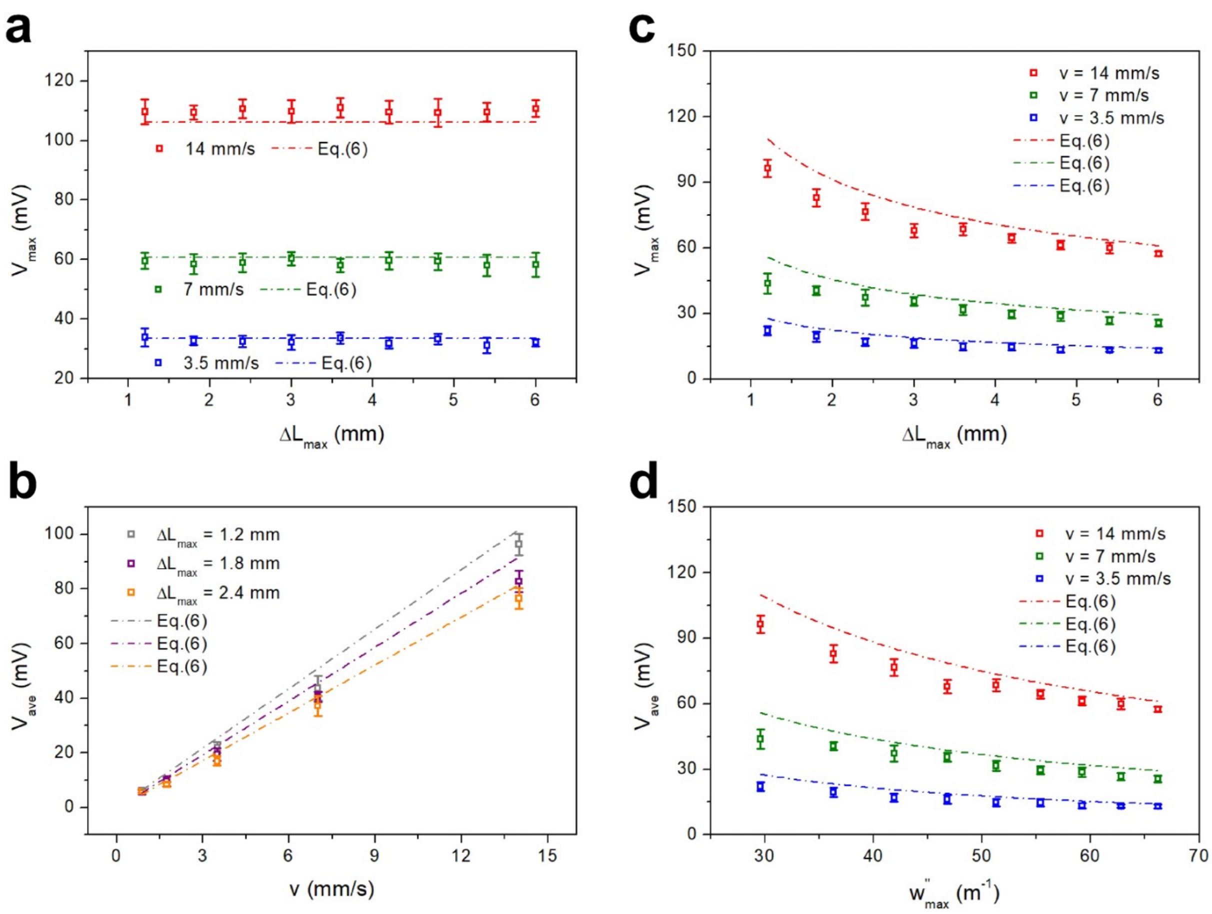

Figure 6.6 Characterization of V_{max} and V_{ave} under bending test. (a) V_{max} as a function of ΔL_{max} under different v. (b) V_{ave} as a function of v under different ΔL_{max}. (c) V_{ave} as a function of ΔL_{max} under different v. (d) V_{ave} as a function of w'' under different v.

values of v, where the data follows the square-root dependence on ΔL_{max} predicted by theory. For real application and bending sensing purposes, it is important to know the relation between the measured electric signal (I_{sc-ave} in this case) and bending curvature. Given that w'' is linearly proportional to ϵ_{11}, which is also linearly proportional to $\sqrt{\Delta L}$, I_{sc-ave} also exhibits an inverse dependence on w'', as shown in **Figure** 6.5d.

Given that most of the data acquisition and readout circuits are designed to respond to voltage signals, it is more desirable to have sensors that generate voltage output signals (instead of current signals). Typical commercial voltmeters have internal resistances between 1 MΩ to 10 MΩ, which are much lower than the impedance of PPFE. Therefore, in the interest of completing a study that makes the proposed bending sensor more compatible with typical measuring instruments, the rest of the work is focused on the measured voltage V, instead of the ideal V_{oc} value. As discussed above, V can be approximated as $I_{sc}R$, and it is expected to exhibit similar dynamic profile as I_{sc}; which is observed experimentally (**Figure** 6.6). It should be noted that V_{oc} (**Figure** 6.3c) shows a different dynamic profile than V (**Figure** 6.4d-f); and the relationship between I_{sc} and V through the instrument's internal resistance ($V = I_{sc}R$) is validated in the experimental results shown in **Figure** 6.5 and **Figure** 6.6.

6.3 Application of PPFE-based Bending Sensor

In this section, a study on the degradation of PPFE films in terms of mechanical robustness, resistance to humidity and thermal stability is performed next. The acquired models discussed above are implemented in an athletic monitoring system, based on the comparison of generated electric waveforms.

6.3.1 Device Robustness

Figure 6.7 shows the performance of PPFE as a function of bending cycles for an axial compression velocity of 14 mm/s and maximum bending curvature of 46.8 m^{-1}. This experiment was carried out using the same setup described for all the previous bending experiments. No significant degradation is observed during the repeated cycling test, indicating the PPFE film as a bending sensor exhibits long term mechanical stability. Wearable sensors can be implemented in systems that allow for the assessment of an athlete's performance in sports. However, there are several factors that can deteriorate the device's reliability. For example, resistance to humidity is a key parameter which could significantly reduce the performance of the sensor, especially for those have the capacitive impedance. Triboelectric sensors with an air gap will experience a change in their performance due to the absorption of the ambient

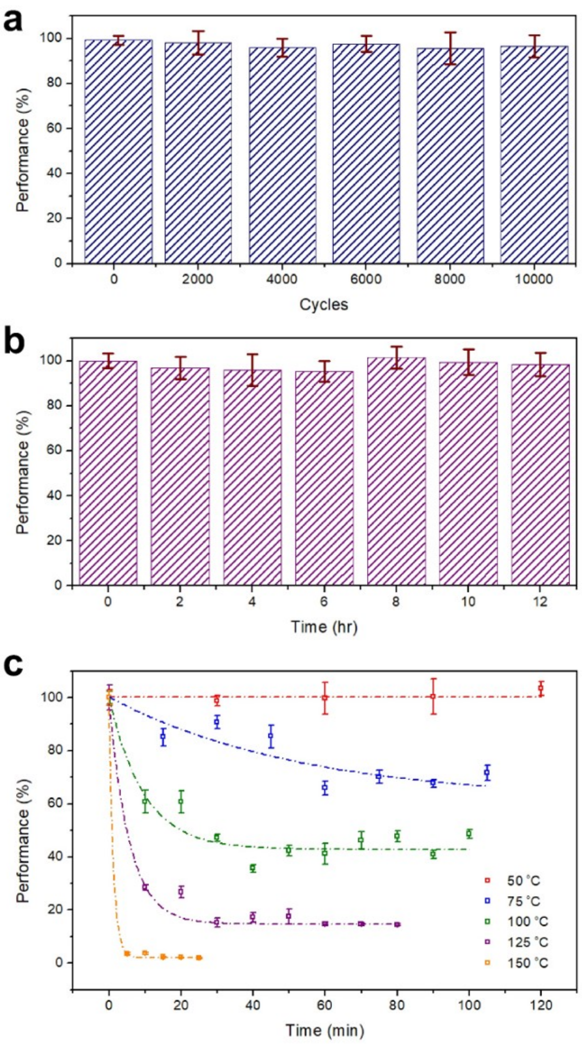

Figure 6.7 Demonstration of performance degradation under different testing conditions. (a) Test of mechanical robustness under repeated bending cycling up to 10000 bending and releasing operation. (b) Test of humidity resistance by immersion into water for up to 12 hours. (c) Test of thermal stability under different baking temperatures.

water and therefore require additional packaging methods[165, 166, 167]. Even tough PPFE has a porous structure, it is sandwiched in between two continuous PPFE films, which prevent the swelling of the voids due to water absorption. Thus, it proves to be water-resistant as demonstrated in **Figure** 6.7b. When using polymer as the base material for piezoelectric applications, the flexibility of the polymer may experience poor thermal stability. **Figure** 6.7c shows the thermal degradation percentage under different baking temperatures as a function of time. No degradation is observed for baking temperature of 50°C. As the temperature increases, the material starts to degrade. When baked at 75°C, no degradation is measured until baking for 60 min, the performance saturates at the level of around 65%. Significant degradation appears at the temperature of 125°C and above. For a short time and low-temperature processes such as encapsulating PPFE into PDMS and PI layers, it is acceptable to sacrifice some of the performance. However, higher temperatures should be avoided, since a temperature of 150°C would destroy the quasi-piezoelectric property of the material due to the collapsing of the voided structure.

6.3.2 Athletic Assessment

Based on the analysis above, it can be seen that V_{max} and V_{ave} exhibit different behaviors under the same bending condition. This suggests that by monitoring these two parameters, information about the bending curvature and speed can be extracted. A potential application for this can be found in monitoring the bending curvature and speed of an athlete's wrist during a baseball throw or a basketball shoot. Hence, this flexible self-powered PPFE bending sensor can be attached to the player's wrist to monitor the posture and movement profile when participating in those sports. In the present application, we suggest a way to compare the bending profile of an athlete with what can be considered an "ideal movement behavior"; perhaps coming from a coach or a database that holds a history of "good throws". **Figure** 6.8a shows a demonstration of throwing a baseball from the player. **Figure** 6.8b and **Figure** 6.8c show the measured voltage waveforms from a coach and the athlete, respectively. By comparing the V_{max} and V_{ave} values obtained by the coach and the athlete, a learning score can be generated from the algorithm described above. This way, the athlete can monitor his/her athletic performance and even have a database with a history of the progress made.

The score used for determining the learner's athletic performance is described below. First, the performance of throwing a baseball is assumed to be equally determined by two factors with the same weights (50%): speed and curvature of wrist bending. As indicated

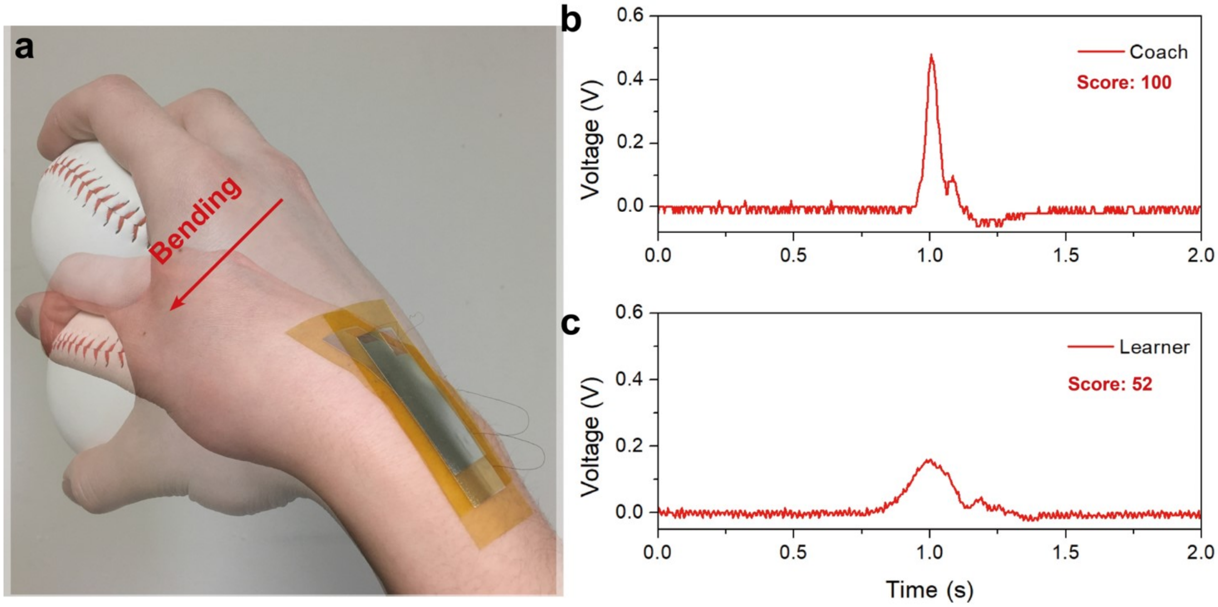

Figure 6.8 Demonstration of application in the athletic assessment. (a) Photography of showing bending of the wrist during throwing a baseball. (b) Voltage output signal from the coach throwing the baseball. (c) Voltage output signal from the learner throwing the baseball.

by Equation (6.21), (6.24), and (6.25), V_{max} is proportional to v and V_{ave} is proportional to $v\Delta L_{max}{}^{-1}$. Therefore, comparing the V_{max} value obtained by the coach with the V_{max} obtained for the learner yields a "performance score" in terms of velocity parameter v. Then, the value of V_{ave} for the coach is compared to the V_{ave} value obtained for the learner. The ratio of these two V_{ave} values is proportional to v and inversely proportional to the bending curvature. Since the comparison for v was obtained from the V_{max} values, the comparison between V_{ave} values can be used to obtain a "performance score" in terms of the radius of curvature. In **Figure** 6.8, the V_{max} is 0.48 V and 0.16 V for the coach and the learner respectively while V_{ave} is 0.167 V and 0.066 V. By defining the score of the coach is 100, the score of the learner is about 52.

6.4 Summary

The porous flexible polypropylene ferroelectret (PPFE) thin film is introduced in this work as a bending sensor. The bending operation is provided by an axial displacement and the bending profile follows the fundamental mechanical analysis. The output of PPFE film in terms of open circuit voltage, short circuit current, and measured voltage is characterized under different bending conditions. Given that the PPFE can be considered as a current source with large internal impedance, its open circuit voltage is heavily dependent on the internal resistance of the voltage measurement instrument. To clarify the bending dependency of an electric output, I_{sc-ave} and V_{ave} are used instead of I_{sc-max} and V_{max}. The average electric output values are found to have a similar behavior due to the approximation under a condition of using low internal resistance voltmeter. Both outputs show linear dependency on v and inverse square-root dependency on ΔL_{max}. The robustness of the material in terms of bending repeatability, resistance to humidity, and thermal stability are also presented for considerations in real applications, such as the sports assessment application demonstrated in this chapter.

CHAPTER 7

FERROELECTRET NANOGENERATORS FOR SELF-POWERING SYSTEMS

Applying flexible materials for energy scavenging from ambient mechanical vibrations is a clean energy solution that can help alleviate electrical power demands in portable devices and wearable electronics. This chapter presents fundamental studies on a flexible ferroelectret polymer with a strong piezoelectric effect and its interface with self-powered and energy storage systems. A single-layered device with a thickness of 80 µm was used for characterizing the device's output voltage, current, transferred charge, and energy conversion efficiency. The potential capability of harvesting mechanical energy and delivering to system load is demonstrated by integrating the device into a fully integrated power management system. The theory for determining the harvested energy that is ultimately delivered to external electronic loads (or stored in a battery) is discussed. The maximum power delivery is found to be for a 600 MΩ load, which results in a device power density of 14.0 Wm^{-3} for input mechanical forces with frequency around 2 Hz[168].

7.1 Power Output of FENG

In the section, we fully describe the corresponding, applicable theory for characterizing the generated and stored power; as well as the system's energy efficiency. The device physics is briefly explained, followed by a study where the effects of the force amplitude and frequency variations in the mechanical input on the generated output are described. Characterization experiments are carried out in terms of open circuit voltage (V_{oc}), short circuit current (I_{sc}) and output charges (Q_{sc}) on a 20 mm × 40 mm single layer device. The maximum power is measured under different loads with various input mechanical forces and the maximum surface energy density is determined.

7.1.1 Materials and Experimental Procedures

The device used in this work is a thin film flexible multilayer structural device with an 80 µm PPFE film sandwiched in between two 500 nm thin film metal electrodes. The device is then encapsulated in between two 20 µm thick PI protective layers. The PPFE film is the active material of the device that contributes to the conversion of mechanical energy to electrical energy, and it consists of continuously distributed ellipsoid air voids, each with two oppositely charged surfaces (see **Figure** 7.1a). Each giant engineered void forms a permanent macro-scale dipole moment and constitutes a polarization field across the PPFE film thickness. When an external mechanical load is applied that generates compression of the film along the thickness direction, the size of the dipoles changes, generating a change in the polarization field and a time-varying electric field. This time-varying electric field (and the generated displacement current) can be applied to an external load by the metal electrodes on each surface of the film. Given the capacitive nature of the material, the accumulated free charges generate an open circuit voltage (V_{oc}) across the film and can be expressed as:

$$V_{oc}(t) = \frac{Q(t)g(t)}{\epsilon A}, \tag{7.1}$$

where Q is the accumulated charge at electrodes, g is the thickness of the PPFE film, ϵ is the dielectric constant of PPFE and A is the contact area of the device. This $V_{oc}(t)$ is the generated electric field to compensate for the change in the polarization field during mechanical pressing. The direct proportionality between $V_{oc}(t)$ and $Q(t)$ indicates that both quantities follow the same dynamic behavior and are in phase –since $g(t)$ and $Q(t)$ are both synchronized with the applied force. Generated charges (i.e. $Q(t)$) can be collected and sent to external circuits or loads. When the external load is a short circuit, the short circuit current (I_{sc}) is given by:

$$I_{sc}(t) = \frac{dQ(t)}{dg}U_{in}, \tag{7.2}$$

where U_{in} is the compression velocity due to mechanical input. It is shown in Equation

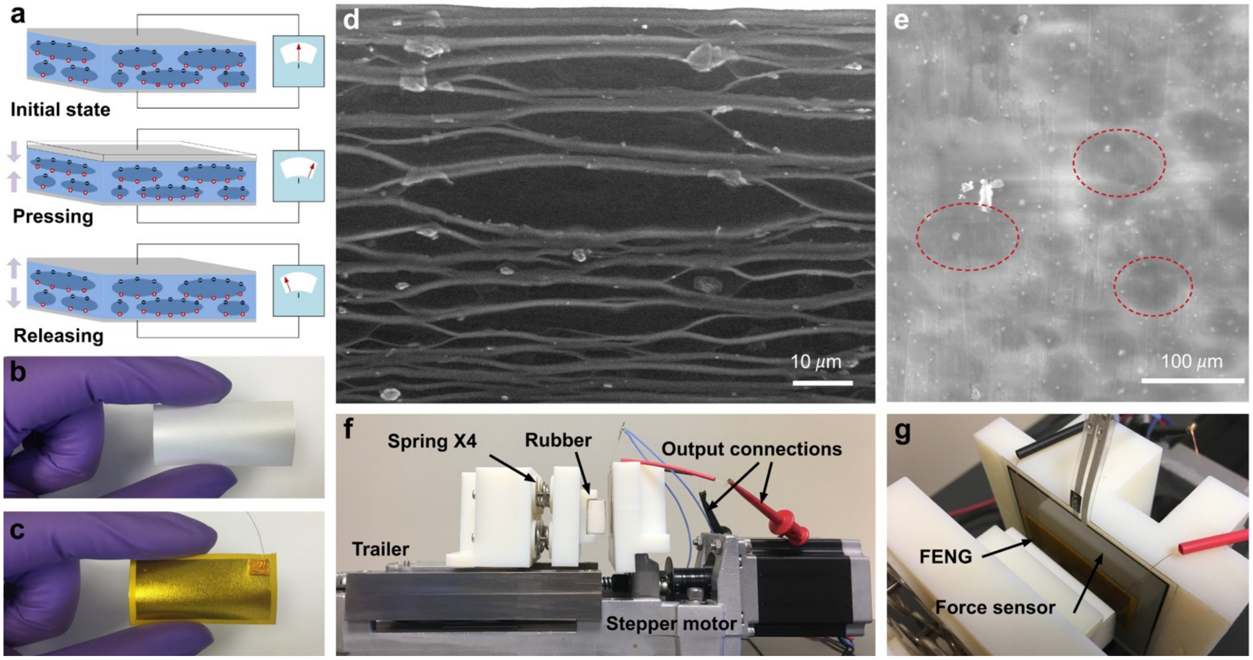

Figure 7.1 (a) Working principle of ferroelectric nanogenerator. (b) Photography of a 20 mm × 40 mm PPFE film. (c) Photography of final device with PI protective layer (20 mm × 40 mm). (d) Cross-section view SEM image of PPFE film with cellular structure. (e) Top-view SEM image (backscattered electrons) of PPFE film, where darker regions are observed where voids are present. (f) Photography of the experimental setup for characterizing the electric output under various mechanical loads. (g) A close-up view of (f).

(7.1) and Equation (7.2) that, although the fundamental operation mechanism is different from piezoelectric materials (piezoelectricity is at the atomic scale, while PPFE films are based on macro-scale dipoles), it still exhibits a piezoelectric electromechanical response - i.e. it generates a voltage signal of increasing magnitude upon compressive mechanical load until maximum compression is achieved; followed by a voltage signal of decreasing magnitude when released. **Figure** 7.1b and **Figure** 7.1c show photographs of a 20 mm × 40 mm PPFE film and a single layer device of the same size with protective polyimide (PI) coatings and connection wires, respectively. **Figure** 7.1d and e provide scanning electron microscopy (SEM) images of PPFE films. Since the inorganic silica stress concentrators (particles in **Figure** 7.1d) are randomly distributed, ellipsoid shape voids with very different sizes are created upon the bidirectional stretching process. The top SEM image shown in **Figure** 7.1e shows darker regions where ellipsoids are present.

The following describes the experiments that were completed to characterize the electrical signals and maximum power output generated by a single-layer device due to mechanical input. As shown in **Figure** 7.1f, a stepper motor is used as a linear actuator, which pushes a rubber piston towards a single layer device (surface area of 20 mm × 40 mm) mounted on the back scaffold. A trailer is used to transfer the rotation of the motor to a linear displacement of the piston and the linear mechanical load is realized by using four mechanical springs connected in parallel. The applied force amplitude and its velocity are computer-controlled by programming the duty cycle and number of pulses applied to the stepper motor. A force sensor (A502, Tekscan, Inc) is placed behind the device to monitor the real time force applied to the device (**Figure** 7.1g shows a close-up view for clarity).

7.1.2 Characterization of Electric Output

For the single-layer device used in this experiment, a linear external mechanical load is applied periodically to the device, where each cycle contains a pressing stage, followed by a releasing stage with a symmetric profile. The electrical outputs in terms of V_{oc}, I_{sc}, and transferred charges Q_{sc} –which in the ideal case would be equal to the accumulated charge at the electrodes [156] are measured and presented in **Figure** 7.2. **Figure** 7.2a shows V_{oc} for a periodic force with the profile shown in **Figure** 7.3a corresponding to F_1. For this cyclic load with peak force of 78 N and frequency of 2 Hz (period of 0.5 s), a single layer device outputs a maximum V_{oc} of around 56 V, given that the root mean square voltage V_{RMS} can be expressed as $V_{RMS}^2 = \frac{1}{T}\int_o^T {V_{oc}}^2(t)dt$, thus V_{RMS} is calculated to be 29 V. It should be noted how the V_{oc} profile follows an increasing/decreasing profile that follows the compression/release profile of the applied force (F_1). This is the expected behavior for linear coupling between mechanical domain and electrical domain of piezoelectric material but is different from the one observed for the same type of device, or in other reports of nanogenerators that operate under similar phenomena based on displacement current. The rationale for these differences lies in the mismatch of the internal impedance of FENG and the voltmeter for V_{oc} measurement. When V_{oc} is being measured, there should be no current flowing through the device-voltmeter circuit loop. V_{oc} should be proportional to the strain (relative change in film thickness), which is also linearly related to the applied mechanical stress. Therefore, profiles for V_{oc} (see **Figure** 7.2a) and force F_1 (**Figure** 7.3a) follow a similar pattern. However, unlike V_{oc}, I_{sc} is originated from the displacement current, which is proportional to the derivative of polarization charge (or accumulated charge Q_{sc}, in this case). Therefore, I_{sc} shows a bipolar square wave profile as the derivative form of a triangular wave. When a voltmeter with much lower internal resistance R, (note that the capacitance of FENG is $\sim$ 17 - 30 pF $\cdot$ cm^{-2}[169]) is connected for obtaining V_{oc}, the measured voltage V is determined by $V = IR$; where I is the non-zero current flowing through the device-voltmeter loop. During each pressing and releasing time period T, the transferred charge can be determined by taking the integral of I_{sc} as $Q(t) = \int_0^T \mid I_{sc}(t) \mid dt$, which is equal to 11.5 nC (see **Figure** 7.2b), which also follows the same profile as V_{oc} and Equation (7.1). However, I_{sc} comes from the change in that charge ($Q(t)$) per unit change in thickness ($g(t)$), and therefore presents a bi-polar profile for every V_{oc} cycle. Instruments with relatively low internal resistance will dissipate the generated displacement current in their internal resistance and display a voltage profile that follows the product of the displacement current and the internal resistance. The profiles for $V_{oc}(t)$ and the applied force F_1 become closer to each other and more synchronized in time as this internal resistance increases[163]. In this case, the device supplies a peak current I_{sc} of 0.1 µA, which corresponds to a root mean square current I_{RMS} of 73 nA. Here, the same method of determining V_{RMS} is used for calculating I_{RMS} by substituting V_{oc} with I_{sc} (see **Figure** 7.2c), with a cyclic profile that crosses $I_{sc} = 0\ nA$ at the time of peak voltage in $V_{oc}(t)$. To increase the output current, the simplest way is to increase the capacitance of the device by increasing the area. This can be easily achieved by folding a larger device multiple times into a smaller size or by stacking the several single-layer devices into a multi-layer structure. **Figure** 7.2d shows the relation between I_{sc} output and stacking layers; where an increasing current peak is found

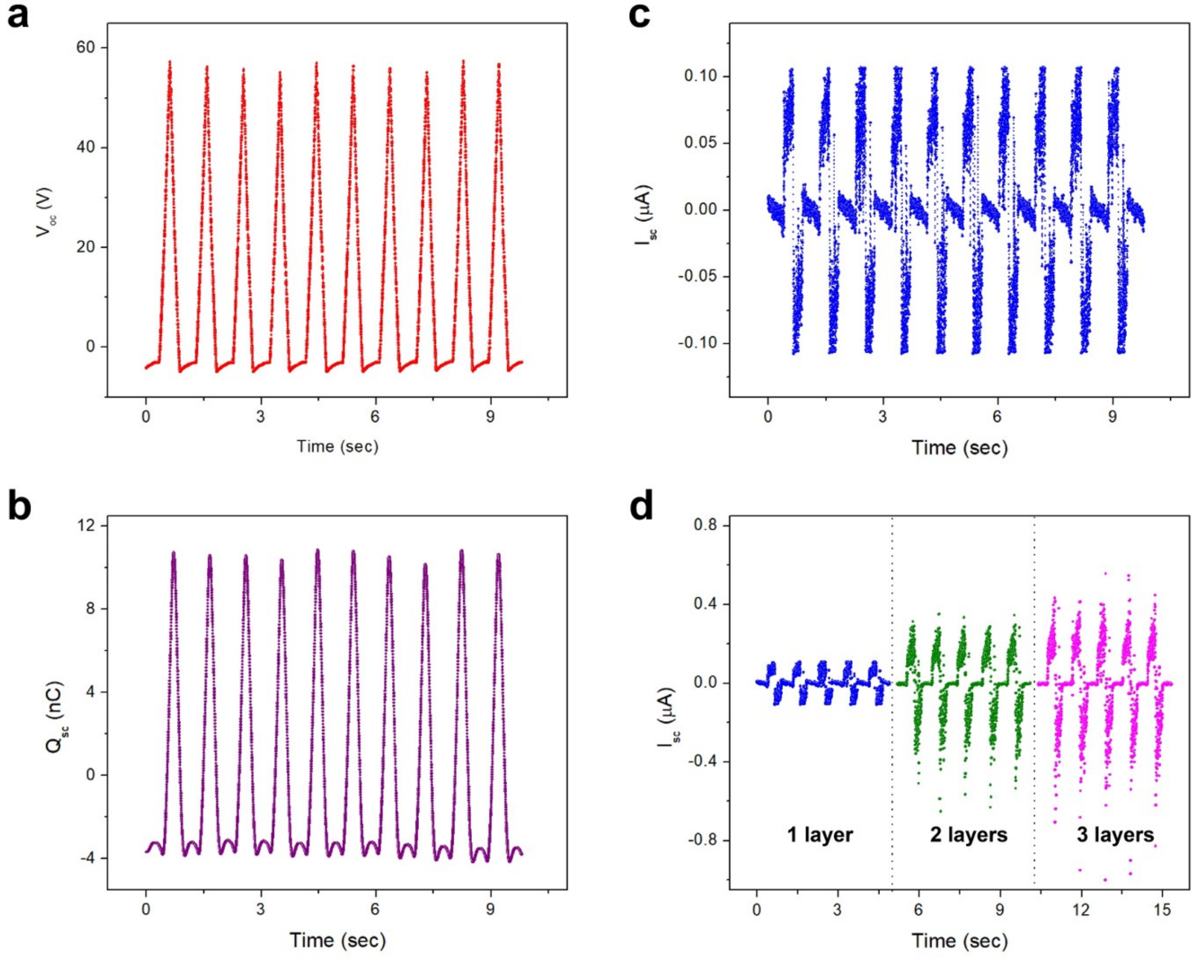

Figure 7.2 Electrical output for single layer device. (a) Experimental measurement of open circuit voltage (V_{oc}). (b) Transferred charge output (Q_{sc}). (c) Experimental measurement of short circuit current (I_{sc}). (d) I_{sc} for multiple-layered devices.

to be proportional to the number of layers.

To obtain optimal power delivery, it is necessary to look at both electric output parameters: voltage and current, produced by mechanical forces with different profiles. For this characterization, linear forces with different amplitudes and velocities are introduced (see **Figure** 7.3a) and the electromechanical responses due to various resistive loads are measured. F_1, F_2, and F_3 have the same pressing and releasing cycle but different force amplitudes: $A_1 > A_2 > A_3$; where A_i is the force amplitude of force F_i. On the other hand, F_4 and F_5 have the same force amplitude as F_1 but longer cycles: $T_5 > T_4 > T_1$, where T_i

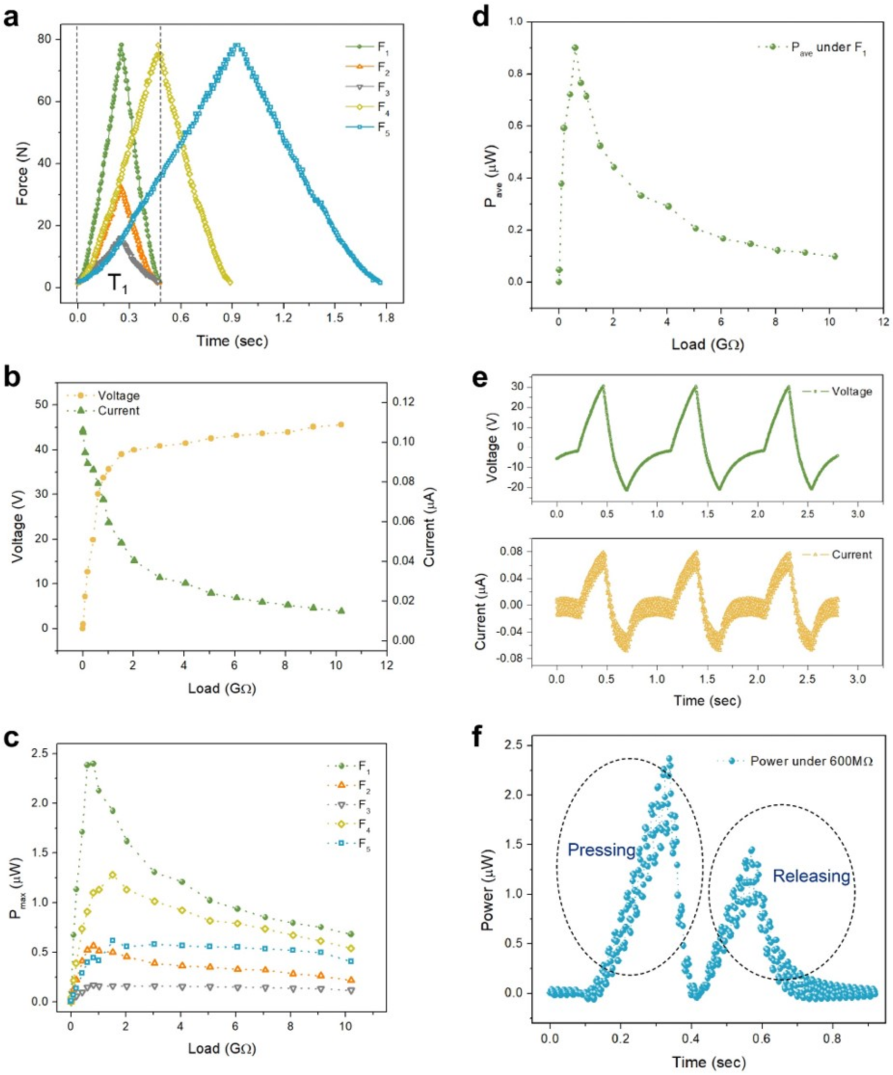

Figure 7.3 Electrical response of single-layer device for different mechanical input. (a) Forces with different amplitudes and velocities used for electromechanical characterization. (b) Voltage and current output with various resistive loads under F_1. (c) The maximum instantaneous power with various loads under different force inputs described in (a). (d) Average power delivery from a single press and release cycle with various loads. (e) Output voltage and current under F_1 with a 600 MΩ load. (f) Output power under F_1 with a 600 MΩ load.

is the duration of a single pressing/releasing cycle of force F_i. Since $V_{oc}(t)$ is proportional to the compression distance and $I_{sc}(t)$ is proportional to the compression velocity, the force with greater amplitude and shorter pressing/releasing cycle should deliver higher voltage and current output, therefore higher power to the external loads.

This would correspond to F_1 from the applied forces (see **Figure** 7.3a). **Figure** 7.3b shows the voltage and current output under F_1, for a wide range of load resistances. The instantaneous peak power delivered to the load is also measured for all forces and plotted as a function of load resistance as shown in **Figure** 7.3c. Table 7.1 summarizes the amplitude and cycle of each force with related output instantaneous peak power. The maximum power delivery is found to be at around 600 MΩ. It is noted that the power output is more sensitive to force amplitude than to speed or frequency. Doubling the force amplitude produces a 4X increase in power output while decreasing the cycle by a half produces a 2X increase in that same parameter. This measurement is in agreement with theory, since increasing the force amplitude has an effect on $V_{oc}(t)$ (force amplitude is directly proportional to $g(t)$) and $I_{sc}(t)$ (force amplitude is directly proportional to the generated displacement current); while the compression/releasing velocity only affects $I_{sc}(t)$ (see Equation (7.1) and Equation (7.2)). Therefore, the device is more suitable for harvesting energy from environments involving large, slow-motion mechanical energy sources, such as human footstep [170], ocean waves [171], and wind blow [172, 173], etc. **Figure** 7.3d shows the average power output delivered by each pressing and releasing cycle with various loads. The maximum average power $P_{ave} = \frac{1}{T}\int_0^T I(t) \cdot V(t)\, dt$ is estimated to be around 0.902 µW with a 600 MΩ load, with a device power density (P_v) of $\sim$ 14.09 Wm^{-3}, for input force F_1, which has a frequency of 2.13 Hz. The voltage and current output for this load are also plotted in **Figure** 7.3e, and the instantaneous power as a function of time during a single cycle is shown in **Figure** 7.3f.

Table 7.1 Power delivery under different loads

Force: F_i	F_1	F_2	F_3	F_4	F_5
Amplitude: $A_i(N)$	78	33	16	78	78
Cycle: $T_i(s)$	0.47	0.47	0.47	0.89	1.76
Peak power: $P_{max}(\mu W)$	2.38	0.56	0.17	1.28	0.61

7.1.3 Energy Conversion Efficiency

This subsection provides a detailed calculation of the energy conversion efficiency. The linear coupling between the mechanical domain and electrical domain considering the full spring-mass-dashpot model can be expressed as the following equation [174]:

$$\begin{pmatrix} \delta V \\ \\ \delta F \end{pmatrix} = \begin{pmatrix} \frac{g}{\epsilon A} & \frac{Q}{\epsilon A} \\ \\ \frac{Q}{\epsilon A} & k \end{pmatrix} \begin{pmatrix} \delta Q \\ \\ \delta g \end{pmatrix}, \tag{7.3}$$

where δV, δF, δQ, and δg represent the variations in output voltage, input force amplitude, output charges, and input compression velocity, respectively. Variable g is the thickness of the PPFE film, ϵ is the dielectric constant, A is the area, and k is the spring constant. By using the Laplace transform, we obtain the expression for δQ and δg as:

$$\delta Q = \int \delta I dt = \frac{\delta I}{s}, \tag{7.4}$$

and

$$\delta g = \int \delta U_{in} dt = \frac{\delta U_{in}}{s}. \tag{7.5}$$

Therefore, we have

$$\delta F = \frac{Q}{s\epsilon A}\delta I + \frac{k}{s}\delta U_{in}, \tag{7.6}$$

and

$$\delta g = \frac{\delta F}{k} - \frac{Q\delta Q}{k\epsilon A}. \tag{7.7}$$

The second term on the right side of Equation (7.7) represents the spring-softening effect due to electrostatic forces generated by the accumulated charges. Considering $Q = 45.5t\ nC$ and $\epsilon = 10 \times 10^{-12} F \cdot\ m^{-1}$ [175], the second term becomes three orders smaller than the first term; which simplifies Equation (7.7) to:

$$\delta F \approx k\delta g, \tag{7.8}$$

which indicates a simple spring model operating in the linear region of the elastic material. Therefore the energy conversion efficiency is defined as:

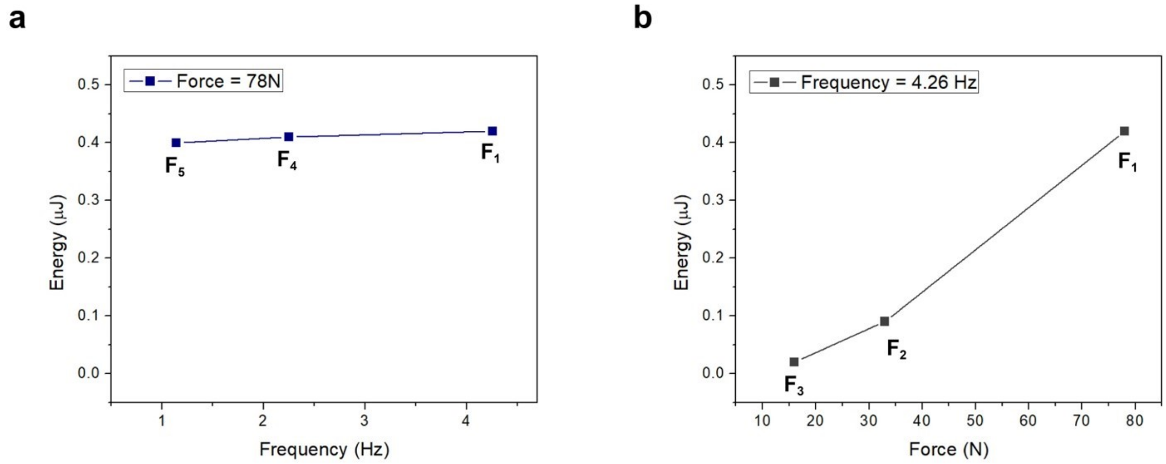

Figure 7.4 Comparison of energy output under different forces. (a) Energy output under forces with same peak amplitude and different frequencies. (b) Energy output under forces with the same frequency and different peak amplitudes.

$$\eta_S = \frac{W_{out}}{W_{in}} = \frac{\int V \cdot I dt}{\frac{1}{2k}[\int F' dt]^2} = 0.14\%. \tag{7.9}$$

It is also necessary to discuss the energy output behavior under forces with different amplitudes and frequencies. Since the output charges are proportional to the change in thickness, the same force amplitude should result in the same energy output. On the other hand, increasing compression velocity (or input mechanical frequency) results in higher output current. **Figure** 7.4 validates this statement by showing the energy output from the forces F_1, F_2, F_3, F_4, and F_5 reported in previous subsections.

7.2 Power Management System

This section introduces a fully integrated power management circuit for energy harvesting devices with ultra-high impedance; which is a major current bottleneck in nanogenerator technologies. With either periodic or random mechanical force input, the circuit can deliver a regulated direct current (DC) power. Finally, the complete system is characterized and integrated into multiple real applications; which include charging a lithium battery; and powering an LCD screen, thermometer, and humidity sensor.

7.2.1 Integrated Energy Harvesting System

The simplest energy harvesting system can be achieved by direct charging[176] through a bridge rectifying diode circuit. However, the unregulated voltage output has been proven to deliver very low efficiencies and will significantly reduce the life-span of a rechargeable battery or electric device which often requires a constant DC input. To effectively harvest the energy from ambient energy sources for consumer electronics, a comprehensive power management system is necessary [177, 178]. To meet the DC power supply requirement of most electronic devices, the AC electric output from piezoelectric material is first converted to DC signal by using a rectifying bridge [179, 180]. Then, a DC-DC buck converter is often used for impedance adaption and voltage regulation [181]. In this work, the comprehensive energy harvesting system uses an energy harvesting module based on a nanopower energy harvesting power supply (LTC3588-1, Linear Technology Corp.) to harvest the mechanical energy as shown in **Figure** 7.5a. The FENG generates random electric pulses that are managed by LTC3588-1 as the first stage, which produces a DC output. As long as a continuous mechanical energy source is present, the harvested and regulated energy can be used to power electronic devices or to charge a rechargeable battery (CBC012, a cutoff voltage of 3 V) for energy storage. Here, we present a method for powering an electronic device, while charging a backup battery by implementing an integrated power management chip (CBC3112) as a second stage. CBC3112 is able to supply a constant DC voltage, typically of 3.3 V, which can be connected to the electronic device to be powered. Meanwhile, it sends any excessive energy to an internal secondary battery (cutoff voltage of 2.75 V) for energy storage. As shown in **Figure** 7.5a, V_{DD} is internally applied to a charge pump V_{CHG}, which contains a flying capacitor C_{FLY} in its voltage doubler circuit for charging the internal integrated backup battery V_{BAT}. When EN terminal asserts high (i.e. when CBC3112 senses a voltage generated by the device), the charge pump is activated and V_{BAT}

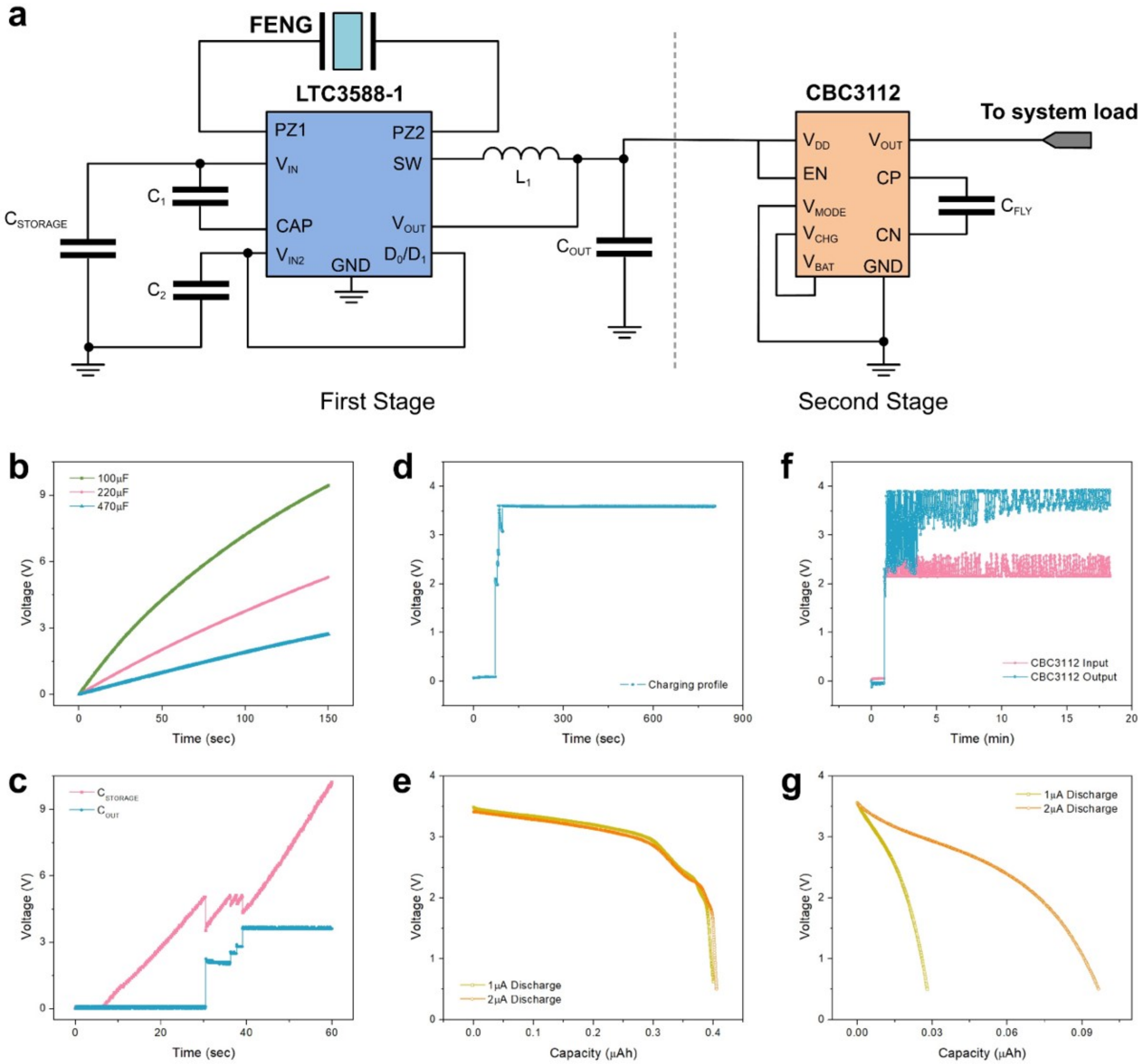

Figure 7.5 Energy harvesting module. (a) A comprehensive energy harvesting system, $C_1 = 1\ \mu F$, $C_2 = 4.7\ \mu F$, $C_{OUT} = 47\ \mu F$, $L_1 = 22\ \mu H$ and $C_{FLY} = 0.1\ \mu F$. (b) Direct charge of capacitors with different capacitances. (c) Voltage regulation of nanopower energy harvesting power supply LTC3588-1. (d) Charging profile of rechargeable solid state battery CBC012. (e) Discharging profile of rechargeable solid state battery CBC012. (f) Voltage regulation of integrated power management chip CBC3112. (g) Discharging profile of integrated energy storage unit in CBC3112.

is being charged by V_{DD}. The output voltage V_{OUT} can either be supplied from V_{DD} or V_{BAT} depending on the switchover voltage threshold determined by V_{MODE}.

Figure 7.5b shows unregulated direct charging profiles for capacitors with different capacitances, where the voltage across the capacitor continuously increases with the charging operation. The voltage output regulation realized by LTC3588-1 is shown in **Figure** 7.5c, where the output voltage is regulated at a constant voltage of 3.6 V. After the system enters the regulation mode, the excessive energy is stored in $C_{STORAGE}$ with increasing voltage measured across the capacitor. By further comparing the voltage drop at $C_{STORAGE}$ and increase in C_{OUT}, the energy transfer efficiency of this energy harvesting module is estimated to be 38.5%. The output DC power can be directly used for powering electronic devices (load) or charging a battery (energy storage). **Figure** 7.5d shows the charging profile of a rechargeable solid-state chip battery CBC012. The battery is being charged at a constant voltage of 3.6 V, and is partially-charged after 15 min of a mechanical force of amplitude 78 N and frequency 4.26 Hz applied to the device. The discharging profile is presented in **Figure** 7.5e to demonstrate the energy stored in the battery. When a second stage power management chip CBC3112 is connected to the output terminal of LTC3588-1, the combined system is able to simultaneously output a constant DC power and transfer the excessive energy from $C_{STORAGE}$ to an embedded integrated battery. **Figure** 7.5f shows the input and output voltage of CBC3112 as a second stage. Since CBC3112 sends part of the energy to the internal battery as energy storage, fluctuations are observed in the voltage, which is not observed when charging battery chip CBC012 as shown in **Figure** 7.5d. **Figure** 7.5g shows the discharging profile of the internal battery. More details on the operation of the energy harvesting module are found in the next subsection.

7.2.2 Operation of Energy Harvesting Module

This subsection provides a brief introduction of the operation mechanism of the energy harvesting module and the energy storage system. The complete two-stage energy harvesting system shown in **Figure** 7.5a contains a first stage energy management module LTC3588-1 and a second stage integrated energy chip CBC3112. The LTC3588-1 chip includes a full-wave rectify bridge in its first stage which converts the AC input voltage from PZ1 and

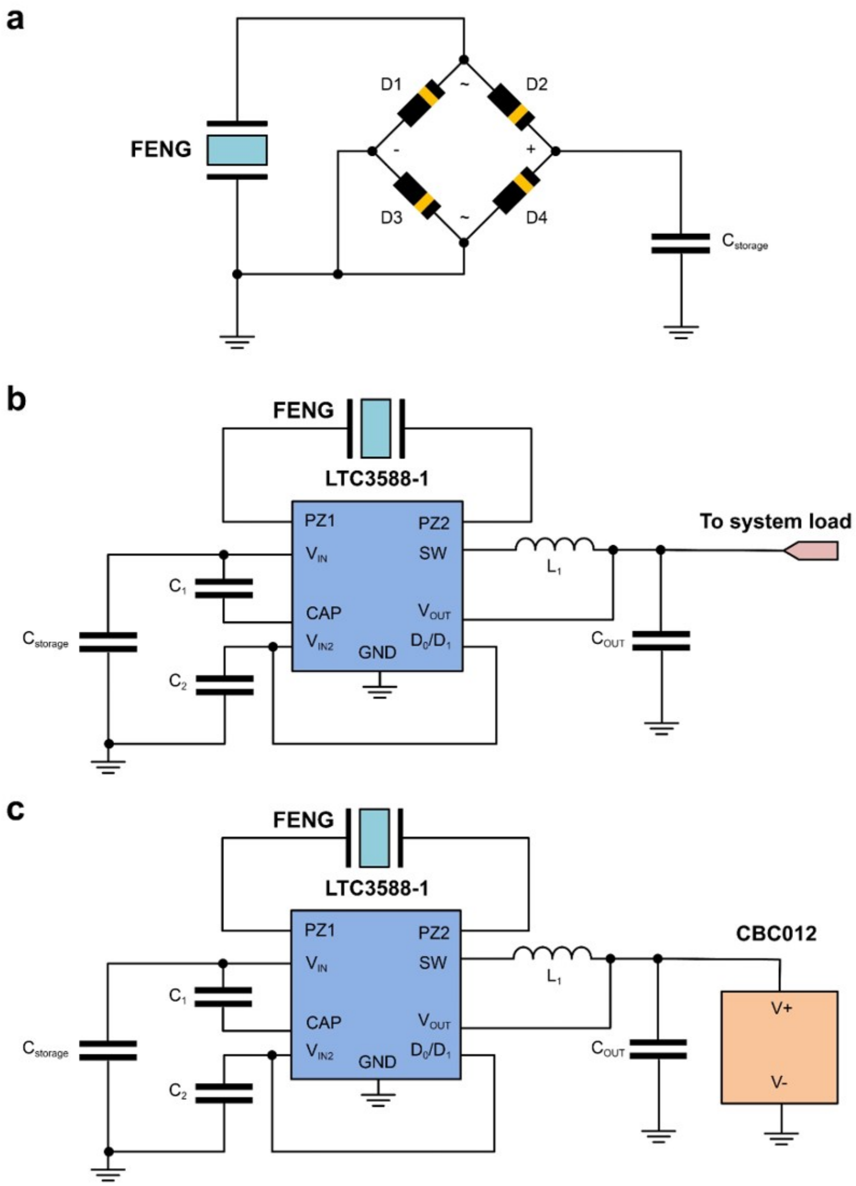

Figure 7.6 Energy harvesting system. (a) Schematic diagram of energy harvesting through direct charge. (b) Schematic diagram of energy harvesting through LTC3588-1 to power electronic device. (c) Schematic diagram of energy harvesting through LTC3588-1 to charge CBC012 rechargeable chip battery.

PZ2 to a DC voltage. Two output voltage selectors D_0 and D_1 are used to program the output voltage V_{OUT} by assigning different combinations of high and low voltages. The harvested energy is first stored in an input capacitor $C_{STORAGE}$ and transferred to the output capacitor C_{OUT} through a buck converter. Two bypass capacitors C_1 and C_2 are connected to terminals V_{IN2} and CAP as energy reservoirs to drive the buck switches. When the voltage across $C_{storage}$ is above the regulation point of around 4.5 V, the buck converter is enabled, and the stored energy is delivered to C_{OUT} through an inductor. To minimize the energy loss in the energy transfer process, the buck converter first ramps the inductor current up to 260 mA through an internal P-MOS switch and then ramps it down to 0 mA through an N-MOS switch. When the voltage across C_{OUT} reaches the setpoint determined by D_0 and D_1, the system is in a regulation mode and the buck converter is forced into a sleep state with the ultra-low quiescent current. In this case, the harvested charges are continuously accumulated in the $C_{STORAGE}$ and the voltage across $C_{STORAGE}$ increases until it reaches the limit.

The second stage CBC3112 chip is able to provide a constant DC output at 3.3 V while charging the internal backup Lithium-ion battery with the excessive energy. A 0.1 µF flying capacitor C_{FLY} is used in the voltage doubler circuit for the charge pump. With the EN pin is asserted high, the charge pump is enabled and the internal energy storage unit is being charged from the power supply (V_{DD}) through the charge pump. V_{OUT} can either be supplied from V_{DD} or internal backup battery V_{BAT}. **Figure** 7.6 shows designs of different energy harvesting systems. **Figure** 7.6a shows the schematic circuit for direct charging, where the AC output signal is converted into a DC signal by a rectifying bridge. The unregulated output pulses cannot be directly supplied to an electronic device or battery and can only be stored in a capacitor. This configuration is also considered as the first stage AC-DC converter in an energy harvesting module. To obtain a regulated constant DC voltage, an integrated system with a buck converter or buck-boost converter is required. **Figure** 7.6b shows the energy harvesting system by only using the first stage LTC3588-1 energy management module. This configuration is able to provide a constant DC output for powering the electronic devices or charging a battery by the regulation of the energy output from $C_{storage}$. Even though the system is able to harvest and store the energy, the long-time energy storage is still limited by the leakage current of the capacitor. Thus, as

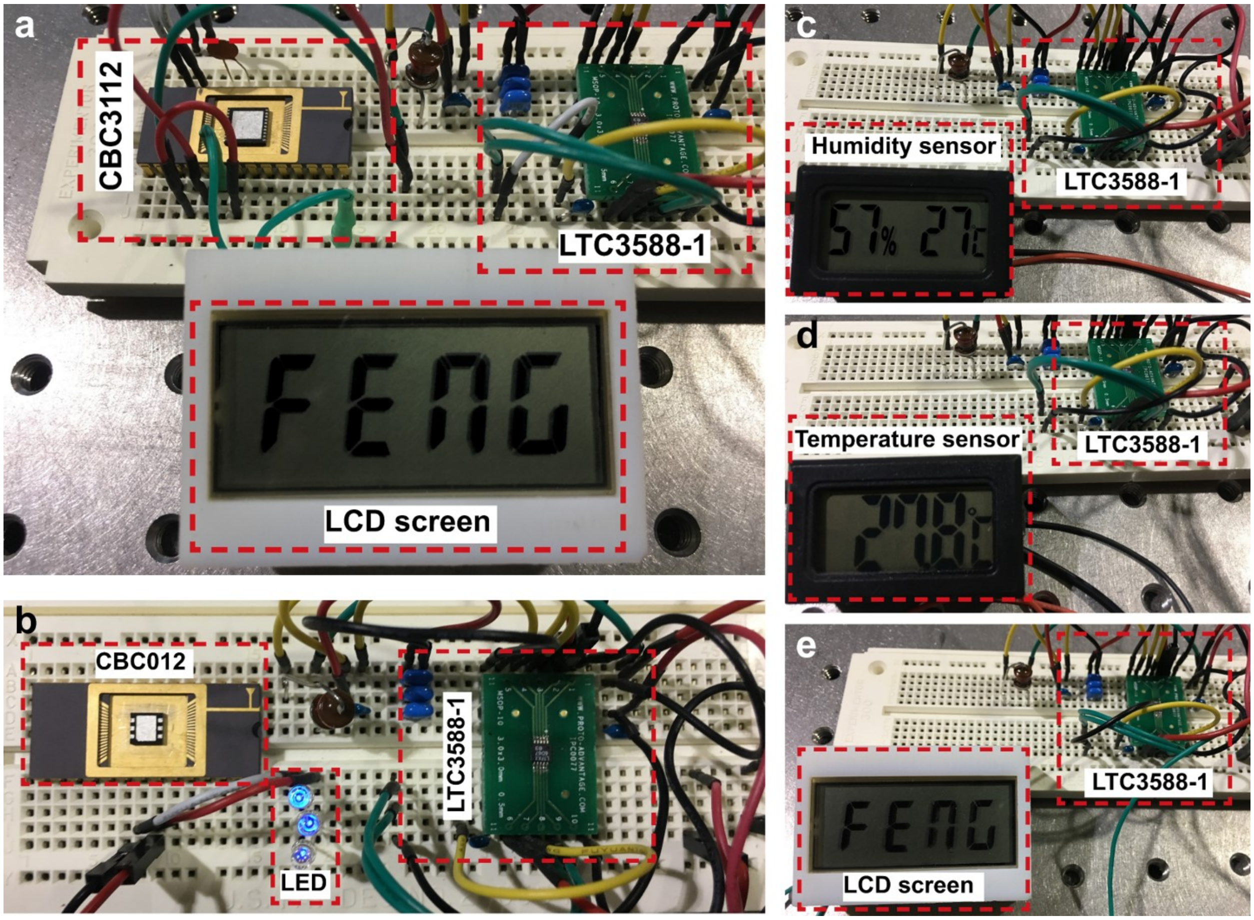

Figure 7.7 Energy harvesting demonstration of powering electronic devices and charging a battery. (a) Powering LCD screen by combing a two-stage energy harvesting system. (b) Charging rechargeable solid-state battery CBC012, the stored energy is used for powering three blue LED lights. (c) Powering humidity sensor by a one-stage energy harvesting system. (d) Powering temperature sensor by a one-stage energy harvesting system. (e) Powering LCD screen by a one-stage energy harvesting system.

shown in **Figure** 7.6c, a rechargeable lithium-ion chip battery is connected to the output terminal of LTC3588-1, which can be used for energy storage.

7.2.3 Demonstration of Powering Commercial Electronics

By utilizing ambient mechanical energy, electronic devices can be powered solely by the energy harvesting modules like the ones described earlier. **Figure** 7.7a shows the demonstration of powering a commercial 3V LCD screen by combining an 8-layer FENG device with a two-stage energy harvesting system. This system is capable of delivering a constant DC power while storing the excessive energy to an integrated chip battery. During the normal operation, the word ”FENG” is displayed on the screen, while storing the energy shown in **Figure** 7.5g. **Figure** 7.7b shows the implementation of the energy harvesting system (one-stage) for the application of charging a rechargeable solid-state battery. The charged battery is used to power three LED lights. **Figure** 7.7c and **Figure** 7.7d demonstrate utilizing harvested energy to power commercial 1.8 V humidity sensor and temperature sensor, respectively. The same LCD screen which is shown in **Figure** 7.7a can also be self-powered by this one-stage energy harvesting module as shown in **Figure** 7.7e.

7.3 Summary

In summary, this chapter shows a comprehensive approach that describes the use of PPFE films as nanogenerators and their integration into systems that can convert mechanical energy to electrical energy for either energy storage or powering of electronic devices. The generated electric output and its dynamic behavior is characterized in terms of open circuit voltage, short circuit current, transferred charge, the efficiency of the complete system and delivered power. The output current and voltage are found to be related to the input mechanical loads and velocities. Various resistive loads have been used to find the maximum power output, which is around 0.902 µW under a linear F_1 with 600 MΩ. Therefore the energy conversion efficiency is calculated to be 0.14% for the performed experiment. To effectively harvest the energy from ambient mechanical sources, a comprehensive energy harvesting module with a corresponding power management circuitry has been proposed; which can be used for powering electronic devices, charging a solid-state chip battery, or both.

CHAPTER 8

SUMMARY

8.1 Summary of Contributions

In this work, VO_2 thin films are combined with polypropylene ferroelectret films to develop self-powered tunable cantilever and bridge MEMS resonator devices. The phase change across the VO_2 thin film is responsible for the frequency tuning capability, while the piezoelectric properties of the PPFE film (with a strong piezoelectric coefficient of $\sim$ 300 pC/N) enables self-powering. The analysis of the film residual thermal stress is performed in order to explain the different buckling orientations and amplitudes in bridge structures. FEM simulations are carried out for the first mode natural resonant frequencies estimation, taking into consideration the residual thermal stress. Bridge and cantilever resonators with various aspect ratios are used to study the influence of VO_2 thin coatings on resonant frequency shifts. It is found that the cantilever structure presents a smaller relative frequency change ($\sim$ 7%), dominated by geometric modifications during actuation, and the change is independent of the beam length. On the other hand, due to a large residual axial stress, bridge resonators exhibit a structure-dependent relative frequency shift with a significantly larger tuning range of up to 37%. The resonant frequency tuning was demonstrated on three bridge resonators with different buckling states. Peltier and Joule heating are used as actuation methods, and the results are compared. A bi-directional tuning behavior is observed in the Peltier heating method for all three bridges while the same monotonic change in frequency is shown when Joule heating is used. This phenomenon is attributed to a transition in the boundary condition, which only occurs when substrate heating is used. Besides the studies on frequency tunability, resonant frequency programmability is also demonstrated in both structures. Here, FENG is introduced as a transducer to provide the programming current pulse. In order to effectively program a frequency state, the device power consumption and time constant are determined first by using the PWM method. Experimental results reveal that sending a short current pulse with a much higher amplitude could reduce the power consumption from mW to µW range. This demonstrates the potential application of integrated VO_2-based resonators and FENG devices into HITS systems. A prototype of VO_2-based MEMS bandpass filter is demonstrated by exciting and measuring two identical on-chip resonators. The bandwidth can be extended to 2.62X by using two bridges or 2.39X by one pair of cantilevers.

Further studies were designed to demonstrate self-powering, sensing, and energy harvesting capabilities of FENG. The electromechanical response is first characterized by applying a periodic external mechanical input. Electric output in terms of open circuit voltage, short circuit current, and transfer charges are analyzed; and the electromechanical coupling is described. The discrepancies in voltage measurements caused by different instruments' internal resistance are discussed in detail and a lumped parameter model has been proposed to explain the mismatch at the device-machine interface. The lumped model is validated with experimental data for both dynamic and static electromechanical responses. A design platform for implementing FENG-based devices into self-powered tactile systems and a human-controlled micro-robotic controller has been demonstrated. Furthermore, based on the excellent flexibility of PPFE, a FENG-based bending sensor is also developed using the large transverse piezoelectric effect. The electromechanical responses are well characterized and predicted by the constitutive equations. Extra attention has been paid to the evaluation methods where the average value of voltage reveals a correlation between both the bending velocity and the bending curvature while the peak value is only related to the velocity. The robustness of the device is also demonstrated in terms of thermal stability, humidity resistance, and mechanical repeatability. In the last chapter, a complete energy harvesting system is developed by integrating FENG with a power management circuit. The system is capable of effectively converting random ambient mechanical energy to regulated

DC electrical power with an efficiency of ~ 38%. The developed technology is able to power commercially available electronic devices or charge a lithium-ion battery.

8.2 List of Problems Solved in This Thesis

This work addresses the following:

1. Designed and fabricated VO_2-based MEMS resonators with fully integrated metal heaters. Different structures including clamped-clamped and clamped-free beams have been developed and the first mode resonant frequencies are estimated by FEM simulation.

2. Developed ferroelectret nanogenerators based on flexible polypropylene ferroelectret polymer films with a high d_{33} value of ~ 300 pC/N.

3. Performed Characterizations of VO_2-based tunable MEMS resonators, demonstrated resonant frequency tunability as high as 37.2%, studied the influence of VO_2 coatings on different structures with various aspect ratios.

4. Studied the buckling effect of VO_2-based bridge resonators, analyzed the effect of buckling directions and amplitudes on the resonant frequency tunability.

5. Studied the influence of applying different electro-thermal actuation methods on pre-buckled bridge resonators. Explained the bi-directional tunability observed in the substrate heating.

6. Studied the power consumption of programming resonant frequency status in VO_2--based MEMS resonators, developed a new type of HITS by combining VO_2-based resonators with FENG.

7. Proposed the prototype of VO_2-based tunable MEMS bandpass filters with off-chip connection configuration, demonstrated $\sim 7.3\%$ tunability of the central frequency and $\sim 262\%$ tunability of the bandwidth.
8. Designed, fabricated FENG-based self-powered flexible sensors with a pixelated configuration, the sensor is able to map the force distribution of an impact.
9. Studied the influence of measuring instruments on the electric output of FENG, modeled the material as a second-order system and explained the measuring discrepancies with different instruments.
10. Demonstrated FENG as bending strain gauges, characterized electric output under different bending conditions, validated the device robustness in terms of thermal stability, humidity resistance and mechanical repeatability.
11. Designed and developed a power management system for converting random AC electric current from nanogenerator to regulated DC voltage, the system has an energy delivery efficiency of $\sim 38\%$ and is able to effectively charge a rechargeable Lithium-ion battery.

BIBLIOGRAPHY

BIBLIOGRAPHY

[1] Y. Cao, D. Torres, T. Wang, and N. Sepúlveda, "Influence of vo$_2$ thin film coatings on the performance of integrated mems bridges and cantilevers," in *ASME 2016 Conference on Smart Materials, Adaptive Structures and Intelligent Systems*, pp. V001T02A010–V001T02A010, American Society of Mechanical Engineers, 2016.

[2] F. Morin, "Oxides which show a metal-to-insulator transition at the neel temperature," *Physical review letters*, vol. 3, no. 1, p. 34, 1959.

[3] Y. Wu, L. Fan, W. Huang, S. Chen, S. Chen, F. Chen, C. Zou, and Z. Wu, "Depressed transition temperature of $W_xV_{1\text{-}x}O_2$: mechanistic insights from the x-ray absorption fine structure (xafs) spectroscopy," *Physical Chemistry Chemical Physics*, vol. 16, no. 33, pp. 17705–17714, 2014.

[4] A. Zylbersztejn and N. F. Mott, "Metal-insulator transition in vanadium dioxide," *Physical Review B*, vol. 11, no. 11, p. 4383, 1975.

[5] M. M. Qazilbash, Z. Li, V. Podzorov, M. Brehm, F. Keilmann, B. Chae, H.-T. Kim, and D. Basov, "Electrostatic modification of infrared response in gated structures based on vo$_2$," *Applied Physics Letters*, vol. 92, no. 24, p. 241906, 2008.

[6] S. Lysenko, A. Rua, V. Vikhnin, J. Jimenez, F. Fernandez, and H. Liu, "Light-induced ultrafast phase transitions in vo$_2$ thin film," *Applied Surface Science*, vol. 252, no. 15, pp. 5512–5515, 2006.

[7] K. Abbas, J. Hwang, G. Bae, H. Choi, and D. J. Kang, "Control of multilevel resistance in vanadium dioxide by electric field using hybrid dielectrics," *ACS applied materials & interfaces*, vol. 9, no. 15, pp. 13571–13576, 2017.

[8] J. Figueroa, Y. Cao, T. Wang, D. Torres, and N. Sepúlveda, "Programming emissivity on fully integrated vo2 windows," 2018.

[9] J. Figueroa, Y. Cao, H. Dsouza, J. Pastrana, and N. Sepúlveda, "A simplified approach for obtaining optical properties of vo$_2$ thin films, and demonstration of infrared shape-shifting devices," *Advanced Materials Technologies*, p. 1800599, 2019.

[10] K. J. Miller, K. A. Hallman, R. F. Haglund, and S. M. Weiss, "Silicon waveguide optical switch with embedded phase change material," *Optics express*, vol. 25, no. 22, pp. 26527–26536, 2017.

[11] D. Torres, J. Zhang, S. Dooley, X. Tan, and N. Sepúlveda, "Hysteresis-based mechanical state programming of mems mirrors," *Journal of Microelectromechanical Systems*, vol. 27, no. 2, pp. 344–354, 2018.

[12] D. Torres, T. Wang, J. Zhang, X. Zhang, S. Dooley, X. Tan, H. Xie, and N. Sepúlveda, "Vo_2-based mems mirrors," *Journal of Microelectromechanical Systems*, vol. 25, no. 4, pp. 780–787, 2016.

[13] S. Wang, L. Kang, and D. H. Werner, "Hybrid resonators and highly tunable terahertz metamaterials enabled by vanadium dioxide (vo_2)," *Scientific reports*, vol. 7, no. 1, p. 4326, 2017.

[14] Y. Fan, Y. Qian, S. Yin, D. Li, M. Jiang, X. Lin, and F. Hu, "Multi-band tunable terahertz bandpass filter based on vanadium dioxide hybrid metamaterial," *Materials Research Express*, vol. 6, no. 5, p. 055809, 2019.

[15] A. Rua, F. E. Fernandez, and N. Sepulveda, "Bending in vo_2-coated microcantilevers suitable for thermally activated actuators," *Journal of Applied Physics*, vol. 107, no. 7, p. 074506, 2010.

[16] J. Cao, W. Fan, Q. Zhou, E. Sheu, A. Liu, C. Barrett, and J. Wu, "Colossal thermal-mechanical actuation via phase transition in single-crystal vo_2 microcantilevers," *Journal of Applied Physics*, vol. 108, no. 8, p. 083538, 2010.

[17] T. Huffman, C. Hendriks, E. Walter, J. Yoon, H. Ju, R. Smith, G. Carr, H. Krakauer, and M. Qazilbash, "Insulating phases of vanadium dioxide are mott-hubbard insulators," *Physical Review B*, vol. 95, no. 7, p. 075125, 2017.

[18] Y. Cao, D. Torres, T. Wang, X. Tan, and N. Sepúlveda, "Enabling tunable micromechanical bandpass filters through phase-change materials," *Smart Materials and Structures*, vol. 26, no. 8, p. 085032, 2017.

[19] T. Driscoll, H.-T. Kim, B.-G. Chae, B.-J. Kim, Y.-W. Lee, N. M. Jokerst, S. Palit, D. R. Smith, M. Di Ventra, and D. N. Basov, "Memory metamaterials," *Science*, vol. 325, no. 5947, pp. 1518–1521, 2009.

[20] Y. Cao, W. Li, J. Figueroa, T. Wang, D. Torres, C. Wang, Z. L. Wang, and N. Sepúlveda, "Impact-activated programming of electro-mechanical resonators through ferroelectret nanogenerator (feng) and vanadium dioxide," *Nano energy*, vol. 43, pp. 278–284, 2018.

[21] E. Merced, R. Cabrera, N. Dávila, F. E. Fernández, and N. Sepúlveda, "A micromechanical resonator with programmable frequency capability," *Smart Materials and Structures*, vol. 21, no. 3, p. 035007, 2012.

[22] E. Sazonov, V. Krishnamurthy, and R. Schilling, "Wireless intelligent sensor and actuator network-a scalable platform for time-synchronous applications of structural health monitoring," *Structural Health Monitoring*, vol. 9, no. 5, pp. 465–476, 2010.

[23] W.-T. Hsu, "Recent progress in silicon mems oscillators," tech. rep., DISCERA INC ANN ARBOR MI, 2008.

[24] Y. Yang, C. Callegari, X. Feng, K. Ekinci, and M. Roukes, “Zeptogram-scale nanomechanical mass sensing,” *Nano letters*, vol. 6, no. 4, pp. 583–586, 2006.

[25] Q. Ma, T. Rossmann, and Z. Guo, “Temperature sensitivity of silica micro-resonators,” *Journal of Physics D: Applied Physics*, vol. 41, no. 24, p. 245111, 2008.

[26] C. T.-C. Nguyen, “Mems technology for timing and frequency control,” *IEEE transactions on ultrasonics, ferroelectrics, and frequency control*, vol. 54, no. 2, 2007.

[27] J. Lee and Y. Kwak, “5g standard development: technology and roadmap,” *Signal Processing for 5G*, 2016.

[28] H. C. Kim and K. Chun, “Rf mems technology,” *IEEJ Transactions on Electrical and Electronic Engineering*, vol. 2, no. 3, pp. 249–261, 2007.

[29] A. Partridge, H.-C. Lee, P. Hagelin, and V. Menon, “We know that mems is replacing quartz. but why? and why now?,” in *2013 Joint European Frequency and Time Forum & International Frequency Control Symposium (EFTF/IFC)*, pp. 411–416, IEEE, 2013.

[30] M. G. Pecht, R. Agarwal, and D. Quearry, “Plastic packaged microcircuits: Quality, reliability, and cost issues,” *IEEE transactions on reliability*, vol. 42, no. 4, pp. 513–517, 1993.

[31] C. Zuo, N. Sinha, and G. Piazza, “Very high frequency channel-select mems filters based on self-coupled piezoelectric aln contour-mode resonators,” *Sensors and Actuators A: Physical*, vol. 160, no. 1-2, pp. 132–140, 2010.

[32] Z. Feng, W. Zhang, B. Su, K. F. Harsh, K. Gupta, V. Bright, and Y. Lee, “Design and modeling of rf mems tunable capacitors using electro-thermal actuators,” in *1999 IEEE MTT-S International Microwave Symposium Digest (Cat. No. 99CH36282)*, vol. 4, pp. 1507–1510, IEEE, 1999.

[33] T. G. Thundat, E. A. Wachter, and J. K. Davis, “Electrostatically tunable resonance frequency beam utilizing a stress-sensitive film,” July 24 2001. US Patent 6,263,736.

[34] D. Joachim and L. Lin, “Selective polysilicon deposition for frequency tuning of mems resonators,” in *Technical Digest. MEMS 2002 IEEE International Conference. Fifteenth IEEE International Conference on Micro Electro Mechanical Systems (Cat. No. 02CH37266)*, pp. 727–730, IEEE, 2002.

[35] M. Chiao and L. Lin, “Post-packaging frequency tuning of microresonators by pulsed laser deposition,” *Journal of Micromechanics and Microengineering*, vol. 14, no. 12, p. 1742, 2004.

[36] R. Syms and D. Moore, “Focused ion beam tuning of in-plane vibrating micromechanical resonators,” *Electronics Letters*, vol. 35, no. 15, pp. 1277–1278, 1999.

[37] D. Vick, V. Sauer, A. Fraser, M. Freeman, and W. Hiebert, "Bulk focused ion beam fabrication with three-dimensional shape control of nanoelectromechanical systems," *Journal of Micromechanics and Microengineering*, vol. 20, no. 10, p. 105005, 2010.

[38] W. J. Tanski, "Method for post fabrication frequency trimming of surface acoustic wave devices," Dec. 14 1982. US Patent 4,364,016.

[39] R. C. Ruby, "Post-fabrication tuning of acoustic resonators," July 14 1998. US Patent 5,780,713.

[40] K. Wang, A.-C. Wong, W.-T. Hsu, and C.-C. Nguyen, "Frequency trimming and q-factor enhancement of micromechanical resonators via localized filament annealing," in *Proceedings of International Solid State Sensors and Actuators Conference (Transducers' 97)*, vol. 1, pp. 109–112, IEEE, 1997.

[41] F. Huang, S. Fouladi, and R. R. Mansour, "High- q tunable dielectric resonator filters using mems technology," *IEEE Transactions on Microwave Theory and Techniques*, vol. 59, no. 12, pp. 3401–3409, 2011.

[42] A. Norouzpour-Shirazi, M. Hodjat-Shamami, R. Tabrizian, and F. Ayazi, "Dynamic tuning of mems resonators via electromechanical feedback," *IEEE transactions on ultrasonics, ferroelectrics, and frequency control*, vol. 62, no. 1, pp. 129–137, 2015.

[43] E. Moore, D. Langley, M. Jussaume, L. Rederus, C. Lundell, R. Coutu, P. Collins, and L. Starman, "Srrs embedded with mems cantilevers to enable electrostatic tuning of the resonant frequency," *Experimental mechanics*, vol. 52, no. 4, pp. 395–403, 2012.

[44] K. B. Lee and Y.-H. Cho, "A triangular electrostatic comb array for micromechanical resonant frequency tuning," *Sensors and Actuators A: Physical*, vol. 70, no. 1, pp. 112–117, 1998.

[45] A. M. Elshurafa, K. Khirallah, H. H. Tawfik, A. Emira, A. K. A. Aziz, and S. M. Sedky, "Nonlinear dynamics of spring softening and hardening in folded-mems comb drive resonators," *Journal of Microelectromechanical Systems*, vol. 20, no. 4, pp. 943–958, 2011.

[46] U. Hofmann, J. Janes, and H.-J. Quenzer, "High-q mems resonators for laser beam scanning displays," *Micromachines*, vol. 3, no. 2, pp. 509–528, 2012.

[47] W. C. Tang, T.-C. H. Nguyen, M. W. Judy, and R. T. Howe, "Electrostatic-comb drive of lateral polysilicon resonators," *Sensors and Actuators A: Physical*, vol. 21, no. 1-3, pp. 328–331, 1990.

[48] T. Remtema and L. Lin, "Active frequency tuning for micro resonators by localized thermal stressing effects," *Sensors and Actuators A: Physical*, vol. 91, no. 3, pp. 326–332, 2001.

[49] V. Pini, J. Tamayo, E. Gil-Santos, D. Ramos, P. Kosaka, H.-D. Tong, C. van Rijn, and M. Calleja, "Shedding light on axial stress effect on resonance frequencies of nanocantilevers," *Acs Nano*, vol. 5, no. 6, pp. 4269–4275, 2011.

[50] R. B. Karabalin, L. Villanueva, M. Matheny, J. E. Sader, and M. L. Roukes, "Stress-induced variations in the stiffness of micro-and nanocantilever beams," *Physical review letters*, vol. 108, no. 23, p. 236101, 2012.

[51] D. Southworth, L. Bellan, Y. Linzon, H. Craighead, and J. Parpia, "Stress-based vapor sensing using resonant microbridges," *Applied physics letters*, vol. 96, no. 16, p. 163503, 2010.

[52] S. S. Verbridge, D. F. Shapiro, H. G. Craighead, and J. M. Parpia, "Macroscopic tuning of nanomechanics: substrate bending for reversible control of frequency and quality factor of nanostring resonators," *Nano Letters*, vol. 7, no. 6, pp. 1728–1735, 2007.

[53] M. E. Warwick and R. Binions, "Advances in thermochromic vanadium dioxide films," *Journal of Materials Chemistry A*, vol. 2, no. 10, pp. 3275–3292, 2014.

[54] N. Sepúlveda, A. Rúa, R. Cabrera, and F. Fernández, "Young's modulus of vo_2 thin films as a function of temperature including insulator-to-metal transition regime," *Applied Physics Letters*, vol. 92, no. 19, p. 191913, 2008.

[55] T. Maruyama and Y. Ikuta, "Vanadium dioxide thin films prepared by chemical vapour deposition from vanadium (iii) acetylacetonate," *Journal of materials science*, vol. 28, no. 18, pp. 5073–5078, 1993.

[56] D. Yin, N. Xu, J. Zhang, and X. Zheng, "High quality vanadium dioxide films prepared by an inorganic sol-gel method," *Materials research bulletin*, vol. 31, no. 3, pp. 335–340, 1996.

[57] G. A. Nyberg and R. A. Buhrman, "Vanadium dioxide film deposition," Mar. 31 1987. US Patent 4,654,231.

[58] H. Takei and S. Koide, "Growth and electrical properties of vanadium-oxide single crystals by oxychrolide decomposition method," *Journal of the Physical Society of Japan*, vol. 21, no. 5, pp. 1010–1010, 1966.

[59] J. Bae, T. An, Y. Kim, and C. Ryu, "Analysis of digital load cell using 2.4 ghz band's zig-bee," in *2008 3rd IEEE Conference on Industrial Electronics and Applications*, pp. 1358–1361, IEEE, 2008.

[60] R. Srivastava and J. Chattopadhyay, "Design and fabrication of nanomaterial-based device for pressure sensorial applications," in *Advanced Nanomaterials in Biomedical, Sensor and Energy Applications*, pp. 1–14, Springer, 2017.

[61] Z. Zhan, R. Lin, V.-T. Tran, J. An, Y. Wei, H. Du, T. Tran, and W. Lu, "Paper/carbon nanotube-based wearable pressure sensor for physiological signal acquisition and soft robotic skin," *ACS applied materials & interfaces*, vol. 9, no. 43, pp. 37921–37928, 2017.

[62] S. R. Larimi, H. R. Nejad, M. Oyatsi, A. O'Brien, M. Hoorfar, and H. Najjaran, "Low-cost ultra-stretchable strain sensors for monitoring human motion and bio-signals," *Sensors and Actuators A: Physical*, vol. 271, pp. 182–191, 2018.

[63] D. Y. Choi, M. H. Kim, Y. S. Oh, S.-H. Jung, J. H. Jung, H. J. Sung, H. W. Lee, and H. M. Lee, "Highly stretchable, hysteresis-free ionic liquid-based strain sensor for precise human motion monitoring," *ACS applied materials & interfaces*, vol. 9, no. 2, pp. 1770–1780, 2017.

[64] A. Razak, A. Hadi, A. Zayegh, R. K. Begg, and Y. Wahab, "Foot plantar pressure measurement system: A review," *Sensors*, vol. 12, no. 7, pp. 9884–9912, 2012.

[65] X. Liao, Z. Zhang, Q. Liang, Q. Liao, and Y. Zhang, "Flexible, cuttable, and self-waterproof bending strain sensors using microcracked gold nanofilms@ paper substrate," *ACS applied materials & interfaces*, vol. 9, no. 4, pp. 4151–4158, 2017.

[66] A. M. Almassri, W. Wan Hasan, S. A. Ahmad, A. J. Ishak, A. Ghazali, D. Talib, and C. Wada, "Pressure sensor: State of the art, design, and application for robotic hand," *Journal of Sensors*, vol. 2015, 2015.

[67] S. Chen, Y. Wei, S. Wei, Y. Lin, and L. Liu, "Ultrasensitive cracking-assisted strain sensors based on silver nanowires/graphene hybrid particles," *ACS applied materials & interfaces*, vol. 8, no. 38, pp. 25563–25570, 2016.

[68] S. Gong, D. T. Lai, B. Su, K. J. Si, Z. Ma, L. W. Yap, P. Guo, and W. Cheng, "Highly stretchy black gold e-skin nanopatches as highly sensitive wearable biomedical sensors," *Advanced Electronic Materials*, vol. 1, no. 4, p. 1400063, 2015.

[69] L. Wang, Y. Chen, L. Lin, H. Wang, X. Huang, H. Xue, and J. Gao, "Highly stretchable, anti-corrosive and wearable strain sensors based on the pdms/cnts decorated elastomer nanofiber composite," *Chemical Engineering Journal*, vol. 362, pp. 89–98, 2019.

[70] T. Yamada, Y. Hayamizu, Y. Yamamoto, Y. Yomogida, A. Izadi-Najafabadi, D. N. Futaba, and K. Hata, "A stretchable carbon nanotube strain sensor for human-motion detection," *Nature nanotechnology*, vol. 6, no. 5, p. 296, 2011.

[71] Z. Yang, Y. Pang, X.-l. Han, Y. Yang, J. Ling, M. Jian, Y. Zhang, Y. Yang, and T.-L. Ren, "Graphene textile strain sensor with negative resistance variation for human motion detection," *ACS nano*, vol. 12, no. 9, pp. 9134–9141, 2018.

[72] Y. Zhu, H. Cai, H. Ding, N. Pan, and X. Wang, "Fabrication of low-cost and highly sensitive graphene-based pressure sensor by direct laser scribing polydimethylsiloxane," *ACS applied materials & interfaces*, 2019.

[73] H. Shi, T. Pinto, Y. Zhang, C. Wang, and X. Tan, "Soft capacitive sensors for measurement of both positive and negative pressures," in *Nano-, Bio-, Info-Tech Sensors, and 3D Systems II*, vol. 10597, p. 105971E, International Society for Optics and Photonics, 2018.

[74] H. Shi, M. Al-Rubaiai, C. M. Holbrook, J. Miao, T. Pinto, C. Wang, and X. Tan, "Screen-printed soft capacitive sensors for spatial mapping of both positive and negative pressures," *Advanced Functional Materials*, p. 1809116, 2019.

[75] X. Wang, L. Dong, H. Zhang, R. Yu, C. Pan, and Z. L. Wang, "Recent progress in electronic skin," *Advanced Science*, vol. 2, no. 10, p. 1500169, 2015.

[76] S.-J. Woo, J.-H. Kong, D.-G. Kim, and J.-M. Kim, "A thin all-elastomeric capacitive pressure sensor array based on micro-contact printed elastic conductors," *Journal of Materials Chemistry C*, vol. 2, no. 22, pp. 4415–4422, 2014.

[77] M. I. Tiwana, S. J. Redmond, and N. H. Lovell, "A review of tactile sensing technologies with applications in biomedical engineering," *Sensors and Actuators A: physical*, vol. 179, pp. 17–31, 2012.

[78] Z. L. Wang and J. Song, "Piezoelectric nanogenerators based on zinc oxide nanowire arrays," *Science*, vol. 312, no. 5771, pp. 242–246, 2006.

[79] Y.-F. Lin, J. Song, Y. Ding, S.-Y. Lu, and Z. L. Wang, "Piezoelectric nanogenerator using cds nanowires," *Applied Physics Letters*, vol. 92, no. 2, p. 022105, 2008.

[80] K.-I. Park, J. H. Son, G.-T. Hwang, C. K. Jeong, J. Ryu, M. Koo, I. Choi, S. H. Lee, M. Byun, and Z. L. Wang, "Highly-efficient, flexible piezoelectric pzt thin film nanogenerator on plastic substrates," *Advanced materials*, vol. 26, no. 16, pp. 2514–2520, 2014.

[81] M. Ha, J. Park, Y. Lee, and H. Ko, "Triboelectric generators and sensors for self-powered wearable electronics," *Acs Nano*, vol. 9, no. 4, pp. 3421–3427, 2015.

[82] J. H. Jung, M. Lee, J.-I. Hong, Y. Ding, C.-Y. Chen, L.-J. Chou, and Z. L. Wang, "Lead-free nanbo3 nanowires for a high output piezoelectric nanogenerator," *ACS nano*, vol. 5, no. 12, pp. 10041–10046, 2011.

[83] S.-H. Shin, Y.-H. Kim, M. H. Lee, J.-Y. Jung, and J. Nah, "Hemispherically aggregated batio$_3$ nanoparticle composite thin film for high-performance flexible piezoelectric nanogenerator," *Acs Nano*, vol. 8, no. 3, pp. 2766–2773, 2014.

[84] K.-I. Park, M. Lee, Y. Liu, S. Moon, G.-T. Hwang, G. Zhu, J. E. Kim, S. O. Kim, D. K. Kim, and Z. L. Wang, "Flexible nanocomposite generator made of batio$_3$ nanoparticles and graphitic carbons," *Advanced Materials*, vol. 24, no. 22, pp. 2999–3004, 2012.

[85] Y. Zang, F. Zhang, C.-a. Di, and D. Zhu, "Advances of flexible pressure sensors toward artificial intelligence and health care applications," *Materials Horizons*, vol. 2, no. 2, pp. 140–156, 2015.

[86] Q. Jing and S. Kar-Narayan, "Nanostructured polymer-based piezoelectric and triboelectric materials and devices for energy harvesting applications," *Journal of Physics D: Applied Physics*, vol. 51, no. 30, p. 303001, 2018.

[87] Y. Hu and Z. Zheng, "Progress in textile-based triboelectric nanogenerators for smart fabrics," *Nano energy*, vol. 56, pp. 16–24, 2019.

[88] X. Wang, H. Zhang, L. Dong, X. Han, W. Du, J. Zhai, C. Pan, and Z. L. Wang, "Self-powered high-resolution and pressure-sensitive triboelectric sensor matrix for real-time tactile mapping," *Advanced Materials*, vol. 28, no. 15, pp. 2896–2903, 2016.

[89] Y.-C. Lai, J. Deng, R. Liu, Y.-C. Hsiao, S. L. Zhang, W. Peng, H.-M. Wu, X. Wang, and Z. L. Wang, "Actively perceiving and responsive soft robots enabled by self-powered, highly extensible, and highly sensitive triboelectric proximity-and pressure-sensing skins," *Advanced Materials*, vol. 30, no. 28, p. 1801114, 2018.

[90] C. Yeom, K. Chen, D. Kiriya, Z. Yu, G. Cho, and A. Javey, "Large-area compliant tactile sensors using printed carbon nanotube active-matrix backplanes," *Advanced Materials*, vol. 27, no. 9, pp. 1561–1566, 2015.

[91] S. Park, G. Pitner, G. Giri, J. H. Koo, J. Park, K. Kim, H. Wang, R. Sinclair, H.-S. P. Wong, and Z. Bao, "Large-area assembly of densely aligned single-walled carbon nanotubes using solution shearing and their application to field-effect transistors," *Advanced Materials*, vol. 27, no. 16, pp. 2656–2662, 2015.

[92] E. Mu, Z. Wu, Z. Wu, X. Chen, Y. Liu, X. Fu, and Z. Hu, "A novel self-powering ultrathin teg device based on micro/nano emitter for radiative cooling," *Nano Energy*, vol. 55, pp. 494–500, 2019.

[93] S. Sun, D. Ning, J. Yang, H. Du, S. Zhang, W. Li, and M. Nakano, "Development of an mr seat suspension with self-powered generation capability," *Smart Materials and Structures*, vol. 26, no. 8, p. 085025, 2017.

[94] X. Chen, K. Parida, J. Wang, J. Xiong, M.-F. Lin, J. Shao, and P. S. Lee, "A stretchable and transparent nanocomposite nanogenerator for self-powered physiological monitoring," *ACS Appl. Mater. & Interfaces*, vol. 9, no. 48, pp. 42200–42209, 2017.

[95] C. Shen, S. Xu, Y. Xie, M. Sanghadasa, X. Wang, and L. Lin, "A review of on-chip micro supercapacitors for integrated self-powering systems," *Journal of Microelectromechanical Systems*, vol. 26, no. 5, pp. 949–965, 2017.

[96] M. J. Talite, H.-Y. Huang, Y.-H. Wu, P. G. Sena, K.-B. Cai, T.-N. Lin, J.-L. Shen, W.-C. Chou, and C.-T. Yuan, "Greener luminescent solar concentrators with high loading contents based on in situ cross-linked carbon nanodots for enhancing solar energy harvesting and resisting concentration-induced quenching," *ACS Appl. Mater. & Interfaces*, vol. 10, no. 40, pp. 34184–34192, 2018.

[97] R. Li, X. Xiang, X. Tong, J. Zou, and Q. Li, “Wearable double-twisted fibrous perovskite solar cell,” *Advanced Materials*, vol. 27, no. 25, pp. 3831–3835, 2015.

[98] M. Thielen, L. Sigrist, M. Magno, C. Hierold, and L. Benini, “Human body heat for powering wearable devices: From thermal energy to application,” *Energy Conversion and Management*, vol. 131, pp. 44–54, 2017.

[99] V. Kotipalli, Z. Gong, P. Pathak, T. Zhang, Y. He, S. Yadav, and L. Que, “Light and thermal energy cell based on carbon nanotube films,” *Appl. Physics Letters*, vol. 97, no. 12, p. 124102, 2010.

[100] S. P. Beeby, M. J. Tudor, and N. White, “Energy harvesting vibration sources for microsystems applications,” *Measurement Science and Technology*, vol. 17, no. 12, p. R175, 2006.

[101] A. C. Turkmen and C. Celik, “Energy harvesting with the piezoelectric material integrated shoe,” *Energy*, vol. 150, pp. 556–564, 2018.

[102] C. Lagomarsini, C. Jean-Mistral, G. Lombardi, and A. Sylvestre, “Hybrid piezoelectric-electrostatic generators for wearable energy harvesting applications,” *Smart Materials and Structures*, vol. 28, p. 035003, 2018.

[103] G. Zhu, Z.-H. Lin, Q. Jing, P. Bai, C. Pan, Y. Yang, Y. Zhou, and Z. L. Wang, “Toward large-scale energy harvesting by a nanoparticle-enhanced triboelectric nanogenerator,” *Nano letters*, vol. 13, no. 2, pp. 847–853, 2013.

[104] Y. Huan, X. Zhang, J. Song, Y. Zhao, T. Wei, G. Zhang, and X. Wang, “High-performance piezoelectric composite nanogenerator based on ag/(k, na) nbo3 heterostructure,” *Nano energy*, vol. 50, pp. 62–69, 2018.

[105] H. Parangusan, D. Ponnamma, and M. A. A. Al-Maadeed, “Stretchable electrospun pvdf-hfp/co-zno nanofibers as piezoelectric nanogenerators,” *Scientific Reports*, vol. 8, no. 1, p. 754, 2018.

[106] X.-S. Zhang, M.-D. Han, R.-X. Wang, F.-Y. Zhu, Z.-H. Li, W. Wang, and H.-X. Zhang, “Frequency-multiplication high-output triboelectric nanogenerator for sustainably powering biomedical microsystems,” *Nano Letters*, vol. 13, no. 3, pp. 1168–1172, 2013.

[107] J. Chun, J. W. Kim, W.-s. Jung, C.-Y. Kang, S.-W. Kim, Z. L. Wang, and J. M. Baik, “Mesoporous pores impregnated with au nanoparticles as effective dielectrics for enhancing triboelectric nanogenerator performance in harsh environments,” *Energy & Environmental Science*, vol. 8, no. 10, pp. 3006–3012, 2015.

[108] R. Zhang, M. Hummelgard, J. Ortegren, M. Olsen, H. Andersson, Y. Yang, and H. Olin, “Human body constituted triboelectric nanogenerators as energy harvesters, code transmitters, and motion sensors,” *ACS Appl. Energy Materials*, vol. 1, no. 6, pp. 2955–2960, 2018.

[109] X. Zhao, Z. Kang, Q. Liao, Z. Zhang, M. Ma, Q. Zhang, and Y. Zhang, “Ultralight, self-powered and self-adaptive motion sensor based on triboelectric nanogenerator for perceptual layer application in internet of things,” *Nano Energy*, vol. 48, pp. 312–319, 2018.

[110] Y. Zhang, C. R. Bowen, S. K. Ghosh, D. Mandal, H. Khanbareh, M. Arafa, and C. Wan, “Ferroelectret materials and devices for energy harvesting applications,” *Nano Energy*, vol. 57, pp. 118–140, 2019.

[111] S. K. Ghosh, M. Xie, C. R. Bowen, P. R. Davies, D. J. Morgan, and D. Mandal, “A hybrid strain and thermal energy harvester based on an infra-red sensitive er 3+ modified poly (vinylidene fluoride) ferroelectret structure,” *Scientific reports*, vol. 7, no. 1, p. 16703, 2017.

[112] Z. L. Wang, “On maxwell’s displacement current for energy and sensors: The origin of nanogenerators,” *Materials Today*, vol. 20, no. 2, pp. 74–82, 2017.

[113] N. Sepúlveda, A. Rúa, R. Cabrera, and F. E. Fernández, “Young’s modulus of vo_2 thin films as a function of temperature including insulator-to-metal transition regime,” *J. Appl. Phys Lett.*, vol. 92, 2008.

[114] F. Beer, “Johnston er jr,” *Mechanics of Materials. Toronto: McGraw-Hill Ryerson*, 1981.

[115] J. Song, Y. Huang, J. Xiao, S. Wang, K. Hwang, H. Ko, D.-H. Kim, M. Stoykovich, and J. Rogers, “Mechanics of noncoplanar mesh design for stretchable electronic circuits,” *Journal of Applied Physics*, vol. 105, no. 12, p. 123516, 2009.

[116] W. Fang, C.-H. Lee, and H.-H. Hu, “On the buckling behavior of micromachined beams,” *Journal of Micromechanics and Microengineering*, vol. 9, no. 3, p. 236, 1999.

[117] B. Bhushan, S. Murarka, and J. Gerlach, “Stress in silicon dioxide films deposited using chemical vapor deposition techniques and the effect of annealing on these stresses,” *Journal of Vacuum Science & Technology B: Microelectronics Processing and Phenomena*, vol. 8, no. 5, pp. 1068–1074, 1990.

[118] K.-Y. Tsai, T.-S. Chin, and H.-P. D. Shieh, “Effect of grain curvature on nano-indentation measurements of thin films,” *Japanese journal of applied physics*, vol. 43, no. 9R, p. 6268, 2004.

[119] P. Jin, S. Nakao, S. Tanemura, T. Bell, L. Wielunski, and M. Swain, “Characterization of mechanical properties of vo_2 thin films on sapphire and silicon by ultra-microindentation,” *Thin Solid Films*, vol. 343, pp. 134–137, 1999.

[120] R. Heckingbottom and J. Linnett, “Structure of vanadium dioxide,” *Nature*, vol. 194, no. 4829, p. 678, 1962.

[121] J. Wei, Z. Wang, W. Chen, and D. H. Cobden, "New aspects of the metal–insulator transition in single-domain vanadium dioxide nanobeams," *Nature nanotechnology*, vol. 4, no. 7, p. 420, 2009.

[122] E. Merced, R. Cabrera, H. Coy, F. E. Fernández, and N. Sepúlveda, "Frequency tuning of vo$_2$-coated buckled microbridges," *Journal of Microelectromechanical Systems*, vol. 20, no. 3, pp. 558–560, 2011.

[123] K. Kirjavainen, "Electromechanical film and procedure for manufacturing same," Mar. 31 1987. US Patent 4,654,546.

[124] J. Lekkala and M. Paajanen, "Emfi-new electret material for sensors and actuators," in *Electrets, 1999. ISE 10. Proceedings. 10th International Symposium on*, pp. 743–746, IEEE, 1999.

[125] M. Paajanen, H. Välimäki, and J. Lekkala, "Modelling the electromechanical film (emfi)," *Journal of Electrostatics*, vol. 48, no. 3-4, pp. 193–204, 2000.

[126] M. Paajanen, J. Lekkala, and K. Kirjavainen, "Electromechanical film (emfi) - a new multipurpose electret material," *Sensors and Actuators A: Physical*, vol. 84, no. 1-2, pp. 95–102, 2000.

[127] M. Wegener and S. Bauer, "Microstorms in cellular polymers: A route to soft piezoelectric transducer materials with engineered macroscopic dipoles," *ChemPhysChem*, vol. 6, no. 6, pp. 1014–1025, 2005.

[128] J. Döring, V. Bovtun, M. Gaal, J. Bartusch, A. Erhard, M. Kreutzbruck, and Y. Yakymenko, "Piezoelectric and electrostrictive effects in ferroelectret ultrasonic transducers," *Journal of Applied Physics*, vol. 112, no. 8, p. 084505, 2012.

[129] R. Melamud, S. A. Chandorkar, B. Kim, H. K. Lee, J. C. Salvia, G. Bahl, M. A. Hopcroft, and T. W. Kenny, "Temperature-insensitive composite micromechanical resonators," *Journal of Microelectromechanical Systems*, vol. 18, no. 6, pp. 1409–1419, 2009.

[130] R. B. Karabalin, L. Villanueva, M. Matheny, J. E. Sader, and M. L. Roukes, "Stress-induced variations in the stiffness of micro-and nanocantilever beams," *Physical review letters*, vol. 108, no. 23, p. 236101, 2012.

[131] P. Lu, H. Lee, C. Lu, and S. O'shea, "Surface stress effects on the resonance properties of cantilever sensors," *Physical Review B*, vol. 72, no. 8, p. 085405, 2005.

[132] M. J. Lachut and J. E. Sader, "Effect of surface stress on the stiffness of cantilever plates," *Physical review letters*, vol. 99, no. 20, p. 206102, 2007.

[133] G.-F. Wang and X.-Q. Feng, "Effects of surface elasticity and residual surface tension on the natural frequency of microbeams," *Applied physics letters*, vol. 90, no. 23, p. 231904, 2007.

[134] R. M. Jones, *Buckling of bars, plates, and shells.* Bull Ridge Corporation, 2006.

[135] Y. Cao and N. Sepúlveda, "Interface stress for bidirectional frequency tuning of prebuckled vanadium dioxide mems resonators," *Advanced Materials Interfaces*, p. 1900887, 2019.

[136] A. Rúa, F. E. Fernández, M. A. Hines, and N. Sepúlveda, "Study of the resonant frequencies of silicon microcantilevers coated with vanadium dioxide films during the insulator-to-metal transition," *Journal of Applied Physics*, vol. 107, no. 5, p. 053528, 2010.

[137] R. Cabrera, E. Merced, N. Sepúlveda, and F. E. Fernández, "Dynamics of photothermally driven vo2-coated microcantilevers," *Journal of Applied Physics*, 2011.

[138] E. Merced, N. Dávila, D. Torres, R. Cabrera, F. E. Fernández, and N. Sepúlveda, "Photothermal actuation of v o2: Cr-coated microcantilevers in air and aqueous media," *Smart Materials and Structures*, vol. 21, no. 10, p. 105009, 2012.

[139] H. Ma, J. Hou, X. Wang, J. Zhang, Z. Yuan, L. Xiao, Y. Wei, S. Fan, K. Jiang, and K. Liu, "Flexible, all-inorganic actuators based on vanadium dioxide and carbon nanotube bimorphs," *Nano letters*, vol. 17, no. 1, pp. 421–428, 2016.

[140] N. Manca, L. Pellegrino, T. Kanki, S. Yamasaki, H. Tanaka, A. S. Siri, and D. Marré, "Programmable mechanical resonances in mems by localized joule heating of phase change materials," *Advanced Materials*, vol. 25, no. 44, pp. 6430–6435, 2013.

[141] K. Okimura, N. Hanis Azhan, T. Hajiri, S.-i. Kimura, M. Zaghrioui, and J. Sakai, "Temperature-dependent raman and ultraviolet photoelectron spectroscopy studies on phase transition behavior of vo2 films with m1 and m2 phases," *Journal of Applied Physics*, vol. 115, no. 15, p. 153501, 2014.

[142] A. Cavalleri, T. Dekorsy, H. H. Chong, J.-C. Kieffer, and R. W. Schoenlein, "Evidence for a structurally-driven insulator-to-metal transition in vo 2: A view from the ultrafast timescale," *Physical Review B*, vol. 70, no. 16, p. 161102, 2004.

[143] M. M. Qazilbash, A. Tripathi, A. Schafgans, B.-J. Kim, H.-T. Kim, Z. Cai, M. Holt, J. Maser, F. Keilmann, O. Shpyrko, *et al.*, "Nanoscale imaging of the electronic and structural transitions in vanadium dioxide," *Physical Review B*, vol. 83, no. 16, p. 165108, 2011.

[144] K. Ito, K. Nishikawa, and H. Iizuka, "Multilevel radiative thermal memory realized by the hysteretic metal-insulator transition of vanadium dioxide," *Applied Physics Letters*, vol. 108, no. 5, p. 053507, 2016.

[145] Y. V. Pershin and M. Di Ventra, "Memory effects in complex materials and nanoscale systems," *Advances in Physics*, vol. 60, no. 2, pp. 145–227, 2011.

[146] S. Choi, B.-J. Kim, Y. W. Lee, Y. S. Lim, J. Choi, and H.-T. Kim, “Control of current-jump induced by voltage, temperature, light in p-type gaas: Programmable critical temperature sensor,” *Applied Physics Letters*, vol. 95, no. 23, p. 231910, 2009.

[147] K. M. Guskiewicz, J. P. Mihalik, V. Shankar, S. W. Marshall, D. H. Crowell, S. M. Oliaro, M. F. Ciocca, and D. N. Hooker, “Measurement of head impacts in collegiate football players: relationship between head impact biomechanics and acute clinical outcome after concussion,” *Neurosurgery*, vol. 61, no. 6, pp. 1244–1253, 2007.

[148] D. Gever, “Any football helmet hit can cause potential concussion,” *MedPage Today. Retrieved*, pp. 02–27, 2008.

[149] P. Rousseau, A. Post, and T. Hoshizaki, “The effects of impact management materials in ice hockey helmets on head injury criteria,” *Proceedings of the Institution of Mechanical Engineers, Part P: Journal of Sports Engineering and Technology*, vol. 223, no. 4, pp. 159–165, 2009.

[150] M. Mackay, “The increasing importance of the biomechanics of impact trauma,” *Sadhana*, vol. 32, no. 4, pp. 397–408, 2007.

[151] J. McElhaney, “Head injury criteria,” *Mechanics of Composite Materials*, vol. 12, no. 3, pp. 411–429, 1976.

[152] H.-W. Henn, “Crash tests and the head injury criterion,” *Teaching mathematics and its applications*, vol. 17, no. 4, pp. 162–170, 1998.

[153] R. P. Ching, “Relationship between head mass and circumference in human adults,” *University of Washington. Technical Brief*, 2007.

[154] P. J. Petersan and S. M. Anlage, “Measurement of resonant frequency and quality factor of microwave resonators: Comparison of methods,” *J. Appl. Phys*, vol. 84, p. 3392, Sep 1998.

[155] R. B. Karabalin, L. G. Villanueva, M. H. Matheny, J. E. Sader, and M. L. Roukes, “Stress-induced variations in the stiffness of micro- and nanocantilever beams,” *Phys. Rev. Lett*, vol. 108, p. 236101, Jun 2012.

[156] X. Wang, S. Niu, Y. Yin, F. Yi, Z. You, and Z. L. Wang, “Triboelectric nanogenerator based on fully enclosed rolling spherical structure for harvesting low-frequency water wave energy,” *Advanced Energy Materials*, vol. 5, no. 24, p. 1501467, 2015.

[157] R. H. Brown, “Piezo film: Form and function,” *Sensors And Actuators A: Physical*, vol. 22, no. 1-3, pp. 729–733, 1990.

[158] F. Viola, P. Romano, R. Miceli, G. Acciari, and C. Spataro, “Piezoelectric model of rainfall energy harvester,” in *2014 Ninth International Conference on Ecological Vehicles and Renewable Energies (EVER)*, pp. 1–7, IEEE, 2014.

[159] Y. Yang, H. Wu, and C. K. Soh, “Experiment and modeling of a two-dimensional piezoelectric energy harvester,” *Smart Materials and Structures*, vol. 24, no. 12, p. 125011, 2015.

[160] Y. Shu and I. Lien, “Analysis of power output for piezoelectric energy harvesting systems,” *Smart materials and structures*, vol. 15, no. 6, p. 1499, 2006.

[161] Y. Cao, W. Li, and N. Sepúlveda, “Performance of self-powered, water-resistant bending sensor using transverse piezoelectric effect of polypropylene ferroelectret polymer,” *IEEE Sensors Journal*, pp. 1–1, 2019.

[162] L. Persano, C. Dagdeviren, Y. Su, Y. Zhang, S. Girardo, D. Pisignano, Y. Huang, and J. A. Rogers, “High performance piezoelectric devices based on aligned arrays of nanofibers of poly (vinylidenefluoride-co-trifluoroethylene),” *Nature communications*, vol. 4, p. 1633, 2013.

[163] Y. Su, C. Dagdeviren, and R. Li, “Measured output voltages of piezoelectric devices depend on the resistance of voltmeter,” *Advanced Functional Materials*, vol. 25, no. 33, pp. 5320–5325, 2015.

[164] Y. Cao, J. Figueroa, W. Li, Z. Chen, Z. Wang, and S. Nelson, “Understanding the dynamic response in ferroelectret nanogenerators to enable self-powered tactile systems and human-controlled micro-robot,” *Nano Energy*.

[165] V. Nguyen and R. Yang, “Effect of humidity and pressure on the triboelectric nanogenerator,” *Nano Energy*, vol. 2, no. 5, pp. 604–608, 2013.

[166] S. Pence, V. Novotny, and A. Diaz, “Effect of surface moisture on contact charge of polymers containing ions,” *Langmuir*, vol. 10, no. 2, pp. 592–596, 1994.

[167] E. Németh, V. Albrecht, G. Schubert, and F. Simon, “Polymer tribo-electric charging: dependence on thermodynamic surface properties and relative humidity,” *Journal of Electrostatics*, vol. 58, no. 1-2, pp. 3–16, 2003.

[168] Y. Cao, J. Figueroa, J. Pastrana, W. Li, Z. Chen, Z. Wang, and N. Sepulveda, “Flexible ferroelectret polymer for self-powering devices and energy storage systems,” *ACS applied materials & interfaces*, 2019.

[169] X. Zhang, P. Pondrom, G. M. Sessler, and X. Ma, “Ferroelectret nanogenerator with large transverse piezoelectric activity,” *Nano energy*, vol. 50, pp. 52–61, 2018.

[170] L. Xie and M. Cai, “Increased piezoelectric energy harvesting from human footstep motion by using an amplification mechanism,” *Appl. Physics Letters*, vol. 105, no. 14, p. 143901, 2014.

[171] N. Wu, Q. Wang, and X. Xie, “Ocean wave energy harvesting with a piezoelectric coupled buoy structure,” *Applied Ocean Research*, vol. 50, pp. 110–118, 2015.

[172] J. Zhang, Z. Fang, C. Shu, J. Zhang, Q. Zhang, and C. Li, "A rotational piezoelectric energy harvester for efficient wind energy harvesting," *Sensors and Actuators A: Physical*, vol. 262, pp. 123–129, 2017.

[173] T. Chen, Y. Xia, W. Liu, H. Liu, L. Sun, and C. Lee, "A hybrid flapping-blade wind energy harvester based on vortex shedding effect," *Journal of Microelectromechanical Systems*, vol. 25, no. 5, pp. 845–847, 2016.

[174] S. D. Senturia, *Microsystem design*. Springer Science & Business Media, 2007.

[175] S. Kärki and J. Lekkala, "A lumped-parameter transducer model for piezoelectric and ferroelectret polymers," *Measurement*, vol. 45, no. 3, pp. 453–458, 2012.

[176] S. Wang, Z.-H. Lin, S. Niu, L. Lin, Y. Xie, K. C. Pradel, and Z. L. Wang, "Motion charged battery as sustainable flexible-power-unit," *ACS Nano*, vol. 7, no. 12, pp. 11263–11271, 2013.

[177] S. Niu, X. Wang, F. Yi, Y. S. Zhou, and Z. L. Wang, "A universal self-charging system driven by random biomechanical energy for sustainable operation of mobile electronics," *Nature Communications*, vol. 6, p. 8975, 2015.

[178] L. Wu, X.-D. Do, S.-G. Lee, and D. S. Ha, "A self-powered and optimal sshi circuit integrated with an active rectifier for piezoelectric energy harvesting," *IEEE Transactions on Circuits and Systems I: Regular Papers*, vol. 64, no. 3, pp. 537–549, 2017.

[179] D. Guyomar, A. Badel, E. Lefeuvre, and C. Richard, "Toward energy harvesting using active materials and conversion improvement by nonlinear processing," *IEEE Transactions on Ultrasonics, Ferroelectrics, and Frequency Control*, vol. 52, no. 4, pp. 584–595, 2005.

[180] G. K. Ottman, H. F. Hofmann, and G. A. Lesieutre, "Optimized piezoelectric energy harvesting circuit using step-down converter in discontinuous conduction mode," *IEEE Transactions on Power Electronics*, vol. 18, no. 2, pp. 696–703, 2003.

[181] H. Kim, S. Priya, H. Stephanou, and K. Uchino, "Consideration of impedance matching techniques for efficient piezoelectric energy harvesting," *IEEE transactions on Ultrasonics, Ferroelectrics, and Frequency Control*, vol. 54, no. 9, pp. 1851–1859, 2007.